Max-Planck-Institut
für Meteorologie

MAX-PLANCK-GESELLSCHAFT

International Max Planck Research School
on Earth System Modelling

Evaluating the state-of-the-art of and Errors in 1D Satellite Cloud Liquid Water Path Retrievals with Large Eddy Simulations and Realistic Radiative Transfer Models

Chellappan Seethala

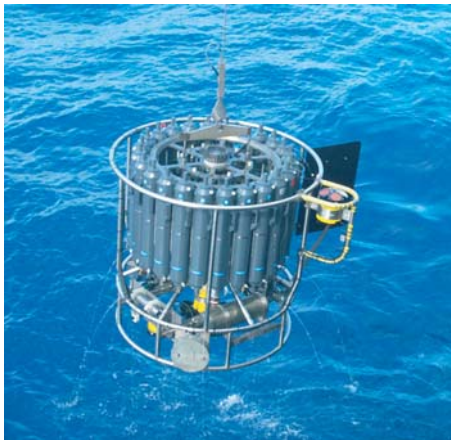

Berichte zur Erdsystemforschung 110
2012

Reports on Earth System Science

Hinweis

Die Berichte zur Erdsystemforschung werden vom Max-Planck-Institut für Meteorologie in Hamburg in unregelmäßiger Abfolge herausgegeben.

Sie enthalten wissenschaftliche und technische Beiträge, inklusive Dissertationen.

Die Beiträge geben nicht notwendigerweise die Auffassung des Instituts wieder.

Die "Berichte zur Erdsystemforschung" führen die vorherigen Reihen "Reports" und "Examensarbeiten" weiter.

Notice

The Reports on Earth System Science are published by the Max Planck Institute for Meteorology in Hamburg. They appear in irregular intervals.

They contain scientific and technical contributions, including Ph. D. theses.

The Reports do not necessarily reflect the opinion of the Institute.

The "Reports on Earth System Science" continue the former "Reports" and "Examensarbeiten" of the Max Planck Institute.

Anschrift / Address

Max-Planck-Institut für Meteorologie
Bundesstrasse 53
20146 Hamburg
Deutschland

Tel.: +49-(0)40-4 11 73-0
Fax: +49-(0)40-4 11 73-298
Web: www.mpimet.mpg.de

Layout:

Bettina Diallo, PR & Grafik

Titelfotos:
vorne:
Christian Klepp - Jochem Marotzke - Christian Klepp
hinten:
Clotilde Dubois - Christian Klepp - Katsumasa Tanaka

Berichte zur Erdsystemforschung 110 2012

Evaluating the state-of-the-art of and Errors in 1D Satellite Cloud Liquid Water Path Retrievals with Large Eddy Simulations and Realistic Radiative Transfer Models

Chellappan Seethala

aus Indien

Hamburg 2012

Reports on Earth System Science 110 2012

ISSN 1614-1199

Chellappan Seethala
Max-Planck-Institut für Meteorologie
Bundesstrasse 53
20146 Hamburg

Als Dissertation angenommen
vom Department Geowissenschaften der Universität Hamburg

auf Grund der Gutachten von
Prof. Dr. Hartmut Graßl
und
Ákos Horváth, PhD

Hamburg, den 30. Januar 2012
Prof. Dr. Jürgen Oßenbrügge
Leiter des Departments für Geowissenschaften

ISSN 1614-1199

Evaluating the state-of-the-art of and Errors in 1D Satellite Cloud Liquid Water Path Retrievals with Large Eddy Simulations and Realistic Radiative Transfer Models

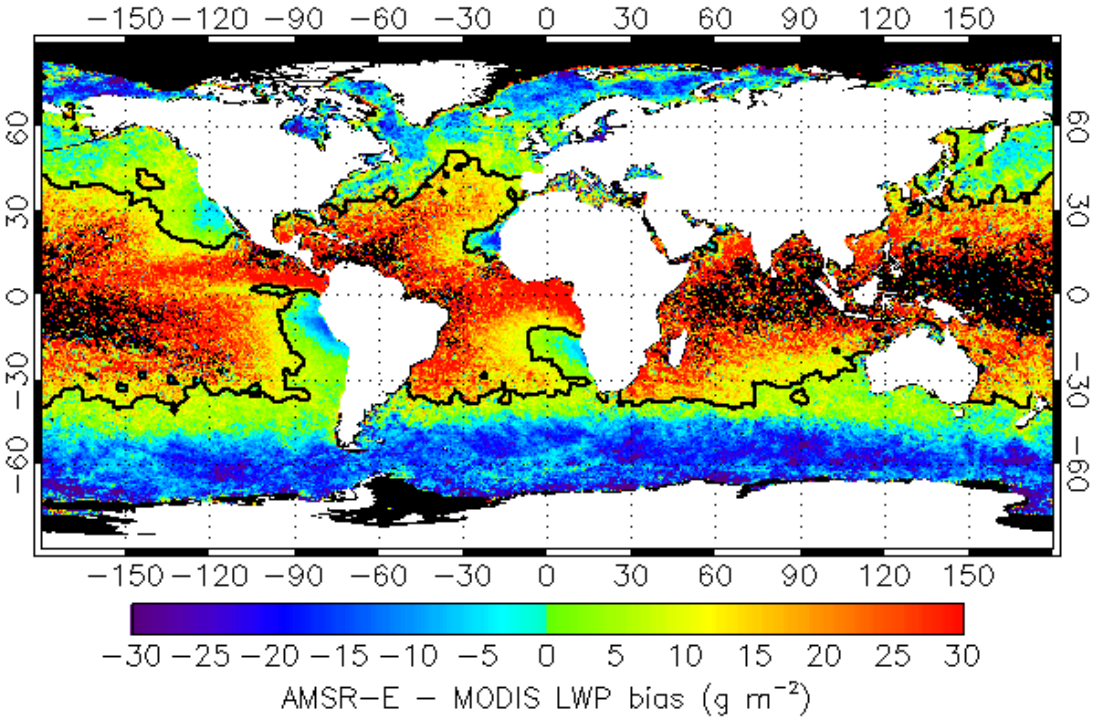

Chellappan Seethala

Hamburg 2012

Acknowledgements

I would like to pay my profound gratitude to my supervisor Dr. Ákos Horváth for his continuous guidance and for the invaluable discussions during the course. I was fascinated to his decisions which always placed me in a step forward. I thank you very much for understanding me and kindly helping me in all the situations.

My PhD advisory panel chair Prof. Hartmut Graßl and panel member Dr. Stefan Kinne were greatly acknowledged for their continuous monitoring and suggestions throughout the course. The person whom I admire most is Prof. Johannes Quaas for his kindness, help and discussions. I also acknowledge for the important discussions with Dr. Robert Pincus from University of Colorado and Dr. Ralf Bennartz from University of Wisconsin.

My PhD is funded by Marie Curie Reintegration project and partially by EUMETSAT CM-SAF Visiting Scientist project, and hereby I would like to acknowledge for both projects. Dr. Jan Fokke Meirink from the Royal Netherlands Meteorological Institute, Dr. Rob Roebeling from EUMETSAT, and Dr. Abhay Devasthale from the Swedish Meteorological and Hydrographical Institute were greatly acknowledged for their countless effort and support to undertake the six months Visiting Scientist Project at KNMI.

I would like to acknowledge Dr. Antje Weitz and Cornelia Kampmann for their kindness and support they offered to me on behalf of International Max Planck Research School and beyond. I would also like to use this opportunity to thank Prof. Bjorn Stevens for his valuable discussions and Angela Gruber for her kind support. In sum, I would like to express my thanks to the Max Planck Institute for Meteorology and International Max Planck Research School for providing me excellent venue and computational facility to perform this research.

The data I used in my dissertation is acknowledged here. The Aqua/Terra MODIS Level-2 data were obtained from http://ladsweb.nascom.nasa.gov/. AMSR-E and TMI data are available at http://www.remss.com/. OMI data is from http://mirador.gsfc.nasa.gov/. The KNMI CPP retrievals were provided by Dr. Jan Fokke Meirink. I thank Dr. Frank Evans for the radiative transfer code SHDOM and for making it available to public; the code is available in http://nit.colorado.edu/shdom/. The Large Eddy Simulations outputs were obtained from Thijs Heus, Irina Sandu, and Malte Reick.

I would like to thank Cathy Hohenegger, Thijs Heus, Juan Pedro Mellado, and Manu Anna Thomas for reading my dissertation chapters and providing me valuable comments. I thank Louise Nuijens and Katrin Lonitz for their discussions and helps during the course. I also would like to thank all my colleagues Verena Grützun, Karsten Peters, Suvarchal Kumar Cheedale, Daniel Klocke, Ritthik Bhattacharya, Malte Rieck, Adrial Valentine, Vera Schemann, etc., my officemates Stergios Misios, Jade Garcia, Anna Jaruga, and friends Natasha Sudarchikova, Armelle Reca Remedio, Harshi Weerasinghe, Swati Gehlot, and Pankaj Kumar Srivastava for giving me a lively environment to work and for their great friendship during the course. A hearty thanks to Elke Ludewig who was almost with me in all the occasions. The time we spend together was really wonderful and I will really miss you a lot.

I pay my thankfulness to Suraj Polade who always stood for me whenever I need his support. Without his care and moral support it could have been impossible for me to reach where I am today. I also send special thanks to my beloved brothers and sisters, especially to Dr. Gnanaseelan for paying their attention and motivating me in all my footsteps. I personally believe that my dissertation is purely an outcome of my parents' blessings and prayers, and hereby I dedicate this dissertation to them.

Hamburg, 17.11.2011 C. Seethala

Abstract

Liquid water path (LWP) is a crucial cloud parameter playing an important role in both atmospheric radiation and hydrology. Comparisons of observations and simulations found large and potentially systematic errors in both the global distribution and diurnal cycle of LWP. Unfortunately, the various observational datasets (microwave and visible/near-infrared) also showed considerable and as yet not fully explained discrepancies in this quantity. Operational visible/near-infrared (VNIR) retrieval algorithms have to reduce natural complexity by treating clouds as plane-parallel, homogeneous layers in order to be practical. The simultaneous presence of cloud liquid and rain poses a fundamental challenge to all microwave measurements, because the component signals cannot be separated from brightness temperatures alone. In addition, both methods suffer from unresolved sub-pixel-scale variability. My research aims at better constraining this quantity by systematically investigating inconsistencies between microwave and VNIR cloud liquid water path estimates and by estimating the observed retrieval differences. First, we have identified differences between AMSR-E and MODIS cloud liquid water retrievals as a function of geographic location, cloud fraction, effective radius profile, cloud heterogeneity, solar/view geometry, and rain rate. In broken scenes AMSR-E increasingly overestimated MODIS, and retrievals became uncorrelated as cloud fraction decreased, while in overcast scenes the techniques showed generally better agreement but with a MODIS overestimation. We found AMSR-E and MODIS retrievals being most consistent in extensive marine Sc clouds. Evaluating the diurnal cycle of South Atlantic low-level cloud properties (LWP) from TMI and SEVIRI retrievals also exhibited qualitatively similar results. Best agreement is observed over the Sc regimes and worse agreement is seen over the trade wind Cu regimes. Finally, we estimate these observed uncertainties in plane-parallel VNIR cloud retrievals, by combining large eddy simulated cloud fields and SHDOM 3D radiative transfer model. Our ultimate goal is to make a significant step toward creation of a consensus satellite cloud liquid water climatology that might be more useful in constraining global climate models than existing datasets.

Zusammenfassung

Der Flüssigwasserweg, das über die Säule integrierte Wolkenwasser, ist ein wichtiger Wolkenparameter, der sowohl bei der Atmosphärischen Strahlung als auch für den hydrologischen Kreislauf eine bedeutende Rolle spielt. Vergleiche von Beobachtungen und Simulationen wiesen große und teilweise systematische Fehler in der globalen Verteilung und im Tagesgang des Flüssigwasserwegs auf. Bedauerlicherweise zeigen auch die verschiedenen auf Beobachtungen basierenden Datensätze (Fernerkundung durch Mikrowellen und sichtbares/nah-infrarotes Licht/VNIR) eine deutliche und bis jetzt noch nicht erklärbare Diskrepanz. Für eine bessere Handhabung muss bei den operationellen VNIR-Fernerkundungs-Algorithmen die natürliche Komplexität der Wolken reduziert werden, indem Wolken als plan-parallele homogene Schichten behandelt werden. Das simultane Vorhandensein von Flüssigwasserwolken und Regen stellt ein fundamentales Problem für die Fernerkundung im Mikrowellenbereich dar, weil das Einkomponentensignal nicht von der Strahlungstemperatur getrennt werden kann. Zusätzlich weisen beide Methoden aufgrund der unaufgelösten sub-skaligen Variabilität Einschränkungen auf. Meine Forschung zielt darauf hin, eine bessere quantitative Charakterisierung des Flüssigwasserwegs aus Fernerkundungsbeobachtungen durch systematisches Erfassen von Inkonsistenzen zwischen Abschätzungen des Flüssigwasserwegs aus Mikrowellen- und VNIR-Beobachtungen zu erlangen. Zuerst identifizierten wir Unterschiede zwischen gemessenem Wolkenwasser des Mikrowellen-Instruments AMSR-E und des VNIR-Instruments MODIS als Funktion des geographischen Ortes, des Wolkenbedeckungsgrads, der Profiln von effektiven Radien, der Wolkenheterogenität, der Solargeometrie, der Sensorgeometrie und der Regenrate. In durchbrochenen Wolkenszenen sind die Flüssigwasserweg-Abschätzungen von AMSR-E systematische größer als die von MODIS, und die Retrievals werden unkorreliert, wenn der Wolkenbedeckungsgrad abnimmt, während in vollständig bedeckten Situationen die Techniken generell in besserer Übereinstimmung sind, teilsweise mit höheren Werfen von MODIS . Weiterhin fanden wir heraus, dass AMSR-E und MODIS Fernerkundungen hauptsächlich in Gebieten mit extensiver mariner Stratocumulusbewölkung übereinstimmen. Eine Evaluierung des Tageszyklus des Flüssigwasserwegs von niedrigen Wolken über dem Südatlantik, gemessen durch das Mikrowellen-Instrument TMI und das VNIR-Instrument SEVIRI, deuten auf ebenfalls qualitativ ähnliche Ergebnisse. Die beste Übereinstimmung kann in Stratocumulus-Regimen beobachtet werden, die schlechteste in PassatwindCumulus

Regimen. Schließlich schätzten wir einige dieser beobachteten Ungewissheiten in plan-parallelen VNIR-Wolkenretrieval ab, indem wir Wolkenfelder von Grobstrukturauflösenden Simulationen (LES) mit 3D-Strahlungstransfer-Modellen kombinierten.

Diese Studien trugen zu einer verbesserten Interpretation der Satelliten-Fernerkundung des Wolkenwassergehalts bei, und erlauben damit eine genauere Evaluierung von Klimamodellen als bisher möglich.

Contents

Acronyms …….. xi

Symbols …….. xiii

1. Introduction …….. 1

2. An Overview of Data and Methodology …….. 5

3. Global Assessment of AMSR-E and MODIS Cloud Liquid Water Path Retrievals in Warm Oceanic Clouds

3.1. Introduction …….. 7

3.2. Data and Methodology …….. 9

3.2.1. AMSR-E Wentz Cloud Liquid Water Path

3.2.2. MODIS Cloud Liquid Water Path

3.2.3. OMI Aerosol Index

3.2.4. Comparison Methodology

3.3. Bias Analysis …….. 13

3.3.1. Clear-Sky Wentz Bias

3.3.2. Global Annual Mean Statistics

3.3.3. Seasonal Variations in Global Means

3.3.4. Cloud Fraction Dependence

3.3.5. Zonal Means

3.3.6. Global Distribution of Bias

3.4. Potential Error Sources …….. 23

3.4.1. Heterogeneity Effects in MODIS LWP

3.4.2. Cloud Temperature Errors in AMSR-E LWP

3.4.3. Cloud Vertical Stratification in MODIS LWP

3.4.4. Absorbing Aerosol Effects in MODIS LWP

3.4.5. Cloud-Rain Partitioning Issues in AMSR-E LWP

3.5. Summary …….. 37

4. Evaluating Diurnal Cycle of South Atlantic Marine Boundary Layer Clouds using SEVIRI VNIR and TMI Microwave Retrievals

4.1. Introduction …….. 41

4.2. Data and Methodology …….. 44
4.2.1. Spinning Enhanced Visible and InfraRed Imager (SEVIRI)
4.2.2. TRMM Microwave Imager (TMI)
4.2.3. Methodology
4.3. Comparison of SEVIRI *versus* TMI LWP …….. 46
4.3.1. Effect of Absorbing Aerosols on SEVIRI Retrievals
4.3.2. Mean Statistics of TMI LWP and SEVIRI CPP
4.3.3. Spatial Distribution of TMI LWP and SEVIRI CPP
4.3.4. Diurnal Cycle of TMI LWP and SEVIRI CPP
4.3.5. Cloud Fraction Dependency of TMI and SEVIRI LWP
4.3.6. Solar Zenith Angle Dependency on SEVIRI LWP
4.4. Comparison of SEVIRI *versus* MODIS CPP …….. 71
4.4.1. Total Sky SEVIRI and MODIS CPP
4.4.2. Overcast Sky SEVIRI and MODIS CPP
4.4.3. Mean Statistics of LWP from SEVIRI and MODIS
4.5. Summary …….. 77

5. Quantifying Uncertainties in 1D VNIR Cloud Retrievals Using LES Cloud Fields and SHDOM Radiative Transfer Model
5.1. Introduction …….. 80
5.2. Datasets, Models, and Methodology …….. 83
5.2.1. The Large-Eddy Simulated Cloud Fields
5.2.2. Radiative Transfer Model
5.2.3. Cloud Retrieval Algorithm
5.2.4. Methodology
5.3. Results and Discussion …….. 91
5.3.1. Spatial Distribution of 3D Radiance
5.3.2. Dependence of Radiance on Sun-view Geometry
5.3.3. Overview of Heterogeneity Parameters
5.3.4. Pixel-Level Analyses
5.3.5. Domain Mean Cloud Properties
5.3.6. Scale Effect on Retrievals
5.3.7. Cloud Fraction Dependency of Biases
5.3.8. Sun-view Geometry Dependence

5.3.9. Error in Cloud Retrieval and Heterogeneity Measures
5.3.10. Error Estimation for 1D VNIR Cloud Retrievals
5.3.11. Multi-Linear Regression Analysis
5.3.12. Optimal Error in Sun-view Geometry
5.4. Summary …….. 136

6. Conclusions and Future Scope
6.1. Conclusions …….. 141
6.2. Future Scope …….. 145

References …….. 147

Acronyms

AI	Aerosol Index
AirMISR	Airborne Multi-angle Imaging SpectroRadiometer
AMSR-E	Advanced Microwave Scanning Radiometer for Earth Observing Systems
ASTEX	Atlantic Stratocumulus Transition Experiment
AVHRR	Advanced Very High Resolution Radiometer
CALIPSO	Cloud-Aerosol Lidar and Infrared Pathfinder Satellite Observations
CDNC	Cloud droplet number concentration
CM-SAF	Satellite Application Facility on Climate Monitoring
CPP	Cloud Physical Properties
CTT	Cloud-Top-Temperature
Cu	Cumulus
DISORT	Discrete Ordinates Radiative Transfer
DJF	December-January-February
ECMWF	European Centre for Medium-Range Weather Forecasts
EPIC	East Pacific Investigation of Climate
ERBE	Earth Radiation Budget Experiment
ESA	European Space Agency
EUMETSAT	European Organization for the Exploitation of Meteorological Satellites
FIRE	First ISCCP Regional Experiment
GCM	General Circulation Model
GFDL	Geophysical Fluid Dynamics Laboratory
INTEX-A	Intercontinental Chemical Transport Experiment - North America Phase A
ISCCP	International Satellite Cloud Climatology Project
ITCZ	Intertropical Convergence Zone
JJA	June-July-August
KNMI	Koninklijk Nederlands Meteorologisch Instituut
LCF	Liquid Cloud Fraction
LES	Large Eddy Simulation
LTS	Lower Tropospheric Stability
LUT	Look-up-table
LWP	Liquid Water Path
MAM	March-April-May
McSI	Monte Carlo spectral integration
MISR	Multi-angle Imaging SpectroRadiometer
MODIS	Moderate Resolution Imaging Spectroradiometer
NIR	Near-InfraRed
OMI	Ozone Monitoring Instrument

POLDER	Polarization and Directionality of the Earth's Reflectances
RICO	Rain in Cumulus over the Ocean
RSS	Remote Sensing Systems
SAFARI	Southern African Regional Science Initiative
Sc	Stratocumulus
SEVIRI	Spinning Enhanced Visible and Infrared Imager
SHDOM	Spherical Harmonic Discrete Ordinate Method
SHDOMPP	Spherical Harmonic Discrete Ordinate Method – plane-parallel
SON	September-October-November
SSM/I	Special Sensor Microwave/Imager
SST	Sea Surface Temperature
St	Stratus
SZA	solar zenith angle
TMI	TRMM Microwave Imager
TRMM	Tropical Rainfall Measuring Mission
UCLA	University of California, Los Angeles
VIS	visible
VNIR	visible/near-infrared
VZA	view zenith angle

Symbols

τ	cloud optical thickness
r_e	droplet effective radius
θ	view zenith angle
φ	view azimuth angle
θ_o	solar zenith angle
σ_{CTOP}	standard deviation of cloud top height in individual scenes
H_σ	σ/R the ratio of (σ) standard deviation to (R) mean of visible reflectance (0.86 μm)
χ	the ratio of the logarithmic and linear average of 1 km cloud optical thicknesses

Chapter 1
Introduction

Clouds strongly affect the earth's climate by altering the radiative fluxes. The low-level marine clouds are particularly important because they constitute a main source of uncertainty in simulated cloud feedbacks [*Bony and Dufresne,* 2005]. Globally, boundary-layer clouds act to decrease the net radiative forcing by 15 Wm^{-2} due to their large reflectivity [*Hartmann et al*., 1992]. This reflectivity varies with cloud parameters such as cloud fraction, column integrated liquid water or liquid water path, and the droplet effective radius. *Cess et al.,* [1989] indicated that different GCMs (general circulation models) disagree on the magnitude and also, on the sign of the cloud feedback. Recent studies reported that the general circulation models [*Ma et al*., 1996; *Jacob,* 1999; *Li et al*., 2008; *Medeiros and Stevens,* 2011] and the so-called single column models [*Duynkerke et al.,* 2004] under-predicted the cloud cover and liquid water path of subtropical marine stratiform clouds. *Williams and Tselioudis* [2007] analysed the output from several GCMs and found that much of the disparity in GCMs climate sensitivity arises from the inability of the models to represent the state of the present-day cloud radiative effect. Moreover, in the Fourth Assessment Report of Intergovernmental Panel on Climate Change (IPCC-AR4), *Forster et al.* [2007] highlights the diurnal cycle of thin, stratiform clouds as one of the major uncertainties in current estimates of cloud radiative forcing. *Wilson and Mitchell* [1986] and *Rozendaal et al.* [1995] showed that, changing the resolution of the diurnal cycle of cloud and radiative fluxes in GCMs can affect the cloud forcing and hence, the simulated climate. Comparisons of the observed diurnal cycle of clouds with that simulated by models also show large and potentially systematic errors in the modelled diurnal cycle [*O'Dell et al.,* 2008; *Roebeling and van Meijgaard,* 2009], and also in the global distribution [*Borg and Bennartz,* 2007; *Wilcox et al.*, 2009]. Thus, knowledge of the temporal and spatial variability of these cloud parameters is a prerequisite for understanding feedbacks between boundary layer cloud properties and climate change [*Williams and Tselioudis,* 2007].

Given the scarcity of global measurements of the vertical distribution of cloud macrophysical and microphysical properties, it is not surprising that uncertainties associated with cloud feedbacks remain the largest contributors to differences in model (/simulated) projections of climate warming [*Dufresne and Bony,* 2008]. With the exception of a few field studies, observationally, the global cloud properties can be estimated

by only satellite-based instruments, the diurnal variation of cloud properties are far more limited. Retrieval of cloud properties has been made using a variety of methods and satellite instruments [*Minnis,* 1989; *Nakajima and King,* 1990; *Wentz,* 1997; *Ackerman et al.,* 1998; *Rossow and Schiffer,* 1999; *Wylie and Menzel,* 1999; *Platnick et al.,* 2003; *Heidinger,* 2003; *Frey et al.,* 2008; *Hilburn and Wentz,* 2008]. The more fundamental differences leading to discrepancies in the comparisons include instrument capabilities (spectral coverage, spatial resolution, and swath), retrieval algorithms (microwave and visible/near-infrared), and the spatio-temporal sampling available from the satellite orbit. The main source of error is the cloud-rain separation in microwave techniques. The basic microwave observable is total liquid water; the simultaneous presence of cloud liquid and rain poses a fundamental challenge to all microwave methods, because the component signals cannot be separated from brightness temperatures alone. Moreover, a positive bias of passive-microwave derived LWP in cloud-free situations is in the order of 10-15 g m^{-2} [*Greenwald* 2009; *Greenwald et al.* 2007], in addition to the unresolved sub-pixel-scale variability. On the other hand, operational visible/near-infrared (VNIR) retrieval algorithms have to reduce natural complexity by treating clouds as plane-parallel, homogeneous layers in order to be practical. These simplifications might work well for extensive Sc sheets but are less suitable for broken, heterogeneous cloud fields. Due to the complex 3D structure of clouds, 1D retrievals can significantly underestimate or overestimate the true LWP at certain view geometries (e.g., shadowed vs. illuminated cloud sides). These 3D effects are generally larger in broken clouds and at oblique solar and view angles. In addition, the relationship between cloud optical thickness and reflectance is non-linear; therefore, sub-pixel-scale variability can also introduce large errors in retrieved cloud properties (plane-parallel bias). The retrieval artifacts in 1D VNIR retrievals due to the cloud 3D structure have been assessed in *Loeb and Davies* [1996], *Zhao and Di Girolamo* [2004], *Horváth and Davies* [2004], *Kato et al*. [2006, 2009], *Várnai and Marshak* [2007]. *Cahalan et al.,* [1994] claimed that albedo biases of 10% or greater would be introduced into large regions of current climate models if clouds were given their observed liquid water amounts because of the treatment of clouds as plane parallel, moreover, an increase in the planetary albedo of the earth-atmosphere system by only 10% can decrease the equilibrium surface temperature to that of the last ice age. Using Multiangle Imaging SpectroRadiometer (MISR) data *Girolamo et al.* [2010] showed that the view-angular distribution of the retrieved cloud optical thickness measured at 1 km resolution are indistinguishable from plane-parallel clouds 79% of the time, for the oceanic stratiform clouds when solar zenith angle is below 60^{o} and for all other cloud types and Sun angles, the

frequency in which clouds are indistinguishable from plane-parallel drops sharply to as low as a few percent. Unfortunately, neither satellite technique has been comprehensively validated. An alternative to episodic validation campaigns is evaluation of the two fully independent satellite methods (microwave and visible/near-infrared) against each other using a large set of coincident retrievals. Recently, a large number of papers have studied the differences in liquid water path retrieval based on passive microwave and visible/near-infrared satellite observations [*Wilcox et al.,* 2009; *Greenwald,* 2009; *Bennartz,* 2007; *Borg and Bennartz,* 2007; *Horvath and Davies,* 2007]. Differences between the two methods have been shown to be correlated with various factors, including cloud fraction, observation geometry, retrieval assumptions, aerosol above clouds, and others. In broken cloud fields the Wentz algorithm has been found to increasingly overestimate MODIS with decreasing cloud fraction, and the techniques have been found considerably better correlated in overcast scenes, but with the opposite tendency of MODIS overestimations [*Bennartz,* 2007; *Horváth and Davies,* 2007; *Greenwald et al.,* 2007; *Horváth and Gentemann,* 2007, *Borg and Bennartz,* 2007]. These are important results, but more robust comparisons are needed because all previous studies had serious temporal or regional limitations.

Therefore, understanding and interpreting satellite data records is a significant step forward in representing climate variability. My research aims at better constraining this quantity by systematically investigating inconsistencies between microwave and optical cloud liquid water path estimates and quantifying the observed retrieval differences. Thus, in **Chapter 3**, we performed a systematic global comparison of AMSR-E and MODIS LWP estimates from one year of data, and identified differences between microwave and VNIR cloud liquid water retrievals as a function of geographic location, cloud fraction, effective radius profile, cloud heterogeneity, solar/view geometry, and rain rate. In **Chapter 4** we have evaluated the diurnal cycle of South Atlantic marine boundary layer clouds using one year of SEVIRI and TMI measurements. SEVIRI is the first space-borne instrument with the necessary temporal, spatial, and spectral resolution to resolve the diurnal cycle of clouds, and the non sun-synchronous orbit of TRMM Microwave Imager (TMI) allows for a comparison of observations at different local times. Once we identified the various error sources from microwave and VNIR measurements, it is ideal to estimate these errors quantitatively by combining simulated cloud fields and both microwave and VNIR radiative transfer models. However, due to the limited time and resources, in this study we decided to quantify only the retrieval errors of VNIR technique. Thus, the quantification of the uncertainties in the 1D VNIR satellite cloud retrievals from large-eddy simulated cloud fields and Spherical

Harmonic Discrete Ordinate Method (SHDOM) 3D radiative transfer model is presented in **Chapter 5**. This will be helpful to identify and modify future satellite measurements, and ultimately the climate-modeling efforts would greatly benefit from accurate cloud LWP measurements with well-established error characteristics.

Chapter 2
An Overview of Data and Methodology

This chapter briefly summarizes the data and methodology utilized for this study, although a detailed discussion is provided in the respective result chapters. In **Chapter 3**, we assess one year of global cloud liquid water path from AMSR-E (Advanced Microwave Scanning Radiometer for Earth Observing System) version 5 and MODIS (Moderate Resolution Imaging SpectroRadiometer) level 2 database. AMSR-E and MODIS aboard polar orbiting Aqua satellite of A-Train constellations, with the equatorial crossing time of 13:30 UTC. Thus, the global comparison of clouds is performed for simultaneous, collocated, coincidence measurements, however, the analysis is restricted to non-raining warm clouds, as ice pixels introduce complexity in the VNIR retrievals and rain poses problems in the microwave retrievals. In **Chapter 4** we evaluate the diurnal cycle of South Atlantic stratocumulus and trade wind Cu clouds using SEVIRI (Spinning Enhanced Visible Infrared Measurements) and TMI (Tropical Rainfall Measuring Mission – Microwave Imager). SEVIRI aboard METEOSAT-9 in geostationary orbit and measures the cloud properties each 15 minutes at 3 km resolution, and therefore provides excellent database for the study of diurnal variation of the cloud properties. On the otherhand TMI aboard TRMM in equatorial orbit samples the globe at different local times and collecting a month of data would ideally sufficient to study the diurnal variability in LWP. Moreover, we use ultra-violet aerosol index data from OMI (Ozone Monitoring Instrument) aboard Aura satellite, to study the influence of absorbing aerosols above South Atlantic stratocumulus clouds. In **Chapter 5** we have quantified the uncertainties in 1D VNIR cloud retrievals by combining hundreds of LES (Large Eddy Simulation) cloud fields with SHDOM (the Spherical Harmonic Discrete Ordinate Method) 3D Radiative Transfer model. We implement a 2-channel retrieval technique similar to the operational MODIS algorithm to estimate cloud optical thickness and droplet effective radius from 0.86 μm and 2.13 μm radiances. The 3D SHDOM radiative transfer model was used to calculate accurate radiances for LES cloud fields. These radiances were then inverted for optical thickness and effective radius with the help of 1D look-up tables generated by the plane-parallel SHDOMPP. The retrieved cloud properties are compared back to the true LES cloud properties and the error is determined in different Sun-view geometry.

Chapter 3
Global Assessment of AMSR-E and MODIS Cloud Liquid Water Path Retrievals in Warm Oceanic Clouds

We compared one year of AMSR-E Wentz and MODIS cloud liquid water path estimates in warm marine clouds. In broken scenes AMSR-E increasingly overestimated MODIS, and retrievals became uncorrelated as cloud fraction decreased, while in overcast scenes the techniques showed generally better agreement but with a MODIS overestimation. We found microwave and visible/near-infrared retrievals being most consistent in extensive marine Sc clouds with correlations up to 0.95 and typical rms differences of 15 g m^{-2}. The overall MODIS high bias in overcast domains could be removed, in a global mean sense, by adiabatic correction; however large regional differences remained. Most notably, MODIS showed strong overestimations at high latitudes, which we traced to 3D effects in plane-parallel visible/near-infrared retrievals over heterogeneous clouds at low Sun. In the tropics/subtropics, AMSR-E – MODIS differences also depended on cloud type, with MODIS overestimating in stratiform and underestimating in cumuliform clouds, resulting in large-scale coherent bias patterns where marine Sc transitioned into trade wind Cu. We noted similar geographic variations in Wentz cloud temperature errors and MODIS 1.6-3.7 μm droplet effective radius differences, suggesting that microwave retrieval errors due to cloud absorption uncertainties, and visible/near-infrared retrieval errors due to cloud vertical stratification might have contributed to the observed liquid water path bias patterns. Finally, cloud-rain partitioning was found to introduce a systematic low bias in Wentz retrievals above 180 g m^{-2} as the microwave algorithm erroneously assigned an increasing portion of the liquid water content of thicker non-precipitating clouds to rain.

3.1. Introduction

The weakest link in climate simulations is the poor representation of clouds, particularly of marine boundary layer clouds, which constitute the main source of uncertainty in modeled cloud feedbacks [*Bony and Dufresne*, 2005]. The dominant part of predicted global cloud forcing change is produced by these ubiquitous warm clouds, the radiative

Seethala, C., and Á. Horváth (2010), Global assessment of AMSR-E and MODIS cloud liquid water path retrievals in warm oceanic clouds, *J. Geophys. Res.*, 115, D13202, doi:10.1029/2009JD012662.

fluxes of which are very sensitive to their vertically integrated liquid water content or liquid water path (LWP) [*Turner et al.*, 2007]. Therefore, climate-modeling efforts would greatly benefit from accurate cloud LWP measurements with well-established error characteristics.

The longest global climatologies of cloud LWP have been derived from space-borne passive microwave and visible/near-infrared (VNIR) observations. The microwave record now spans 20+ years and comprises Special Sensor Microwave/Imager (SSM/I), Tropical Rainfall Measurement Mission Microwave Imager (TMI), and Advanced Microwave Scanning Radiometer for Earth Observing System (AMSR-E) measurements. High quality VNIR LWP estimates, however, have only been available since the launch of the Moderate Resolution Imaging Spectroradiometer (MODIS) a decade ago.

The de facto microwave retrieval standard is the Wentz algorithm developed by Remote Sensing Systems (RSS) [*Wentz,* 1997; *Wentz and Spencer*, 1998; *Wentz and Meissner*, 2000; *Hilburn and Wentz*, 2008]. RSS derives cloud liquid water path directly from brightness temperatures using essentially the same multi-channel algorithm for SSM/I, TMI, and AMSR-E. VNIR LWPs, on the other hand, represent indirect estimates being parameterized from cloud optical thickness and droplet effective radius, which are retrieved from solar reflectances. The current state-of-the-art MODIS algorithm [*Platnick et al*., 2003] is an updated version of the classic *Nakajima and King* [1990] bi-spectral method.

Unfortunately, neither satellite technique has been comprehensively validated. Comparisons with in situ and ground-based measurements, although useful in case studies, suffer from representativeness and sample size issues as well as from significant biases in surface microwave retrievals [*Turner et al.*, 2007]. An alternative to episodic validation campaigns is evaluation of the two fully independent satellite methods against each other using a large set of coincident retrievals. Several such studies have assessed Wentz and MODIS LWPs recently.

In broken cloud fields the Wentz algorithm has been found to increasingly overestimate MODIS with decreasing cloud fraction [*Bennartz*, 2007; *Horváth and Davies*, 2007]. Analysis of cloud-free scenes has also indicated a Wentz overestimation, the magnitude of which decreases with surface wind speed and increases with column water vapor [*Greenwald et al.*, 2007; *Horváth and Gentemann*, 2007]. Taken together, these findings have strongly suggested potential beamfilling, surface emission, and gaseous absorption errors in the Wentz algorithm, although significant heterogeneity errors in MODIS retrievals could not be ruled out either.

The techniques have been found considerably better correlated in overcast scenes, but with the opposite tendency of MODIS overestimations. *Borg and Bennartz* [2007] have shown that this positive MODIS bias could be eliminated, at least in a global mean sense, by replacing the operational vertically homogeneous cloud model with an adiabatically stratified one. However, even after adiabatic corrections systematic differences remain with AMSR-E increasingly underestimating MODIS for cloud optical thicknesses above ~20 [*Wilcox et al.*, 2009]. Some of these discrepancies might be due to assumptions about the partitioning of cloud water and rainwater in the Wentz algorithm, as pointed out by *Horváth and Davies* [2007], and *O'Dell et al*. [2008].

These are important results, but more robust comparisons are needed because all previous studies had serious temporal or regional limitations. In this work, we performed a systematic global comparison of AMSR-E and MODIS LWP estimates from one year of data. Section 2 describes our satellite datasets and analysis methodology. Section 3 gives a detailed account of microwave-VNIR differences. Section 4 then discusses potential first-order error sources that might explain the observed biases. Finally, Section 5 summarizes our findings.

3.2. Data and Methodology

Our dataset comprised cloud retrievals from AMSR-E and MODIS on the Aqua satellite, and near-simultaneous aerosol observations from Ozone Monitoring Instrument (OMI) aboard the Aura platform, covering the period December 2006 to November 2007. Only high quality retrievals were used from the latest available products: version 5 for AMSR-E, collection 5 for MODIS, and version 3 for OMI. Below, we summarize the relevant aspects of each algorithm.

3.2.1. AMSR-E Wentz Cloud Liquid Water Path

The Wentz algorithm is an absorption-emission based method sequentially retrieving sea surface temperature (SST), surface wind speed (W), water vapor path (V), liquid water path (LWP), and rain rate (R), both day and night but only over ocean. Our primary interest, LWP, is derived from 37 GHz observations at a resolution of 13 km, but here we used the 0.25° gridded daytime product. These microwave LWPs can be interpreted as gridbox means (averages over clear sky and cloud), because the relationship between 37 GHz retrievals and sub-field-of-view cloud amount is nearly linear [*Greenwald et al*., 1997; *Lafont and Guillemet*, 2004]. First, a preliminary value is computed assuming the atmospheric column contains only cloud liquid but no rain. Then, rain retrieval is performed for preliminary LWPs

above a fixed rain-threshold of 180 g m^{-2}. Although this step concerns only ~5% of all data, it is a source of systematic error due to its built-in assumptions; therefore, it warrants a more detailed discussion.

The simultaneous presence of cloud liquid and rain poses a fundamental challenge to *all* microwave methods and not only to the Wentz algorithm, because the component signals cannot be separated from brightness temperatures alone. The basic microwave observable is total liquid water columnar attenuation A_{L37}. In the first pass through data, no rain is assumed and a preliminary LWP proportional to A_{L37} is retrieved. For a preliminary $\mathrm{LWP} > 180$ g m^{-2}, however, precipitation is diagnosed and the governing equation becomes [*Hilburn and Wentz*, 2008]:

$$A_{L37} = a_{37}(1 - b_{37}\Delta T)\mathrm{LWP}_R \times 10^{-3} + c_{37}(1 + d_{37}\Delta T)\mathrm{H}R^{e_{37}} \quad (1a)$$

$$\Delta T = T_L - 283\mathrm{K}. \quad (1b)$$

Here, a_{37}, b_{37}, c_{37}, d_{37}, and e_{37} are coefficients derived using the Marshall-Palmer raindrop size distribution, T_L is liquid cloud temperature in K, H is rain column height in km, R is column-average rain rate in mm/hr, and LWP_R is the rain-adjusted cloud liquid water path in mm. Cloud temperature is parameterized from SST and water vapor, while rain column height is fitted to freezing level heights from reanalysis data and varies linearly with SST from 0.46 km at 0°C to 5.26 km at 30°C. In order to solve (1) with two unknowns, LWP_R and R, the Wentz algorithm further assumes that cloud liquid water scales as the square root of rain rate [*Hilburn and Wentz*, 2008]:

$$\mathrm{LWP}_R = \alpha\left(1 + \sqrt{\mathrm{HR}}\right), \quad (2)$$

where $\alpha = 180$ g m^{-2} is the rain threshold LWP. With (2) and the above parameterizations (1) can now be solved for R. The resulting rain rate is then substituted back in (2) in order to obtain the final rain-adjusted cloud liquid water path replacing the preliminary rain-free value.

This specific cloud-rain partitioning was derived from a study of northeast Pacific extratropical cyclones. Changing (2) or even the assumed raindrop size distribution would result in a different cloud-rain partitioning. The value of $\alpha = 180$ g m^{-2} was chosen because it yields good agreement between Wentz and other rain climatologies [*Hilburn and Wentz*, 2008]. From the perspective of LWP retrievals, however, use of a relatively low and globally fixed cloud-rain threshold entails underestimations whenever non-raining clouds with LWPs exceeding the threshold are encountered, because some of the cloud water is erroneously

assigned to precipitation. As we show in section 4.5, this negative bias explains some of the observed discrepancies between Wentz and MODIS LWPs.

3.2.2. MODIS Cloud Liquid Water Path

Here, cloud LWP is indirectly estimated from cloud optical thickness (τ) and droplet effective radius (r_e), themselves inferred from bi-spectral solar reflectances at 1-km resolution (MYD06 product). Over ocean, MODIS uses the 0.86-μm visible band containing optical thickness information, in conjunction with one of three water-absorbing near-infrared bands located at 1.6, 2.2, and 3.7 μm, which are sensitive to droplet effective radius. Although all three near-infrared channels generally observe the upper portion of clouds, vertical sampling of droplets becomes progressively deeper from 3.7 to 1.6 μm due to decreasing absorption [*Platnick*, 2000]. The operational LWP parameterization relies on the 2.2 μm band and assumes no vertical variation in cloud droplet size, leading to

$$\mathrm{LWP} = \frac{4\rho_w}{3Q_e}\tau r_{e,2.2}, \tag{3}$$

where $Q_e \approx 2$ is the extinction efficiency at visible wavelengths, and $\rho_w = 1$ g cm^{-3} is water density. (Note that LWP is only estimated when both τ and r_e retrievals are successful; the latter often fail in thin clouds leading to fewer LWP retrievals than cloudy pixels.) Presumed vertical homogeneity in combination with cloud-top effective radius retrievals can lead to LWP biases of both signs depending on the actual droplet profile. For example, in the absence of τ and r_e retrieval errors, (3) would be an overestimate in marine Sc clouds, where effective radius often increases linearly from cloud base to top. For such boundary layer clouds an adiabatic model has been proposed, based on cloud-top effective radius $r_{e,top}$ [*Wood and Hartmann*, 2006]:

$$\mathrm{LWP} = \frac{10\rho_w}{9Q_e}\tau r_{e,top}. \tag{4}$$

Theoretically, $r_{e,3.7}$ is closest to $r_{e,top}$; however, $r_{e,3.7}$ has an unexplained low bias (see section 4.3). In practice, therefore, $r_{e,2.2}$ is used in (4) as well, which reduces (3) by a factor of 5/6 or 17%. Because this model does not consider entrainment mixing, it represents only a first-order LWP correction in mostly subadiabatic marine Sc. In addition, when r_e decreases with height, which might occur in drizzling or raining clouds, (4) could even exacerbate the underestimation of (3). At least in theory, a better approach would be to estimate droplet size profile on a case-by-case basis from the three effective radii. Unfortunately, vertical

weighting functions of the three MODIS near-infrared channels are quite similar and correlated, rendering droplet profile inversion questionable [*Platnick*, 2000]. Nevertheless, we show in section 4.3 that in certain geographic regions large-scale variations of microwave-VNIR LWP bias appear correlated with 1.6-3.7 μm effective radius difference.

Another significant error source in MODIS LWP estimates is the potential breakdown of 1D plane-parallel radiative transfer used in the calculations [*Horváth and Davies*, 2004]. The impact of heterogeneity (3D) effects on 1D cloud optical thickness has been extensively studied, but that on 1D droplet effective radius has only been recently considered and is still rather uncertain [*Marshak et al*., 2006]. Possible 3D errors in VNIR LWP are also poorly known; we investigate such errors in section 4.1 by analyzing AMSR-E – MODIS retrieval differences as a function of horizontal cloud heterogeneity.

3.2.3. OMI Aerosol Index

Because absorbing aerosols can apparently reduce MODIS LWP [*Haywood et al.*, 2004], we used OMI ultraviolet Aerosol Index (AI) to identify areas affected by biomass smoke or desert dust, and estimated the resulting LWP retrieval bias in section 4.4. OMI AI represents the deviation of measured 354-nm radiance from model calculations in a purely molecular atmosphere bounded by a Lambertian surface, and has the unique ability to detect aerosols above clouds [*Torres et al*., 2007]. Specifically, we used the daily Level-2 gridded product (OMAERUVG) with values above 1 indicating substantial amounts of absorbing particles.

3.2.4. Comparison Methodology

In this study, all higher resolution retrievals were averaged down to the 0.25° scale of the regular AMSR-E grid. Performing the analysis on microwave footprint-level as done by *Greenwald et al*. [2007] would have offered slightly more detailed error information; however, at the cost of greatly increased computational burden and reduced data volume. Our choice was further motivated by climate model diagnostics strongly favoring the gridded Wentz product.

Because microwave LWPs represented gridbox means but MODIS LWPs were in-cloud retrievals, the latter were multiplied by the gridbox-mean fraction of successful MODIS retrievals, henceforth referred to as ‘cloud fraction’. The presence of cloud-top ice generally makes comparisons ambiguous due to different instrument sensitivities [*Horváth*

and Davies, 2007]; therefore, we restricted our analysis to ice-free gridboxes as identified by the MODIS cloud phase product. In addition, we only considered non-precipitating clouds with zero AMSR-E rain rates; the sole exception was section 4.5 discussing cloud-rain partitioning issues.

3.3. Bias Analysis

3.3.1. Clear-Sky Wentz Bias

Before analyzing cloudy scenes we evaluated Wentz LWP retrievals in clear-sky conditions in order to gain some measure of their uncertainties. We only considered domains where all MODIS pixels were classified as confident clear, still obtaining more than three million samples. The global annual mean clear-sky LWP bias was ~12 g m^{-2} in good agreement with the 12-15 g m^{-2} found by *Horváth and Gentemann* [2007] and *Bennartz* [2007], but higher than either the 7 g m^{-2} obtained by *Greenwald et al.* [2007] or the 5 g m^{-2} estimated by *Wentz* [1997]. Seasonal and hemispheric variations were small (1-2 g m^{-2}), which was in contrast to *Greenwald et al.* [2007] whose results exhibited considerably larger hemispheric differences of 12 g m^{-2} for the north and 4 g m^{-2} for the south; however, they only analyzed a 3-week period in July 2002, which might explain these discrepancies.

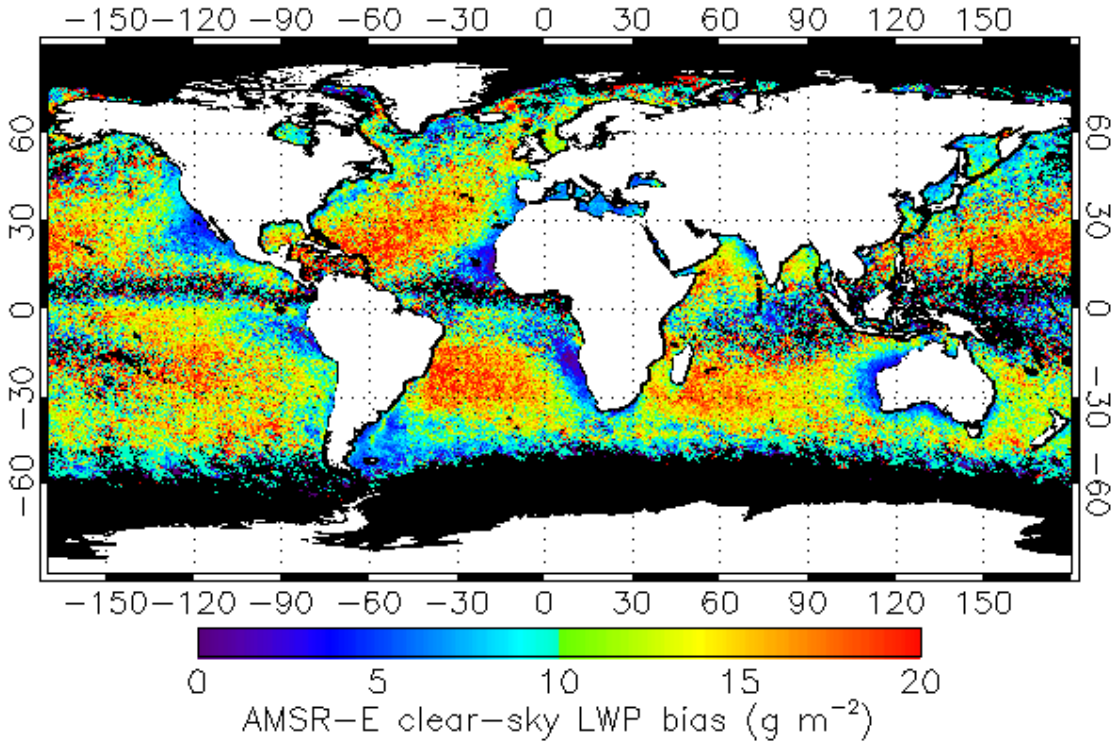

Figure 3.1. Geographic distribution of annual mean AMSR-E clear-sky LWP bias. In this and subsequent maps black indicates no data.

Geographic variations were far more significant in our dataset, as shown in Figure 3.1 for annual means. (Seasonal bias patterns were very similar.) We found the smallest clear-sky biases below 7 g m^{-2} in extensive marine Sc regions as well as in the Mediterranean, Black Sea, Red Sea, and Persian Gulf. Warmer tropical/subtropical oceanic areas, on the other hand, exhibited the largest biases up to 20 g m^{-2}. These clear-sky biases most likely corresponded to uncertainties in the sea surface emissivity, and water vapor and oxygen absorption models; however, cloud detection errors could not be ruled out. The global performance of the MODIS cloud mask is unknown, but in trade wind cumuli it has been shown to agree with a 15-m-resolution cloud mask only 62% of the time [*Zhao and Di Girolamo*, 2006]. Thus, cloud contamination might partly explain larger "clear-sky" LWPs in regions with frequent popcorn Cu.

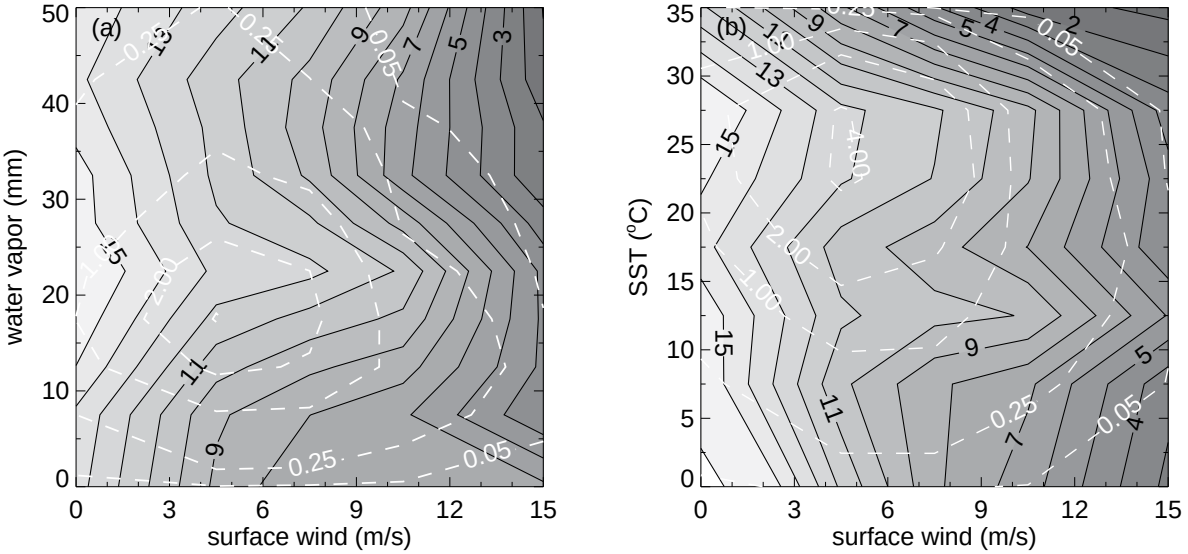

Figure 3.2. Annual mean AMSR-E clear-sky LWP bias binned according to (a) surface wind and column water vapor, and (b) surface wind and SST. Solid black lines are LWP bias contours at 1 g m^{-2} intervals, while dashed white lines indicate data frequency ($\times 10^5$).

Cloud detection errors aside, one would prefer microwave-derived parameters to be independent of one another. Unfortunately, this is not the case as demonstrated in Figure 3.2, where we plotted the mean clear-sky LWP bias binned according to surface wind speed, water vapor, and SST. We found a negative correlation with wind in all seasons and latitude bands, whereby the LWP bias decreased from 15-16 g m^{-2} to 2-3 g m^{-2} as wind increased from 0 to 15 m/s. Dependence on water vapor was generally weaker and more variable. In

drier conditions ($V < 22$ mm) the LWP bias increased, while in wetter conditions ($V > 22$ mm) decreased or leveled off with vapor amount. The influence of SST was even more variable and was overall the weakest, except maybe in the warmest regions above 28ºC where the bias rapidly decreased.

These results were qualitatively consistent with findings by *Greenwald et al.* [2007], and indicated possible shortcomings in the surface emission and gaseous absorption models of the Wentz algorithm. We emphasize that while these clear-sky uncertainties might also be representative of low cloud fraction scenes, it is not obvious how they relate to retrieval errors in highly cloudy domains. Undoubtedly, more work is needed to understand and remove these unwanted interdependencies in clear-sky observations. Henceforth, we focus on cloud retrievals.

3.3.2. Global Annual Mean Statistics

Annual statistics of AMSR-E and MODIS LWPs in ice- and rain-free domains, totaling more than 60 million retrievals, are summarized in Table 1. When all liquid cloud fractions (LCFs) were considered AMSR-E overestimated MODIS by 18 g m^{-2} with respective means of 58 g m^{-2} and 40 g m^{-2}. The datasets were moderately correlated with a coefficient of 0.74 and root-mean-square (rms) difference of 41 g m^{-2}, which was larger than the 25 g m^{-2} random error estimated by *Wentz* [1997] for microwave retrievals. Adiabatic correction made the overall comparison worse by further reducing MODIS LWPs and increasing the bias to 25 g m^{-2}.

Table 1. Global annual statistics of AMSR-E Wentz and MODIS LWP retrievals in warm non-precipitating marine clouds for three liquid cloud fraction (LCF) ranges. Means, biases (AMSR-E – MODIS), and rms differences are given in g m^{-2}.

	All Domains (LCF = 0-100%)		Overcast Domains (LCF = 95-100%)		Broken Domains (LCF = 0-50%)	
MODIS Model	Standard	Adiabatic	Standard	Adiabatic	Standard	Adiabatic
AMSR-E Mean	58	58	91	91	44	44
MODIS Mean	40	33	109	90	13	11
Bias	18	25	-18	1	31	33
Rms	41	36	38	31	35	35
Correlation	0.74	0.72	0.83	0.83	0.45	0.45
Sample Number	6.1E+7		1.1E+7		3.6E+7	

In overcast domains, defined as LCF=95-100% and constituting 18% of all samples, LWP was significantly higher with means of 91 g m^{-2} and 109 g m^{-2} for AMSR-E and MODIS, respectively. However, the bias was of opposite sign as MODIS overestimated AMSR-E by 18 g m^{-2}. The agreement between the techniques was considerably tighter with an increased correlation of 0.83. Adiabatic correction almost completely removed the MODIS overestimation resulting in a bias of only 1 g m^{-2} and rms difference of 31 g m^{-2}. This corroborated *Bennartz* [2007] that the adiabatic cloud model is superior to the operational vertically homogeneous one, at least in a global mean sense.

The above results suggested significantly higher microwave LWPs in broken clouds, which was confirmed by statistics for clear-sky dominated regions with LCF<50%. In this category, constituting 59% of all samples, AMSR-E and MODIS estimates were rather poorly correlated at 0.45 and showed the largest biases of 31-33 g m^{-2} due mostly to a steep drop in the MODIS mean. Obviously, adiabatic corrections made matters worst for such broken scenes. Motivated by these findings, we further investigated the cloud fraction dependence of microwave-VNIR consistency in section 3.4. First, however, we discuss seasonal variations in global mean LWP.

3.3.3. Seasonal Variations in Global Means

The month-to-month variation of AMSR-E and MODIS global mean LWPs is shown in Figure 3.3. Here, black corresponds to AMSR-E, while red and green refer to standard and adiabatic MODIS, respectively. When all domains were considered AMSR-E systematically overestimated MODIS similarly to the annual mean. The AMSR-E seasonal cycle had minimum in December (54 g m^{-2}) and a single maximum in August (63 g m^{-2}). Standard MODIS also had minimum in December (38 g m^{-2}); however, it had double maxima in March (42 g m^{-2}) and August (41 g m^{-2}). The resulting bias varied from 15 to 22 g m^{-2} with minimum in March and maximum in August. (The bias increased by a further ~7 g m^{-2} for adiabatic MODIS values.)

By contrast, overcast means showed standard MODIS overestimation in all months. Here, seasonal cycles were in better qualitative agreement with both datasets having minimum in December (102 vs. 86 g m^{-2}), and double maxima in April (120 vs. 94 g m^{-2}) and August (110 vs. 95 g m^{-2}). For MODIS, however, the relative strengths of maxima were markedly different and the amplitude of the seasonal cycle was larger. Adiabatic correction lowered MODIS values to within 5 g m^{-2} (or 6%) of AMSR-E estimates, confirming its overall validity on monthly time scales as well.

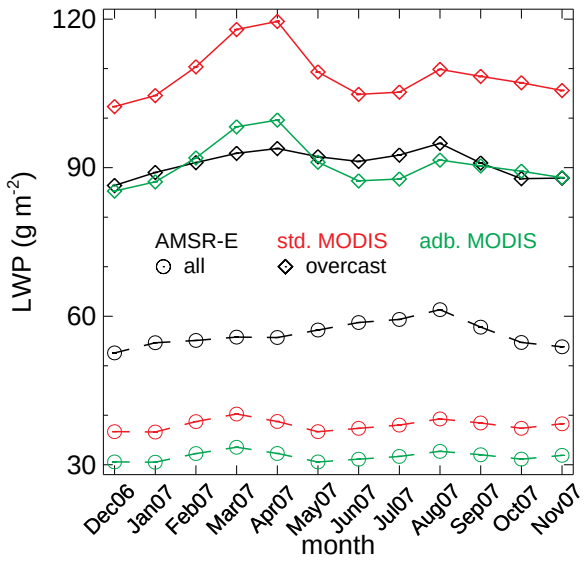

Figure 3.3. Seasonal variation of AMSR-E and MODIS global mean cloud LWP in warm nonprecipitating marine clouds for all domains (circles) and overcast domains (diamonds). Black, red, and green correspond to AMSR-E, standard (std.) MODIS, and adiabatic (adb.) MODIS, respectively.

3.3.4. Cloud Fraction Dependence

Here, we further investigate the strong dependence of microwave-VNIR comparison on scene brokenness. Mean AMSR-E and MODIS cloud LWPs are plotted for 5%-wide liquid cloud fraction bins in Figure 3.4a. Standard MODIS means rapidly increased from 2 g m^{-2} to 108 g m^{-2}, while AMSR-E means, varying from 33 g m^{-2} to 91 g m^{-2}, were usually higher and showed a slower increase with cloud fraction. The corresponding bias steadily increased from -17 g m^{-2} to +35 g m^{-2} as cloud fraction decreased, changing sign at an LCF of ~80% (see Figure 3.4b). Simultaneously, the correlation quickly dropped from 0.83 to 0.27 indicating poor correspondence between the techniques in highly broken scenes. (Similar results were obtained regardless of view zenith angle or potential sunglint contamination.) These findings qualitatively agreed with *Horváth and Davies* [2007] and *Horváth and Gentemann* [2007], and showed adiabatic improvement only for cloud fractions above 90%.

What could possibly cause such behavior? Plane-parallel MODIS retrievals are certainly subject to 3D effects in broken clouds; however, the resulting biases in 1D optical thickness and droplet effective radius are often of opposite sign leading to partial cancellation of errors in 1D LWP. Overall, shadowing dominates brightening, producing substantial r_e overestimations and somewhat smaller τ underestimations, and hence, a positive LWP bias [*Marshak et al.*, 2006; *Evans et al.*, 2008]. Indeed, *Cornet et al.* [2005] has found MODIS

domain-mean LWP overestimating the 3D value by 15% in a broken Sc scene off California. These studies suggest that 3D errors in MODIS retrievals would go the wrong way explaining the observed LWP bias in broken clouds.

Another possibility is microwave beamfilling effects. The Wentz algorithm does not apply beamfilling corrections to rain-free observations, but we made an equivalent first-order correction by scaling MODIS LWPs with the successful-cloud-retrieval fraction. This could lead to a MODIS low bias if cloud amounts were systematically underestimated in broken scenes. Although the MODIS cloud mask is designed to screen conservatively, the findings of *Zhao and Di Girolamo* [2006] have indicated it tends to overestimate cloud fraction in scattered clouds. On the other hand, the fraction of successful MODIS LWP retrievals is usually less than the cloud fraction due to failed r_e retrievals, especially at low LWP. Therefore, uncertainties in cloud-amount-scaling can potentially contribute to the observed biases.

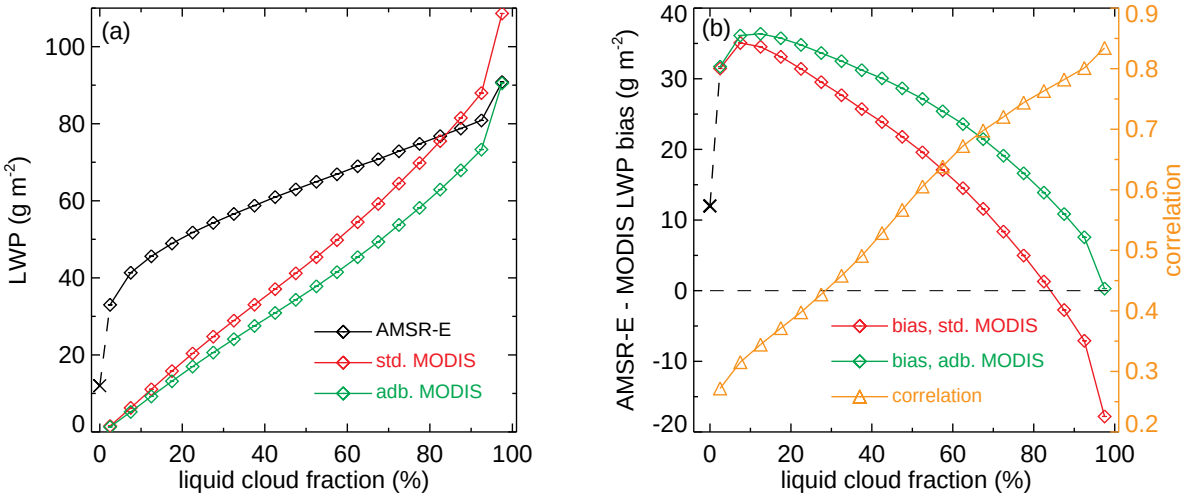

Figure 3.4. Liquid cloud fraction dependence of (a) AMSR-E and MODIS LWP, and (b) the corresponding AMSR-E – MODIS bias and correlation for warm non-precipitating marine clouds. The cross indicates the clear-sky background bias in AMSR-E LWP.

A more likely explanation, however, is reduced microwave sensitivity to low LWPs at 37 GHz, which makes retrievals in broken clouds rather susceptible to water vapor absorption and surface emission uncertainties. In section 3.1, we found a residual microwave clear-sky bias negatively correlated with surface wind and positively with water vapor. Cloud LWP bias showed similar dependencies, particularly at lower cloud amounts: AMSR-E overestimation decreased with wind speed and increased with water vapor. In addition, the

older gaseous absorption and liquid dielectric models of the Wentz algorithm have been shown by *Zuidema et al.* [2005] to cause LWP overestimations compared to more recent models. All this suggests that updated surface emission and atmospheric absorption parameterizations might reduce the disagreement between Wentz and MODIS LWPs at the low end of the distribution; however, improved MODIS cloud fraction estimates might also have a positive impact.

3.3.5. Zonal Means

Henceforward, we focus on overcast clouds because in broken cloud scenes the dominant AMSR-E overestimation makes analysis of other error sources difficult. Figure 3.5 plots the zonal variation of AMSR-E and MODIS LWP (panels a-c), and that of the resulting bias (panels d-f), separately for annual, boreal summer, and boreal winter periods. Annual results showed the LWP peak of the Inter Tropical Convergence Zone (ITCZ) in both datasets, somewhat more strongly in AMSR-E than MODIS. Microwave zonal means had additional mid-latitude maxima, more markedly in the southern hemisphere. The most striking difference between the techniques occurred poleward of 40º where AMSR-E LWP generally decreased but MODIS LWP strongly increased. Overall, standard MODIS overestimated AMSR-E in most regions and increasingly so toward the poles, with the exception of northern equatorial areas where AMSR-E was slightly larger. The results also indicated that the negligible global mean bias between microwave and adiabatic VNIR estimates was due to cancellation of errors: adiabatic MODIS underestimated AMSR-E between 45ºS-45ºN and overestimated it at higher latitudes.

Comparing seasonal results yielded some clues regarding the cause of the strong poleward increase in MODIS LWP. In boreal summer, the qualitative agreement between AMSR-E and MODIS was reasonably good in the northern hemisphere, including mid- to high latitudes. However, in the southern hemisphere MODIS showed a very rapid increase poleward of 30ºS in contrast to AMSR-E. The situation was approximately reversed in boreal winter, when the largest MODIS overestimations occurred in the northern hemisphere poleward of 30ºN, although biases were rather large in the southern hemisphere as well. In sum, the largest zonal differences occurred at high latitudes in the winter hemisphere.

These large discrepancies cannot be explained by AMSR-E LWP biases caused by Wentz cloud temperature errors, as shown by the orange lines in panels d-f (see also section 4.2). However, in section 4.1 we offer evidence that they were the likely result of MODIS LWP overestimations due to 3D retrieval errors in heterogeneous clouds at low Sun.

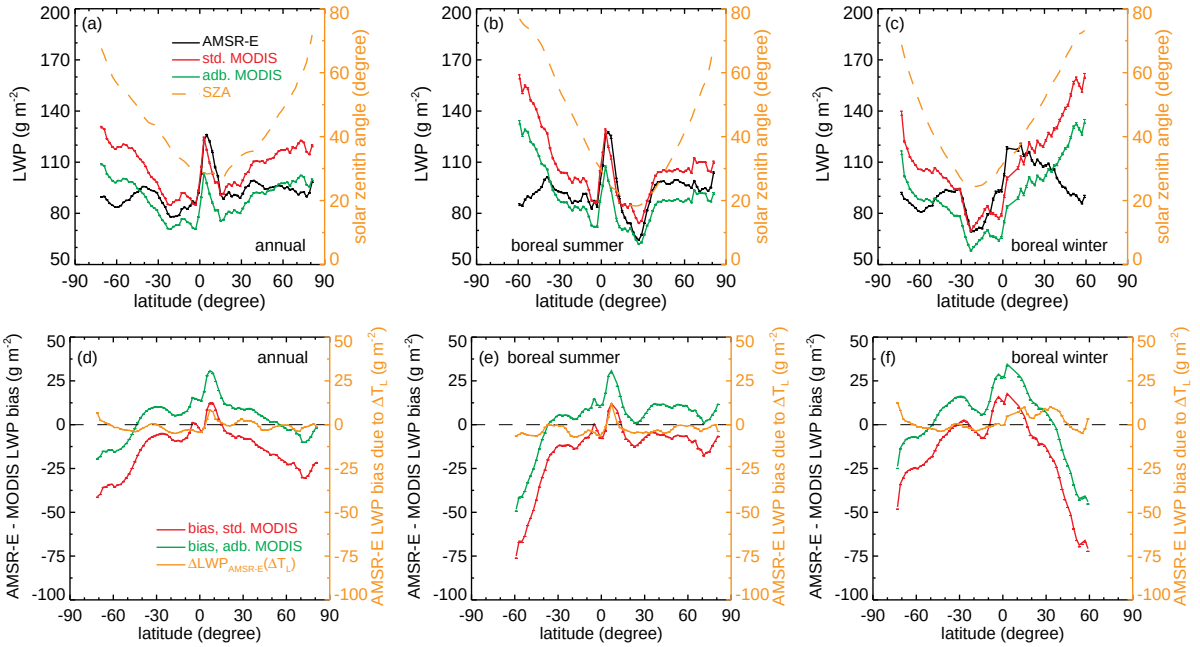

Figure 3.5. (a-c) Annual, boreal summer, and boreal winter zonal mean AMSR-E LWP (black), standard MODIS LWP (red), and adiabatic MODIS LWP (green) in overcast domains of warm non-precipitating marine clouds. Dashed orange line is solar zenith angle (SZA). (d-f) Corresponding AMSR-E – MODIS LWP bias. Orange line indicates estimated AMSR-E LWP bias due to cloud temperature errors assuming a 3%/K sensitivity (see Figure 3.11). Bars depict the standard error of the mean.

3.3.6. Global Distribution of Bias

Because zonal means can mask large regional differences, we extended the bias analysis to the full globe. Geographic variation of annual mean AMSR-E – standard MODIS LWP bias is mapped in Figure 3.6a for overcast domains. The strong zonal variation of the bias was evident here as well (cf. Figure 3.5d). Poleward of 40º MODIS consistently and increasingly overestimated AMSR-E at all longitudes. In the tropics/subtropics (30ºS-30ºN), however, large regional differences occurred corresponding to varying cloud regimes. In extensive marine Sc regions MODIS showed significantly higher values, while in areas where cumuliform clouds were more frequent AMSR-E LWPs were larger. This produced large-scale coherent bias gradients wherever marine Sc transitioned into mostly convective cloud regimes, with the two most notable areas being the Tropical Eastern/South East Pacific, and Gulf of Guinea/South East Atlantic.

In the first region, marine Sc forming over the cold Peru Current showed AMSR-E – standard MODIS LWP biases of -15 to -30 g m^{-2}. This region of negative bias also included

the Pacific Cold Tongue. Parallel to its northern edge ran an equally narrow band of positive LWP biases (up to +30 g m^{-2}) producing sharp zonal gradients in this region. A similar but more extensive LWP bias pattern occurred in the South East Atlantic off the African coast. Here, higher standard MODIS LWPs in marine Sc developing over the cold Benguela Current smoothly transitioned into higher AMSR-E LWPs in the more cumuliform clouds of the Gulf of Guinea.

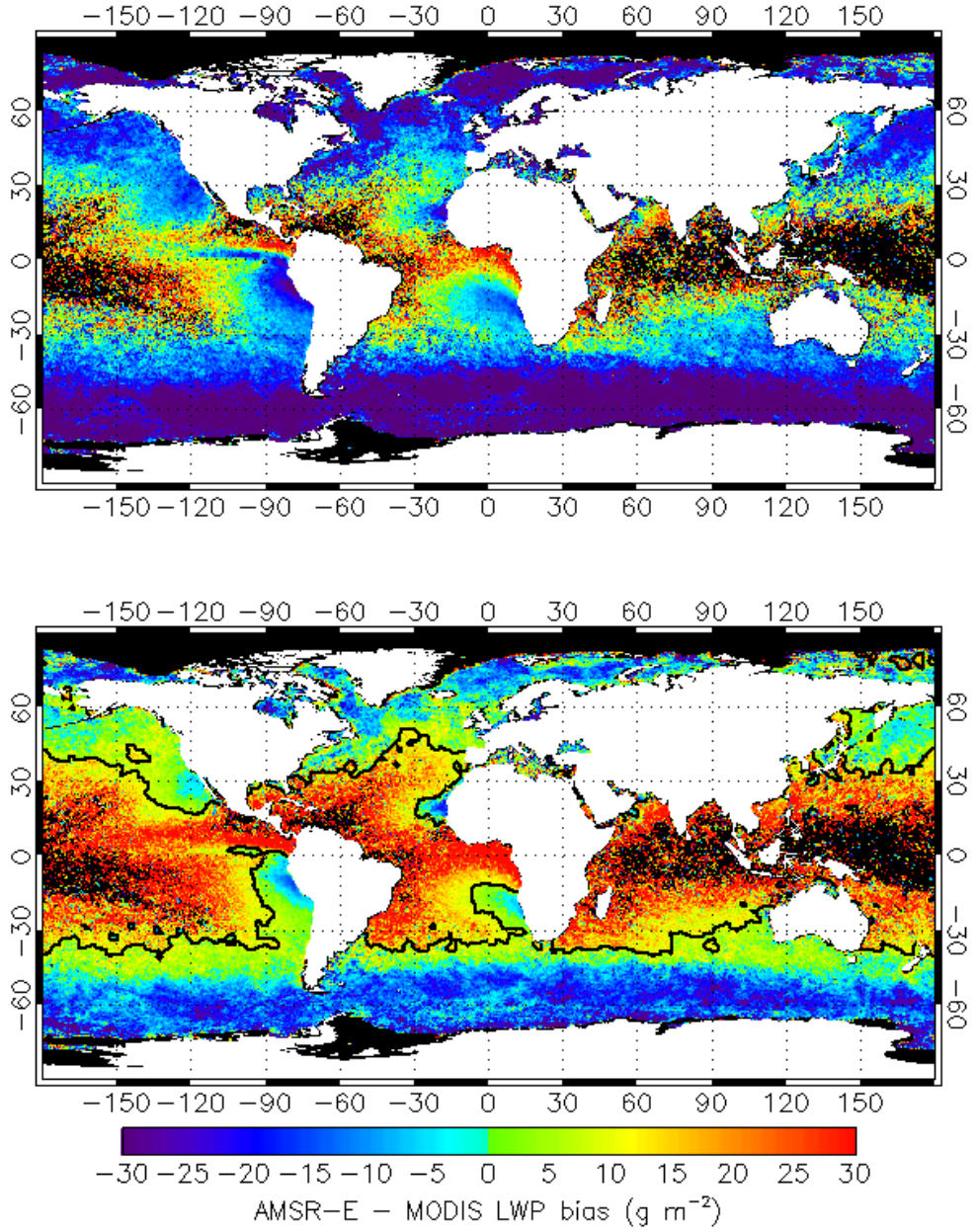

Figure 3.6. Annual AMSR-E – MODIS LWP bias map in overcast situations for (a) standard, and (b) adiabatic optical model. The black line marks the boundary between adiabatic improvement and deterioration.

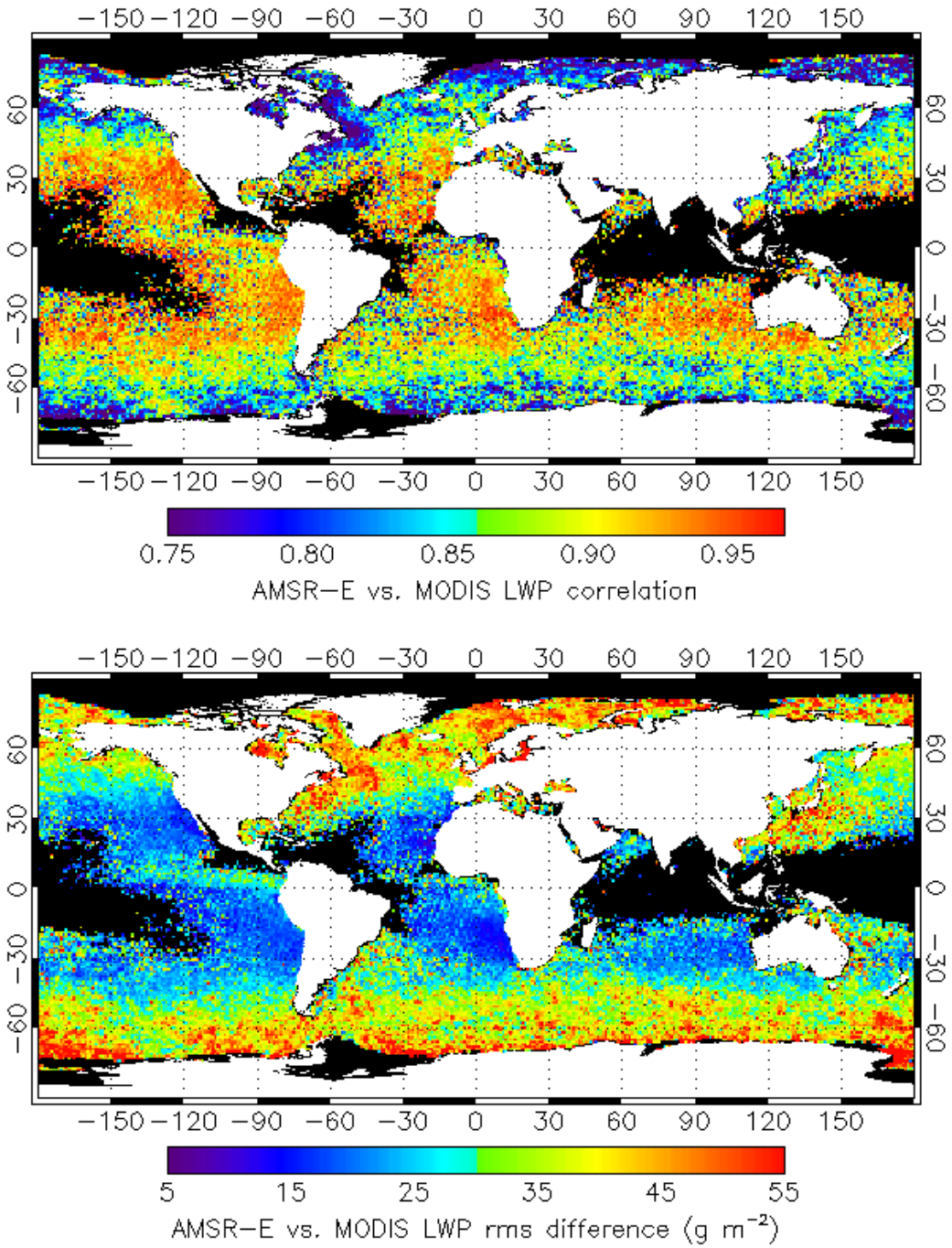

Figure 3.7. Annual AMSR-E vs. standard MODIS LWP (a) correlation, and (b) rms difference map for overcast domains. Shown results are above the 99% confidence limit.

The bias map for adiabatically corrected MODIS is plotted in Figure 3.6b. Adiabatic correction reduced the bias wherever standard MODIS overestimation was higher than 8%. (The black line delineates the border between adiabatic improvement and deterioration.) These areas were primarily mid- to high latitude oceans poleward of 40º, but also included low-latitude marine Sc regions. Within the tropics/subtropics, however, adiabatic correction

mostly increased the AMSR-E – MODIS LWP bias. Overall, we found that adiabatic LWP was an improvement over standard LWP in 75% of individual MODIS retrievals. In this data subset, the standard MODIS high bias of 23 g m^{-2} reduced to 5 g m^{-2} after the correction. In the remaining quarter of data, on the other hand, the AMSR-E high bias increased from ~0 to 16 g m^{-2}. When averaging over all data, this eliminated the global mean standard MODIS high bias of 18 g m^{-2} (see Table 1).

Finally, we investigated geographic variations in the correlation and rms difference between AMSR-E and MODIS LWPs, as illustrated in Figure 3.7. Overall, the datasets were correlated at 0.83 with an rms of 38 g m^{-2} but regional differences were non-negligible. The lowest correlations (down to 0.75) and largest rms differences (up to and above 55 g m^{-2}) were found mostly at high latitudes above 55-60º, especially in the northern hemisphere; for example, Hudson Bay, James Bay, and areas surrounding the Labrador Peninsula and Newfoundland. Encouragingly, the correspondence between the techniques was excellent in marine Sc regions with correlations up to 0.95 and typical rms differences of only 10-20 g m^{-2}, albeit with a systematic MODIS overestimation as shown before.

3.4. Potential Error Sources

3.4.1. Heterogeneity Effects in MODIS LWP

As shown previously, a strong feature of AMSR-E – MODIS LWP differences was an increasing MODIS overestimation at higher latitudes poleward of 40º. These latitudes are generally observed at lower Sun (see Figure 3.5) suggesting that different solar zenith angle (SZA) dependencies of microwave and VNIR retrievals might contribute to the observed discrepancies. Indeed, previous studies found systematic SZA-dependent biases in 1D plane-parallel cloud optical thickness retrievals. Based on Earth Radiation Budget Satellite observations, *Loeb and Davies* [1996] noted an increasing overestimation in nadir-view cloud optical thickness at higher SZAs, particularly above 60º. *Loeb and Coakley* [1998] obtained similar results in AVHRR measurements even for marine Sc, which is arguably the closest to being plane-parallel.

The strong increase in optical thickness was traced back to the fact that plane-parallel model reflectances, on average, decreased with SZA, while observed reflectances increased. The hypothesis that this discrepancy was due to neglected 3D effects, such as cloud side illumination and bumpy cloud tops was later confirmed through Monte Carlo simulations by *Loeb et al*. [1998] and *Várnai and Marshak* [2001]. The above studies only considered near-

nadir views; however, *Várnai and Marshak* [2007] found similarly strong SZA-dependent increases in MODIS cloud optical thickness at all view angles.

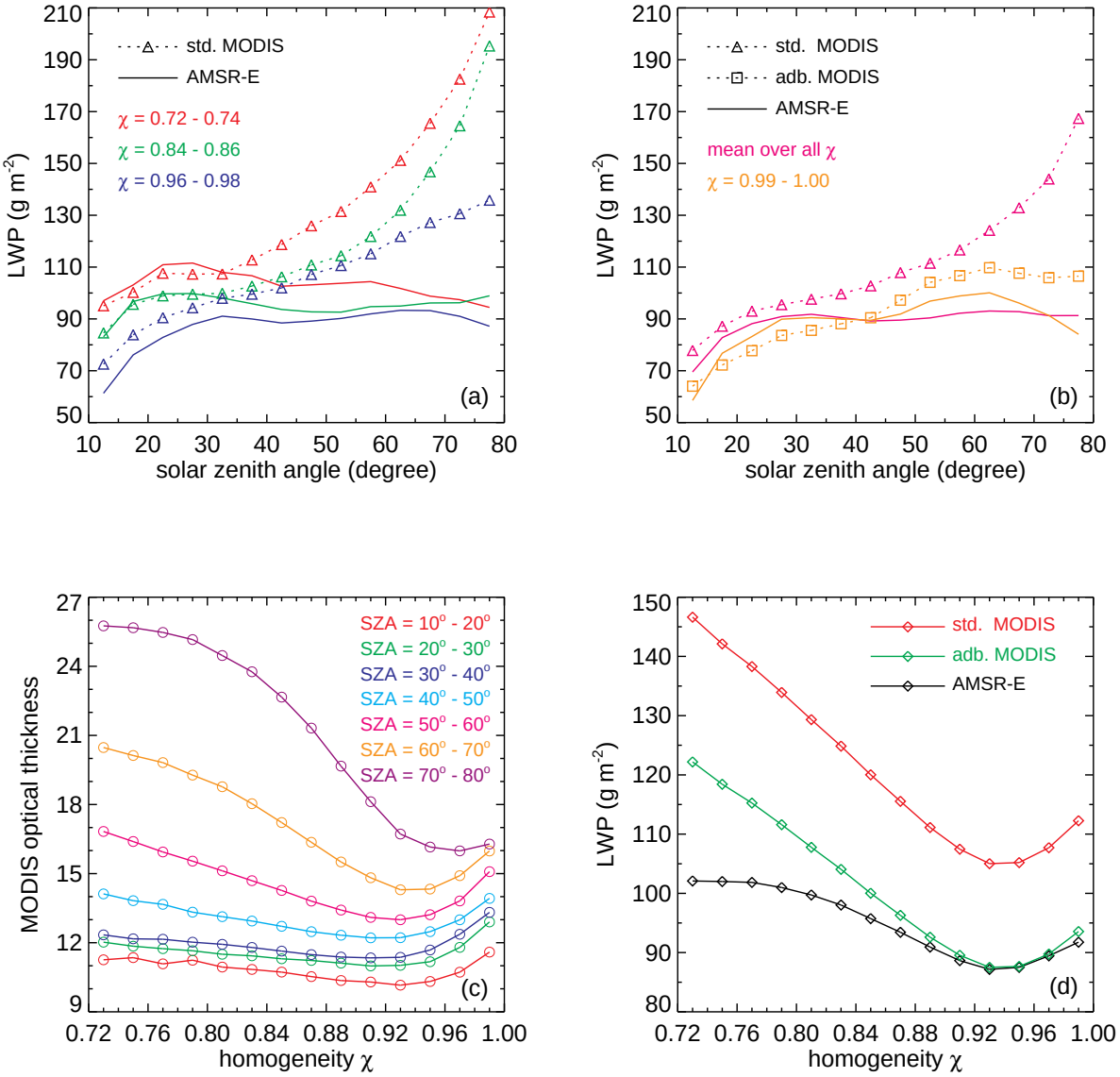

Figure 3.8. (a)-(b) Solar zenith angle (SZA) dependence of MODIS and AMSR-E LWP for various homogeneity classes. (c) MODIS cloud optical thickness versus scene homogeneity for different SZA ranges, and (d) mean (average over all SZAs) MODIS and AMSR-E LWP versus scene homogeneity. Results are for warm non-precipitating overcast domains with χ calculated at the 0.25° scale.

Motivated by these findings we analyzed AMSR-E and MODIS LWPs as a function of SZA and scene heterogeneity. Heterogeneity of a 0.25º domain was characterized by *Cahalan's* [1994] χ parameter defined as the ratio of the logarithmic and linear average of 1-

km cloud optical thicknesses. In general, χ varies from 0 to 1 with larger values indicating less heterogeneity; for the overcast domains considered in our analysis it ranged from 0.7-1.0. A detailed analysis of cloud heterogeneity from MODIS is deferred to *Oreopoulos and Cahalan* [2005]; however, two caveats are worth noting here. First, the χ parameter cannot distinguish if heterogeneity is due primarily to cloud-top height or cloud extinction variations. Second, it measures "apparent" cloud heterogeneity because it is calculated from plane-parallel retrievals, themselves affected by 3D effects. Consequently, χ may overestimate "true" heterogeneity in cases with significant shadowing and side illumination.

The SZA dependence of AMSR-E and MODIS LWP is shown in Figure 3.8a-b for four χ bins of increasing homogeneity (red, green, blue in panel a, and orange in panel b). Up to a SZA of ~35º microwave and VNIR estimates were in relatively good agreement both exhibiting modest increases, which most likely represented zonal variations in LWP. At higher SZAs, however, they showed strikingly different behavior. While AMSR-E LWP leveled off or even slightly decreased with SZA, MODIS LWP rapidly increased. The MODIS LWP increase was largest and non-linear in SZA for the most heterogeneous scenes. As homogeneity increased, the MODIS LWP rise gradually became smaller and more linear with SZA. Only in the most homogeneous clouds ($\chi = 0.99 - 1.00$) did MODIS LWP level off with SZA, *qualitatively* similarly to AMSR-E LWP; these clouds were overwhelmingly marine Sc, thus, adiabatic correction to MODIS also resulted in good *quantitative* agreement between VNIR and microwave estimates (orange curve in Figure 3.8b). The SZA dependencies of mean LWPs averaged over all χ bins are given by the magenta curves in Figure 3.8b. As before, AMSR-E and MODIS LWPs started to diverge for $SZA > 35°$, reaching a maximum MODIS overestimation of ~80 g m^{-2}, or ~90% of the AMSR-E value, at the most oblique Sun. (Restricting the analysis to fixed geographic locations, thereby eliminating zonal variations, yielded similar differences between AMSR-E and MODIS SZA dependencies.)

Our calculations confirmed optical thickness as the primary driver of the MODIS LWP rise with SZA. Up to a SZA of 35º, cloud optical thickness retrievals remained remarkably consistent irrespective of scene heterogeneity. At higher SZAs, however, optical thickness rapidly increased, especially in heterogeneous scenes. For example, between overhead and oblique Sun τ varied from 11 to 16 in the most homogeneous clouds and from 11 to 28 in the most heterogeneous clouds. Droplet effective radius, on the other hand, showed a considerably smaller increase in the 11-13.5 μm range.

Figure 3.8a also indicated a general decrease in both MODIS and AMSR-E LWP with increasing homogeneity, which we investigated in more detail. The variation of MODIS τ with homogeneity is plotted in Figure 3.8c for different SZA ranges. In accordance with our previous findings, τ systematically increased with SZA for all homogeneity values. However, at high Sun cloud optical thickness varied relatively weakly with χ, while at oblique Sun retrievals became very sensitive to scene heterogeneity. An interesting general pattern emerged whereby cloud optical thickness first decreased with increasing homogeneity reaching a minimum value at $\chi \approx 0.93$, then it started to increase for even more homogeneous clouds. In essence, this figure summarizes our findings, which are: (i) heterogeneity effects are most important at oblique Sun (maybe above a SZA of 50º), and (ii) the increase in optical thickness with SZA is significantly larger for heterogeneous than for homogeneous clouds.

Finally, Figure 3.8d depicts the overall variation of AMSR-E and MODIS LWP with cloud homogeneity, averaged for all Sun elevations. Both LWP estimates exhibited qualitatively similar behavior, suggesting that the general τ–χ dependence in Figure 3.8c was due to the nature of clouds and not 3D effects. However, MODIS retrievals were significantly more sensitive to scene heterogeneity than AMSR-E ones. In addition, standard MODIS overestimated AMSR-E by an increasing amount as heterogeneity increased. We found that in relatively homogeneous scenes adiabatic correction could remove the mean MODIS overestimation almost entirely, resulting in excellent agreement between microwave and VNIR estimates for $\chi > 0.87$. Although the adiabatic model reduced VNIR LWP biases in more heterogeneous clouds as well, here corrections exceeding adiabatic would have been needed to fully compensate for the large MODIS 3D-effect overestimations at low solar elevations.

3.4.2. Cloud Temperature Errors in AMSR-E LWP

AMSR-E LWPs are sensitive to the assumed liquid temperature because microwave absorption is stronger in colder than in warmer clouds. Therefore, underestimation of cloud temperature, that is overestimation of absorption, implies an underestimation in microwave LWP, and vice versa. Earlier versions of the Wentz algorithm specified liquid cloud temperature T_L simply as the mean temperature between the sea surface and the freezing level, the current algorithm, however, uses a parameterization based on column water vapor and SST [*Wentz and Meissner*, 2000; *Hilburn and Wentz*, 2008]. *O'Dell et al.* [2008]

investigated the errors in T_L by using temperature and cloud profiles from the European Centre for Medium-Range Weather Forecasts (ECMWF) global model. Compared to this model, they found a negative global mean bias of -1 °C and an rms error of 5 °C in the Wentz parameterization, which, they estimated, would translate to an LWP low bias and rms error of ~3% and ~13%, respectively.

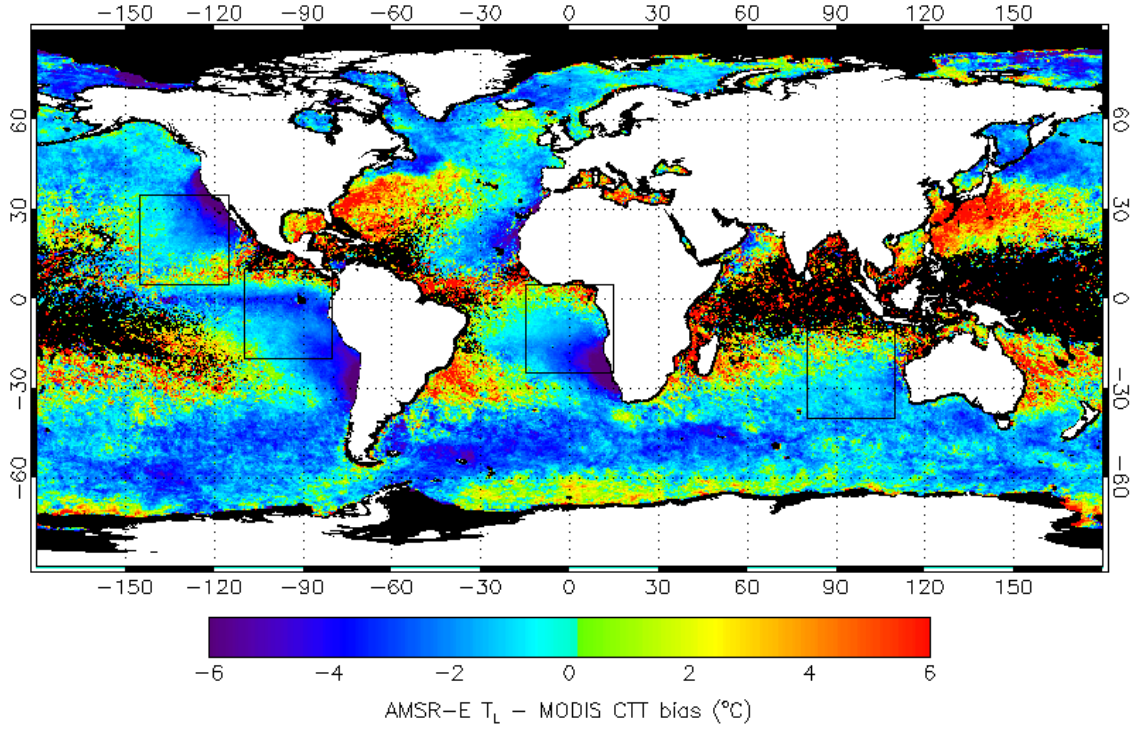

Figure 3.9. Annual bias between AMSR-E liquid cloud temperature (T_L) parameterization and MODIS cloud-top temperature (CTT) measurements for warm non-precipitating overcast domains. The relationship between LWP bias and cloud temperature bias in the four marked subregions is plotted in Figure 3.12.

In this work, we evaluated the Wentz T_L parameterization against MODIS cloud-top temperature (CTT) retrievals. In good agreement with *O'Dell et al.* [2008], we found a global annual mean temperature bias of -1.5 °C and an rms error of 5-6 °C in T_L. The bias was somewhat smaller in boreal winter (-1.2 °C) and spring (-1.2 °C), and larger in boreal summer (-2.0 °C) and fall (-1.8 °C), with an absolute minimum in March (-1 °C) and maximum in July (-2 °C). Although these global mean biases were relatively small, they resulted from partial cancellation of significantly larger regional differences as demonstrated in Figure 3.9 for annual results. Over cold oceans AMSR-E cloud temperature was generally underestimated with the largest errors, up to and beyond -6 °C, occurring in marine Sc

regions; this indicated that the current T_L parameterization did not adequately account for the temperature inversion associated with these clouds. In contrast, AMSR-E cloud temperature was overestimated by a similar amount above warm ocean currents (Kuroshio and Brazil Current, Gulf Stream) reflecting the SST dependence of the Wentz parameterization.

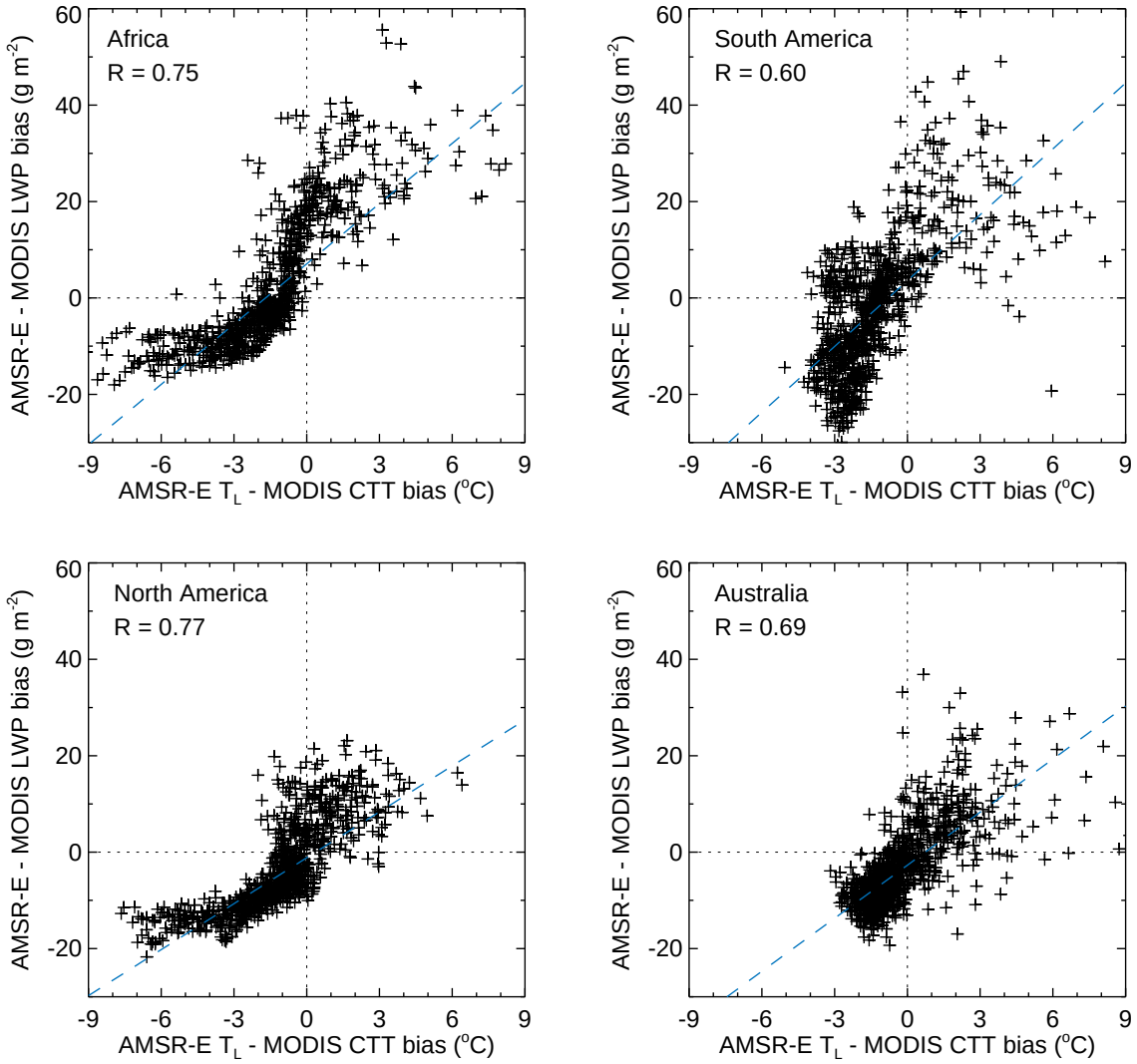

Figure 3.10. AMSR-E – standard MODIS LWP bias versus AMSR-E T_L – MODIS CTT bias in the four marked regions of Figure 3.11. Data are 1º annual means in warm non-precipitating overcast clouds, and the correlation coefficients and dashed lines correspond to linear fits.

Comparison of Figures 3.8 and 3.11 suggested that large-scale LWP bias variations might have been partly related to similar variations in cloud temperature error, particularly in marine Sc transition regions. In order to demonstrate this, we selected four such areas marked by black boxes in Figure 3.9: Africa (25ºS-5ºN, 15ºW-15ºE), South America (20ºS-10ºN,

110ºW-80ºW), North America (5º-35ºN, 145ºW-115ºW), and Australia (40ºS-10ºS, 80ºE-110ºE). Fortunately, the strong SZA-dependent MODIS overestimation, which was the dominant bias at higher latitudes/SZAs, was reduced in these low latitude/SZA areas. Scatter plots of 1º annual mean AMSR-E – standard MODIS LWP bias versus AMSR-E T_L – MODIS CTT bias are given in Figure 3.10.

In all four regions, LWP bias and cloud temperature bias showed moderately strong positive correlations. The relationship was tightest in North America and Africa, the latter even suggesting a non-linear relationship between the quantities, as indicated by a considerably higher rank correlation of 0.91. Everything else being equal, a negative liquid temperature bias should cause a negative microwave LWP bias and vice versa. In broad agreement with this expectation, AMSR-E LWP mostly underestimated/overestimated MODIS LWP below/above a cloud temperature error of -1/0 °C, but clearly, additional effects were at play as well. The absolute LWP biases in Figure 3.10 corresponded to relative biases of ±20%. If one uses *O'Dell et al.*'s [2008] sensitivity estimate of ~3%/°C, temperature errors of ±6 °C would yield relative AMSR-E LWP errors of similar magnitude. The actual temperature sensitivity of operational Wentz LWPs will be quantified in a future study, by replacing the existing T_L parameterization with MODIS cloud-top temperatures.

3.4.3. Cloud Vertical Stratification in MODIS LWP

A potentially significant error source in VNIR LWP retrievals is neglecting cloud vertical stratification. As explained in section 2.2, the standard MODIS parameterization assumes a constant r_e throughout the cloud. Because the water-absorbing MODIS channels favorably sample towards cloud top, this might lead to both negative and positive LWP biases depending on the actual effective radius profile. The adiabatic parameterization constitutes a first-order correction in marine Sc often characterized by r_e increasing from cloud base to top, but exacerbates microwave-VNIR LWP differences when the droplet profile is neutral or decreasing with height.

In theory, a better approach would be to estimate droplet profile on a case-by-case basis from the three near-infrared MODIS size retrievals. *Platnick* [2000], however, expressed serious doubts regarding the possibility of such an inversion due to the relatively little difference in the information content of the 1.6 and 2.2 μm bands. Nevertheless, *Chen et al.* [2007] made an attempt to derive linear r_e profiles in a dataset limited to one day, and claimed a small but systematic improvement of ~10% in corresponding VNIR LWPs

compared to AMSR-E. *Chen et al.* [2008] further applied this method to data from the East Pacific Investigation of Climate (EPIC) Stratocumulus Study, and found that r_e vertically increased in non-drizzling clouds, but often decreased in drizzling cases.

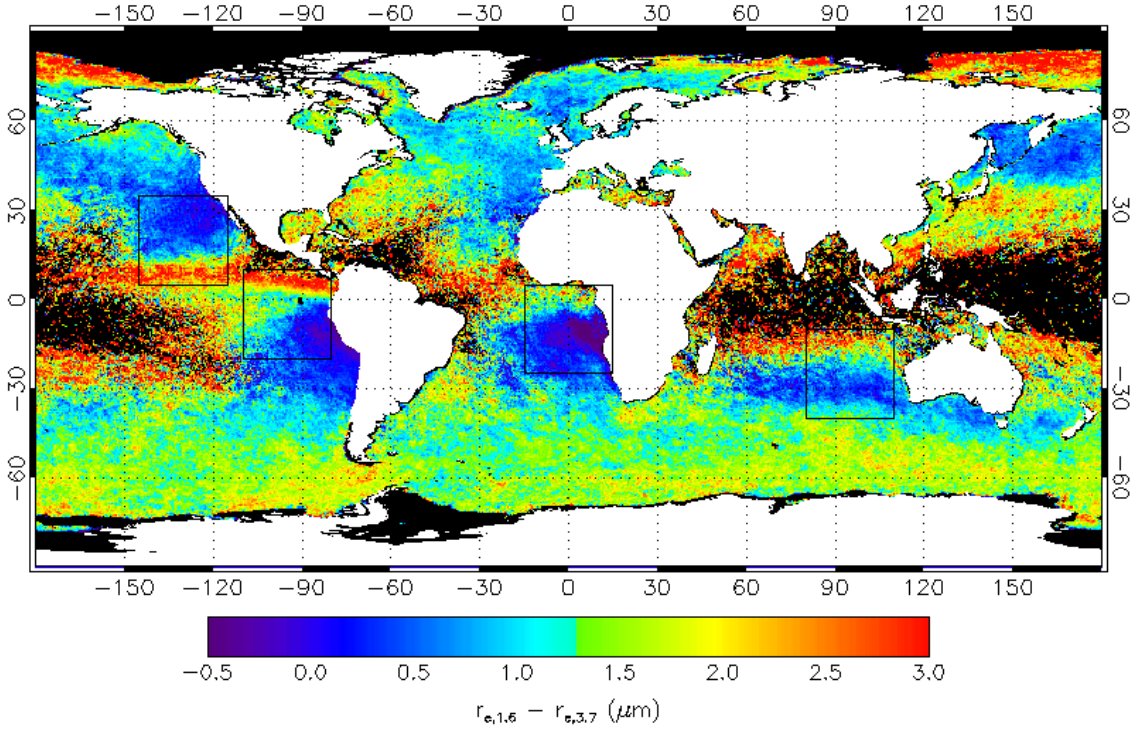

Figure 3.11. Annual mean effective radius difference between the 1.6 μm and 3.7 μm MODIS channels for warm non-precipitating overcast domains. The relationship between LWP bias and effective radius difference in the four marked sub-regions is plotted in Figure 3.14.

Here, we only investigated if large-scale LWP bias variations in Figure 3.6 might be related to variations in cloud vertical stratification, but did not derive VNIR LWP corrections. To this effect, we analyzed the geographical distribution of MODIS effective radius differences focusing primarily on the least noisy 1.6-3.7 μm discrepancies. However, in the regional analysis off the Namibian coast we relied on 2.2-3.7 μm differences in order to minimize absorbing aerosol effects, which introduce the largest negative biases in 1.6-μm r_e retrievals [*Haywood et al.*, 2004]. Nominally, negative/positive 1.6-3.7 μm or 2.2-3.7 μm r_e differences would indicate drop sizes increasing/decreasing from cloud base to top.

Annual mean results, given in Figure 3.11, indicated that the geographic distribution of Δr_e was not random; in the tropics/subtropics it appeared to broadly vary with cloud type. Marine Sc was characterized by small negative/positive values, which systematically

increased to larger positive values in cumuliform cloud regimes. The southern oceans and Arctic regions also showed large positive values, suggesting that undetected cloud-top ice might be partially responsible for the observed spatial pattern. In order to reduce possible ice effects, we also made calculations restricted to cloud-top temperatures above 273 K and 278 K. In both cases, spatial variations were very similar to Figure 3.11 showing the sharp transitions in the tropics/subtropics.

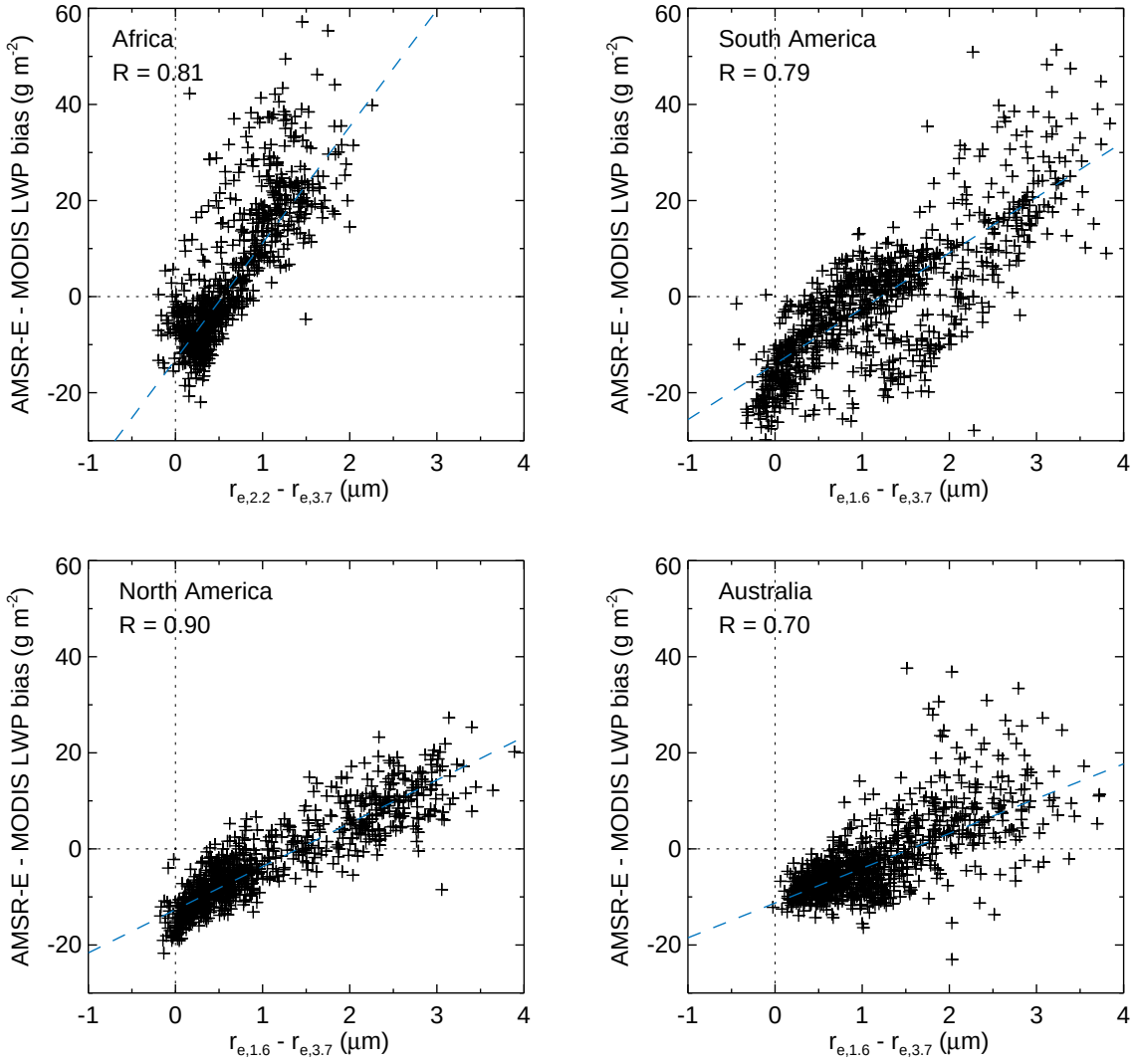

Figure 3.12. AMSR-E – standard MODIS LWP bias versus MODIS effective radius difference in the four marked regions of Figure 3.13. Effective radius difference is between the 2.2 μm and 3.7 μm channels for Africa in order to minimize absorbing aerosol effects, everywhere else it is between the 1.6 μm and 3.7 μm channels. Data are 1° annual means in warm non-precipitating overcast clouds, and the correlation coefficients and dashed lines correspond to linear fits.

Contrary to expectations, annual mean Δr_e tended to be mostly positive, even in marine Sc, suggesting a decrease in drop size from cloud base to top. In Sc areas Δr_e was mostly negative up to -1 μm in boreal summer, in boreal winter, however, it shifted to larger positive values resulting in small positive annual means. Consequently, although LWP bias was better correlated with Δr_e than with microwave cloud temperature error, the sign of Δr_e could not generally differentiate between MODIS LWP overestimation and underestimation. This is clearly demonstrated in Figure 3.12 plotting LWP bias as a function of effective radius difference for 1º annual means in our four selected transition regions. As shown, LWP bias switched sign at a positive Δr_e between 0.5 and 1.5 μm instead of near zero. Boreal summer and boreal winter scatter plots were similar but with the former shifted to lower Δr_e by 0.5-1 μm and the latter to larger Δr_e by ~0.5 μm. As a result, the sign of Δr_e was indicative of that of LWP bias only in boreal summer.

At this point, we do not have an explanation for this puzzling result and can only list a number of potential causes. Although the 3.7 μm band is well calibrated, the complicated separation of thermal and solar components might introduce r_e retrieval errors. Another possibility is that positive vertical drop size gradients tend to be larger than negative ones, leading to mostly positive average values [*Chang and Li*, 2003]. Cloud-top entrainment might also play a role. Both in-situ measurements and large eddy simulations show that a sharp decrease in liquid water content and effective radius could occur in the topmost few dozen meters of Sc clouds due to mixing with drier ambient air [*Stevens*, 2005]. This drop-off might reduce effective radius retrievals particularly in the 3.7 μm band as its weighting function peaks closest to cloud top.

Concerning entrainment effects we note that POLDER (Polarization and Directionality of the Earth's Reflectances) drop size estimates in Sc also showed a low bias of ~2 μm compared to MODIS 2.2-μm values [*Bréon and Doutriaux-Boucher*, 2005]. Because the polarization technique is based on single scattering it is probably even more sensitive to cloud-top than the 3.7 μm MODIS channel. Although a satisfactory explanation was not found for the POLDER-MODIS r_e bias either, entrainment mixing was offered as a possible contributing factor. The impact of this effect on MODIS drop size retrievals will have to be quantified by recalculating near-infrared weighting functions using more realistic vertical profiles than the ones considered by *Platnick* [2000], which ignored the cloud-top drop-off.

As a final note, we warn against over-interpreting the above results. Instantaneous retrievals are noisy and subject to a multitude of possible errors, making it difficult to gauge the exact information content of near-infrared channels regarding cloud stratification. What can be said with some certainty is that in the tropics/subtropics, large-scale variations of AMSR-E – MODIS LWP bias appear associated with Sc to Cu transition, and so do variations of effective radius difference. However, more detailed algorithm sensitivity studies will be needed to establish if this correlation is fortuitous or indeed physical.

3.4.4. Absorbing Aerosol Effects in MODIS LWP

In this section, we estimate the effect of absorbing aerosols, which can introduce a negative bias in both droplet effective radius and optical thickness, and hence in MODIS LWP, when they reside above low-level clouds. This negative bias in the baseline 2.2-μm effective radius is usually less than 1 μm; however, it can be up to 30% in optical thickness according to calculations by *Haywood et al.* [2004]. *Bennartz* [2007] noted a systematic MODIS LWP underestimation in Sc off southern Africa during the biomass-burning season, which was attributed to overlying absorbing aerosols by *Bennartz and Harshvardhan* [2007]. In the same region and season, *Wilcox et al.* [2009] estimated a domain-mean absorbing aerosol effect of 5.6 g m^{-2}, defined as AMSR-E – MODIS LWP bias for all samples minus that for unpolluted/weakly polluted samples with OMI AI ≤ 1.

Using this definition, we first estimated the annual global mean absorbing aerosol effect in our data, and found it a trivial -1 g m^{-2}. This was not surprising considering that absorbing aerosols are highly seasonal and cover only a small portion of oceans at any given time. Next, we made calculations for the period July-August-September in the study area of *Wilcox et al.* [2009] (20°S-0°, 10°W-15°E), which was a subset of our previously defined Africa domain. As shown in Figure 3.6, this region is characterized by a marked south-north LWP bias gradient, in all seasons and independently of the presence of smoke aerosols. Neglecting this underlying LWP bias pattern could distort estimates of aerosol effect because different AI bins sample different parts of the domain as demonstrated in Figure 3.13a for 2007. Here, the unpolluted background bias was calculated from cases with AI ≤ 1, and the contour lines encompass 67% of observations in the given AI bins. The smallest AI bin mostly sampled the southern portion of the domain further out at sea, but as AI increased sampling moved north and east, closer to shore (the source region). Similar results were

obtained for the biomass burning seasons in 2005 and 2006 considered by *Wilcox et al.* [2009], with AI bin locations showing some interannual variations.

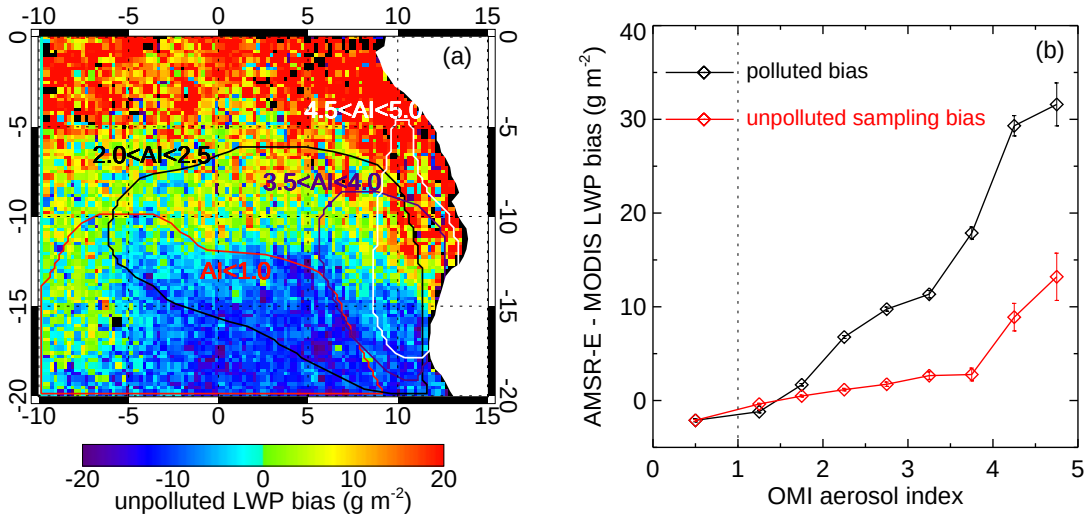

Figure 3.13. (a) Geographic distribution of AMSR-E – standard MODIS LWP bias in the African biomass smoke region calculated for warm non-precipitating overcast clouds with OMI AI ≤ 1 and averaged over July-August-September 2007. Contour lines encompass 67% of observations in the given AI bins. (b) LWP bias as a function of aerosol index with bars depicting the standard error of the mean. The black curve represents smoke-affected retrievals, while the red curve is the spatial sampling bias obtained from panel a. Note: for the red ("unpolluted") curve OMI AI indicates geographic location within the region, rather than actual aerosol load.

The resulting sampling effect is depicted in Figure 3.13b, which plots domain-mean AMSR-E – standard MODIS LWP bias for AI values 1-5, corresponding to MODIS aerosol optical depths between 0.1 and 2.1. The black curve shows retrievals actually affected by smoke, while the red curve is the sampling artifact estimated as the average background (unpolluted) LWP bias at the locations of AI measurements in a particular bin. For weakly polluted cases with AI ≤ 1, the LWP bias was very close to zero due to cancellation of errors between the southern and northern parts of the domain. At higher aerosol loads, however, MODIS increasingly underestimated AMSR-E as a result of reduced cloud optical thickness. (The MODIS LWP underestimation increased with optical thickness in agreement with *Haywood et al.* [2004] and *Wilcox et al.* [2009].) As indicated by the red curve, part of the

apparent absorbing aerosol bias was in fact caused by larger AI values preferably occurring in areas where MODIS generally underestimated AMSR-E. Neglecting such sampling artifacts, as in *Wilcox et al.* [2009], could lead to overestimating absorbing aerosol effects by 30-40% at larger AI values.

As shown above, absorbing aerosols can introduce significant VNIR LWP biases at the highest aerosol loads; however, most of our data in Figure 3.13b were only weakly polluted, resulting in a rather small mean effect. For example, the apparent reduction in domain-mean MODIS LWP during the 2007 biomass burning season was only ~3 g m^{-2} (average of black curve), which further reduced to slightly below 2 g m^{-2} after sampling issues were accounted for (average of the difference between the black and red curves). The apparent and corrected MODIS underestimations for the 2005-2006 biomass burning season were 4-5 g m^{-2} (in reasonable agreement with *Wilcox et al.* [2009]) and 2-3 g m^{-2}, respectively.

3.4.5. Cloud-Rain Partitioning Issues in AMSR-E LWP

Up to this point, we only considered non-raining clouds in our comparison. In this section, we extend the analysis to rain-flagged cases; however, still excluding broken or ice-contaminated scenes. These criteria yielded a further 1.4 million samples, but limited rain rates to below 5 mm/hr because higher values were associated with the presence of ice. As explained in section 2.1, rain seriously complicates any microwave retrieval technique because it requires a priori partitioning of total water into cloud and rain components. Specifically, the Wentz algorithm uses a globally fixed rain threshold of 180 g m^{-2} and parameterizes LWP in precipitating clouds as proportional to the square root of rain rate.

In order to gain some insight into the validity of these assumptions, we evaluated AMSR-E LWP as a function of MODIS adiabatic LWP for the combined (rain-free plus rain-flagged) dataset. (We used adiabatic MODIS retrievals as reference here because they are unbiased compared to AMSR-E in a global mean sense.) Annual results are plotted in Figure 3.14 by the solid red curve, showing quite good agreement between microwave and VNIR estimates up to the rain threshold, above which, however, AMSR-E increasingly underestimated MODIS. The mean underestimation reached ~150 g m^{-2} (or 30%) at the largest MODIS LWPs.

What could cause these discrepancies? As noted earlier, MODIS increasingly overestimated AMSR-E at larger solar zenith angles, particularly in heterogeneous clouds, which could produce qualitatively similar results. Prompted by this, we made separate

calculations for the most heterogeneous and most homogeneous third of clouds. In heterogeneous cases, retrievals started to diverge at a slightly smaller LWP, while in homogeneous cases the divergence occurred at a somewhat larger LWP, otherwise results were comparable and stayed within ±30 g m^{-2} of the overall average (red curve). Furthermore, *Wilcox et al.* [2009] found similar AMSR-E underestimations at lower latitudes as well, where MODIS heterogeneity effects were generally reduced. These findings suggested that VNIR heterogeneity effects alone could not explain the observed discrepancies.

The fact that microwave and VNIR estimates started to diverge above the rain threshold LWP pointed to possible cloud-rain partitioning issues in AMSR-E retrievals. A relatively low precipitation threshold means that part of the water content of thicker rain-free clouds might be erroneously assigned to rain. In fact, CloudSat retrievals indicate only ~30% probability of precipitation in warm clouds at an LWP of 180-200 g m^{-2} [*Lebsock et al.*, 2008]. This suggests that a significant portion of rain-flagged AMSR-E retrievals might actually be rain-free, and as such, subject to the above error. (It should be noted, however, that a large number of low-level liquid clouds are below the detection limit of the CloudSat radar or are otherwise missed due to surface contamination.)

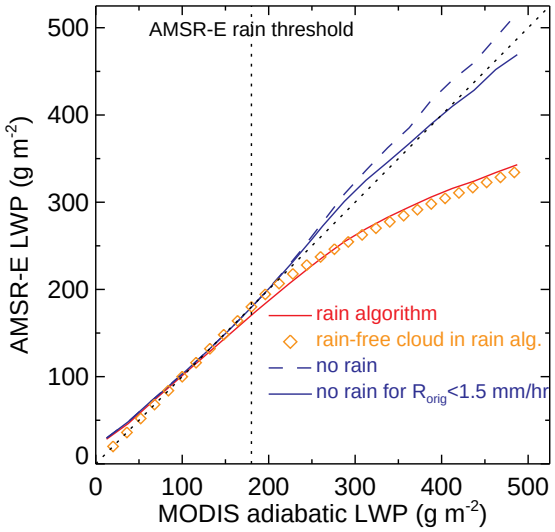

Figure 3.14. Cloud-rain partitioning effects on AMSR-E – adiabatic MODIS LWP comparison. The solid red curve corresponds to actual retrievals with the operational Wentz rain algorithm. Gold diamonds are estimates of what the rain algorithm would retrieve in rain-free clouds. The blue curves are modified Wentz retrievals with rain removal turned off (i) completely (dashed), and (ii) only for rain rates below 1.5 mm/hr (solid).

We investigated the effect of rain removal by estimating what LWP the operational AMSR-E algorithm would retrieve in rain-free clouds above the precipitation threshold (see gold diamonds in Figure 3.14). These estimates were derived from the governing equations in section 2.1 and confirmed the observed biases: an increasing portion of the water content of thicker rain-free clouds was assigned to precipitation. Obviously, a fraction of clouds with LWP between 180 and 500 g m^{-2} bound to precipitate, thus, the excellent fit between rain-free cloud estimates and actual observations must also have been due to the presence of additional biases (liquid temperature error, heterogeneity effects, etc.). Nevertheless, these results demonstrated the general effect of cloud-rain partitioning errors.

As a further step, Remote Sensing Systems reprocessed our boreal summer and boreal winter data with rain removal completely turned off. These modified AMSR-E LWPs, indicated by the dashed blue line, compared considerably better with MODIS LWPs, but now exhibited slight overestimations. We found the best agreement between microwave and VNIR estimates when rain removal was only turned off for rain rates below 1.5 mm/hr, as shown by the solid blue line. Taken together, these findings suggested that the 180 g m^{-2} precipitation threshold was too low; at least in a global mean sense.

Finally, we note that the Wentz algorithm is tuned to produce reasonable rain rates and rain coverage in comparison with other well-known precipitation climatologies. It might be impossible to optimize the algorithm simultaneously for LWP and rain. However, a separate product specifically minimizing discrepancies with MODIS LWPs could be introduced. Alternatively, rain removal could be turned off entirely in order to retrieve total (cloud plus rain) water path, which is the quantity microwave techniques are ultimately sensitive to. This could facilitate more straightforward comparisons with climate models by eliminating differences due to dissimilar cloud-rain partitioning in models and satellite retrievals.

3.5. Summary

We analyzed one year of AMSR-E Wentz and MODIS cloud liquid water path estimates, representing the current state-of-the-art in microwave and VNIR retrievals. The comparison was made over the global oceans on a quarter-degree scale and only included warm clouds in order to avoid ambiguities due to ice; however, both standard (vertically homogeneous), and adiabatically stratified MODIS LWPs were evaluated. Our goal was to characterize microwave-VNIR LWP differences in a statistically robust dataset, and identify their potential causes for future studies. Main findings are summarized as follows.

When all scenes were considered, AMSR-E overestimated MODIS by 45% on average, and retrievals were only moderately correlated with a coefficient of 0.74 and rms difference of 41 g m^{-2}. However, we found the microwave-VNIR comparison strongly dependent on cloud fraction and geographic location. In overcast scenes, estimates were generally better correlated at 0.83, but with significant regional variations. The relationship between the techniques was loosest at high latitudes above 55º, and tightest in marine Sc regions with correlations up to 0.95 and typical rms differences of 10-20 g m^{-2}. Overcast domains were also characterized by a MODIS high bias. In broken scenes, on the other hand, AMSR-E increasingly overestimated MODIS and retrievals became gradually uncorrelated as cloud fraction decreased below 80%.

Although we could not fully explain this microwave high bias at low cloud fractions, we noted a global mean AMSR-E LWP bias of 12 g m^{-2} in cloud-free scenes as well. This clear-sky microwave bias showed systematic geographic variations, being smallest in colder marine Sc regions and largest over warm oceans. In addition, the AMSR-E clear-sky bias and low-cloud-fraction bias both had similar dependencies: a negative correlation with surface wind speed and a weaker positive correlation with water vapor. These results suggested that uncertainties in surface emission and gaseous absorption models were partly responsible for Wentz overestimation in thin broken clouds.

The remainder of the study focused exclusively on overcast domains. In this subset, the global annual mean MODIS overestimation of ~17% could be almost completely eliminated by adiabatic correction, which worked equally well on monthly time scales, with MODIS global means being within 5 g m^{-2} (or 6%) of AMSR-E means. However, the excellent mean performance of the adiabatic model masked significant regional differences. Zonal means showed AMSR-E overestimation between 45ºS-45ºN, and rapidly increasing MODIS overestimation at higher latitudes, particularly in the winter hemisphere. This was the result of strikingly different latitudinal variations in LWP, whereby AMSR-E generally decreased but MODIS increased toward the poles.

In the tropics/subtropics, the AMSR-E – MODIS LWP bias also showed systematic variations with cloud regimes. In marine Sc regions MODIS overestimated AMSR-E, while in areas frequented by cumuliform clouds the reverse was true. This resulted in large-scale coherent spatial patterns in LWP bias wherever Sc transitioned into trade wind Cu. Most notably, there were marked zonal LWP bias gradients at the Pacific Cold Tongue, and in an extensive area stretching from the Namibian coast to the Gulf of Guinea.

Prompted by the existence of systematic LWP bias variations in the African Sc region, generally regarded as a test bed of aerosol-cloud interactions, we estimated absorbing aerosol effects on VNIR retrievals. In a global annual mean sense, absorbing aerosols introduced a trivial (-1 g m^{-2}) low bias in MODIS LWPs. The regional-mean bias during the biomass-burning season was only slightly larger -3 to -5 g m^{-2}, although locally it could be as high as -30 g m^{-2} in heavily polluted areas. However, 30-40% of the apparent absorbing aerosol bias could be attributed to sampling artifacts due to systematic zonal variations in AMSR-E – MODIS LWP difference. These results implied that neglecting persistent geographic variations in the background (unpolluted) microwave-VNIR LWP bias could lead to overestimating aerosol effects in VNIR retrievals.

In pursuit of an explanation for the increasing MODIS overestimation at high latitudes, we analyzed the solar zenith angle dependence of microwave and VNIR retrievals. Up to a SZA of 35º the techniques showed good agreement, at lower Sun, however, they diverged: AMSR-E leveled off, but MODIS rapidly increased with SZA driven by an increase in cloud optical thickness. In addition, while the SZA dependence of microwave estimates was relatively insensitive to scene type, the increase in MODIS LWPs with SZA was significantly larger in heterogeneous than in homogeneous clouds. Only in the most homogeneous clouds did VNIR LWPs show SZA dependence qualitatively similar to microwave LWPs. These findings suggested that microwave-VNIR differences at high latitudes were largely due to 3D effects in the 1D MODIS retrievals over heterogeneous clouds at low Sun.

Such heterogeneity effects were significantly reduced at lower latitudes; hence, they were unlikely to play a major role in the emergence of the coherent tropical LWP bias patterns. A more likely candidate was systematic errors in the Wentz cloud temperature parameterization, which we evaluated against MODIS cloud-top temperatures. Although the global mean cloud temperature bias was only -1.5 °C, regional errors were as high as ±6 °C and showed geographic variations similar to LWP bias variations. In marine Sc (over colder oceans) the Wentz parameterization underestimated, while in cumuliform clouds (over warmer oceans) overestimated liquid temperature, resulting in moderately strong (R = 0.6-0.8) large-scale correlations between temperature error and LWP bias in Sc transition regions.

Systematic errors in standard MODIS LWP due to geographic variations in vertical cloud stratification might have also contributed to the tropical LWP bias patterns. Although the adiabatic model removed the MODIS high bias in a global mean sense, regionally it represented an improvement in marine Sc only, while exacerbated differences in cumuliform

clouds where standard MODIS generally underestimated AMSR-E. Motivated by this, we investigated if MODIS effective radius difference offered some clues about vertical cloud stratification. We found that *relative* variations in 1.6-3.7 μm effective radius difference also showed similar large-scale patterns as microwave-VNIR LWP bias, resulting in significant correlations (R = 0.7-0.9) between the quantities. However, effective radius difference was mostly positive; thus, its sign was generally a poor indicator of the sign of LWP bias. We realize that interpreting the information content of MODIS near-infrared channels is rather ambiguous; nevertheless, we believe these apparent large-scale correlations do warrant further study.

Finally, we investigated cloud-rain partitioning uncertainties in Wentz retrievals, prompted by the fact that AMSR-E increasingly underestimated MODIS at LWPs above the microwave precipitation threshold. The fixed rain threshold of only 180 g m^{-2} resulted in a significant number of rain-free clouds being processed as raining clouds. We found that the AMSR-E low bias could be well explained by the Wentz algorithm erroneously assigning an increasing portion of the liquid water content of such clouds to precipitation. In fact, when rain retrieval was completely turned off, AMSR-E LWPs compared significantly better with MODIS values, but now exhibited slight overestimations. The agreement between microwave and VNIR estimates was best when rain removal was only turned off for rain rates below 1.5 mm/hr. Taken together, these findings indicated that the Wentz precipitation threshold was too low.

Of the potential error sources listed above, the ones affecting microwave retrievals appear somewhat easier to tackle. The sensitivity of Wentz LWPs to cloud temperature uncertainties could be straightforwardly evaluated by replacing the current parameterization with MODIS cloud-top temperatures. Some progress could also be made in deriving a more realistic cloud-rain partitioning formulation, either from CloudSat retrievals or cloud resolving models. Quantifying and correcting for VNIR retrieval errors due to heterogeneity effects or cloud vertical stratification remain significantly more challenging. Perhaps a statistical inversion technique utilizing 3D radiative transfer calculations in a large number of simulated cloud fields offers the best hope to handle such errors in an operational context.

Chapter 4

Evaluating Diurnal Cycle of South Atlantic Marine Boundary Layer Clouds using SEVIRI VNIR and TMI Microwave Retrievals

The main objective of this chapter is to evaluate the diurnal cycle of South Atlantic marine boundary layer clouds and its seasonal variability using cloud microphysical and optical properties from SEVIRI VNIR measurements, as well as cloud liquid water path from TMI microwave observations. The best agreement between SEVIRI VNIR and TMI microwave technique is observed over the marine Sc region, with least bias within ±5 g m^{-2} and high correlation of 0.9. The diurnal cycle of TMI and SEVIRI liquid water path also showed very good agreement within ±5 g m^{-2} over this Sc regime in all seasons except JJA and SON (JASO is affected by absorbing aerosols, and neglecting those aerosols affected datasets from the analysis showed better comparison). In terms of diurnal cycle, both TMI and SEVIRI LWP decreased from morning to late afternoon and thereafter a slight increase was observed. The diurnal variation of SEVIRI LWP followed the variation in cloud optical thickness and in fact the cloud fraction and cloud physical thickness; whereas droplet effective radius and droplet number concentration showed less variability with time. The largest disagreement is observed in the trade wind Cu, due to the deficit in both microwave and VNIR measurement techniques in the partial cloudy scenes. Comparison of SEVIRI and MODIS CPP retrievals showed very good agreement between SEVIRI and MODIS with correlation ≥ 0.9 in the fully overcast cases; on the otherhand MODIS overestimated SEVIRI values over broken cases. We have noticed that the use of 1.6 μm channel effective radius applies automatic adiabatic correction to the Sc clouds in SEVIRI LWP retrievals, otherwise a 5/6 correction factor has to be applied for MODIS LWP retrievals (which is based on 2.2 μm channel retrieved effective radius) while comparing them with microwave retrieved LWP.

4.1. Introduction

The low-level marine clouds are particularly important because they constitute the main source of uncertainty in simulated cloud feedbacks [*Bony and Dufresne,* 2005]. These clouds typically occur persistently in the subtropical subsidence areas and reflect around 30% of the incoming solar radiation back to space. At the same time, longwave cooling rates are not affected very strongly because of the comparably low temperature difference between the ocean surface and the cloud top. The net energetic effect of these clouds is therefore a cooling

of the atmosphere [*Manabe and Strickler,* 1964; *Manabe and Wetherald,* 1967]. Recent observational evidence indicates that low clouds reduce the net radiation balance on a global annually averaged basis by about 15 Wm^{-2} [*Hartmann et al.,* 1992]. Because of the sensitivity of the earth's radiation budget to low clouds, understanding the characteristics of low clouds is a crucial climate question [*Randall et al.,* 1984].

The diurnal cycle of marine stratiform clouds has an important influence on their radiative effectiveness, as it affects the radiation budget primarily through their albedo. Stratocumulus clouds can exhibit a marked diurnal cycle [*Wood et al.,* 2002]. During the night, turbulence is driven by a strong long-wave radiative cooling near the top of the Sc clouds and results in a vertically well-mixed stable boundary layer. In contrast, during daytime the transport of heat and moisture from the surface into the cloud layer is effectively reduced or even cut off due to the absorption of solar radiation in the cloud layer and hence the stable boundary layer become decoupled. Because entrainment maintains a steady supply of relatively warm and dry air from above the inversion into the cloud layer, the cloud layer can rapidly thin or even disappear during daytime. In its Fourth Assessment Report of the Intergovernmental Panel on Climate Change (IPCC-AR4), *Forster et al.* [2007] highlights the diurnal cycle of thin, stratiform clouds to be one of the major uncertainties in current estimates of cloud radiative forcing. *Wilson and Mitchell* [1986] showed that, changing the resolution of the diurnal cycle of cloud and radiative fluxes in an AGCM can affect the simulated climate. *Rozendaal et al.* [1995] inferred that, calculated with diurnally averaged cloud fraction overestimate cloud forcing by up to 3 Wm^{-2} (16%) at the surface and 3 Wm^{-2} (7%) at the top of the atmosphere compared to calculations that account for the diurnal cycle. Comparisons of the observed diurnal cycle of clouds with models also find large and potentially systematic errors in the modelled diurnal cycle [*O'Dell et al.,* 2008; *Roebeling and van Meijgaard,* 2009]. Similarly, a recent study on aerosol climate effects by the U.S. Climate Change Science Program [*Chin et al.,* 2009] identified the diurnal cycle of clouds as one important outstanding scientific issue. These results suggest that accurate measurements of diurnal properties of Sc clouds are crucial for radiation budget calculations in climate model simulations.

SEVIRI is the first space-borne instrument with the necessary temporal, spatial, and spectral resolution to resolve the diurnal cycle of clouds. Thus, this study uses cloud products retrieved from SEVIRI measurements using the algorithm developed and run operationally in the CM-SAF. A general overview on the CM-SAF is given in [*Schulz, et al.,* 2009]. Basic information on the CM-SAF cloud products used in this study can be found in *Roebeling et*

al. [2006] and *Meirink et al*. [2010]. Validation of CM-SAF LWP estimates using ground-based radiometers and radiometer networks have been reported in [*Greuell and Roebeling,* 2009; *Roebeling et al*., 2008a; *Roebeling et al*., 2008b]. While this approach can take advantage of the greater accuracy of the ground-based instruments, these are not available for the study area.

Recently, a large number of papers have studied the differences in liquid water path retrieval based on passive microwave and visible/near-infrared (VNIR) satellite observations [*Seethala and Horvath,* 2010; *Wilcox et al.,* 2009; *Greenwald,* 2009; *Bennartz,* 2007; *Borg and Bennartz,* 2007; *Horvath and Davies,* 2007]. Differences between the two methods have been shown to be correlated with various factors, including cloud fraction, observation geometry, retrieval assumptions, aerosol above clouds, and others. No clear picture has yet emerged. This is partly due to the correlative nature of the satellite studies, which does not necessarily allow establishing causal relations. A few issues are relatively clear. A slight (mostly) positive bias of passive-microwave derived LWP in cloud-free situations in the order of 10-15 g m^{-2} exists, which is cross-correlated with other retrieved variables [*Greenwald,* 2009; *Greenwald et al.,* 2007]. Also, agreement appears better for more stratiform clouds, where a near-adiabatic cloud liquid water profile can be assumed.

Because microwave and VNIR techniques represent fully independent approaches the analysis of retrieval discrepancies can reveal major algorithmic shortcomings, without necessarily establishing absolute accuracies. Here, the approach of comparing SEVIRI VNIR observations with passive microwave observations is followed. Since the diurnal cycle is targeted here, the use of TRMM observations appears particularly useful. The non sun-synchronous orbit of TRMM allows for a comparison of observations at different local times. Over the course of a month the entire (daylight) diurnal cycle can be evaluated. The TRMM data used in this study were obtained from Remote Sensing Systems and were derived using the algorithms described in [*Hilburn and Wentz,* 2008]. The error characteristics and uncertainties of these data are similar to SSM/I and AMSR-E estimates. Various sources of error and potential uncertainties are listed in [e.g., *O'Dell et al.,* 2008].

We also have evaluated the impact of cloud variability at sub-pixel scale in SEVIRI retrievals. Geostationary imagers sample at a coarser resolution than polar imagers. The SEVIRI cloud properties are retrieved at 3 x 3 km^2 resolution but the MODIS retrievals are done at 1 x 1 km^2 resolution. A coarser resolution gives rise to systematic biases in the derived cloud physical properties, especially when the cloud is heterogeneous. According to *Henrich et al.* [2010] the resolution with the least bias in the retrieval of optical thickness

seems to be the 1 × 1 km^2 pixel. Thus, to investigate the pixel size effect on SEVIRI retrieved cloud properties, we compare them with the high resolution MODIS retrievals.

This chapter is structured as follows. The SEVIRI and TMI datasets are described in Section 2 while the description of MODIS and OMI were already given in Chapter 3. Methodology is given in Section 3. The results are discussed in Section 4, basically the domain mean statistics, spatial distribution, and the diurnal cycle of cloud properties from SEVIRI and LWP comparison with TMI. We also evaluate the retrieval artifacts of absorbing aerosols over the Sc clouds, and overview the cloud fraction dependence and solar zenith angle effect on SEVERI CPP. Finally, the effect of sub-pixel-scale variability in SEVIRI retrievals is investigated in comparison with MODIS high resolution retrievals. Results are summarized in Section 5.

4.2. Data and Methodology

4.2.1. Spinning Enhanced Visible and InfraRed Imager (SEVIRI)

The Spinning Enhanced Visible and Infrared Imager (SEVIRI) is an optical radiometer onboard METEOSAT-9 geostationary satellite developed by the European Space Agency (ESA) and operated by the European Organization for the Exploitation of Meteorological Satellites (EUMETSAT). SEVIRI measures radiances at 12 spectral channels with 4 VNIR channels (0.4 – 1.6 μm) and 8 IR channels (3.9 – 13.4 μm), and produces one image every 15 minutes. The CM-SAF CPP (cloud physical properties) algorithm, developed at KNMI, retrieves cloud optical thickness (τ) and cloud particle effective radius (r_e) based on measured reflectances at 0.6 μm and 1.6 μm channel. The retrieval scheme is described in *Roebeling et al.* [2006], and is based on earlier methods that retrieve cloud optical thickness and cloud particle size from satellite radiances at wavelengths in the non-absorbing visible and the moderately absorbing solar infrared part of the spectrum [*Nakajima and King,* 1990; *Han et al.,* 1994; *Nakajima and Nakajima,* 1995; *Watts et al.,* 1998]. The liquid water path (LWP) is computed from the retrieved τ and r_e by [*Stephens,* 1978]: $LWP = 2/3\ \tau\ r_{e(1.6\mu m)}\ \rho_l$, where ρ_l is the density of liquid water. The SEVIRI retrievals are available only during daytime and the retrievals are performed assuming that the clouds are plane parallel.

The CPP products used in this study have been generated at KNMI. They differ from the official CM-SAF products in a number of ways: (i) a local (KNMI) cloud mask rather than the CM-SAF cloud mask has been used to identify cloudy pixels, (ii) latest information on instrument calibration has been used, (iii) algorithm improvements with respect to atmospheric correction have been introduced [*Meirink et al.,* 2009], (iv) the full 15-minute

SEVIRI dataset was processed instead of an hourly dataset processed operationally in CM-SAF, and (v) compared to the standard CM-SAF products optical thickness and LWP, additional cloud (micro-)physical properties were derived.

4.2.2. TRMM Microwave Imager (TMI)

The TRMM Microwave Imager (TMI) is a well-calibrated, 5 channel, dual-polarized, passive microwave radiometer that orbits at an altitude of 400 km and continuously monitors the tropics between 40°S and 40°N. Unlike SSM/I (in a near-polar, sun-synchronous orbit), the TRMM satellite travels west to east in a semi-equatorial orbit, which produces data at different local times for any location. The radiometer measures the microwave radiation emitted by the Earth's surface and clouds at frequencies of 10.7, 19.4, 21.3, 37, 85.5 GHz. The Wentz' absorption-emission based algorithm [*Wentz,* 1997; *Wentz and Spencer,* 2000] is used to retrieve several important meteorological parameters such as sea surface temperature (SST), surface wind speed (W), water vapor path (V), liquid water path (LWP), and rain rate (R) over the ocean. Our primary interest, LWP, is derived from 37 GHz observations at a resolution of 13 km, but here we used the 0.25° gridded daytime product.

4.2.3. Methodology

To investigate the diurnal cycle of cloud liquid water path annually and in different seasons, we have processed one year (June 2008 to May 2009) of data from SEVIRI, TMI, and MODIS. SEVIRI 3 x 3 km^2 data is downscaled to TMI resolution and collocation is done for those SEVIRI retrievals within TMI observation time of +/-7.5 minutes. As such, the mean LWP is representative of the mean in-cloud LWP. To compare it with TMI grid-box mean, we scaled it with the successful cloud-retrieval-fraction calculated from SEVIRI measurements. Similarly, for a matching comparison, both Terra and Aqua MODIS data have been downscaled independently to 0.25^o x 0.25^o, consistent to TMI resolution. For the comparisons between SEVIRI and MODIS observations, original SEVIRI 3 x 3 km^2 data were downscaled and collocated based on those pixels within MODIS observation time of +/-5 minutes. These collocated SEVIRI data are termed SEVIRI_M.

Our entire study domain is roughly 50^o x 50^o covering [30^oW-20^oE, 35^oS-10^oN] over the South Atlantic Ocean. Near the Namibian coast, abundant Sc sheets form over relatively cold SSTs, and towards the equator these Sc decks transition into scattered Cu. Thus our study domain is frequently covered by extensive sheets of sub-tropical marine Sc clouds, trade wind Cu with significantly lower cloud cover, and deep convective clouds. The

presence of ice cloud masks water clouds below in VNIR retrievals. Also, the microwave signal is sensitive to liquid cloud and rain, and the rain retrieval is performed assuming a fixed rain-threshold of 180 g m^{-2} which can introduce a systematic error in retrieved LWP. Thus, we examine the mean and diurnal characteristics of only low-level non-raining warm (liquid) clouds to avoid instrumental sensitivity to rain and ice. We have noticed that the amount and the location of these Sc decks vary from month to month depending on where the sun is. So, we use "Region Growing" technique to locate the exact Sc regime. This technique takes an initial location of Sc regime (here, we choose the location of 75^{th} percentile cloud fraction threshold on frequently occurring Sc regime) and examines neighboring pixels, and then determines whether the pixel neighbors should be added to the region. The process is iterated on, in the same manner as general data clustering algorithms, until we find reasonable location. However, for more broken trade wind Cu regime we chose a 10^o x 10^o grid box depending on their frequency of occurrence.

4.3. Comparison of SEVIRI *versus* TMI LWP

4.3.1. Effect of Absorbing Aerosols on SEVIRI Retrievals

Before investigating the Sc cloud properties and the emerging diurnal cycle, as a necessary step, we examine the impact of absorbing aerosols residing above the South Atlantic Sc clouds on SEVIRI retrievals. Biomass burning is a significant source of tropospheric aerosols in southwestern Africa during the dry season JASO (July-August-September-October) and produces episodic plumes of dark smoke over the southeast Atlantic Ocean. The mean aerosol index map from OMI for JASO 2008 is depicted in Figure 4.1. The aerosol index is an index that detects the presence of UV-absorbing aerosols where positive values generally represent absorbing aerosols such as dust and smoke and small or negative values represent non-absorbing aerosols and clouds. From the figure it is clear that the smoke absorption is higher near the Namibian coast and reduces as we go away from the coast. Beneath the elevated layer of smoke there is a persistent deck of bright marine Sc cloud. When smoke resides above low-level clouds, the measured visible (0.6 or 0.8 μm) channel reflectance will be underestimated due to the absorption by smoke, which can introduce a negative bias in both droplet effective radius (r_e) and optical thickness (τ), and hence in SEVIRI LWP. This negative bias in the 1.6 μm retrieved r_e is significantly larger compared to r_e from the 2.2 μm channel which is usually less than 1 μm, however, it can be up to 30% in retrieved τ according to calculations by *Haywood et al.* [2004]. In SEVIRI 1.6 μm retrieval, a strong decrease in r_e from 11 to 7 μm is observed (Figures 4.2d and 4.3d) even for

the aerosol index of 3.5. *Bennartz* [2007] noted a systematic MODIS LWP underestimation in Sc off southern Africa during the biomass burning season, which was attributed to overlying absorbing aerosols by *Bennartz and Harshvardhan* [2007]. In the same region and season, *Wilcox et al.* [2009] estimated a mean negative bias of 5.6 g m^{-2}, but for a larger 25° x 25° domain *Seethala and Horvath* [2010] estimated a negative bias of 3 g m^{-2}, in MODIS LWP corresponding to less polluted case.

Here, we estimate the bias in SEVIRI LWP for JASO over the entire study domain and over the aerosol dominated Sc domain. Over this domain the mean AI ranges up to 3.5. As shown in Figure 4.2-4.3, SEVIRI increasingly underestimates TMI LWP as a result of reduced τ and r_e. The TMI-SEVIRI LWP bias increases with aerosol index over the Sc domain and also in the entire domain. Over the entire domain the LWP underestimation due to the presence of smoke is ~27 g m^{-2}, however the individual values can go > 40 g m^{-2} even at an AI of 2.5 (as shown in Figure 4.2b and 4.3b). *Coddington et al.* [2010] also reported an underestimation in retrieved τ and r_e for a stratus residing below an absorbing aerosol layer based on aircraft measurements made during the Intercontinental Chemical Transport Experiment (INTEX-A) and also using a forward radiative transfer model.

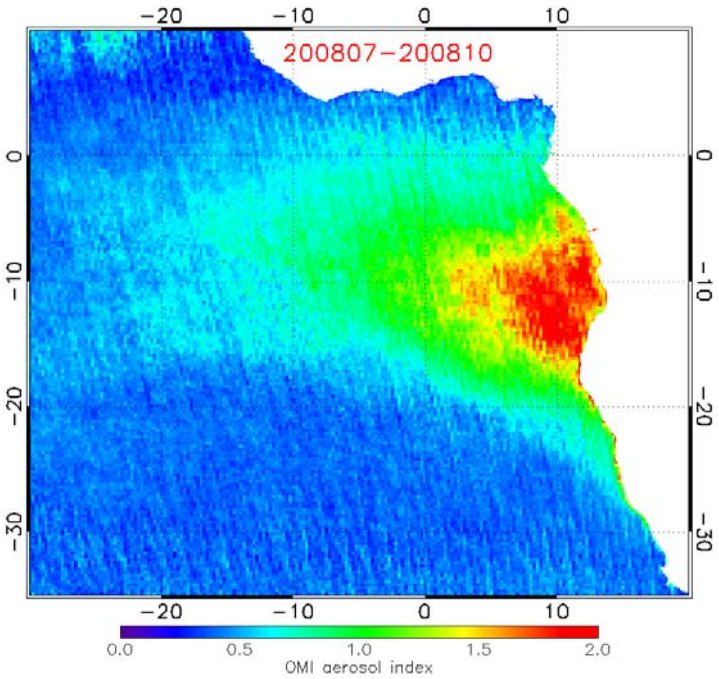

Figure 4.1. OMI ultraviolet aerosol index averaged for JASO 2008.

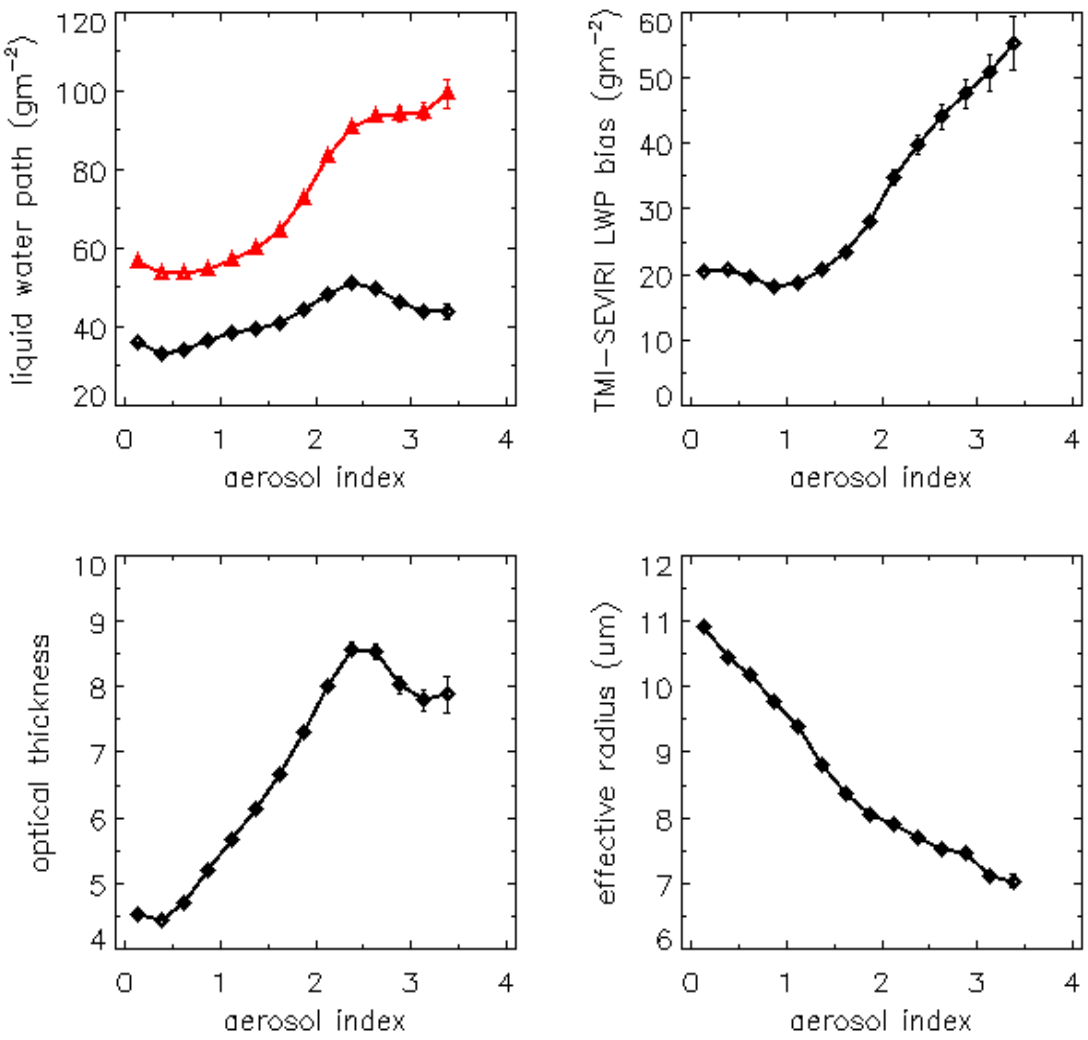

Figure 4.2. Aerosol index versus cloud properties averaged over the entire study domain, for JASO 2008.

The results from Figures 4.2a and 4.3a indicates an increase in LWP with aerosol index, which is observed in both TMI and SEVIRI measurements. TMI shows a strong LWP increase from 60 to 100 g m^{-2} as the aerosol loading increases from 0.25 to 3.5, however the SEVIRI increase is less prominent and decreases drastically with aerosol index. We also notice an increase in cloud physical thickness with AI for SEVIRI measurements. The optical thickness also increases from 4.5-8.5 with aerosol index for the entire domain (7-12 for the Sc domain), however this increase could be even larger for less polluted cases, as absorbing aerosol above the cloud underestimates retrieved τ. These results are similar to a recent observational study by *Wilcox* [2010] where he found that the diurnal mean SW heating rate increased when smoke resides above clouds. This extra heating introduced an additional warming of 1K in the 700 hPa air temperature above the cloud deck, and increased the

buoyancy of free-tropospheric air above the temperature inversion capping the boundary layer. This increased buoyancy inhibits the entrainment of dry air through the cloud top, thereby helping to preserve humidity and cloud cover in the boundary layer; which also coincides with LWP increase of 20 g m^{-2} and lower cloud tops compared to smoke-free environment. The modeling study also confirms these results, for example, *Johnson et al.* [2004] used LES and found an increase in LWP when absorbing aerosols reside above Sc

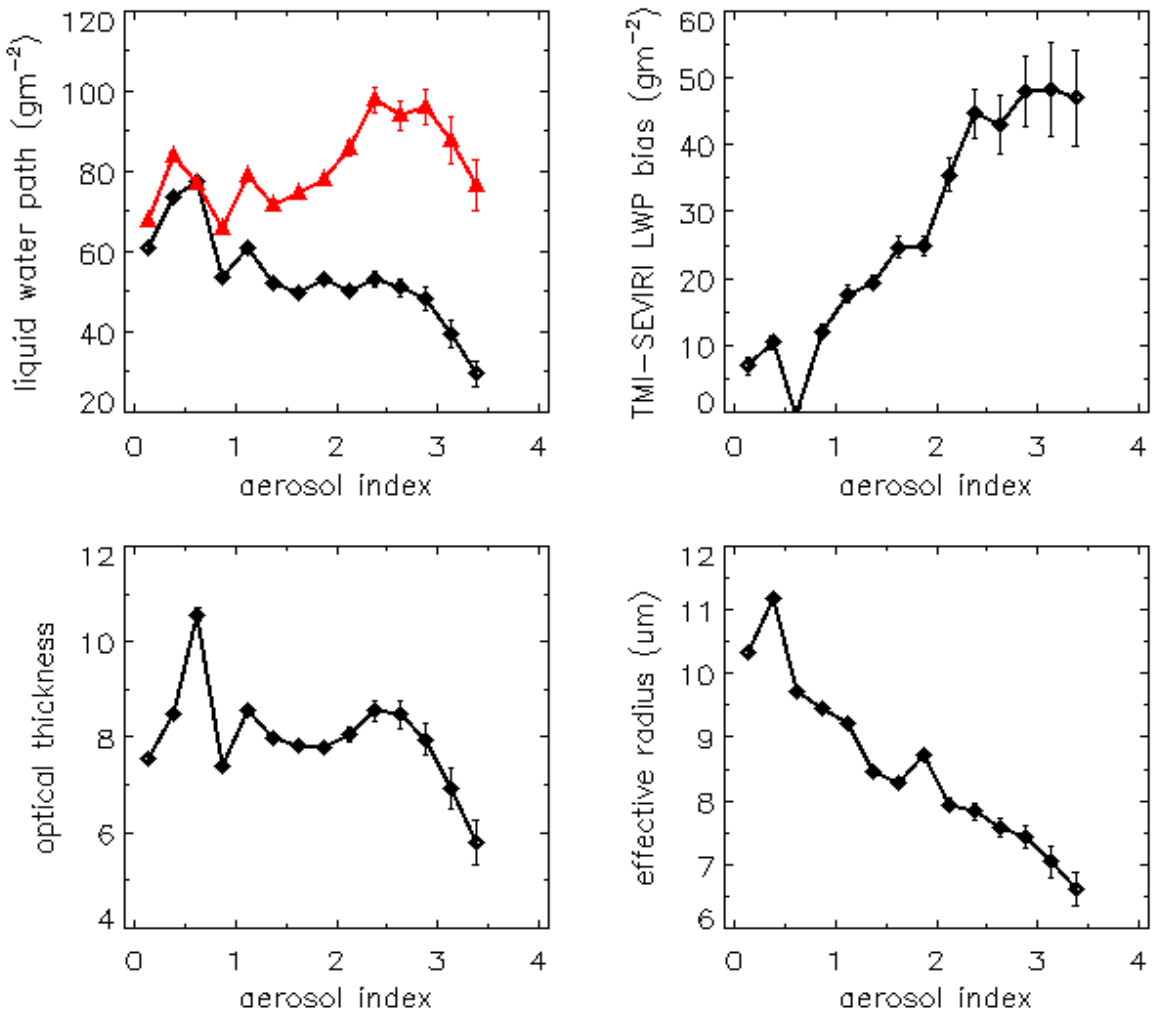

Figure 4.3. Aerosol index versus cloud properties averaged over the Sc domain, for JASO 2008.

clouds. Using an atmospheric general circulation model (GFDL AGCM) *Randles and Ramaswamy* [2010] indicated that strong atmospheric absorption from these particles can cool the surface and increase upward motion and low-level convergence over South Africa during the dry season, thereby increasing clouds. Nevertheless, partially, it could also be due to the fact that higher aerosol loading samples are spatially coincident with thicker clouds.

Further, while sampling SAFARI-2000 data offshore of West Africa, *Hobbs* [2002] *and McGill et al*. [2003] argued that smoke was typically observed in layers that were vertically separated from Sc clouds below and hence the direct microphysical interaction between the aerosols and the Sc clouds was often inhibited by the strong temperature inversion above the cloud layer; which was later confirmed by *Wilcox* [2010] that aerosol layers occur predominantly between 2 km and 4 km, but cloud layers are identified predominantly below 1.5 km altitude and beneath the layer of elevated smoke aerosol.

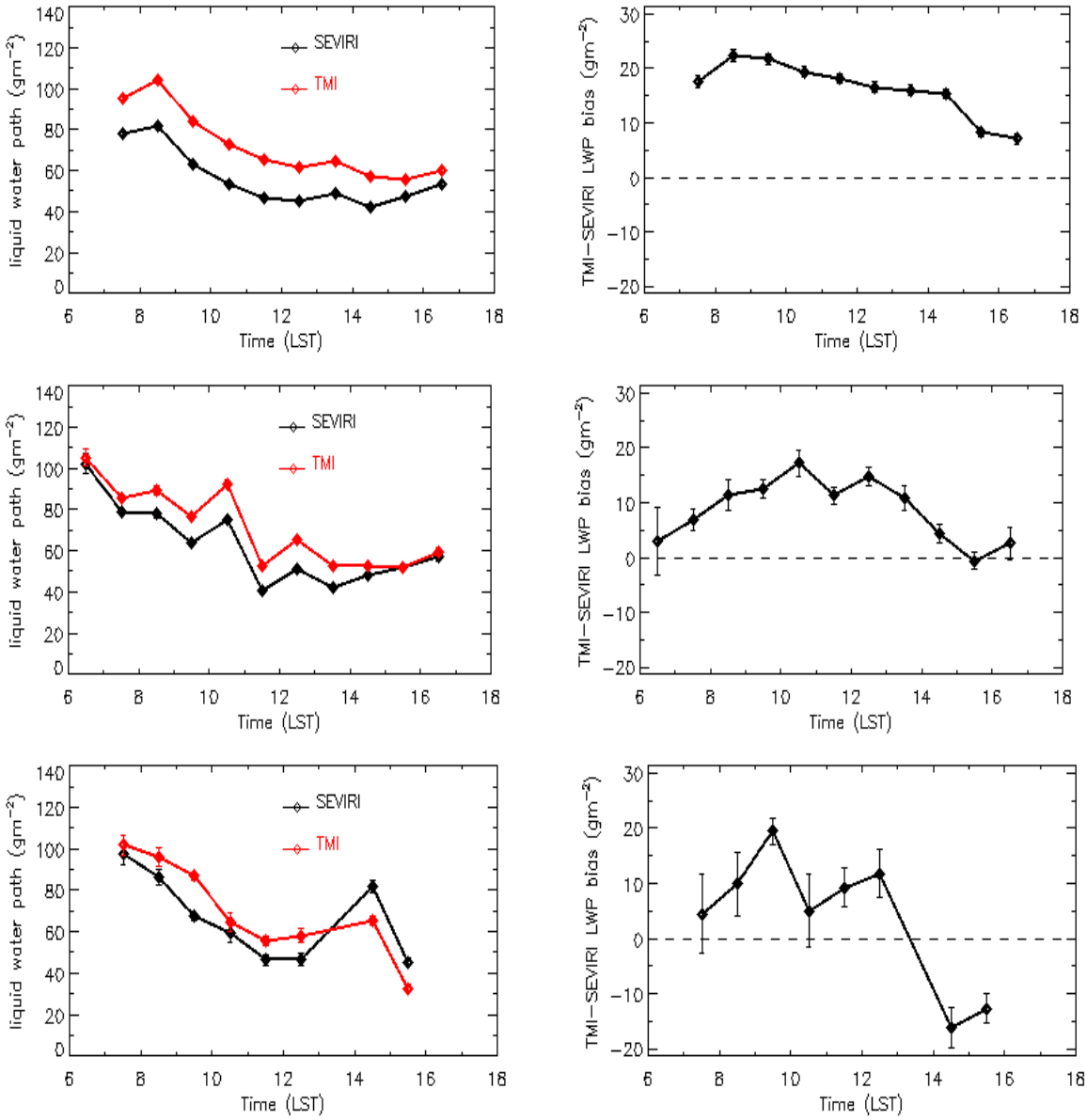

Figure 4.4. Diurnal cycle of CPP over the Sc domain averaged for JASO 2008, based on (top) full data, (middle) data with AI <1, and (bottom) data with AI<0.25.

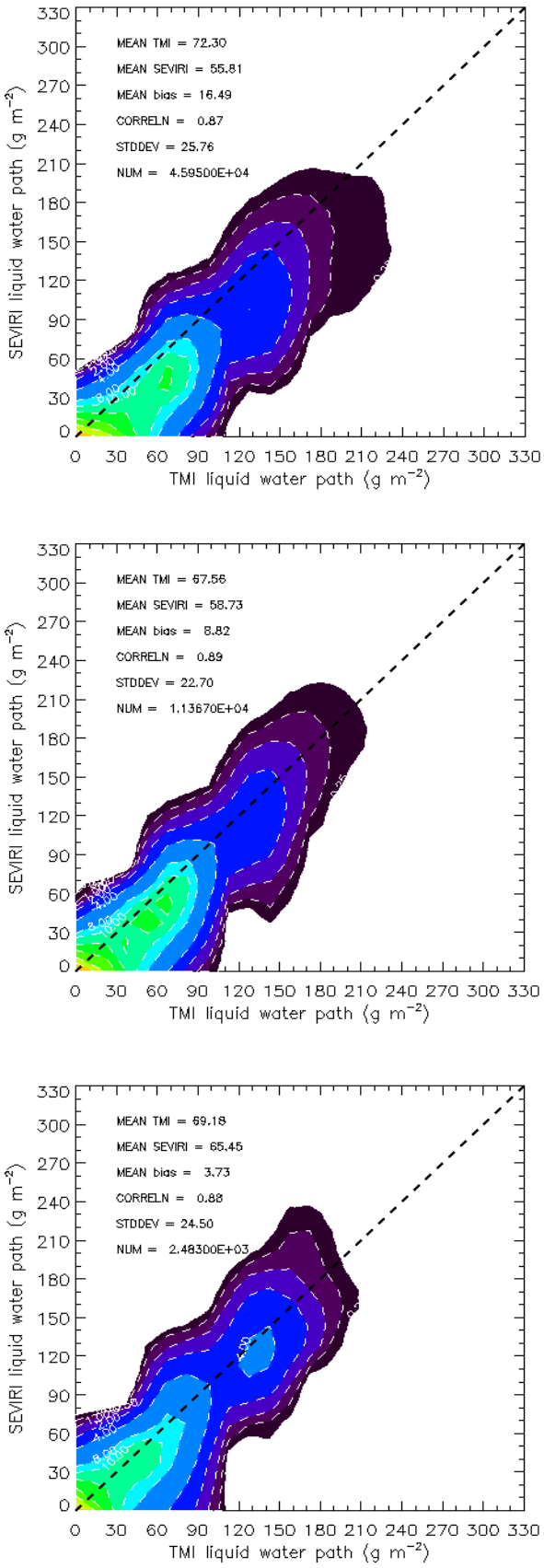

Figure 4.5. JASO mean statistics of SEVIRI versus TMI LWP (top) including all data, (middle) all data but AI<1, and (bottom) all data but AI<0.25 over the Sc regime.

We further evaluate the impact of absorbing aerosols over Sc regime especially in the diurnal cycle representation. The diurnal cycle of TMI and SEVIRI CPP averaged for JASO 2008 is presented in Figure 4.4. The cloud optical thickness decrease by about ~50 % from morning to late afternoon, but the droplet effective radius remains more or less constant with time. Also, a 20 % decrease in cloud fraction, a 100 m decrease in cloud physical thickness, and a 50 cm^{-3} decrease in the cloud droplet number concentration were observed with time (figure not shown). Overall, both TMI and SEVIRI LWP show a 50% decrease from morning to late afternoon. Both SEVIRI and TMI LWP show similar variability in diurnal cycle, however a large bias of 10-20 gm^{-2} is exists between them. This large bias is partially removed by considering least polluted cases in the analysis. Figure 4.4 (middle and bottom panels) shows the diurnal cycle of TMI and SEVIRI CPP where the polluted pixels are removed, and the results are in much better agreement. In Figure 4.5 the JASO mean TMI *versus* SEVIRI LWP statistics is shown, and obviously the LWP bias has been reduced to half for pixels with AI<1 and the bias is further halved for datasets with AI<0.25. It can also be noticed that SEVIRI liquid water path increases with changing AI threshold. The mean LWP bias over the Sc domain is 16.49 g m^{-2}. The LWP bias is reduced 8.82 g m^{-2} if we only consider data where AI<1. Further neglecting those data with AI<0.25 reduces the LWP bias to 3.73 g m^{-2}. From Figure 4.6 it is also very clear that the SEVIRI observations are more and more shifted towards the one-to-one line as we remove the more and more pixels affected by aerosols. As these absorbing aerosols introduce low bias in SEVIRI LWP, for further analysis, we neglect all the aerosol affected pixels i.e., AI>1.

4.3.2. Mean Statistics of TMI and SEVIRI LWP

In this section, we describe the annual and seasonal mean statistics of cloud LWP for the entire South Atlantic study domain, the trade wind Cu, and the Sc regime as obtained from both SEVIRI and TMI and shown in Figures 4.6 – 4.10. Note that Figures 4.6 – 4.10 are only for AI <1. Over the entire South Atlantic domain, the correlation in LWP between the two techniques varies from 0.48 to 0.74 with the domain mean positive (TMI-SEVIRI) LWP bias consisting to 8-18 g m^{-2}. The mean LWP varies with season and is maximum in November and minimum in February. In this case, SEVIRI seems to underestimate the LWP and TMI seems to overestimate it in all the seasons. Similarly, a global mean positive bias of 18 g m^{-2} is observed in AMSR-E and MODIS comparison. So, the microwave technique appears to overestimate the LWP in general, due to the overestimation in broken cloud fields. The annual mean bias is only 12 g m^{-2} with 52 g m^{-2}

deviation from mean. MAM shows the smallest bias with ~7 g m^{-2}, but with a larger mean deviation of 66 g m^{-2} and a smaller correlation of 0.48. The largest bias of 18 g m^{-2} is observed for JJA, with mean deviation of 45 g m^{-2} and correlation of 0.64. But for SON and DJF biases are 12 g m^{-2} and 13 g m^{-2}, with mean deviations of 42.5 g m^{-2} and 48.7 g m^{-2} respectively. Over this domain, the amount of observed mean liquid water path is largest in September-October-November.

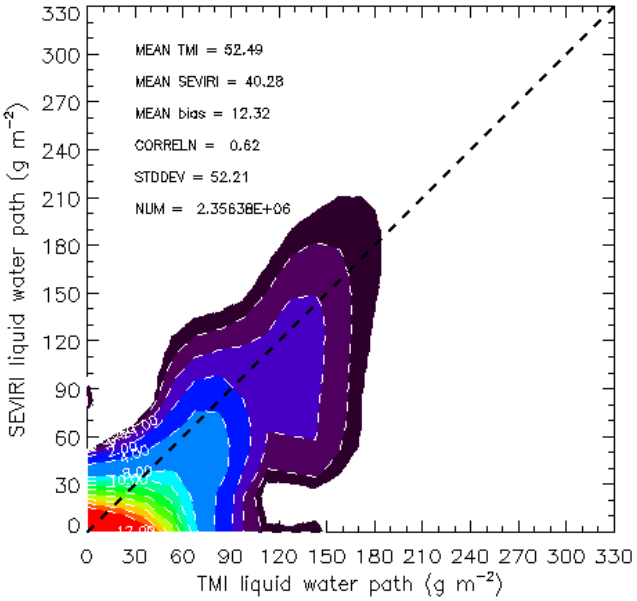

Figure 4.6. Annual mean statistics for the South Atlantic study domain (for liquid cloud fraction: 0-100%, no rain, no ice, AI<1).

Over the South Atlantic Sc region both SEVIRI VNIR and TMI microwave techniques show robust skill to retrieve LWP with a large correlation of 0.9-0.94 annually and in all seasons as shown in Figures 4.8-4.9. Both TMI and SEVIRI show a mean annual LWP of ~45 g m^{-2} with a small bias of 0.26 g m^{-2} and standard deviation of 21 g m^{-2}. The daytime averaged seasonal LWP variation of SEVIRI *vs.* TMI is 35.64 *vs.* 42.51, 69.24 *vs.* 66.66, 52.24 *vs.* 52.15, and 38.27 *vs.* 38.16 (g m^{-2}) in seasons JJA, SON, DJF and MAM, respectively. *Fairall et al.* [1990] estimated a mean Sc LWP of 75 g m^{-2} off the coast of Southern California during FIRE from March through October 1987. An average cloud LWP of 120 ± 320 g m^{-2} is reported by *Zuidema and Hartmann* [1995] from SSM/I data averaged over stratus cloud regime. These LWP values are somewhat larger compared to our mean LWPs. However, the mean TMI-SEVIRI LWP bias in our Sc domain is within ±5 g m^{-2} in all the months/seasons, except those months which are affected by absorbing aerosols. In JASO,

the observed mean bias is 10-25 g m^{-2} and SEVIRI retrievals are artificially affected by the absorbing aerosols in these months.

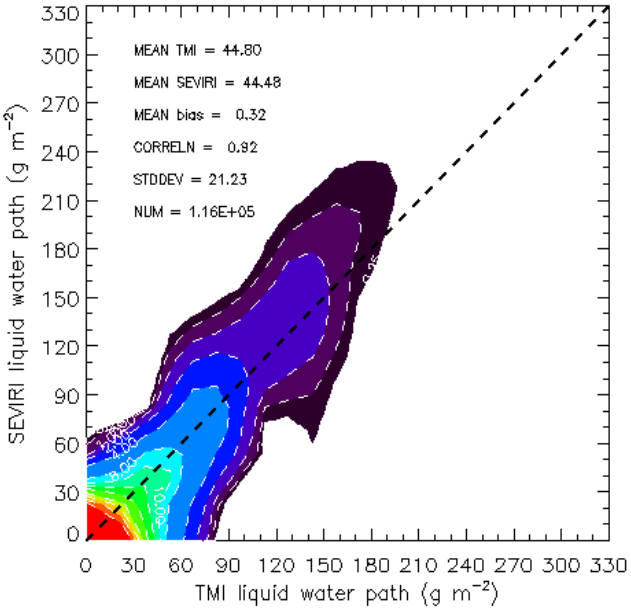

Figure 4.7. Annual mean statistics for the Sc regime. (for liquid cloud fraction: 0-100%, no rain, no ice, AI<1).

As we explained in th previous section, the absorbing aerosols introduce a negative bias in both τ and r_e, and hence in the deduced LWP in SEVIRI retrieval. Neglecting the pixels with larger loading of absorbing aerosols and considering only those pixels with 0<AI<1.0, the bias has been reduced to ~12.5 g m^{-2} in individual months and even to ~7 g m^{-2} seasonally. All together the bias between TMI and SEVIRI LWP is small, compared to the AMSR-E - MODIS LWP bias [refer *Seethala and Horvath,* 2010], where MODIS highly overestimated LWP and the overestimation could only be reduced after applying the adiabatic correction to MODIS LWP. As TMI and AMSR-E retrievals are based on the same Wentz's algorithm, the differences may arise from SEVIRI and MODIS retrieval differences. The basic difference between SEVIRI and MODIS is, that the SEVIRI r_e retrievals are performed based on radiance from the 1.6 µm channel which samples clouds slightly deeper compared to MODIS 2.2 µm channel, which is mostly sensitive to the top layer of clouds leading to larger MODIS r_e in case of more adiabatic Sc clouds. This could have a significant impact, eventhough it is assumed that the r_e retrievals are likely to be the same in both 1.6 µm and 2.2 µm channels. Another possibility could be that for thin clouds of τ below 8, the SEVIRI CPP algorithm weighs r_e towards the r_e-climatology of 8 µm, but MODIS provides true retrieved

values. Again SEVIRI original pixels are an order of magnitude larger than the MODIS pixels, and, as we reduce the resolution, the errors in retrieved τ and r_e may cancel out and get better comparison of SEVIRI with TMI. Another difference could be related to the so-called clear-sky restoral applied to MODIS. MODIS retrieves cloud properties only in confident cloudy conditions which may introduce a high bias in τ. On the other hand, SEVIRI retrievals for partly cloudy pixels may introduce a low bias in τ. These effects would introduce a high/low LWP bias in MODIS/SEVIRI, respectively. Thus, the above listed differences could easily explain the difference in MODIS *vs.* AMSR-E comparison and our SEVIRI *vs.* TMI comparison.

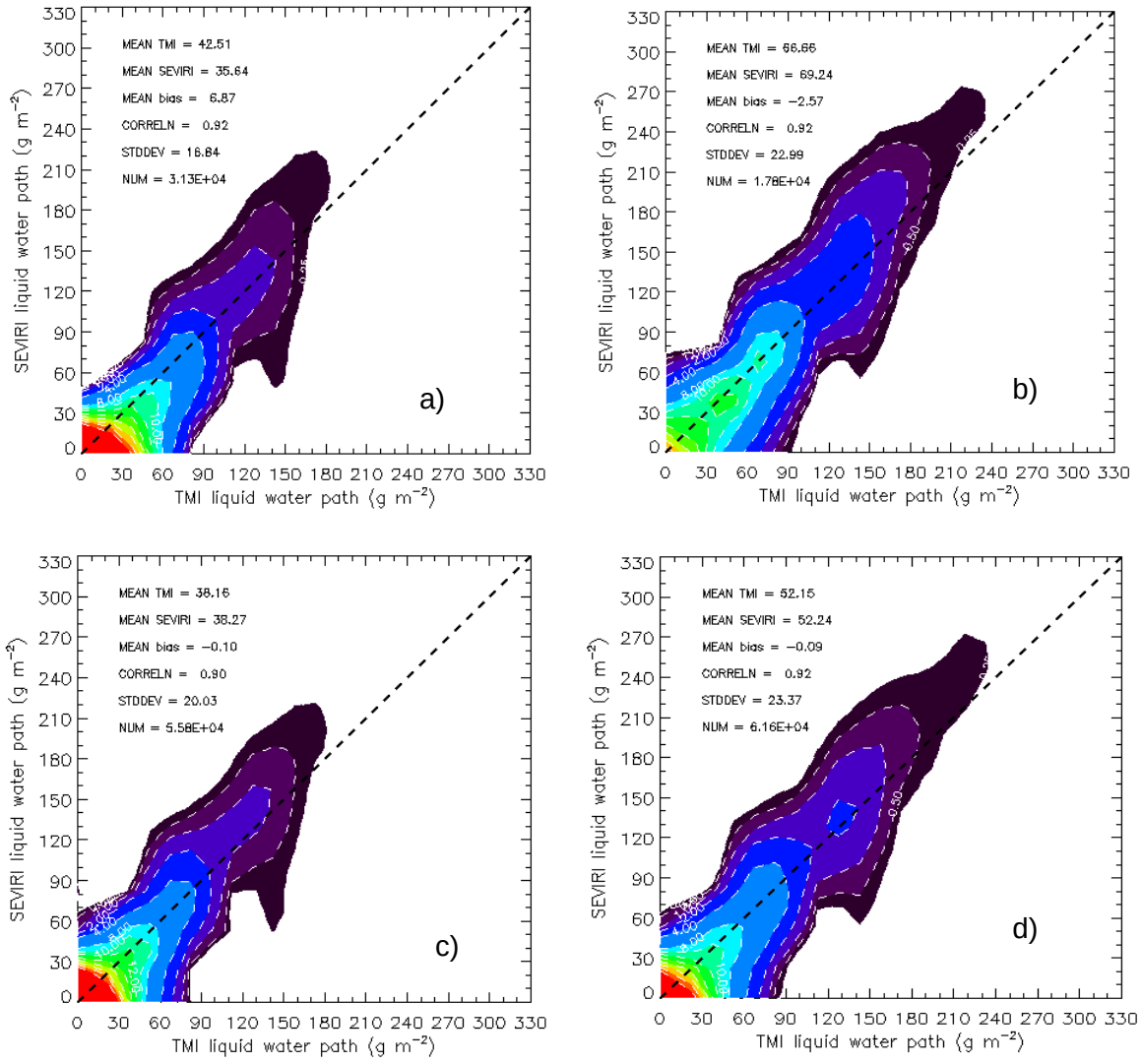

Figure 4.8. Seasonal mean statistics for the Sc regime (a) JJA, (b) SON, (c) DJF, and (d) MAM. (for liquid cloud fraction: 0-100%, no rain, no ice, AI<1) .

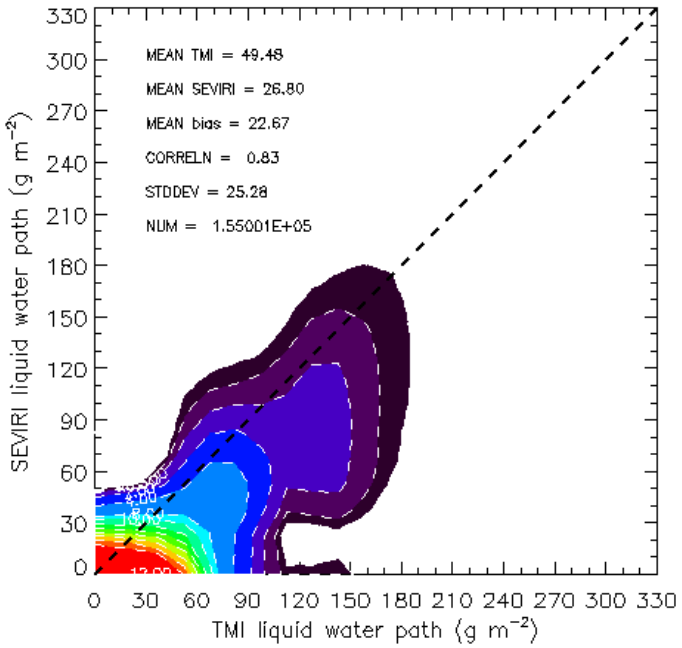

Figure 4.9. Annual mean statistics for the trade wind Cu [10°S-20°S, 10°W-20°W] regime. (for liquid cloud fraction: 0-100%, no rain, no ice, AI<1).

Over the trade wind Cu domain, SEVIRI retrieves smaller LWP and TMI retrieves larger LWP compared to the Sc domain, which yields a very large positive bias of 15-25 g m^{-2} in all seasons, although SEVIRI and TMI showed relatively good correlations of 0.79-0.86. The dominant error sources in both VNIR and microwave technique in the broken cloud fields could explain this bias. Larger 3D radiative effect and non-linear averaging of reflectance and optical thickness in partial cloudy pixels could introduce negative bias in retrieved SEVIRI LWP. Moreover, the weighting of r_e towards the r_e-climatology of 8 μm for optically thin clouds of $\tau<8$ would introduce strong negative bias in the SEVIRI CPP algorithm as these trCu clouds are very thin and often have an optical thickness below 5. Besides, a known positive bias of 12-15 g m^{-2} is also observed in Wentz' microwave algorithm in clear-sky cases which suites for broken cloud scenes as well. Unfortunately, these errors cannot be separated from the measurements, and more modeling study is required to quantify them.

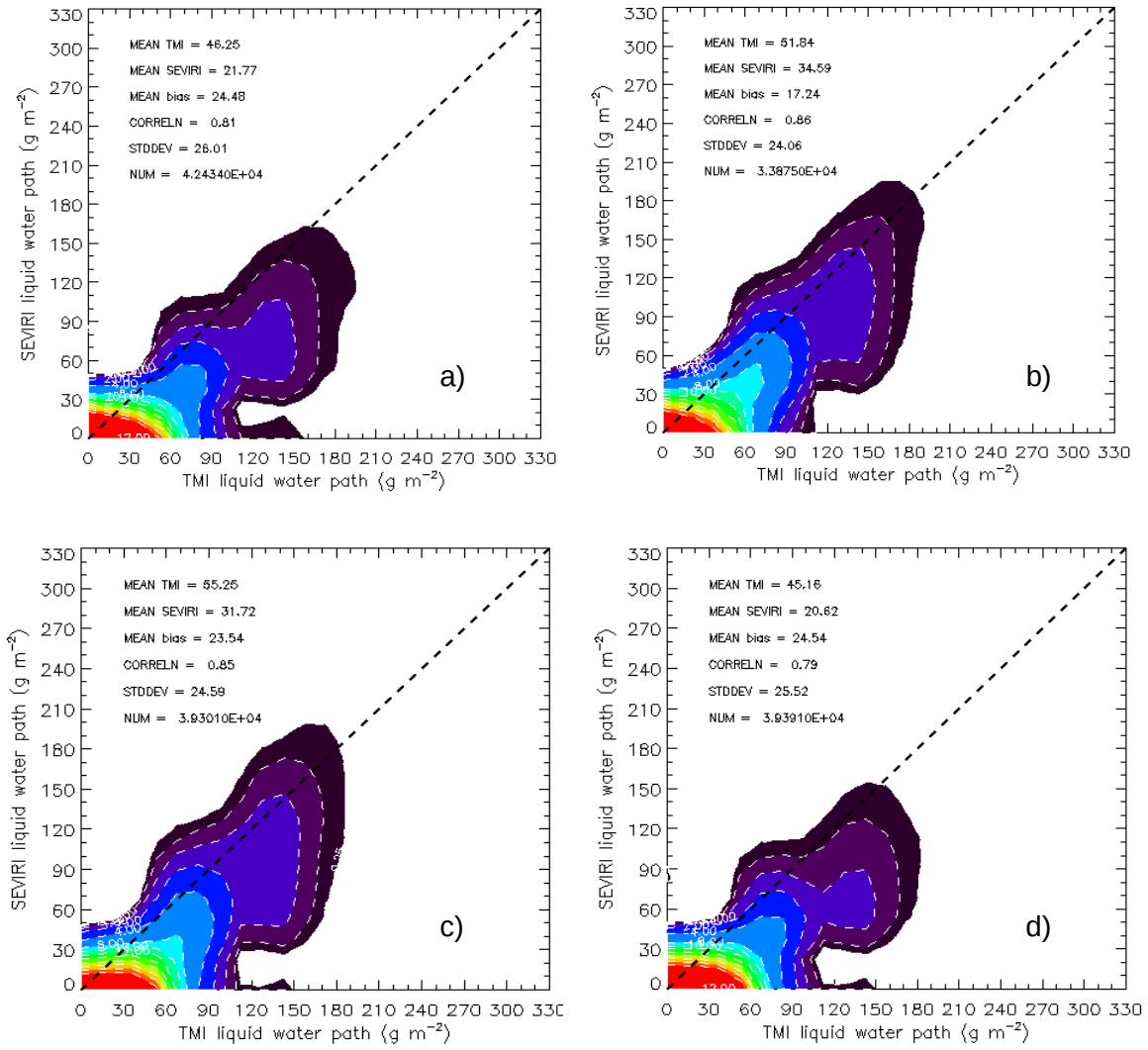

Figure 4.10. Seasonal mean statistics for the trade wind Cu regime (a) JJA, (b) SON, (c) DJF, and (d) MAM. (for liquid cloud fraction: 0-100%, no rain, no ice, AI<1).

4.3.3. Spatial Distribution of TMI LWP and SEVIRI CPP

In this section, we discuss the annual and seasonal mean maps of TMI and SEVIRI LWP, TMI-SEVIRI LWP bias, cloud optical thickness, droplet effective radius, and LCF (liquid cloud fraction) for all four seasons and for our 50^{o} x 50^{o} study domain. *Klein and Hartmann* [1993] used surface-based cloud climatology and showed that there is strong seasonal variability in the amount of stratus clouds, and that the seasonal cycle of Sc cloud amount is closely tied to the seasonal cycle of static stability. For the South Atlantic Sc region, the maximum static stability is observed during SON and the minimum in February. They also revealed from the Earth Radiation Budget Experiment that the strongest net cloud forcing occurs during the months of August through November. Thus, it is important to

examine the seasonal variability of these clouds throughout the year, as it alters the earth's radiation budget directly through net cloud forcing. The annual and seasonal mean maps of SEVIRI and TMI LWP and their biases (shown in Figures 4.11-4.12) are calculated only for no ice and no rain conditions to minimize obvious first order errors. Overall, the SEVIRI mean LWP is much lower compared to the TMI mean LWP except over the South Atlantic Sc region, regardless of seasons. Over the marine Sc domain, both SEVIRI VNIR and TMI microwave retrieval techniques show very good agreement, but often with a very small SEVIRI overestimation. This SEVIRI overestimation over the Sc domain is much smaller compared to the MODIS overestimation in this domain compared to AMSR-E LWP (see AMSR-E-MODIS LWP bias map of *Seethala and Horváth,* 2010 or Chapter 3). The possible reason for the better agreement between TMI and SEVIRI was discussed in the previous section. It is clear that, in JJA and SON, the SEVIRI retrievals seem to highly underestimate LWP over the Sc region, due to the presence of large amounts of absorbing aerosols. Over this Sc domain optical thickness varied from 6 to 10, and the effective radius varied from 7-11. The cloud thickness differs from season to season with annual mean of 350 m.

The worst agreement in retrieved LWP between the two techniques is observed over the trade wind Cu regime. TMI is retrieving higher LWP compared to SEVIRI. The observed discrepancy might be due to the fact that both VNIR and microwave techniques are less accurate in low cloud fraction scenes for the following reasons: (a) There is a known TMI positive clear-sky bias which could also be representative of more broken fields, (b) The performance of the SEVIRI cloud mask is unknown, and the cloud mask algorithm is more similar to MODIS; but *Zhao and Di Girolamo* [2006] showed that with a 15-m-resolution cloud mask, MODIS agreed only 62% of the time in trade wind Cu, thus, cloud detection problems in SEVIRI might partly explain this low LWP bias, (c) 3D radiative effects (solar/view angle effects) are larger over the more broken trade wind Cu, although we found negligible solar zenith angle effect in SEVIRI retrievals (see Section 4.6), (d) SEVIRI may underestimate optical thickness due to the nonlinear relationship between visible reflectance and optical thickness in broken scenes, (e) Underestimation in SEVIRI optical thickness as the retrievals are performed also for partially cloudy scenes (and not applying clear-sky restoral like MODIS does), and, (f) for thin clouds of cloud optical thickness below 8, SEVIRI CPP algorithm weighs r_e towards the r_e-climatology of 8 μm which can underestimate the true r_e and hence LWP. In general, over the broken cloud scenes the optical thickness is below 5 with large number of CDNC and larger droplet effective radii (>11 μm) than over the Sc regime.

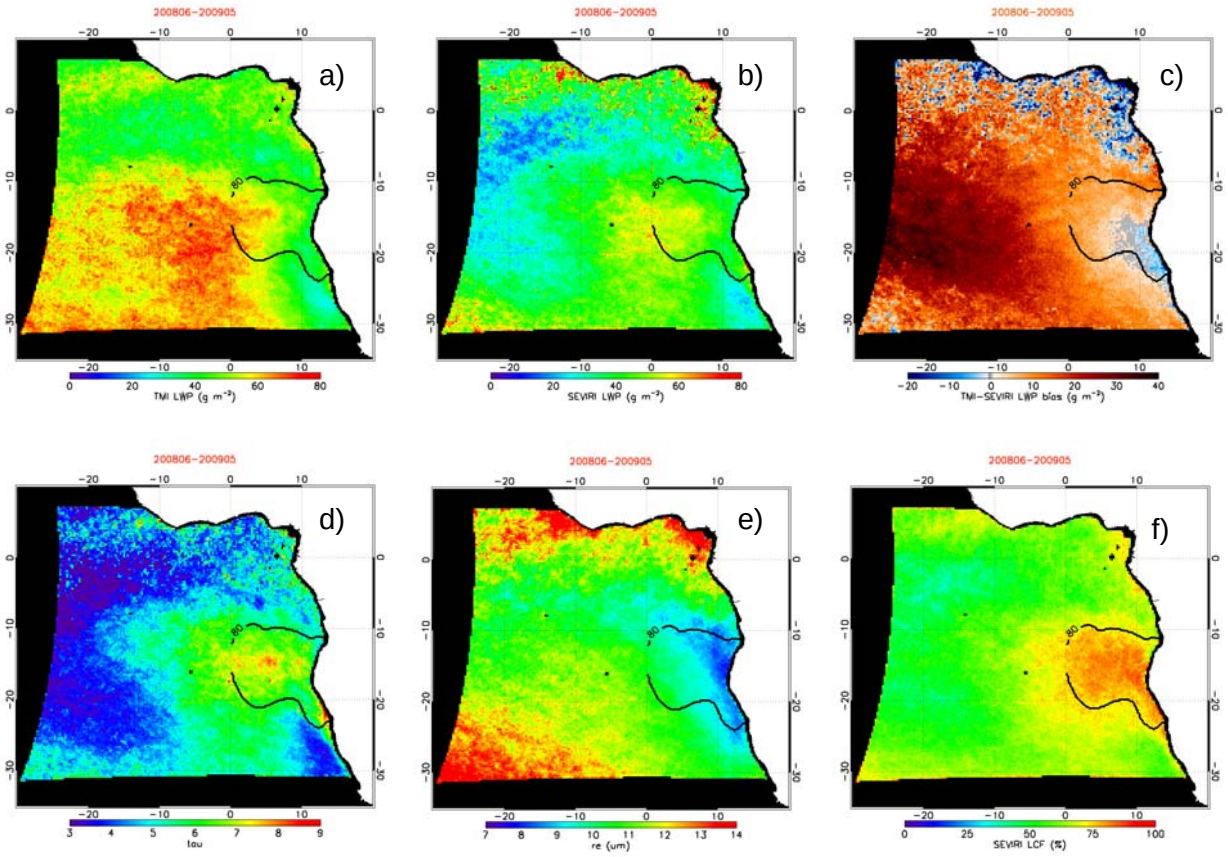

Figure 4.11. Annual mean of (a) TMI LWP, (b) SEVIRI LWP, (c) (TMI – SEVIRI) LWP bias, (d) cloud optical thickness, (e) effective radius, and (f) liquid cloud fraction. (The black contour denotes the 75th percentile of cloud fraction over the study domain.)

Figure 4.13 depicts the monthly/seasonal variation in cloud fraction. We can notice from the cloud fraction map that the distribution and amount of South Atlantic Sc deck is varying from season-to-season or more precisely month-to-month. In SON, we observe a huge amount of these clouds with large spread. In JJA there are relatively less clouds and they are shifted a bit to the north. Lower cloud fraction is seen in MAM, however the lowest fraction is observed in DJF. The results are in agreement with *Klein and Hartmann* [1993] who showed that the season of maximum stratus clouds is associated with the season of greatest lower-tropospheric static stability. From their study over South Atlantic Sc region SON showed largest LTS and DJF showed smallest. They also inferred that a 6% increase in stratus fractional area coverage is associated with a 1^{o}C increase in static stability.

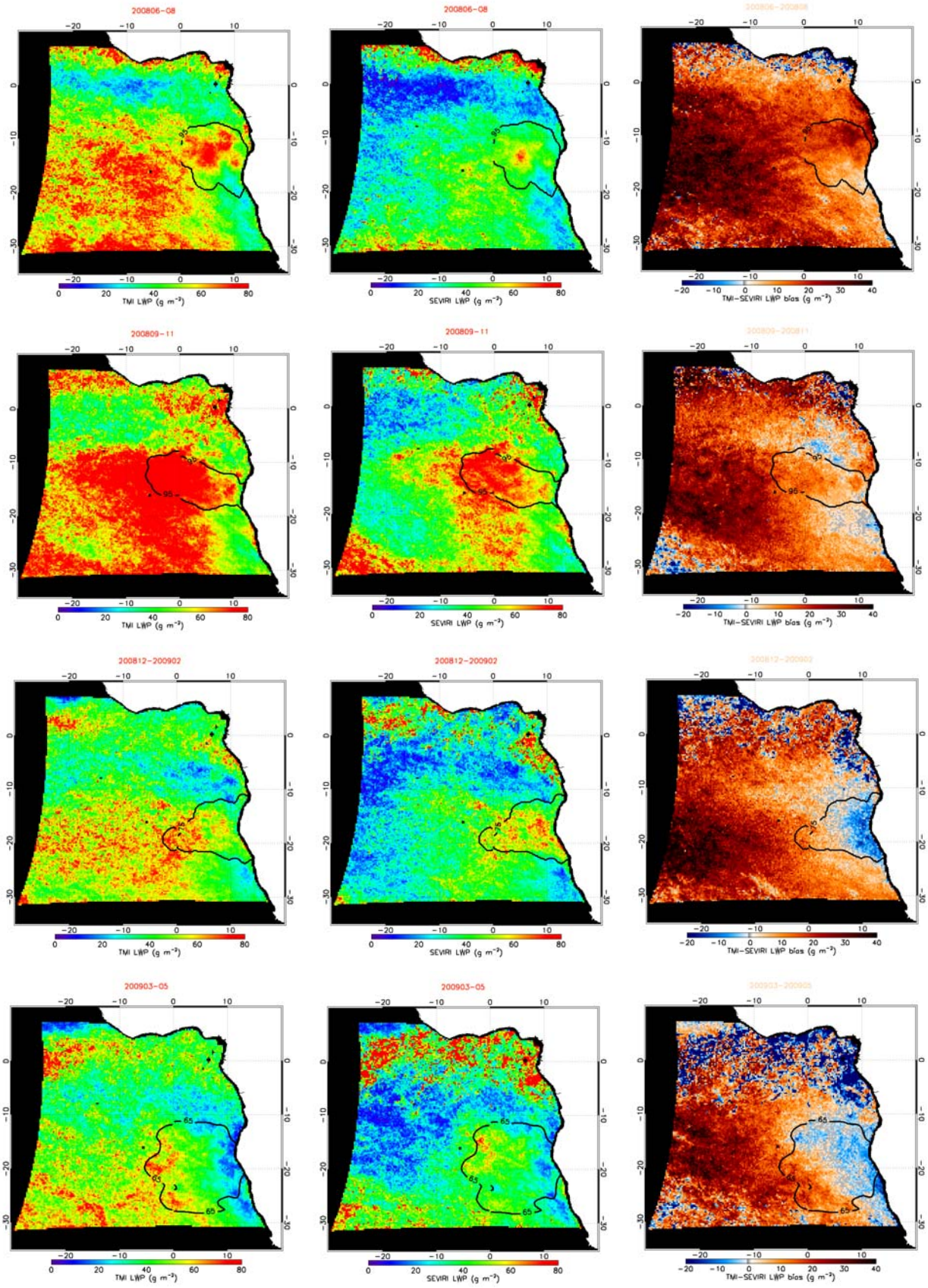

Figure 4.12. Seasonal mean of TMI LWP (left column), SEVIRI LWP (middle column), (TMI – SEVIRI) LWP bias (right column), for JJA (top row), SON (second row), DJF (third row), and MAM (bottom row).

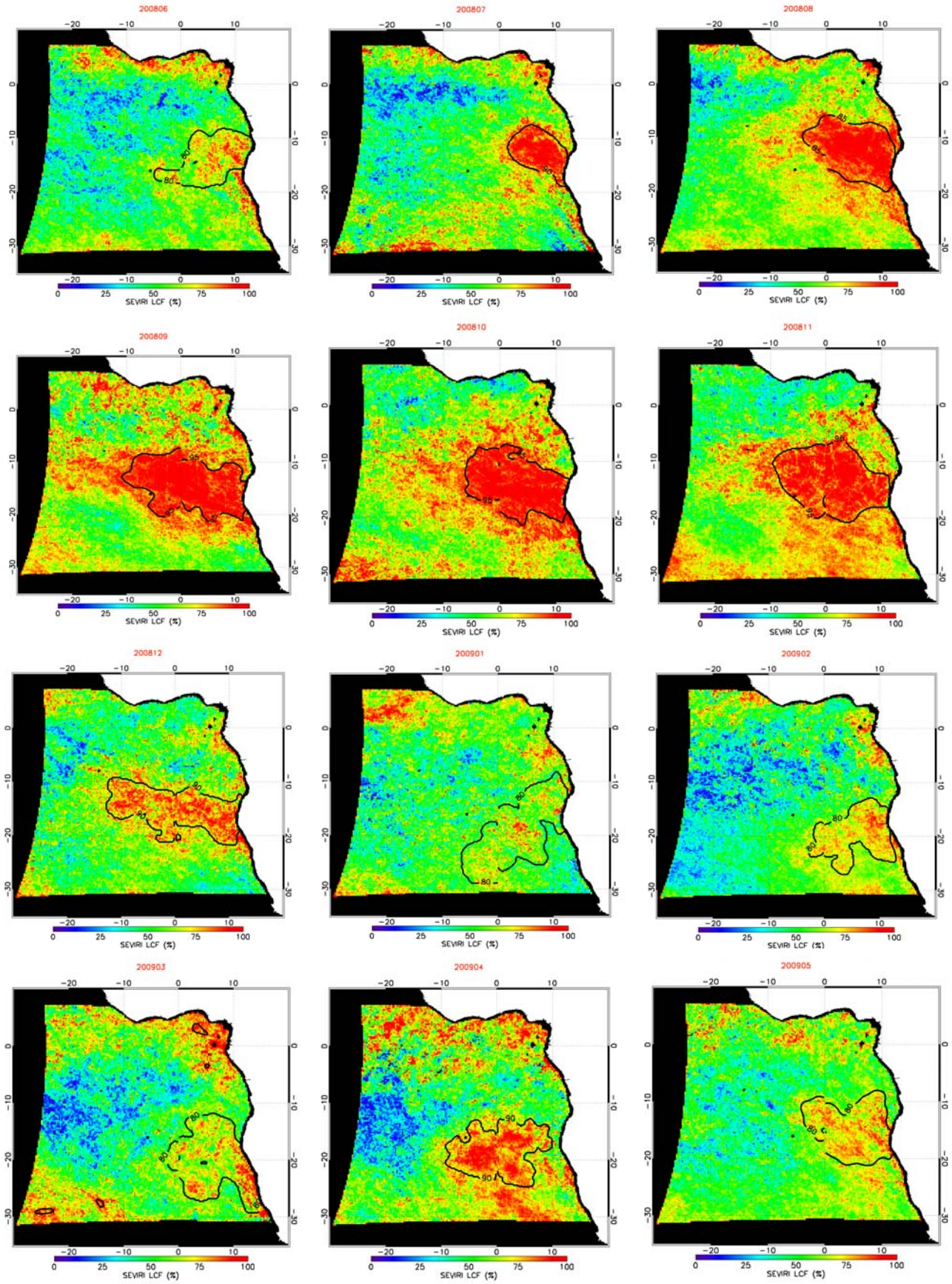

Figure 4.13. Monthly mean variation in liquid cloud fraction for June 2008 through May 2009.

4.3.4. Diurnal Cycle of TMI LWP and SEVIRI CPP

We examine the diurnal cycle of cloud properties over the entire South Atlantic domain, the Sc domain and the trade wind Cu domains. Despite occurring over the oceans in regions of large scale subsidence, marine Sc shows an interesting diurnal variation [*Minnis and Harrison,* 1984]. Over the extensive marine Sc regime, regardless of season, both TMI and SEVIRI LWP decrease with time from sunrise to sunset, and thereafter slight increase as shown in Figures 4.15-4.19. The figures shown here are only for aerosol neglected pixels, to avoid misinterpretations related to retrieval errors caused by aerosols (see Section 4.1). Our results are consistent with *Wood et al.* [2002] who also studied the diurnal variation in LWP over the South Atlantic Sc region, based on two complete years of TMI data and found similar diurnal features. However, there are many other scientists who contributed their effort in investigating the diurnal cycle of Sc clouds which occurs over other parts of globe. Notably, *Blaskovic et al.* [1990] evaluated the diurnal cycle of North-East Pacific Sc clouds off the California coast from the observations taken during FIRE. Their results indicated that cloud thickness and liquid water path exhibit a clear decrease during the day from sunrise to sunset, increasing thereafter. The decrease in LWP is associated with the decrease in cloud thickness. The cloud base height has diurnal range of (150+/-30) m, rising from sunrise till mid-afternoon. The cloud top height has a similar diurnal range of (130+/-30) m, but the main descent occurs in the late afternoon. Surface air temperature also increases at sunrise, directly in phase with the cloud base lifting, and has a diurnal range of 2^{o}C. *Ciesielski et al.* [2001] evaluated the diurnal variation of North Atlantic Sc clouds from the Atlantic Stratocumulus Transition Experiment (ASTEX), his results showed that fractional low cloudiness varies over this region from a maximum of 54% in the predawn hours to a minimum of 39% in the mid-afternoon. These changes in low cloudiness are accompanied by an opposite trend in the boundary layer moisture, which shows a predawn drying and an afternoon moistening. *Duynkerke et al.* [2004] compared the diurnal variation in the cloud liquid water path from six LES models and the observed data from FIRE, and found a fair agreement between them. Their analysis revealed that the diurnal variation in the cloud liquid water path is related to the transition from a decoupled boundary layer during daytime to a vertically well-mixed boundary layer during night. The observed diurnal cycle of Sc is characterized by a cloud layer which gradually thickens during night, whereas during the day, the cloud layer thins due to SW radiative absorption and decoupling. The latter state is characterized by slightly negative buoyancy fluxes and a minimum vertical velocity variance near the cloud base. This

implies that surface-driven, moist thermals cannot penetrate the cloud layer, while entrainment maintains a steady supply of relatively warm and dry air from just above the inversion into the cloud layer. This results in a distinct diurnal cycle of the LWP, which has minimum values during the day. During the night the vertical velocity variance has one single peak near the middle of the boundary layer. Moreover, the diurnal cycle in SEVIRI LWP is mainly driven by the cloud optical thickness rather than by the droplet effective radius, which shows less variability. Cloud optical thickness shows a sharp decrease of ~6 from morning (τ=10) to evening (τ=4) in annual mean results. However individual seasons show even a decrease of ~10 in optical thicknesses (SON) from morning to late afternoon. MODIS Terra+Aqua optical thickness values (green stars) are also shown in Figures 4.15-4.19. MODIS also shows a decrease in optical thickness from morning to afternoon, however less pronounced than SEVIRI. The SEVIRI effective radius and droplet concentration did not show much variability during the day. MODIS optical thickness and effective radius values are always higher than SEVIRI values, with optical thickness of magnitude 1 difference and effective radius of ~3 μm difference. MODIS Terra LWP is in very good agreement with SEVIRI and TMI in terms of magnitude, however MODIS Aqua LWP underestimates SEVIRI and TMI values. This Aqua-MODIS underestimation is mainly due to a lower cloud fraction, as we scale SEVIRI and MODIS LWP by their liquid cloud fraction in order to compare with TMI domain means. (Note that if we compare in-cloud LWP, MODIS is higher than SEVIRI, and this issue is explained in detail in the next section.) Compared to SEVIRI, Aqua-MODIS has ~40% lower cloud fraction while Terra-MODIS agrees within 10%. The large difference in cloud fraction in Aqua-MODIS and SEVIRI could be a consequence of MODIS clear-sky restoral (i.e., retrieval only over confident cloudy pixels), together with larger SEVIRI pixel size. Finally, to represent the entire diurnal cycle, we have plotted TMI LWP (grey curve) which includes both day and night, which clearly represents the observed daytime diurnal cycle and also the variation during night.

Again, the diurnal cycle in LWP consistently follows the variation in the cloud fraction as well. This result is further consistent with *Fairall et al*. [1990] who stated that the cloud fraction is maximum at sunrise (0.74) and minimum at sunset (0.41) with a maximum cloud albedo of 0.61 at sunrise and a minimum value of 0.31 a few hours after local noon. *Zuidema and Hartmann* [1995] stated that the stratus cloud LWP is correlated with cloud amount and is negatively correlated with low cloud-top temperature. They also inferred that no correlation is observed between effective radius and liquid water path, as larger drops are found in the evening and not in the morning, along with lower LWPs and lower albedos. In

our study the occurrence of maximum LWP is between 07 and 09 UTC, but it highly varies with season. The diurnal range in LWP is 60-75% which is fairly high compared to previous studies. *Wood et al.* [2002] reported a diurnal amplitude of 15-35% in low cloud regions to the west of continents using TMI data, *Zuidema and Hartmann* [1995] obtained only a 25% variation in LWP using SSM/I data. However, *Fairall et al.* [1990] found larger values of 60-70% using a 17 day period of near-continuous ground based microwave radiometer data around the time of FIRE.

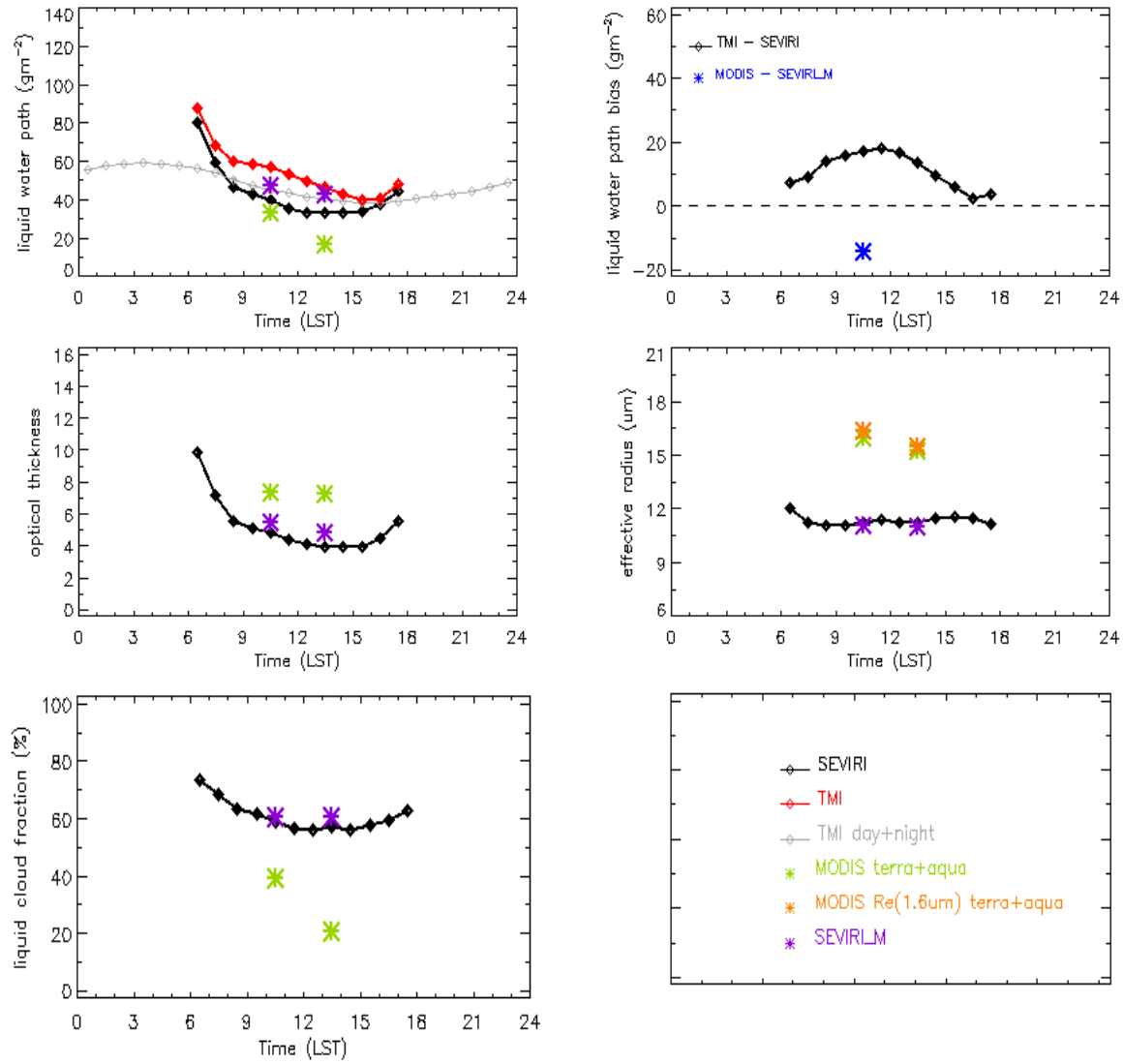

Figure 4.14. Annual mean diurnal cycle of cloud properties averaged over the entire South Atlantic domain (AI<1).

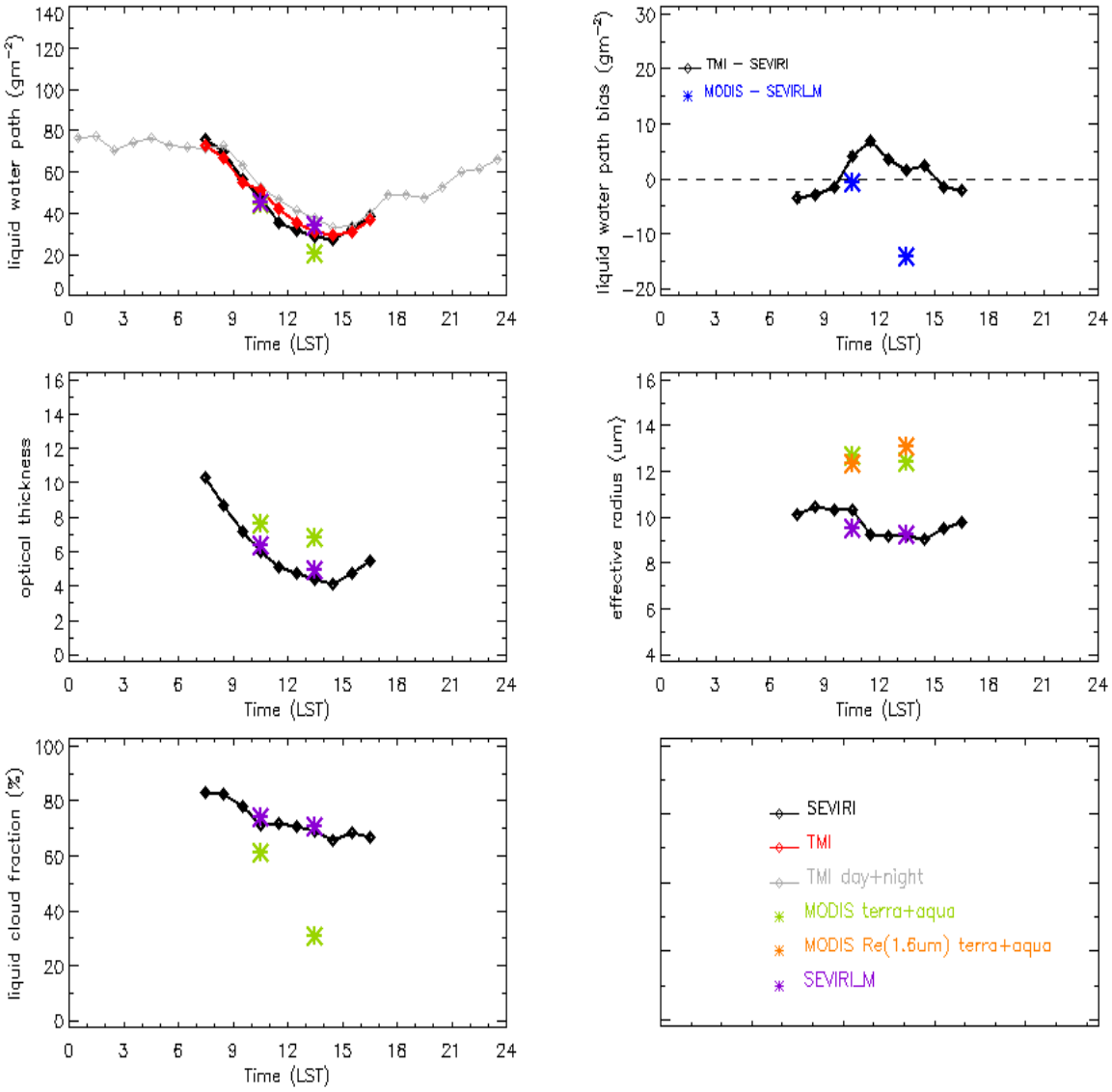

Figure 4.15. Annual mean diurnal cycle of CPP over the South Atlantic Sc domain.

The diurnal variation of TMI and SEVIRI liquid water path is in good agreement within ±5 g m^{-2}, in the aerosol unaffected seasons and also in the annual basis. In JJA and SON, even if we eliminate aerosols affected pixels with AI≥1, the diurnal cycle agreement is within ±10 g m^{-2} only, which is mainly due to a strong underestimation of ~15-20 g m^{-2} in SEVIRI LWP. This is due to the fact that τ and r_e decrease due to the effect of absorbing aerosols above these clouds. This implies that removing the pixels with AI≥1 eliminates only part of the LWP bias and hence that the influence of aerosols is still present in the data. Our analysis indicates that considering another aerosol index threshold of 0.25 leads to much better results and smaller biases.

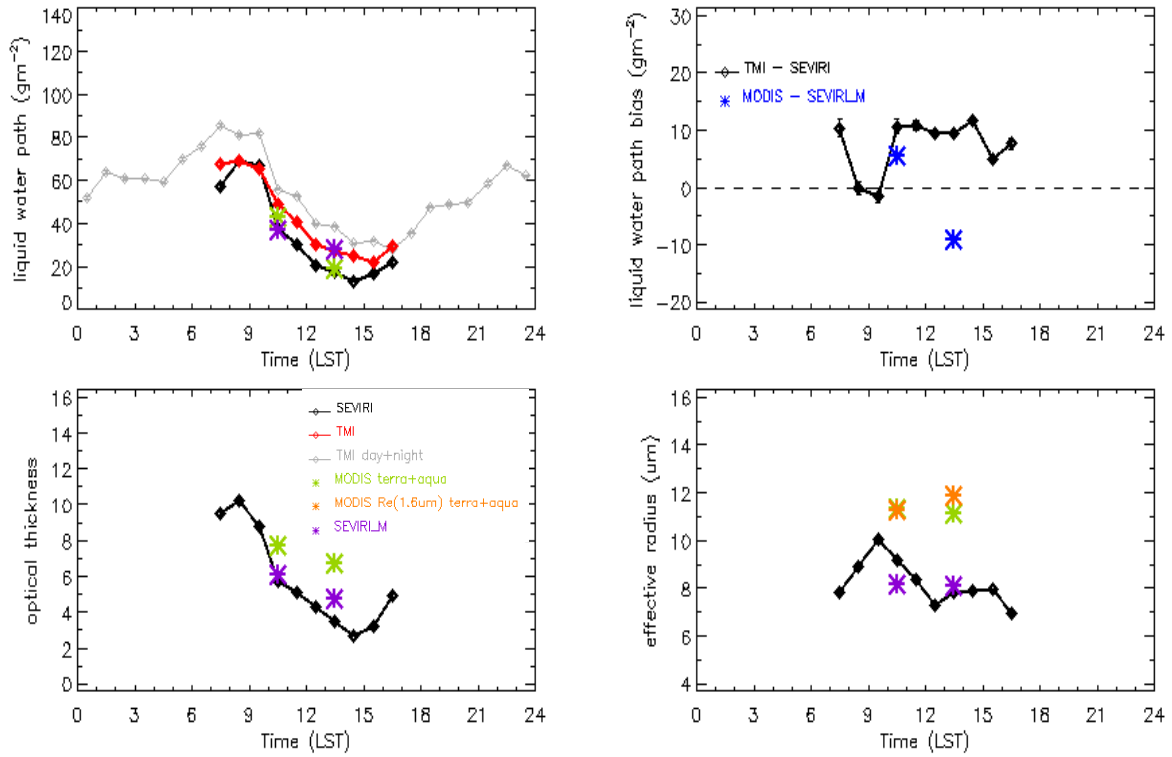

Figure 4.16. JJA mean diurnal cycle of CPP over the South Atlantic Sc domain.

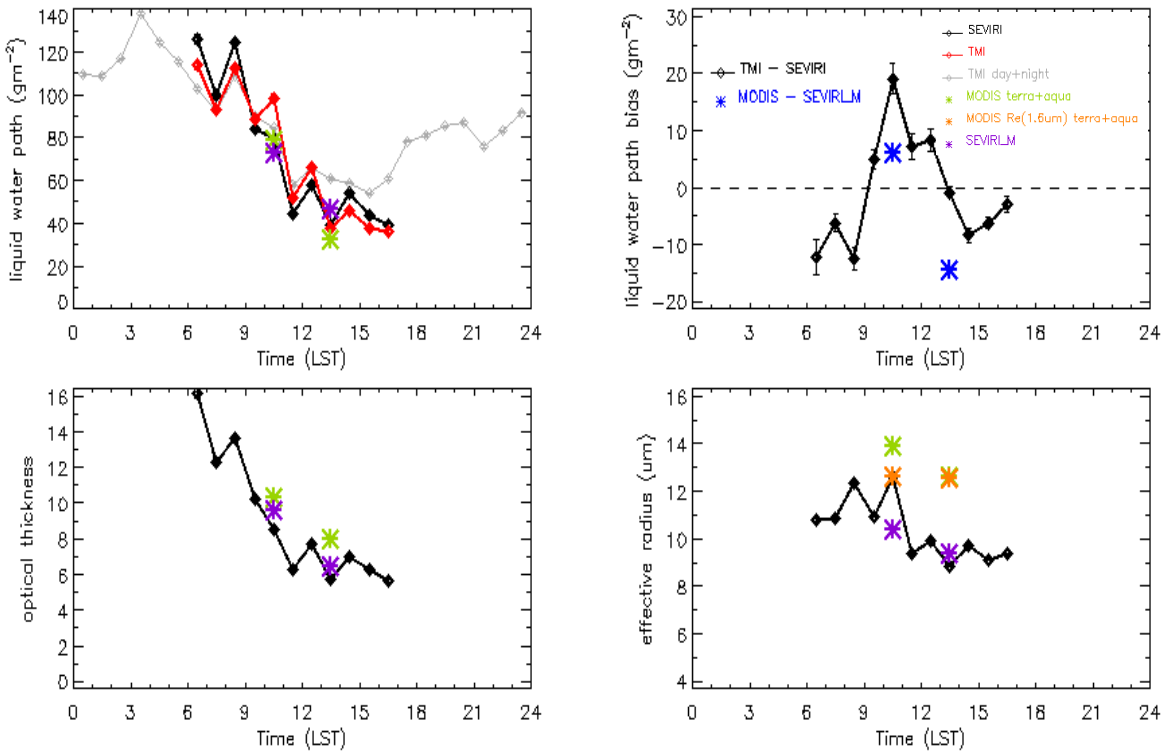

Figure 4.17. SON mean diurnal cycle of CPP over the South Atlantic Sc domain.

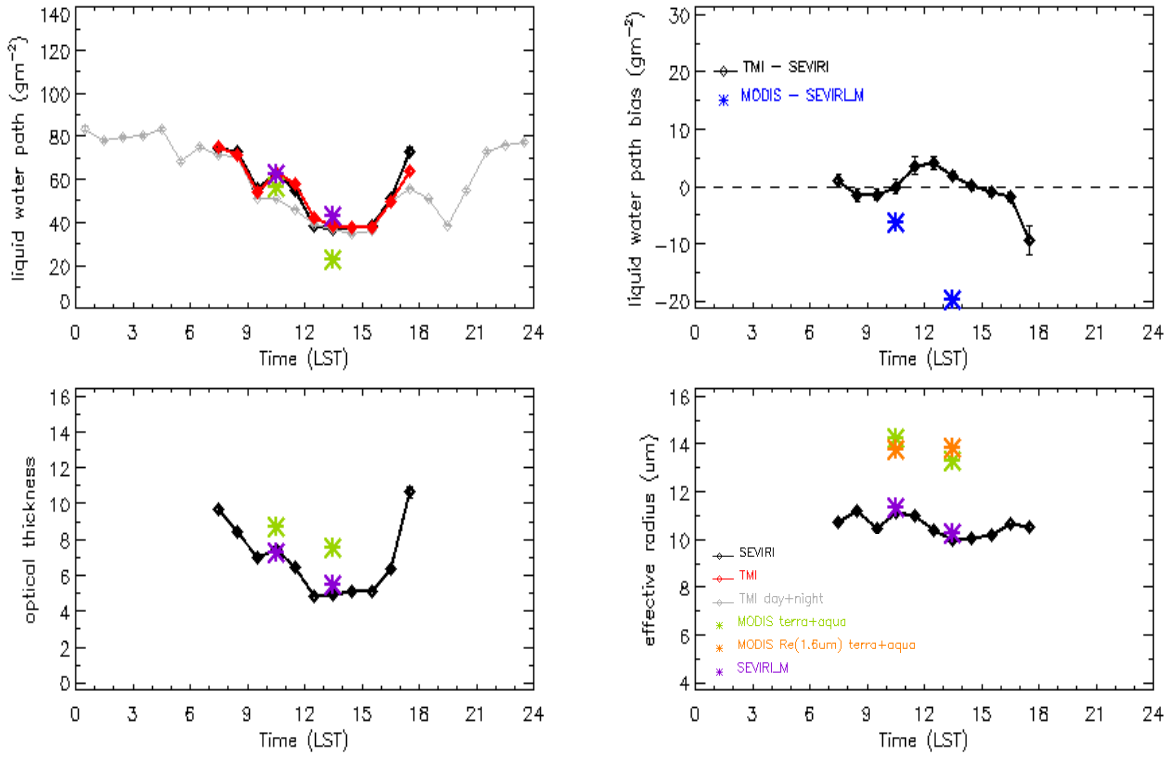

Figure 4.18. DJF mean diurnal cycle of CPP over the South Atlantic Sc domain.

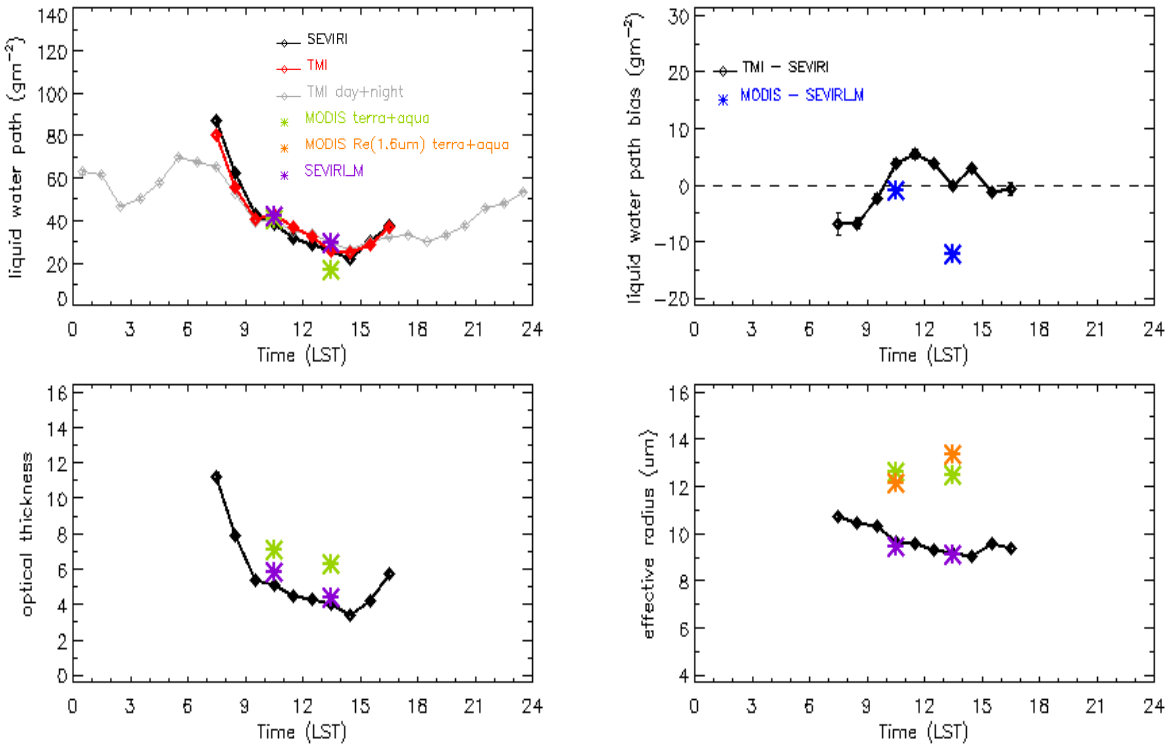

Figure 4.19. MAM mean diurnal cycle of CPP over the South Atlantic Sc domain.

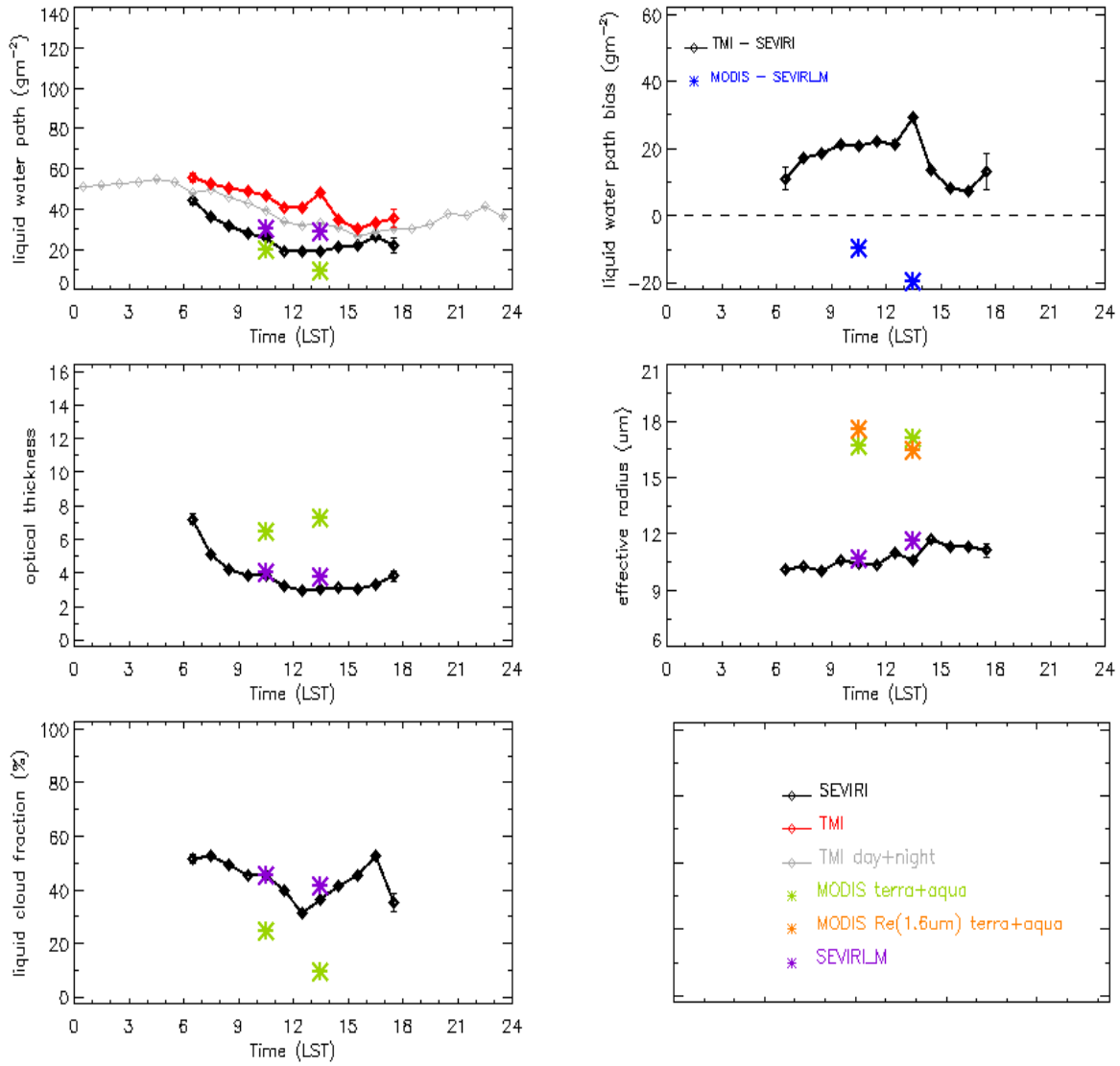

Figure 4.20. Annual mean diurnal cycle of CPP over the trade wind Cu regime.

Figures 4.20-4.21 show the annually and seasonally averaged diurnal cycle of cloud properties in the trade wind Cu regime. Over the trade wind Cu, we can observe different diurnal cycle with season; however, both the SEVIRI and TMI LWP show similar variability, but with a relatively large bias of 10-40 g m^{-2}. This large LWP bias might be partly due to SEVIRI underestimation and partly due to TMI overestimation. Nevertheless, it is interesting to notice a diurnal cycle (eventhough they differ from season to season) over the trade wind cumulus clouds and which is evident in TMI data (grey curve) as well. Finally, we have evaluated the diurnal cycle of liquid clouds over the entire South Atlantic domain as given in Figure 4.14. The LWP decreases mainly during day till late noon and then increases slightly. Both TMI and SEVIRI LWP agree within 10 to 30 g m^{-2}, but with SEVIRI underestimation. Similar variations in diurnal cycle are observed in the optical thickness while the trend is not clear for the droplet effective radius. When we consider the entire domain we still see a clear

diurnal cycle in annual mean LWP which is mainly due to the diurnal cycle in optical thickness. Similar variations are seen in cloud fraction and cloud thickness. The effective radius and droplet number concentration remain constant during the day, as expected.

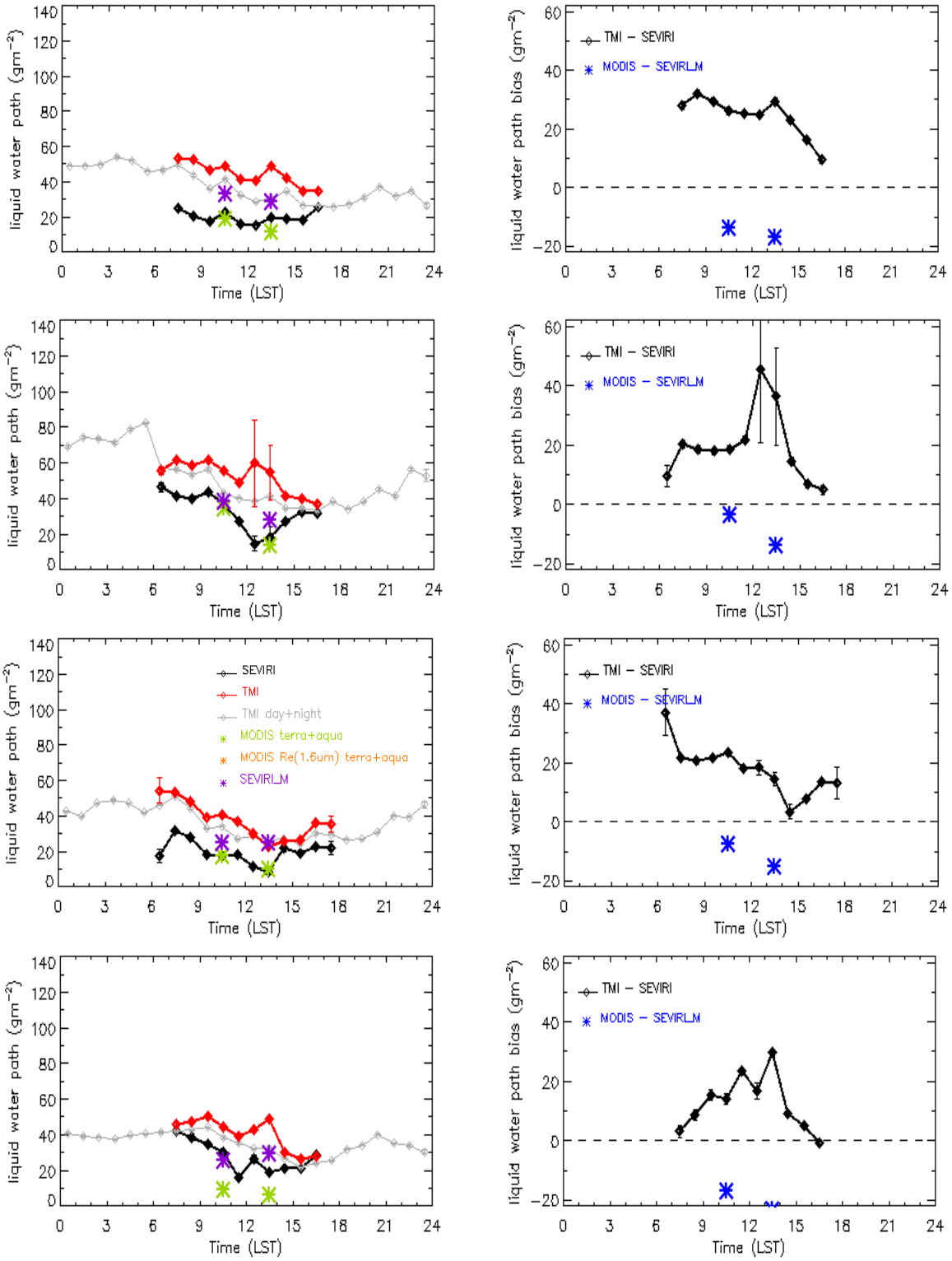

Figure 4.21. Seasonal mean diurnal cycle of CPP over the trade wind Cu regime during JJA (top row), SON (second row), DJF (third row), and MAM (bottom row).

4.3.5. Cloud Fraction Dependency of TMI and SEVIRI LWP

Cloud fraction is an important factor which can introduce errors in both VNIR and microwave retrievals, and the cloud retrievals are largely affected when the pixel/footprint is not completely overcast. The cloud fraction is calculated from SEVIRI valid liquid pixels within the TMI grid box. Most of the grid boxes show the calculated cloud fraction > 95%, which is due to coarse SEVIRI (3 km) resolution. The LWP increases with the cloud fraction in both TMI and SEVIRI; the TMI-SEVIRI LWP bias decreases with increasing cloud fraction. When the cloud fraction is >95%, TMI and SEVIRI show a better agreement in retrieved LWP, with bias ~ -6 g m^{-2}. The bias between AMSR-E and MODIS amounts to ~31 g m^{-2} in the most broken cloud scenes with cloud fraction 0-5% bin [*Seethala and Horvath,* [2010], Figure 4.4]. Unlike in the AMSR-E and MODIS comparison, TMI and SEVIRI show a smaller LWP bias of (~10 g m^{-2}) in the 0-5% cloud fraction bin. The optical thickness, effective radius and droplet number concentration also increase with the cloud fraction (figure not shown).

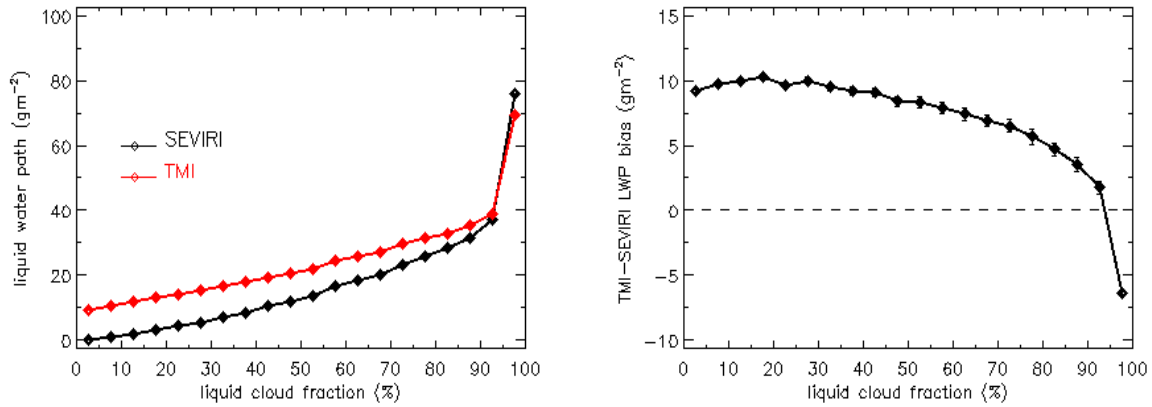

Figure 4.22. Cloud fraction dependence of annual mean cloud properties for the entire South Atlantic domain.

4.3.6. Solar Zenith Angle Dependency on SEVIRI LWP

The 3D effect at large solar zenith angle is a dominant source of error in VNIR retrievals. In this section we discuss the solar zenith angle dependence of SEVIRI cloud properties. TMI uses microwave technique and hence is not subject to this problem. Figure 4.23 gives TMI and SEVIRI cloud properties as a function of solar zenith angle. There is an increase in LWP with sun angle however this increase is observed in both TMI and SEVIRI. Hence this would be a real increase rather than an increase due to the 3D effect. The bias between TMI and SEVIRI is also very small and within ±5 g m^{-2}. The SEVIRI increase in

LWP with sun angle is associated with an increase in cloud optical thickness. The droplet effective radius shows least variation with sun geometry. However CDNC shows an increase with solar geometry. In our previous study *Seethala and Horvath* [2010] (see Figure 4.8b) and many other studies reported a sharp increase in MODIS LWP with solar zenith angle compared to AMSR-E LWP based on microwave technique. The difference between SEVIRI and MODIS is that MODIS retrievals are done at 1 km resolution, whereas SEVIRI uses 3 km pixel resolution. This would imply that 3 km scale SEVIRI retrievals is least affected by 3D effects at large solar zenith angle likely due to cancellation of errors.

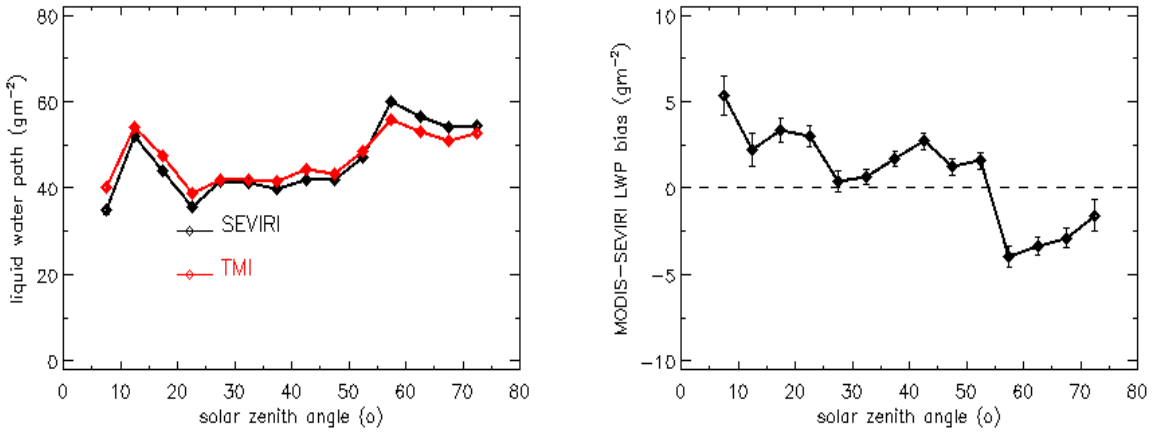

Figure 4.23. Annual mean solar zenith angle dependence in SEVIRI LWP over the entire South Atlantic domain

4.4. Comparison of SEVIRI versus MODIS CPP

Geostationary imagers sample at a coarser resolution than polar imagers. Thus SEVIRI cloud properties are retrieved at 3 km resolution but the MODIS retrievals are done at 1 km resolution. A coarser resolution gives rise to systematic biases in the derived cloud physical properties, especially when the cloud field is heterogeneous. Moreover, most of the SEVIRI pixels within TMI grid boxes have a cloud fraction ≥ 0.95, which is primarily due to the SEVIRI coarser resolution. *Henrich et al*. [2010] reported that 1 km pixel area seems least biased in the retrieval of optical thickness. Thus, to investigate the pixel size effect (sub-pixel scale variability) on SEVIRI retrieved cloud properties, we compare them with the high resolution MODIS retrievals. Comparison is done on monthly, seasonal, and annual means, however the results are shown here only for the annual means. The analysis is done in two steps (1) considering all the pixels (total sky) and (2) considering fully overcast pixels i.e., pixels with 100% cloud fraction in MODIS and SEVIRI at a 25 km resolution.

4.4.1. Total Sky SEVIRI and MODIS CPP

We discuss here certain features of SEVIRI and MODIS cloud properties such as liquid cloud fraction, LWP, cloud optical thickness, droplet effective radius, and their bias and relative biases. The annual mean cloud fraction varies from 30-100% in SEVIRI and 0-70% in MODIS retrievals. Over the extensive marine Sc region the cloud fraction is >75% in SEVIRI but only 50-70% in MODIS. The larger cloud fraction in SEVIRI retrievals is mainly the outcome of clear-sky restoral for MODIS and larger pixel size for SEVIRI. The mean optical thickness over Sc region is 6-8 in SEVIRI and 7-9 in MODIS, whereas over the more broken trade wind Cu regime MODIS values are 6 to 8 but SEVIRI mean optical thickness value is <5. Thus there is a difference of 1-1.5 in optical thickness between both datasets over Sc domain and larger difference in optical thickness over broken fields.

Small optical thickness values would introduce lower retrieved effective radii for SEVIRI as the CPP algorithm weighs r_e towards the r_e-climatology of 8 μm, while MODIS provides actual retrieved values. Moreover SEVIRI effective radius is retrieved from the 1.6 μm channel reflectance while MODIS retrieves effective radius at 1.6 μm, 2.2 μm, and 3.7 μm wavelengths. The 3.7 μm channel samples mostly the top layer of clouds, the 2.2 μm channel samples a little deeper than the 3.7 μm channel and the 1.6 μm channel samples further deeper although all three channels sample near the top of clouds due to the weighting function. SEVIRI and MODIS LWP are deduced from their respective optical thickness and effective radius, however SEVIRI uses optical thickness at 0.6 μm and effective radius at 1.6 μm channel reflectance, whereas MODIS uses optical thickness from 0.8 μm channel over ocean and effective radius from 2.2 μm channel reflectance. So we discuss MODIS effective radius at 1.6 μm and 2.2 μm and SEVIRI r_e at 1.6 μm. Over Sc r_e varies from 9 – 13 μm in both MODIS channels with the 2.2 μm values slightly larger than the 1.6 μm ones, whereas SEVIRI r_e varies from 8 μm to 10 μm. Thus, there is a difference of 2 μm to 4 μm in r_e between SEVIRI and MODIS. Over thin trade Cu regimes MODIS r_e is larger than 15 μm but SEVIRI r_e is between 12 μm to 14 μm. The relative bias in r_e is also less than 40% over Sc regime and larger than 70% over trade Cu regime.

Based on optical thickness and effective radius retrievals, the calculated SEVIRI LWP varies from 40-70 g m^{-2} and MODIS LWP varies from 50-90 g m^{-2} over the Sc regime. The mean bias is ~15 g m^{-2}. Overall SEVIRI LWP is smaller compared to MODIS LWP and the LWP bias is much larger over more broken clouds.

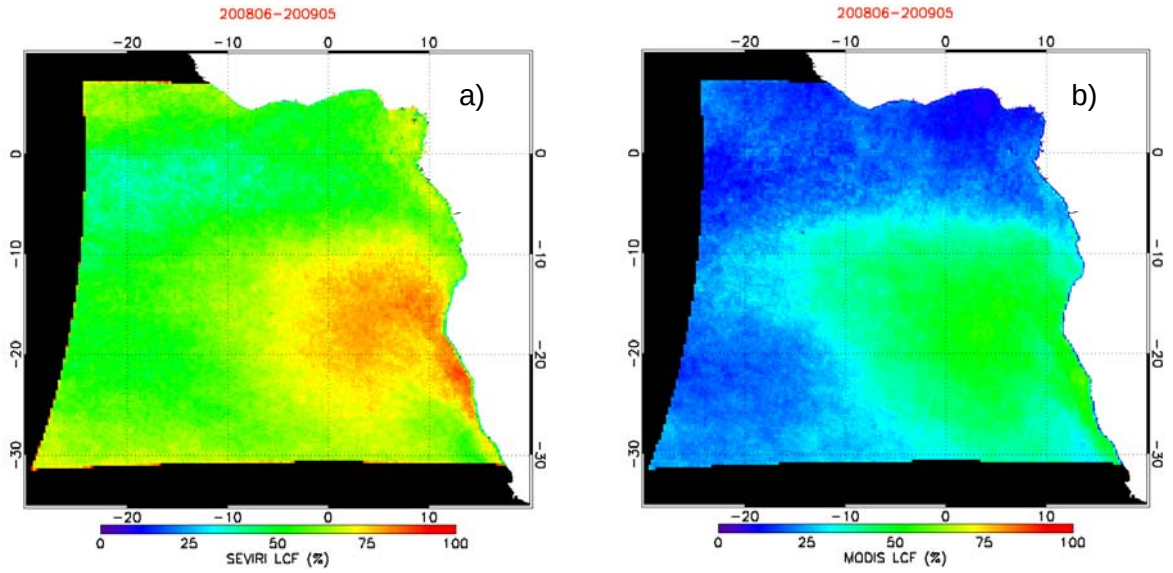

Figure 4.24. Annual mean liquid cloud fraction of (a) SEVIRI, and (b) MODIS.

4.4.2. Overcast Sky SEVIRI and MODIS CPP

In the overcast analysis we consider only those pixels with 100% cloud fraction in SEVIRI and MODIS retrievals. The SEVIRI annual mean LWP is ~100 g m^{-2} and MODIS mean value is ~120 g m^{-2}. The spatial pattern of both SEVIRI and MODIS LWP agrees very well with each other but with MODIS LWP being ~10-20 g m^{-2} higher than SEVIRI. The relative bias varies from 10-40%. The optical thickness mean value is 14 in both SEVIRI and MODIS and almost no bias is observed, especially over Sc. The relative bias is also less than 4% except for very few points. Comparison of r_e from MODIS 1.6 µm and 2.2 µm channels reveals a difference in r_e of 1-2.5 µm over the marine Sc regime. Similarly comparing r_e from SEVIRI 1.6 µm channel and MODIS 2.2 µm channel also reveals a 1.5-3.5 µm difference over the main Sc domain. The larger r_e difference of 2.5 µm (MODIS 1.6 µm vs. 2.2 µm) or 3.5 µm (SEVIRI 1.6 µm vs. MODIS 2.2 µm) is mainly observed over the smoke regions. Very good agreement, with r_e differences below 1, is observed between SEVIRI 1.6 µm and MODIS 1.6 µm. Moreover the relative r_e difference between MODIS 2.2 µm and SEVIRI 1.6 µm channel is ~15-35% and that of MODIS 1.6 µm vs. SEVIRI 1.6 µm is smaller than 10%. Thus, in a mean sense, the use of 2.2 µm channel retrieved r_e in LWP calculation in MODIS would increase the LWP to ~20% compared to SEVIRI LWP (as there is no considerable difference in optical thickness, the difference is only from r_e). From *Wood and Hartmann* [2006], *Greenwald* [2010], *Borg and Bennartz* [2007], *Seethala and Horvath* [2010] it is clear that MODIS operational LWP is larger over Sc compared to microwave measurements

and this overestimation is eliminated by applying sub-adiabatic correction to the MODIS values, which is simply a 17% reduction to the MODIS standard LWP. We have already seen unbiased mean LWP between TMI and SEVIRI (refer Section 4.3.3). This might be due to the fact that SEVIRI uses 1.6 μm r_e, which will automatically reduce LWP by ~20% (compared to standard MODIS), and hence it is not necessary to apply the adiabatic correction as in MODIS. So, SEVIRI LWP can be directly compared with adiabatic MODIS LWP over this Sc regime.

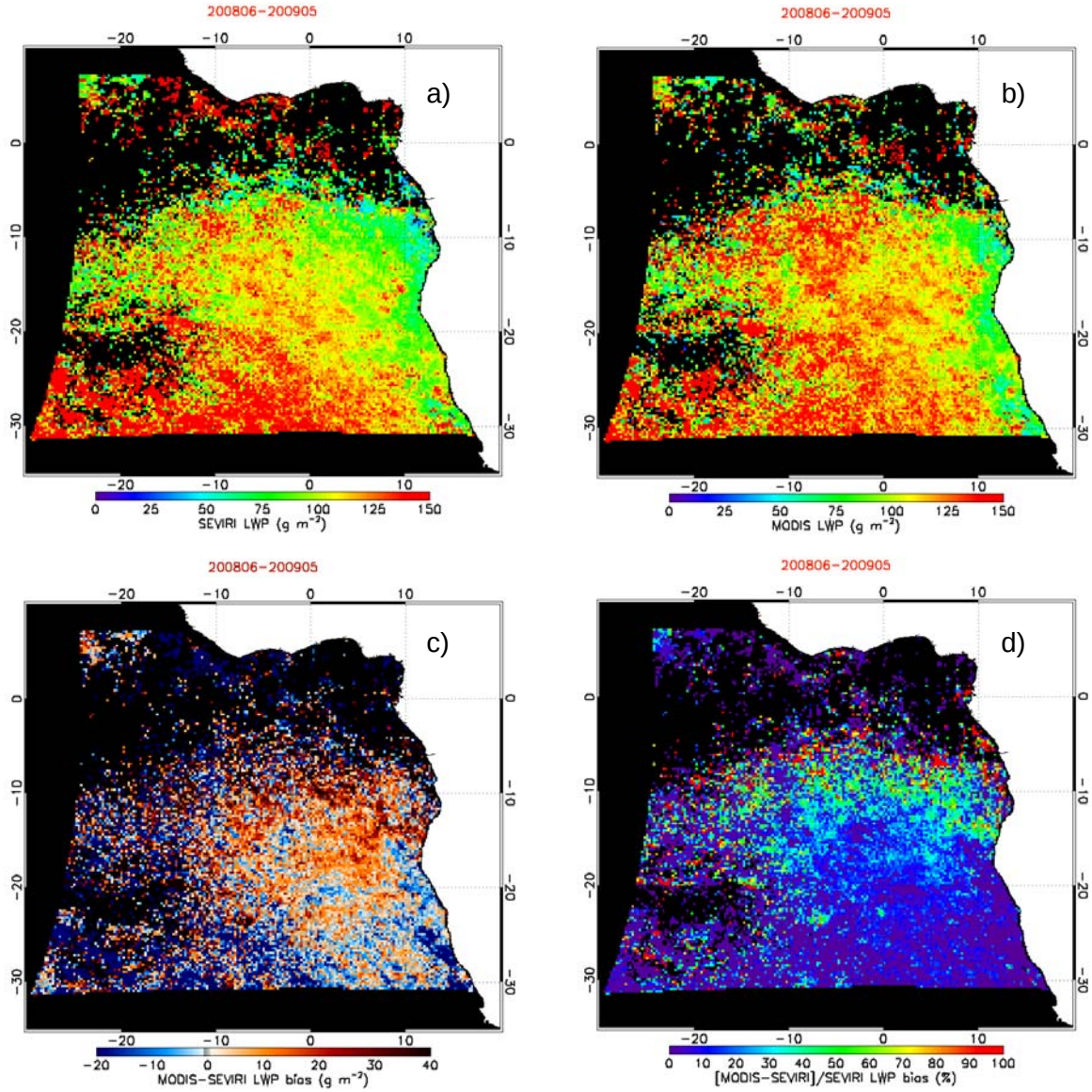

Figure 4.25. Annual mean liquid water path of (a) SEVIRI, (b) MODIS, (c) MODIS - SEVIRI, (d) (MODIS – SEVIRI)/SEVIRI for overcast sky.

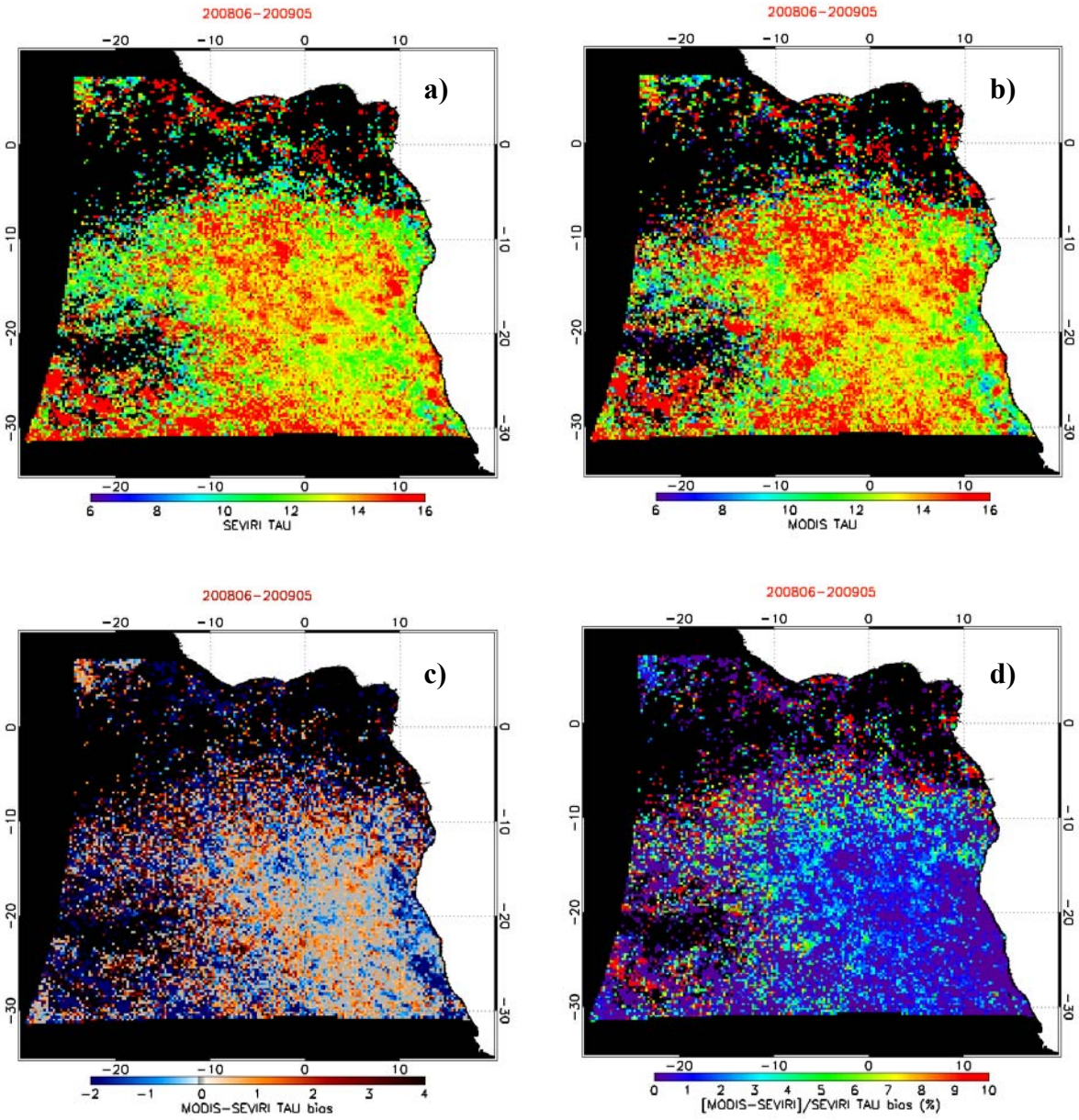

Figure 4.26. Annual mean optical thickness of (a) SEVIRI, (b) MODIS, (c) MODIS - SEVIRI, (d) (MODIS – SEVIRI)/SEVIRI for overcast sky

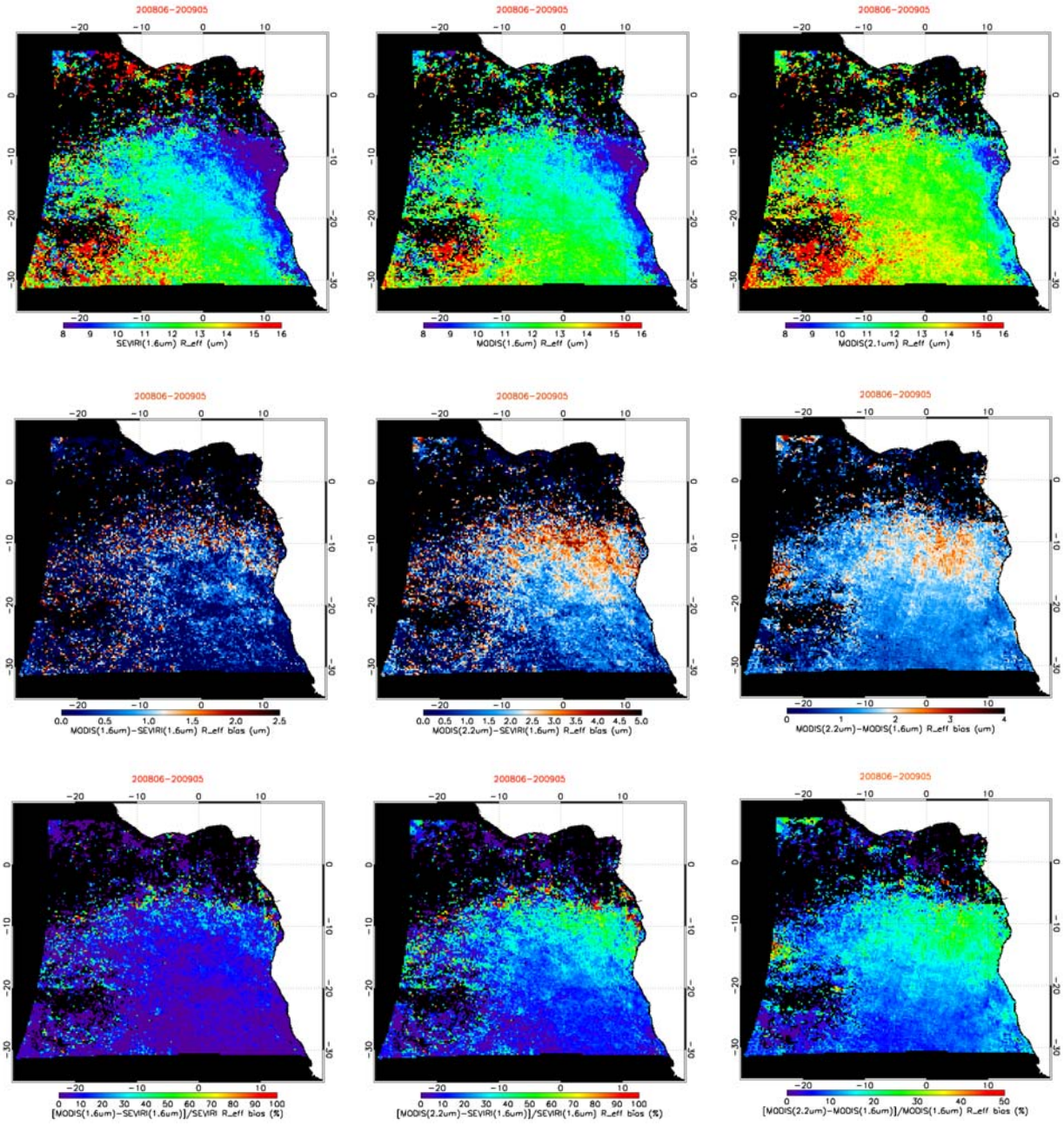

Figure 4.27. Annual mean droplet effective radius of (a) SEVIRI (1.6 μm), (b) MODIS (1.6 μm), (c) MODIS (2.2 μm), (d) MODIS (1.6 μm) – SEVIRI (1.6 μm), (e) MODIS (2.2 μm) –SEVIRI (1.6 μm), (f) MODIS (2.2 μm) - MODIS (1.6 μm), (g) [MODIS (1.6 μm)-SEVIRI (1.6 μm)]/ SEVIRI(1.6 μm), (h) [MODIS (2.2 μm)-SEVIRI (1.6 μm)]/ SEVIRI(1.6 μm), and (i) [MODIS (2.2 μm)-MODIS (1.6 μm)]/ MODIS(1.6 μm) for overcast sky.

4.4.3. Mean Statistics of LWP from SEVIRI and MODIS

Figure 4.28 shows the statistics between SEVIRI and MODIS over Sc domain for February 2009. Mean SEVIRI LWP is 60 g m^{-2} and is ~19% lower compared to MODIS LWP with a bias of 13.54 g m^{-2}. If one applies adiabatic correction to MODIS LWP the bias disappears. Thus there is a very good agreement between SEVIRI and MODIS LWP is confirmed by a high correlation of 0.93.

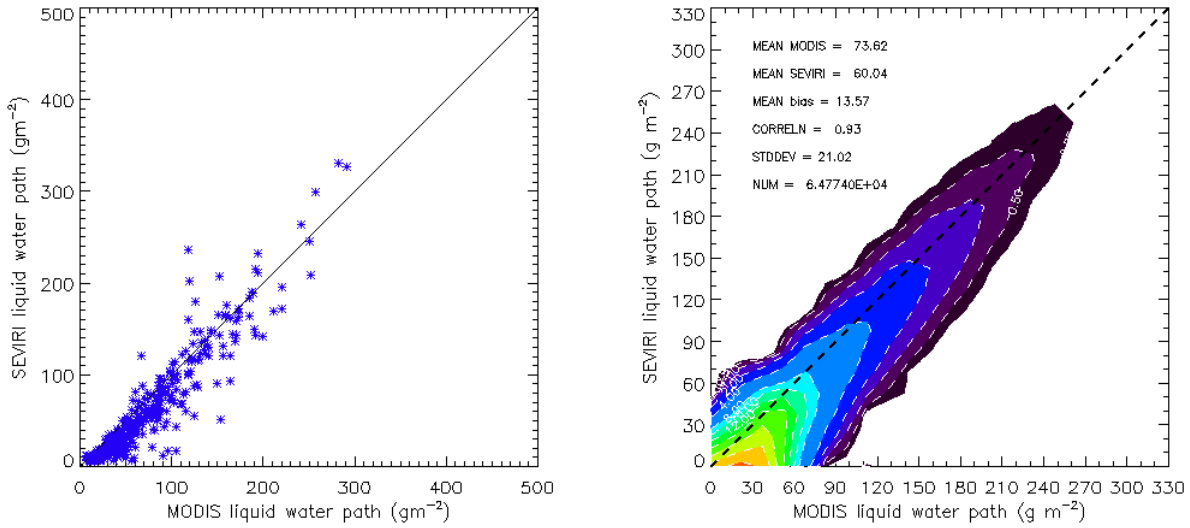

Figure 4.28. SEVIRI *versus* MODIS LWP statistics over Sc regime in February 2009.

4.5. Summary

The objective of this chapter was to evaluate the diurnal cycle of South Atlantic marine boundary layer clouds and its seasonal variability using cloud microphysical and optical properties from SEVIRI VNIR measurements, as well as cloud liquid water path from TMI microwave observations. In general, SEVIRI and TMI showed very good agreement for instantaneous and domain mean LWPs in the Sc regime, while the agreement in the trade wind Cu regime was worse. Spatial distributions showed a high correlation of ~0.9 for Sc regime and negligible bias on seasonal and annual basis.

We investigated the influence of absorbing aerosols over the Sc domain using aerosol index obtained from OMI. Interestingly, both TMI and SEVIRI LWP increased with AI, but the TMI increase was considerably larger. This was because absorbing aerosols above liquid clouds introduced substantial negative retrieval biases in optical thickness and droplet effective radius and, hence, in the deduced SEVIRI LWP. This SEVIRI LWP bias increased with AI and could be as large as 40 g m^{-2} in instantaneous retrievals. Neglecting aerosol affected pixels with AI>1, the domain mean TMI-SEVIRI LWP bias could be either

completely removed (SON) or at least reduced by half (JJA). Overall, a positive correlation between AI and LWP was seen, which could be due to (i) simple spatial correlations, that is, both aerosol load and cloud optical thickness increased toward the coast or (ii) aerosols actually thickening the underlying cloud layer through dynamical processes.

The diurnal cycles of TMI and SEVIRI LWP were in good agreement within ±10 g m^{-2} in all seasons except JJA and SON. In JJA and SON, larger LWP biases of ~15-30 g m^{-2} were observed due to SEVIRI underestimation of LWP in the presence of absorbing aerosols. After neglecting aerosol affected pixels in JJA and SON the calculated bias in diurnal cycle was reduced to less than ±10 g m^{-2}. Irrespective of season, both TMI and SEVIRI LWP decreased from morning to late afternoon and thereafter a slight increase was observed. Prior to sunrise clouds were thicker and as the day progressed the cloud layer got thinner due to the absorption of solar radiation and associated decoupling of the sub-cloud layer. The variation in SEVIRI LWP was mainly due to change in cloud optical thickness/cloud physical thickness as both droplet effective radius and droplet number concentration showed only small diurnal variability.

The largest disagreement was observed over trade wind Cu, due to the deficit in both microwave and VNIR measurement techniques in the low cloud fraction scenes. However, SEVIRI and TMI showed similar variations in diurnal cycle of LWP but with a constant large bias of ~20 g m^{-2} (TMI being higher than SEVIRI). The responsible factors for this large bias could be: a known positive clear-sky bias of 12-15 g m^{-2} and cloud-rain partitioning error in Wentz's microwave algorithm together with microwave less sensitive to low LWP at 37 GHz affecting TMI retrievals; and cloud mask uncertainties, plane-parallel bias, and 3D effects in broken scenes affecting SEVIRI retrievals. We also found that in our study region and at the ~3 km scale of SEVIRI, the VNIR retrievals were rather unaffected by 3D radiative effects at large solar zenith angles.

Finally we have evaluated the sub-pixel scale variability in SEVIRI retrievals based on MODIS Terra+Aqua retrievals. Very good agreement between SEVIRI and MODIS was observed with correlation ≥0.9 in the fully overcast cases. However, over all cloudy cases, SEVIRI showed a considerably lower LWP than MODIS. We also found that with the use of the 1.6 μm channel effective radius no adiabatic correction to the SEVIRI LWP for Sc clouds appeared to be needed to compare it with the microwave retrievals. In contrast, for MODIS LWP retrievals based on the 2.2 μm channel retrieved effective radius, an adiabatic correction factor of 5/6 should be applied.

Chapter 5
Quantifying Uncertainties in 1D VNIR Cloud Retrievals Using LES Cloud Fields and SHDOM Radiative Transfer Model

This chapter is dedicated to quantify the uncertainties in one-dimensional visible/near-infrared satellite cloud retrievals from hundreds of large-eddy simulated cloud fields and a 3D radiative transfer model. To do so, we have investigated the 1D visible/near-infrared cloud retrievals of ~650 LES cloud fields consisting of stratocumulus, unbroken stratus, and broken shallow cumulus clouds. In a plane-parallel model, visible and near-infrared radiances increased with view zenith angle at low Sun, and the increase is 2–3 times larger in the forward scattering direction than in the backscatter direction; however, for high Sun, these radiances decreased with view zenith angle. A case study revealed that the Sc clouds follow this plane-parallel theory very well. However, for a broken shallow Cu cloud, the increase in radiance with VZA is less pronounced, and the visible radiances underestimated the plane-parallel ones. The plane-parallel model radiances decreased from medium to larger values of solar zenith angle, however, 3D radiances increased with SZA. This increase is larger in both the Sc and the shallow Cu field, except that for the shallow Cu fields radiances strongly underestimated the plane-parallel ones at high Sun. The 1D VNIR cloud property retrievals were done at the native and also at the 1 km horizontal resolution for ~650 cloud fields. Initially, the analysis is performed at the pixel-level. The most-homogeneous one-third of the clouds exhibited narrow Gaussian distribution, but skewed negatively, indicating the overestimation in retrieved LWP. Roughly 40-60% of the data showed the relative LWP bias within ±15% depending on SZA. However, the most-heterogeneous one-third of the clouds showed much wider distribution with more than one peak, but skewed negatively, and only 10-25% of data are within ±15% relative bias. Then, the domain mean cloud properties are investigated. For the homogeneous clouds the domain mean retrieved LWP did not show any variability with solar zenith angle or with view zenith angle, and the retrievals are agreed to the true LES values within the 5-10% relative error. However, for the heterogeneous clouds an increase in retrieved LWP with SZA is observed. While comparing with true LES values, the retrieved LWP underestimated 20-30% in high and medium Sun, agreed at 60^{o} Sun angle, and strongly overestimated (LWP doubles) at 70^{o} solar zenith angle. The retrieved LWP decreased with the view zenith angle, and the decrease is largest in the forward scattering direction, and is less pronounced in the backscatter direction. For the homogeneous clouds,

the domain mean relative LWP bias is within ±10% for most of the Sun-view geometries, however for the heterogeneous clouds, the relative bias goes to 40% when the solar zenith angle is below 60^o and above which large bias is observed. We examined the optimal Sun-view geometry for minimum (min) cloud optical thickness retrieval bias. When the min bias is binned according to view zenith angle, maximum (max) of min bias is seen in 30^o (in total 83% of clouds showed min bias in altogether 30^o, 45^o, 60^o VZA). When the min bias is binned according to the view azimuth angle, 70% of clouds showed min bias in the side/backscatter direction. In terms of SZA, the max no. of clouds showed min bias at 60^o, which is mainly due to the cancellation of errors due to the frequent occurrence of cloud illuminated and shadow side viewing in the heterogeneous clouds.

5.1. Introduction

Satellite remote sensing is such a complex task that until now it could be done only by using one-dimensional (1D) radiative transfer theory, which assumes that the cloudy pixels are fully covered by horizontally homogeneous clouds and the pixels' radiative properties are not affected by cloud variability in nearby areas, i.e., the clouds as plane-parallel. By assuming clouds and their radiative boundary conditions to be plane-parallel, the transfer of solar radiation is greatly simplified to one-dimension (the vertical). Based on *Nakajima and King* [1990] cloud optical thickness (τ) and droplet effective radius (r_e) can be estimated from satellite measured visible and near-infrared (VNIR) radiances. This makes radiative transfer calculations computationally fast and solutions to the inverse problem faced in satellite remote sensing tangible. However, a simple look at clouds, either from the ground or from an aircraft, reveals that they are often not horizontally homogenous, and occur with a wide variety of shapes and sizes that have obvious three-dimensional (3D) characteristics, and one might reasonably expect there to be many discrepancies between 1D and 3D approaches. A few major issues which can cause considerable bias in 1D VNIR satellite cloud retrievals are: (1) nonlinear averaging of sub-pixel heterogeneity, (2) the effect of cloud sides, illuminated *versus* shadowed side viewing, (3) cloud top structure, and (4) internal cloud heterogeneity. Using MISR (Multiangle Imaging SpectroRadiometer) data *Girolamo et al.* [2010] showed that the view-angular distribution of the retrieved τ measured at 1 km resolution are indistinguishable from plane-parallel clouds 79% of the time for the oceanic stratiform clouds when solar zenith angle below 60^o, for all other cloud types and Sun angles the frequency in which clouds are indistinguishable from plane-parallel drops sharply to as low as a few

percent. With regard to the horizontal distribution of the cloud water content, neglecting the heterogeneities can lead to an underestimation of the mean τ by 30% even for flat overcast cloud layers [*Cahalan,* 1994]. This departure from the homogeneous plane-parallel model can be highly enhanced because of cloud-top height variations [*Loeb et al*., 1998]. The 3D effects really are important in the interpretation of high-resolution measurements [*Marshak et al.,* 1995], and in the cases of highly oblique solar or viewing directions [*Loeb and Davies,* 1996; *Buriez et al.,* 2001].

Over the years there are many researchers focused on addressing the issue: does 1D radiative theory gives accurate results in satellite remote sensing? and found that under certain conditions 3D effects can cause significant problems. Specifically, they revealed that the 3D effects can make clouds appear too smooth or too rough [*Marshak et al*., 1995; *Davis et al*., 1997; *Oreopoulos et al*., 2000b], too bright and thick [*Loeb and Davies*, 1996; *Loeb and Coakley*, 1998], and artificially asymmetric [*Várnai and Marshak*, 2002a, 2002b, 2007]. Using MISR observations, *Horváth and Davies* [2004] showed that the angular pattern of cloud reflection rarely fits the expectations based on the plane-parallel approximation. Examining data from the Earth Radiation Budget Experiment (ERBE), the Advanced Very High Resolution Radiometer (AVHRR), and the Polarization and Directionality of the Earth's Reflectances (POLDER), some other studies [*Loeb and Davies*, 1997; *Loeb and Coakley*, 1998; *Buriez et al*., 2001] found that for low Sun, the 3D interactions such as shadowing make clouds appear too dark from oblique views facing the Sun, and that this causes 1D retrievals to underestimate τ. *Zuidema et al*. [2003] found that in highly inhomogeneous cumulus (Cu) congestus clouds, oblique backscatter reflectances observed by MISR exceeded 3D radiative transfer calculations based on cloud structure retrieved from the nadir camera using the plane-parallel approximation. *Marchand and Ackerman* [2004] found that stratocumulus (Sc) reflection in backscatter direction was stronger in MISR observations than in 1D/2D simulations for cloud structures derived from a variety of ground-based and satellite observations. Finally, theoretical studies [*Davies*, 1984; *Bréon*, 1992; *Kobayashi*, 1993] also indicated that cloud inhomogeneities can enhance reflection through cloud sides into oblique side scatter directions relative to cloud reflection into overhead direction. Using 1 km MODIS observations, *Várnai and Marshak* [2003] revealed that 1D retrievals yield systematically higher cloud optical thickness values when clouds are viewed from backscatter directions, and their distributions increased by up to 30%. In fact, all these studies explore the importance of Sun-view geometry in the 3D cloud fields and these uncertainties remains significant even if the retrievals are averaged over intermediate scales [*Loeb et al*., 1997;

Várnai and Marshak, 2001], although it disappears in very large scale of MODIS level3 (1^ox1^o) monthly mean regional or global maps (*Maddux* [2010]).

The studies clearly showed that cloud heterogeneity is a significant problem when attempting a 1D retrieval of a cloud property such as optical depth. What is less clear, however, is how to quantify the frequency and degree of cloud heterogeneity on a global scale, in order to understand the errors introduced by the non-critical applications of 1D radiative transfer theory. Satellite-based remote sensing of clouds is clearly an ill-posed problem, and an accurate retrieval should never be expected. Unless 3D effects are parameterized [*Iwabuchi and Hayasaka*, 2002; *Wyser et al*., 2002], implementing a 3D radiative transfer algorithm in the cloud property retrieval is not practical because it is computationally far too expensive and the 3D cloud fields in the actual retrieval process are not known. Recently, a few cloud retrieval methods have been proposed that explicitly take cloud inhomogeneity and 3D radiative transfer into account for Sc clouds [*Iwabuchi and Hayasaka,* 2003; *Cornet et al*., 2004; *Marchand and Ackerman*, 2004; *Zinner et al*., 2006; *Evans et al*., 2008]. *Cornet et al*. [2004] simulated multispectral, single-angle radiances from hundreds of stochastic clouds with 3D radiative transfer and performed retrievals of the mean and standard deviation of τ and r_e with neural networks. Using stochastic cloud fields and Monte Carlo radiative transfer *Iwabuchi and Hayasaka* [2003] developed a multi-regression model to retrieve mean τ and r_e from the radiance of the target pixel and neighboring pixels at two wavelengths. *Marchand and Ackerman* [2004] developed a technique for retrieving a 3D field of Sc liquid water content from AirMISR data using 3D radiative transfer. *Zinner et al*. [2006] developed a technique to retrieve 3D Sc cloud properties from an adiabatic model and high-resolution (15 m) radiance data based on the Green's function deconvolution idea of *Marshak et al*. [1998]. *Evans et al*. [2008] applied ensemble neural network approach similar to *Cornet et al*. [2004], but with the multi-angular data, to retrieve τ from simulated MISR data. They calculated the datasets relating statistics of simulated MISR reflectances and true τ from hundreds of LES scenes for a variety of Sc clouds, broken marine trade Cu, and fair-weather Cu, and thereby retrieved the mean and standard deviation of τ over various size pixel patches from the mean and standard deviation of reflectances from seven MISR cameras. All these approaches found a substantial improvement in the retrieval accuracy; however, these novel methods are not yet ready for the operational use.

A few researchers recognized that selection of preferred Sun-view geometry, however, can significantly reduce this 3D error. A theoretical analysis by *Davies* [1984] showed that the reflection functions of horizontally extensive (stratiform) and horizontally

limited (cumuliform) clouds are generally quite different, and also, that both the nadir and limb viewing directions should be avoided, with the best choice being the measurement of radiances with view zenith angles (VZAs) close to 60^o. He further suggested that, for situations with large potential azimuthal dependence, as for large solar zenith angles (SZAs), the preferred azimuthal viewing directions appear to be approximately 90^o or 270^o with respect to the solar plane. *Loeb and Davies* [1996] highlighted application of 1D theory to the remote sensing of cloud optical thickness from measurements at nadir should therefore be restricted to thin clouds and small SZAs. *Minnis* [1989] revealed that cloud side viewing must occur frequently, because it increases cloud coverage significantly for oblique views. Using 1 km MODIS observations, *Varnai and Marshak* [2003] cautioned that for backward viewing angles larger than 50° one can expect a substantial overestimate in 1D τ retrievals. Recently, *Kato et al*. [2006, 2009] attempted to estimate the error in retrieved τ and r_e from a single Sc and Cu cloud field. They found 1% relative error in domain mean retrieved τ for the overcast scene and 27% for the broken scene.

Motivated by all these studies, we decided to quantify the errors related to 3D cloud structure in 1D VNIR satellite cloud retrievals by looking hundreds of large-eddy simulated (LES) cloud fields ranging from Sc, unbroken St, and broken shallow Cu using a 3D radiative transfer model, hoping that this would be a quick solution for the current 1D VNIR satellite cloud retrievals. This chapter is organized as follows. The 3D cloud fields from LES, the radiative transfer models, the cloud retrieval algorithm, and the comparison methodology are described in Section 2. The results are presented in Section 3, especially the simulated 3D radiances and their comparison with the plane-parallel model; the analysis of the pixel-level and the domain mean retrieved cloud properties in terms of Sun-view geometry. The 3D retrieval error has been quantified for homogeneous and heterogeneous clouds at 200 Sun-view geometry. The optimal Sun-view geometry for the minimum retrieved optical thickness bias is also estimated. Section 4 provides summary of our findings.

5.2. Datasets, Models, and Methodology

5.2.1. The Large-Eddy Simulated Cloud Fields

To estimate an unbiased error in cloud retrieval algorithm that includes 3D radiative transfer requires a large number of cloud fields. We choose to use large-eddy simulated cloud fields because they can provide realistic cloud structure and have the flexibility to produce a wide variety of cloud types. We used cloud fields from seven different LES simulations, and

are listed in Table 1. The mean cloud properties are shown in Figure 5.1. In the figure, different runs were named and indicated by black-dashed lines.

Of which, TRDCT and TRREF runs were performed by *Irina Sandu*, with the University of California, Los Angeles (UCLA) LES [*Stevens and Seifer,* 2008], as a case study of stratocumulus to scattered cumulus transition. The theory is, the Sc clouds form over relatively colder sea-surface temperatures (SSTs), and, as the air masses advect equatorward over warmer SSTs, the Sc decks breaks-up into scattered shallow Cu. The runs were performed to investigate the dominant mechanisms which force this transition of the Sc to the scattered Cu clouds. The setups of these simulations are based on a composite of the large-scale conditions encountered along a set of individual trajectories performed for the north-eastern Pacific during the summer months of 2006 and 2007. The dynamical core of the model is described in *Stevens et al*. [2002], and the cloud microphysics model is described in *Ackerman et al*. [1995]. Radiative processes are represented using the Monte Carlo spectral integration (McSI) method developed by *Pincus and Stevens* [2009], which is based on the delta-four stream radiative transfer code [*Liou et al*., 1988]. The details of LES simulations are described in *Sandu et al.* [2009] and *Sandu and Stevens* [2011]. The LES runs are performed at a domain size of 8.96 x 8.96 km^2. The original horizontal resolution is 70 m, and hence the cloud can be accommodated into 128 x 128 grid cells. The vertical extensions of the Sc clouds are 500 m to 1.5 km, and that for the Cu clouds are 500 m to 2.1 km.

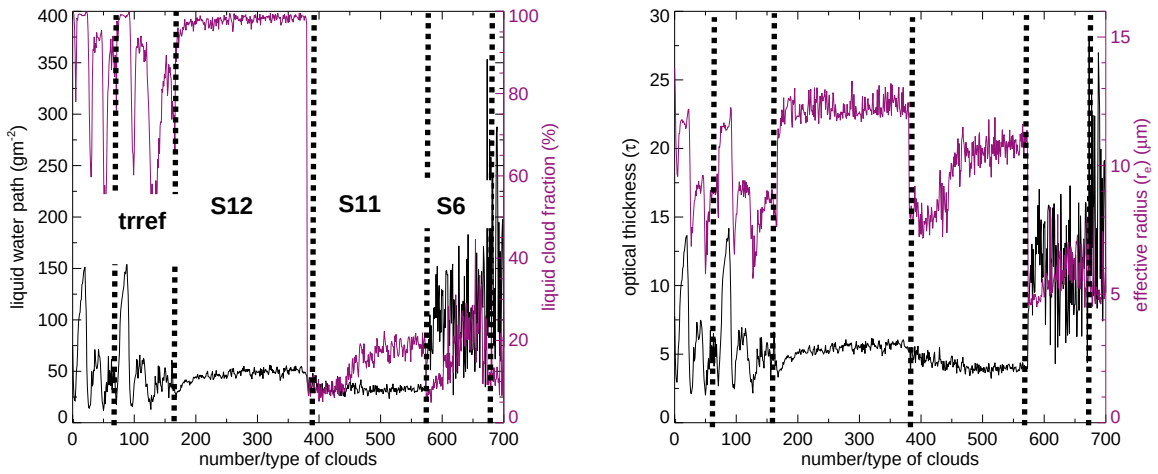

Figure 5.1. The domain mean LES true cloud properties (a) liquid water path and cloud fraction, and (b) cloud optical thickness and droplet effective radius.

The CGILS-S6, CGILS-S11, and CGILS-S12 runs were representative of shallow Cu, Sc, and St regimes respectively, and are provided to us by *Thijs Heus*. The purpose of these runs is to use the cloud responses in the selected region to interpret the cloud feedback in the global models. S6 is at (17^{o}N, 149^{o}W) to represent the shallow Cu regime, S11 is at (32^{o}N, 129^{o}W) near the California coast to represent the Sc regime, and S12 is at (35^{o}N, 125^{o}W) immediately off the California coast to represent the St regime. The forcing conditions are constructed for July conditions over the northeast subtropical Pacific to sample different cloud regimes. Refer http://atmgcm.msrc.sunysb.edu/cfmip_figs/Case_specification.html for more details. The domain size for S6 simulation is 9.6 x 9.6 km^2 and the cloud vertical height varies from 400 m to 3.2 km. S11 simulation is done for a 4.8 x 4.8 km^2 domain, and the cloud vertically extends from 350 m to 800 m. S12 simulations is done for a 3.2 x 3.2 km^2 domain, and the cloud vertically extends from 400 m to 850 m.

The LES simulations based on trade-wind cumulus during the Rain in Cumulus over the Ocean (RICO) field study were performed by *Malte Reick* using *Savic-Jovcic and Stevens* [2008] LES version. RICO was a comprehensive field study [*Rauber et al*., 2007] of shallow Cu convection located in the winter trade-winds of the north-western Atlantic Ocean, conducted late November 2004 until the end of January 2005. The details about the LES runs are described in *Rieck et al*. [2012]. We had 6 scenes of 12.8 x 12.8 km^2 domain size, and the cloud height varies from 600 m to 2.8 km. We have considered only those layers which have clouds, so it is assumed that the effect of rain will not affect our retrievals.

Table 1. Statistics of 3D cloud fields obtained from the LES runs.

LES runs	τ	r_e (μm)	LWP (g m^{-2})	LCF (%)	Domain size (km^2)	Resolution (m)	No. of scenes
TRDCT/TRREF (Sc-shallow Cu)	2-14	6-12	10-150	50-100	8.96 x 8.96	H: 70 V: 20/30	150
CGILS-S6 (shallow Cu)	8-25	8-12	50-350	5-50	9.6 x 9.6	H: 200 V: 40	100
CGILS-S11 (Sc)	<5	6-10	<50	5-25	4.8 x 4.8	H: 100 V: 25	230
CGILS-S12 (stratus)	~5	~12	~50	95-100	3.2 x 3.2	H: 50 V: 20	230
RICO (shallow Cu)	6-12	4-8	40-110	5-15	12.8 x 12.8	H: 200 V: 40	6

Thus we got total 700 cloud fields. The overall cloud scenes consist of variety of cloud types, ranging from unbroken stratus (St), stratocumulus (Sc) to broken shallow cumulus (Cu) scenes. Our clouds are also possible to categorize into optically thick and thin, and respective overcast and broken. The emphasis in the selection of LES cloud fields is to obtain a large number of scenes with a variety of cloud structure (and cloud properties) for the proposed study. However, these sets of LES cloud fields undoubtedly represent a tiny fraction of the real boundary layer clouds and, so, we should consider this as examples of possible clouds rather than a comprehensive set.

5.2.2. Radiative Transfer Model

Three-dimensional radiative transfer calculations for the above described LES cloud fields are performed with the Spherical Harmonics Discrete Ordinate Method (SHDOM) [*Evans,* 1998]. SHDOM computes unpolarized monochromatic or spectral band radiative transfer in a one, two, or three-dimensional medium for collimated solar and/or thermal emission sources of radiation. SHDOM is superior to Monte Carlo methods when many radiative quantities are desired, or when computing pixel-by-pixel intensity in multiple directions. The SHDOM code combines both discrete ordinates and spherical harmonics to solve the radiative transfer equation. Spherical harmonics are used to compute the source functions and the scattering integral. Another advantage is that the scattering integral is more efficiently computed in spherical harmonics than in discrete ordinates. Discrete ordinates are used to compute the radiance field, which is then used to compute the source function, and the process repeats until a stable solution is found. To speed up calculations and to save memory an adaptive grid is used; i.e., the model can start with a rather coarse grid, and fills in extra grid points for better accuracy whenever gradients exceed a certain threshold. The 3D radiative transfer calculations consume a lot of computer memory compared to the 1D calculations, so the methods used here allows us to simulate radiance for cloud fields with adequate spatial resolution. The details of accuracy issues and computational costs are examined in *Pincus and Evans* [2009].

The latest version of SHDOM is utilized in this study. The simulations are done for non-polarized and monochromatic radiation with periodic boundaries. SHDOM accuracy is controlled by both spatial and angular resolution. We used $N_\mu = 16$, $N_\varphi = 32$, the cell splitting accuracy of 0.003, and the solution accuracy of 1.0E-5. We assumed Lambertian surface with 5% albedo, to represent Ocean black surface. The solar flux is set to π so that the radiance output from SHDOM has reflectance units. SHDOM inputs liquid water content (g m^{-3}) and

droplet effective radius (μm) from a 3D cloud field. A gamma distribution with shape parameter 7 is used for the droplet size distribution. The cloud fields were then combined with a Mie scattering table for the particular wavelength to specify the extinction, the single scattering albedo and the phase function at each grid point. Finally, the 3D radiance is simulated for visible (0.86 μm) and near-infrared (2.13 μm) wavelengths at the domain top for various combinations of solar zenith angles (0^o to 70^o with 10^o intervals), view zenith angles (0^o, 30^o, 45^o, 60^o, 70^o), and view azimuths' (30^o, 60^o, 90^o, 120^o, 150^o). Here, the wavelengths for 3D simulations are selected based on MODIS cloud retrieval algorithm.

One-dimensional radiative transfer calculations required for the preparation of lookup table are performed by SHDOMPP [*Evans,* 2007], a plane-parallel version of SHDOM. SHDOMPP is tuned to get an accuracy similar to DISORT. The relative (%) accuracy between SHDOMPP and DISORT is 0.01%, which is considered as highly accurate. With this setup 1D radiance is computed at 0.86 μm and 2.13 μm wavelengths for wide range of effective radius (2 to 100 μm), optical thickness (2 to 150), view zenith angles (0^o to 88^o), view azimuths' (2^o to 180^o), and solar zenith angles (0^o to 88^o) with very fine resolution.

5.2.3. Cloud Retrieval Algorithm

A 1D look-up-table (LUT) based cloud retrieval algorithm is generated from the SHDOMPP VIS and NIR radiances, following *Nakajima and King* [1990]. We developed an algorithm to retrieve the cloud optical thickness and effective particle radius from measured radiances at VIS and NIR wavelengths based on the LUT. The technique is that the reflection function of clouds at a non-absorbing channel in the VIS wavelength region is primarily a function of the cloud optical thickness, whereas the reflection at a water absorbing channel in the NIR is primarily a function of cloud particle size. The algorithm is solely for clouds having $\tau \geq 4$ and $r_e \geq 6$ μm, and for optically thin clouds the retrieval becomes ambiguous, resulting in two possible solutions for τ and r_e.

The retrieval procedure comprises two separate steps: the first one is the angular interpolation, and the second step concerns the cloud parameter retrieval from interpolated and corrected radiance data. For the interpolation along the different directions/angles we used a simple linear interpolation. The retrievals are done for pixels with true LWP above 10 g m^{-2}. The cloud properties such as τ and r_e are retrieved by matching 3D radiance into 1D LUT. However, the chance is small that we find the same radiances in both 3D and 1D LUT. If the exact radiances are not matching, the 1D LUT radiances are interpolated to find the corresponding τ and r_e. To do the interpolations, we choose an optimization technique by

minimizing the difference in (1D and 3D) radiances, which is similar to the one used in MODIS operational retrieval algorithm.

If one assumes that each reflection function measurement is made with equal relative precision, maximizing the probability that $R^i_{meas}(\theta_o,\theta,\varphi)$ observations have the functional form $R^i_{calc}(\tau,r_e,\theta_o,\theta,\varphi)$ is equivalent to minimizing the statistic χ^2, defined as [*Nakajima and King*, 1990]:

$$\chi^2 = \sum_i \left[\ln R^i_{\text{meas}}(\mu, \mu_0, \phi) - \ln R^i_{\text{calc}}(\tau_c, r_e; \mu, \mu_0, \phi)\right]^2,$$

where the summation extends over all wavelengths λ_i for which measurements have been made and calculations performed. The parameters τ and r_e that give the best fit of the measurements R^i_{meas} to the nonlinear function $R^i_{calc}(\tau,r_e)$ are determined by the location of the minimum value of χ^2 in this 2D space. Thus the simultaneous measurements of τ and r_e are performed. The interpolation error or uncertainty in this method is evaluated in detail in following section.

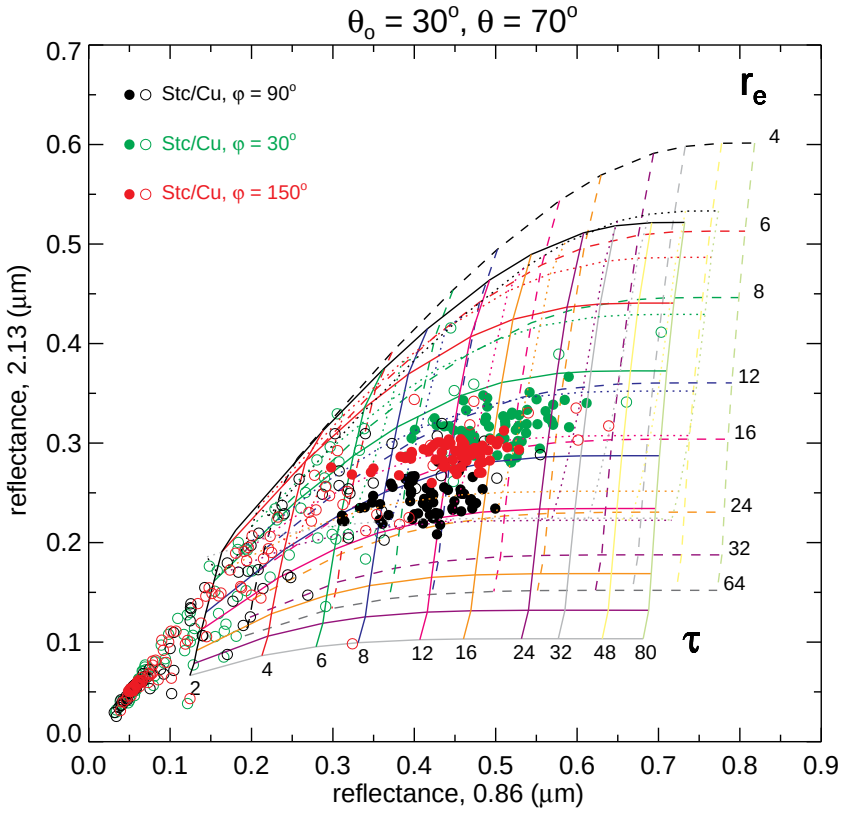

Figure 5.2. The LUT from SHDOMPP based on *Nakajima and King* [1990] for (a) high Sun (30°) and oblique view (70°), in the forward (dashed), side (solid), and backward (dotted) scattering direction. The observed 3D radiances for a Sc and a Cu cloud are over-plotted.

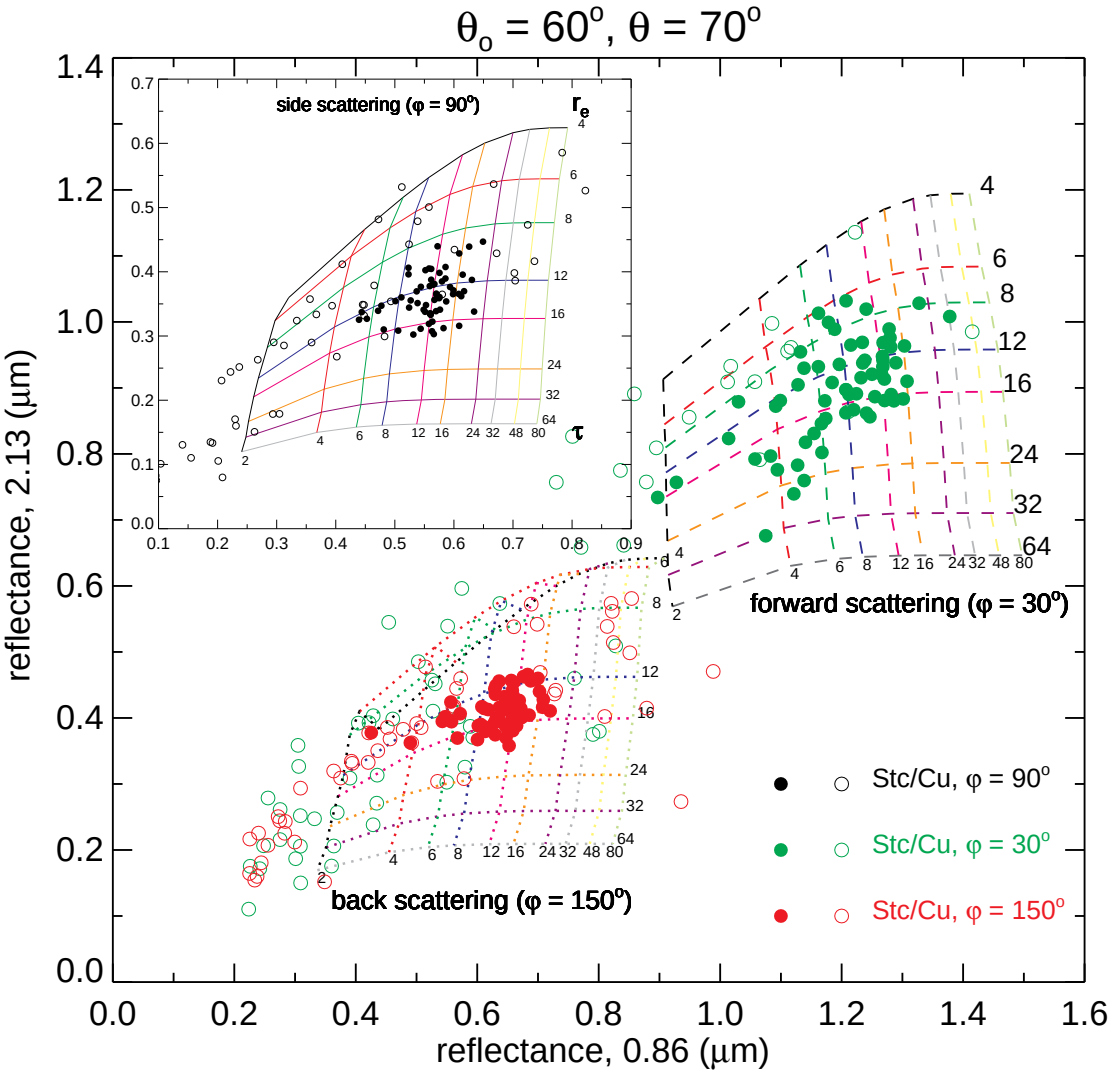

Figure 5.3. The LUT from SHDOMPP based on *Nakajima and King* [1990] for low Sun (60°) and oblique view (70°), in the forward (dashed), side (solid), and backward (dotted) scattering direction are shown. The observed 3D radiances for a Sc and a Cu cloud are over-plotted.

The retrieval algorithm is validated with homogeneous plane-parallel clouds with known cloud properties. The 3D radiance is simulated from SHDOM for a homogeneous cloud of 1.25 x 1.25 km^2 size with a horizontal resolution of 20 m and vertical resolution of 25 m. A constant liquid water content of 0.155 g m^{-3} and constant droplet effective radius of 8.55 μm is specified from 875 m to 1.25 km vertical. The 3D radiative transfer calculations are performed and the retrieval algorithm is applied to compute τ and r_e based on the optimization interpolation technique. We achieved a 3% overestimation in τ and 3.8% underestimation in r_e, finally lead to a 1.7% underestimation in LWP retrievals compared to

the true properties. This ~2% error is very small, and as per MODIS ATBD, their optimization interpolation errors are within 3%. We have also checked a scene with slightly perturbed cloud properties i.e., the same homogeneous scene, but r_e is perturbed. The results indicated only a ~1.3% overestimation in retrieved LWP. This implies that our retrieval algorithm performs equivalent to the operational MODIS cloud retrieval algorithm.

Another factor to consider is the sensitivity of retrievals at low and high end of the LUT. Figure 5.2 and 5.3 represents the LUT at two different Sun-view geometry: at high Sun and oblique view and, low Sun and oblique view respectively, for forward, side, and backscattered directions. From Figure 5.2 it is clear that, at high Sun the plane-parallel model reflectances are similar for forward/side/backscattering direction. However, at low Sun and especially in the oblique view, the plane-parallel model predicts similar radiance for back/side scattering direction, but extremely large values in the forward scattering direction (shown in Figure 5.3). In the low end of the LUT, i.e., for the smaller values of τ, constant r_e lines are much closer to each other, as the difference in NIR radiance is much smaller. Sometimes, different constant r_e lines can even overlap to each other. In these circumstances, the accurate interpolation is not possible and τ and r_e retrievals get complicated, and the results can be erroneous. Moreover, the retrievals can also be influenced by the initial guess values. These errors are assumed to be minimal in the middle of the LUT. In this section we evaluate the sensitivity of our retrievals at low-end and middle portion of LUT from a respective shallow Cu and a Sc cloud field. The 3D radiance from Sc cloud field (filled circles in Figure 5.2 and 5.3) mostly fall in the mid-LUT and as expected the retrievals agreed within 4% uncertainty. Nevertheless, the radiance from broken Cu (open circles in Figure 5.2 and 5.3) is scattered over the LUT and falls mostly in the low-end of LUT, sometimes even exceeding the high-end of LUT, especially in the side/backscattering direction. In this case, the retrievals are obviously uncertain, and the retrievals are strongly affected by the initial guess values too. The retrievals differs upto 20% for certain initial guess values. However, in our retrieval, since the true cloud properties are known, the true values of (τ, r_e) itself is fed as initial guess values, and hence these errors are assumed to be minimal.

5.2.4. Methodology

To calculate the magnitude of the retrieval error in cloud properties, we have developed a 1D retrieval algorithm based on *Nakajima and King* [1990]. The cloud optical thickness and effective radius are retrieved using 3D radiances measured at VNIR wavelengths. The 3D radiances are computed from the 3D LES cloud fields using SHDOM

radiative transfer code. The 3D reflectances are computed at 200 combinations of angles composed of a) 5 instrument viewing zenith angles (θ) = 0^o, 30^o, 45^o, 60^o, and 70^o (similar to MISR viewing angles), b) 5 view azimuth angles (φ) = 30^o, 60^o, 90^o, 120^o, and 150^o (here we excluded most forward (0^o) and most backward (180^o) observing directions in order to eliminate the extreme effects, as these angles are rarely used in practice), and c) 8 solar zenith angles (θ_o) = 0^o, 10^o, 20^o, 30^o, 40^o, 50^o, 60^o, and 70^o. To avoid errors caused by differences in model assumptions, look-up tables for the cloud property retrievals are prepared using SHDOMPP, a plane-parallel version of SHDOM. The retrievals are performed for individual cloud fields at its native resolution and also at standard 1 x 1 km^2 MODIS resolution. The radiances from the plane-parallel model and 3D radiative transfer were compared. The error in retrieved cloud properties is estimated by comparing the true cloud properties with the retrieved cloud properties at different Sun-view geometry. Moreover, we limit this study to only non-raining low-level oceanic water clouds.

5.3. Results and Discussion

5.3.1. Spatial Distribution of 3D Radiance

Passive remote sensing of cloud retrievals is uniquely determined by its reflectance in one particular direction; however, often this implicit assumption fails to produce accurate cloud retrievals. Thus, this section is aimed to address inconsistencies in measured 3D radiance at different directions especially when the cloud is heterogeneous – by comparing it with the radiance from plane-parallel model. Measured VIS and NIR radiances are affected by cloud fraction within satellite pixel size, cloud horizontal/vertical variability, droplet effective radius, absorption, etc.

Thus, the spatial variability of simulated 3D radiance for a Sc (Figure 5.4-5.5) and a shallow Cu (Figure 5.6-5.7) field is discussed here. The general features of Sc cloud are, more variability in spatial distribution of radiance is observed for nadir view, for the side views clouds look much smoother, and for the very oblique view cloud-top-variability is obvious.

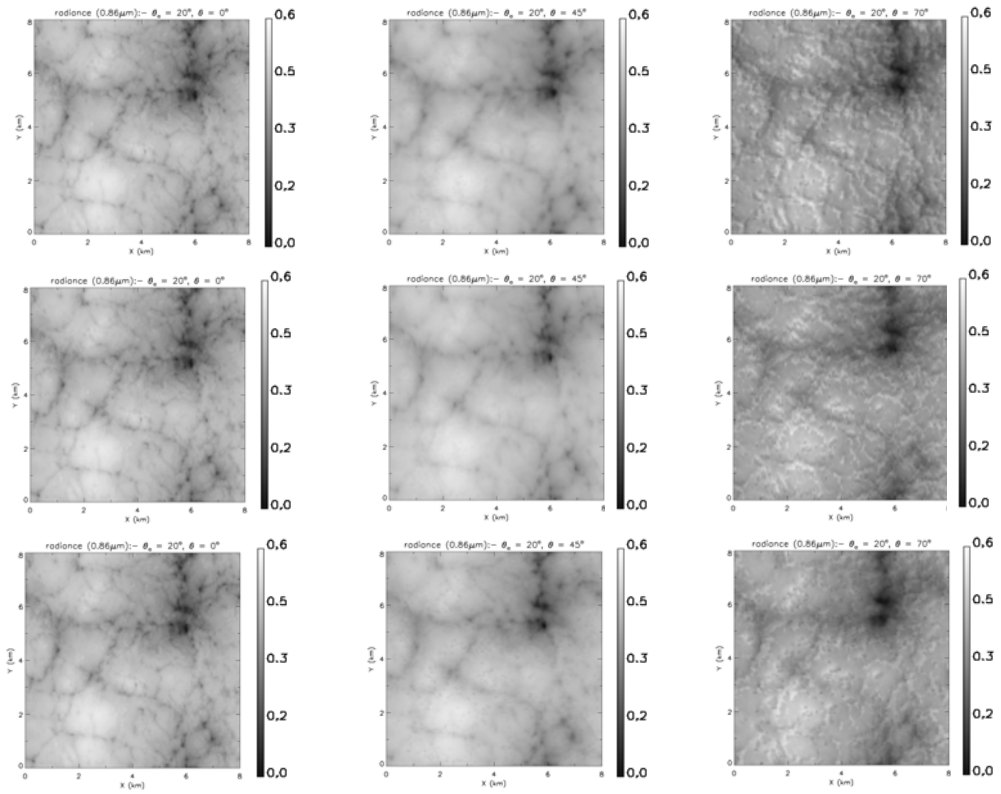

Figure 5.4. Simulated 3D radiance in forward (top row), side (middle row), and backward (bottom row) scattering direction at 0^o, 45^o and 70^o VZAs for 20^o solar zenith angle.

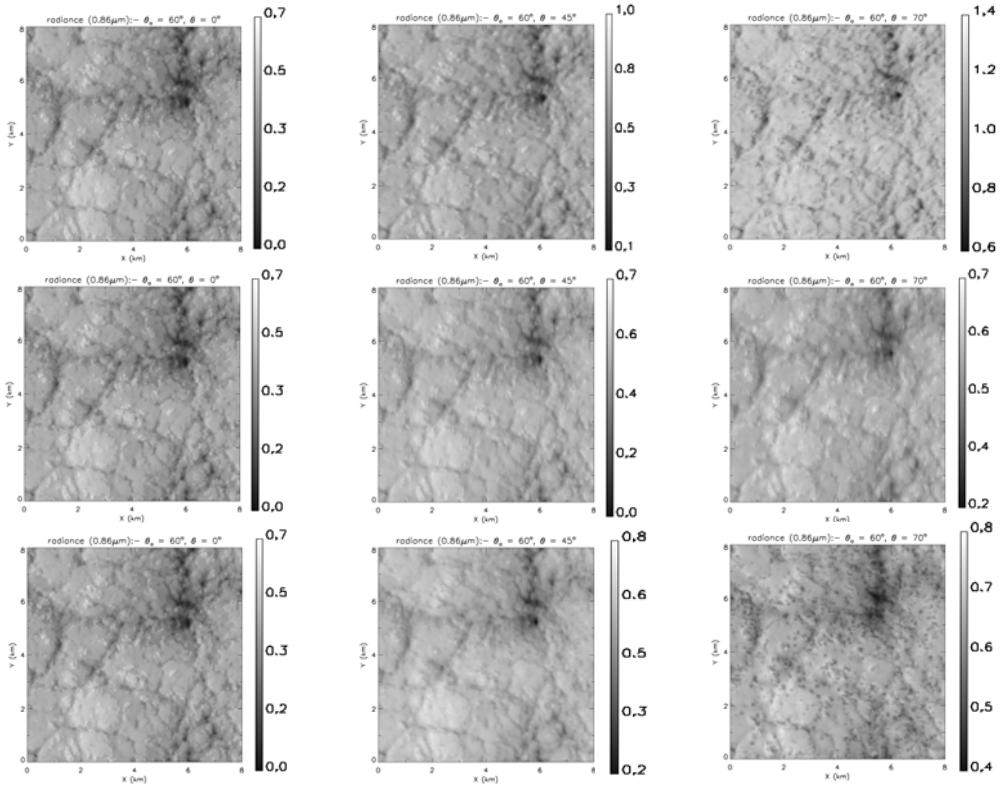

Figure 5.5. Simulated 3D radiance in forward (top row), side (middle row), and backward (bottom row) scattering direction at 0^o, 45^o and 70^o VZAs for 60^o solar zenith angle.

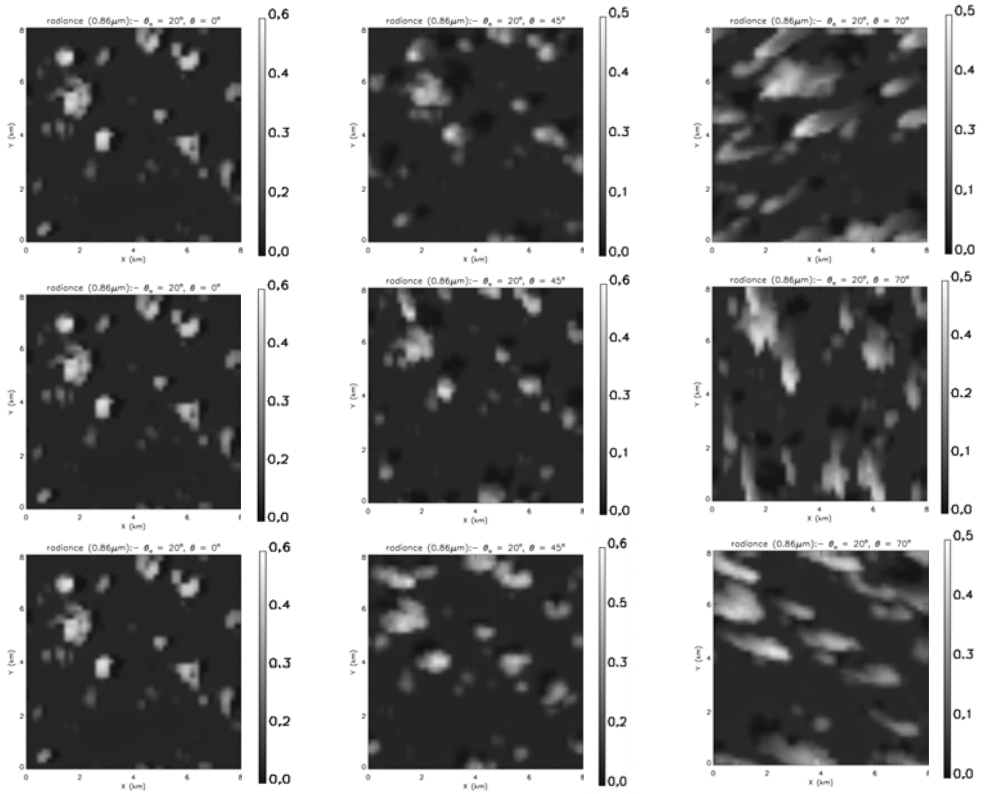

Figure 5.6. Simulated 3D radiance in forward (top row), side (middle row), and backward (bottom row) scattering direction at 0^o, 45^o and 70^o VZAs for 20^o solar zenith angle.

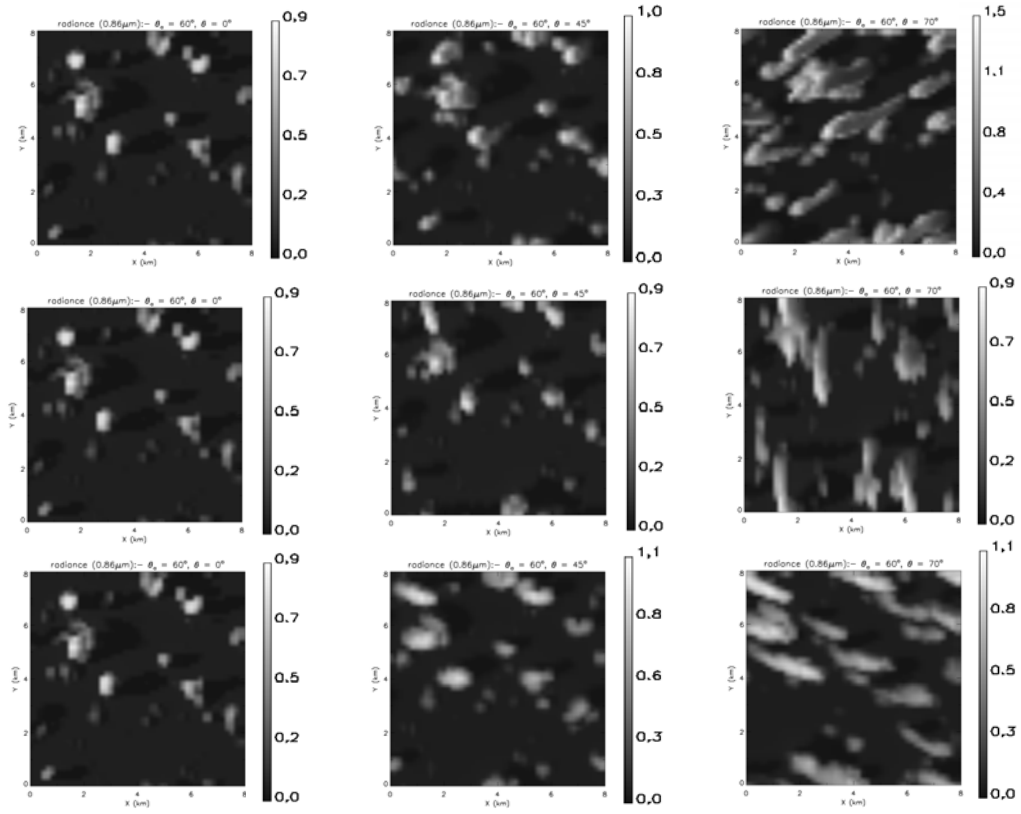

Figure 5.7. Simulated 3D radiance in forward (top row), side (middle row), and backward (bottom row) scattering direction at 0^o, 45^o and 70^o VZAs for 60^o solar zenith angle.

In the Sc field, when the Sun is fairly high (θ_o=0^o to 20^o), larger radiance is observed in the nadir view, and the radiance decreases with VZA. In other words, at high Sun, the Sc clouds appear brighter in the nadir view and darker in the oblique view, regardless of the viewing plane. This result is in agreement with the 1D concept that the 1D radiance is larger in the nadir view and decreases with VZA. However, at oblique Sun, especially at 60^o and 70^o SZA in the backscatter direction, the 3D radiance remains constant until 60^o VZA. Above 60^o (i.e., VZA of 70^o) clouds appear darker (probably because a large part of the radiance may escape through the forward scattering direction and only a single or few scattering events may exhibit in the backscatter direction); in the most forward scattering direction (in our case, a viewing azimuth of 30^o) the radiance increases with VZA, and in the very oblique view clouds appear much brighter, as shown in Figure 5.4-5.5. An explanation for this could be that the cloud field is scattering a large fraction of the radiation close to the forward direction, which is characteristic of Mie scattering. In the Sc cloud, the variability of radiance with SZA is negligible except at very low Sun of 70^o.

For the scattered Cu, a clear and very significant increase in radiance with SZA is noticed. Another striking feature is the increase of apparent cloud fraction with VZA, and is more than doubles at very oblique view, as shown in Figure 5.6-5.7. At high Sun, the 3D radiances are smaller in the oblique view compared to the nadir view, as more photons can escape from the cloudy pixels to clear neighborhoods. Compared to low Sun, smaller radiance is observed at high Sun. One reason could be the fact that the photons can easily escape from the cloudy to neighboring clear pixels, and the second reason could be that neither the shadowing nor the illumination occurs at high Sun, so there is no compensation of errors, and which is assumed to be happen in other (larger) Sun angles. Also, for low Sun (50^o, 60^o, and 70^o) the radiances increase with VZA regardless of the viewing plane. However, the increase is much higher (sometimes even doubles) for the forward scattering direction than for the backscatter direction.

5.3.2. Dependency of Radiance on Sun-view Geometry

In the previous section, we discussed the spatial variability of radiances. In this section, we describe how the corresponding domain mean simulated 3D and calculated 1D reflectance varies with respect to view geometry and solar zenith angle, especially for a thick-unbroken stratocumulus and thick-broken cumulus field, at visible and near-infrared bands.

The view angle dependence of simulated 3D and plane-parallel reflectance are shown in Figure 5.8 for homogeneous (Sc) and heterogeneous (scattered Cu) cloud fields, at VIS and

NIR wavelengths. In a plane-parallel model (*see* Figure 5.8), at high Sun 1D reflectances decrease with VZA, in the moderate Sun the reflectance show very little difference, and, for larger SZA ($\theta_o \geq 40^o$) the reflectances increase with VZA and the increase is roughly four times larger in the forward direction and twice larger in the backward direction compared to the nadir. For a Sc cloud, the view angle dependence of 3D radiances follows the plane-parallel model very well and the radiances agrees within ~5% (*refer* Figure 5.8a-b) in both VIS and NIR wavelengths, also in the forward and backward scattering direction. Similar results are obtained in *Loeb and Davies* [1997], when the plane-parallel reflectance is compared with ERBE observations.

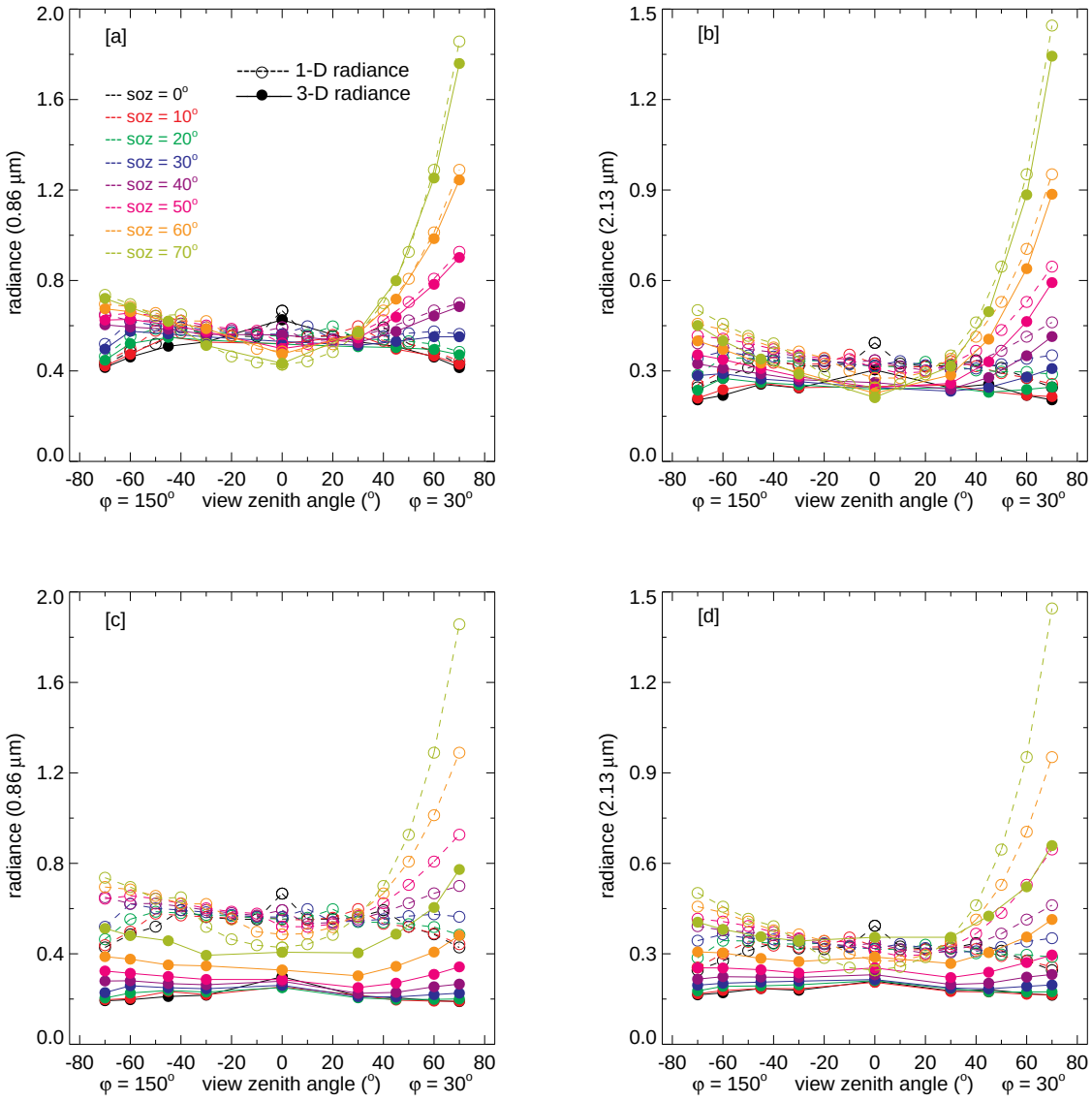

Figure 5.8. The 3D and 1D radiances as a function of VZA in the backscatter direction (φ=150°) and in the forward scattering direction (φ=30°) for different SZA: (a) VIS and (b) NIR bands for stratocumulus, and (c) VIS and (d) NIR bands for scattered cumulus.

However, for a broken Cu field, compared to plane-parallel model VIS and NIR reflectances underestimate and the underestimation is larger in the VIS compared to the NIR reflectance. This would translate into an underestimation in τ and an overestimation in r_e with the former being dominant. The view angle dependence of 3D radiances is also similar to the plane-parallel model reflectances, but less pronounced, even at the very low Sun. From the statistical analysis of a large set of MODIS observations *Varnai and Marshak* [2003] showed that in oblique backscatter directions, cloud reflection is stronger than the 1D theory would predict. However, we haven't seen any such great difference in the 3D radiance at backscatter direction even for thick-broken Cu field. This is because they used 250 m pixel level data, which is much finer resolution than our ~9 km domain mean values.

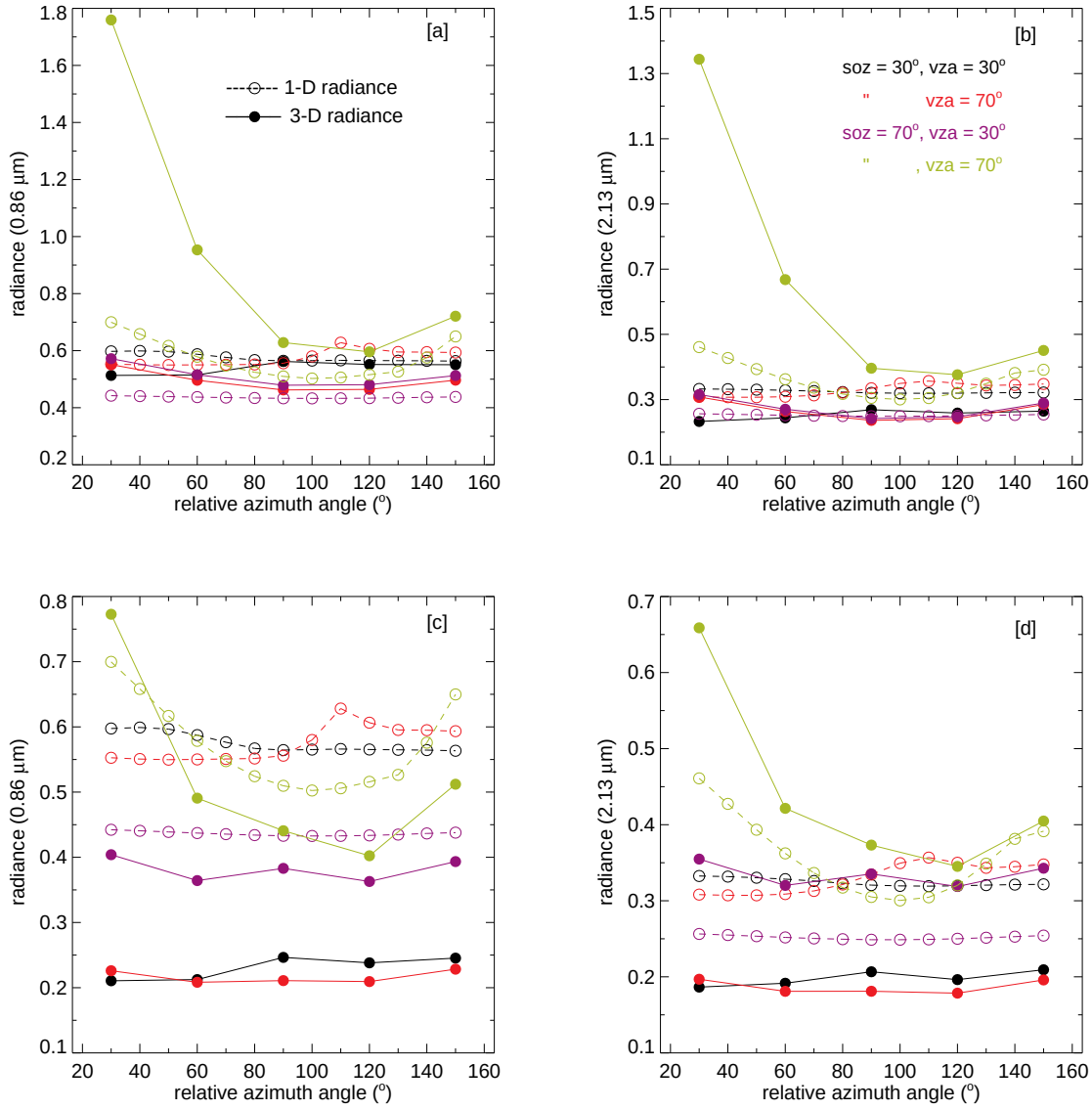

Figure 5.9. The 3D and 1D radiances as a function of relative azimuth angle: (a) VIS and (b) NIR bands for stratocumulus, and (c) VIS and (d) NIR bands for scattered cumulus.

Loeb and Coakley [1998] examined the validity of plane-parallel theory for cloudy atmospheres by directly comparing calculated and observed VIS reflectance from AVHRR observations of marine stratus cloud layers off the coasts of California, Peru, and Angola. When the 1D reflectance is directly compared with the observations at different view angles, relative differences are generally smaller (≤10%) in the backscatter direction for solar zenith angles below 60^o and show no systematic view angle dependence. In the forward scattering direction, the 1D reflectances increases much more rapidly with the view zenith angle than in the observed reflectances. The relative differences in the forward scattering direction are ~2–3 times larger than that in the backscatter direction. For the solar zenith angles above 60^o in the forward scattering direction, the 1D model underestimates observed reflectances at nadir view by 20–30% and overestimates at the most oblique view by 15–20%.

Figure 5.9 compares the 3D and the plane-parallel reflectance as a function of view azimuth angle φ. For moderate Sun the plane parallel model appears to provide a reasonable representation of radiances for the Sc field even at side and oblique views, and the relative difference is within 20%. At very low Sun, side views exhibits very good agreement between the plane-parallel and the 3D reflectances, however for very oblique view both VIS and NIR 3D radiances are larger compared to the plane-parallel, and 2-3 times larger in the forward scattering direction, and agrees within 20% in the backscatter direction. For the broken Cu cloud at moderate Sun, the 3D radiances underestimate the plane-parallel by 2-3 times in the VIS and by 1-1.5 times in the NIR wavelengths. However, at low Sun a 10% underestimation in the 3D visible radiance is compensated by a 10% overestimation in the NIR radiance compared to the plane-parallel values. One can also note that the influence of 3D effects goes in the other direction for the droplet effective radius and for the optical thickness. *Loeb and Davies* [1997] also indicated that 1D reflectances increase more rapidly with VZA than the observed reflectances in the forward scattering direction at low Sun elevations but show similar VZA dependence in the backward direction. In agreement to our findings, *Dagestad* [2005] also found that for a typical Sc cloud the radiance is mainly unaffected by rotating the clouds in the azimuth direction when the pixel size is 3.5 km, however, for a typical 6.7 km Cu field he observed some variability in the radiance while rotating.

We have also evaluated SZA dependence of the 3D and the 1D radiances and are shown in Figures 5.10-5.11. In general, both VIS and NIR radiances from a plane-parallel model decrease for moderate to large SZAs for all the viewing angles except for the very oblique views, where it increases with SZA. For the Sc field, at nadir view the 3D radiance also show a decrease from moderate to larger SZA, in agreement with the plane-parallel

radiance in both forward and backward scattering directions. For all other viewing angles, the 3D radiances increase with SZA and the increase is atleast 4 times larger in the forward scattering direction and is 10-20% larger in the backscatter direction. A slight underestimation in the 3D radiance is noticed at high Sun compared to the 1D radiance.

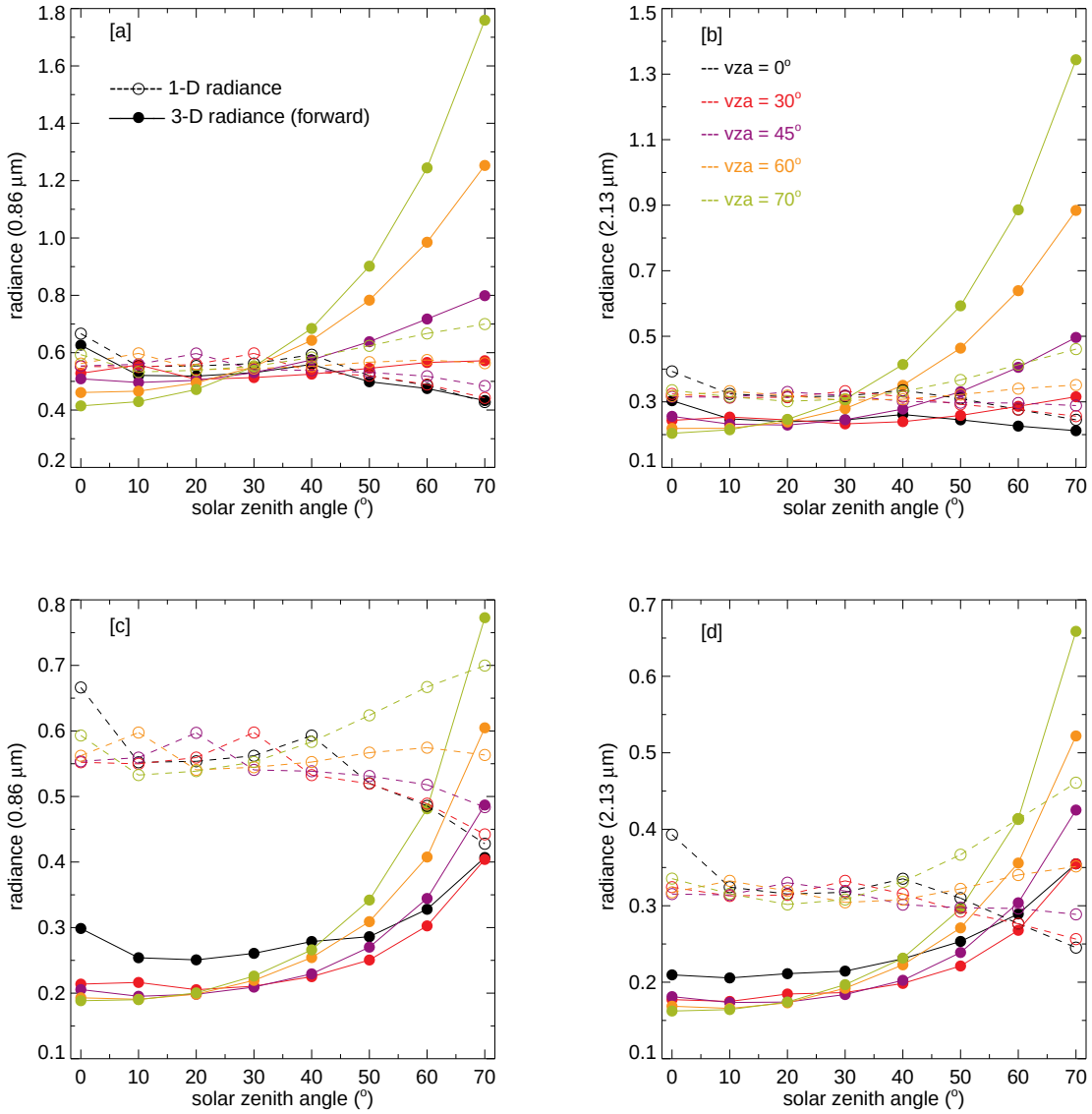

Figure 5.10. The 3D and 1D radiances as a function of SZA: at (a) VIS and (b) NIR wavelengths for the stratocumulus and at (c) VIS and (d) NIR wavelengths for the scattered cumulus, in the forward scattering direction.

However, for the broken Cu field, the 3D radiance is 2-3 times smaller in the VIS and 40-50% smaller in the NIR radiance compared to the plane-parallel radiance, for the solar zenith angle $\leq 60^{o}$. For very oblique Sun, the 3D radiance is in agreement at backscatter radiance, and overestimate at forward scattering direction in compared to the plane-parallel

radiance. The difference in the 3D radiance from the 1D is shown to be explainable by cloud side illumination as well as by the presence of structured cloud tops. Our results are qualitatively consistent with the observational results of *Loeb and Davies* [1996] and *Loeb et al.* [1997] and highlight the importance of 3D cloud effects.

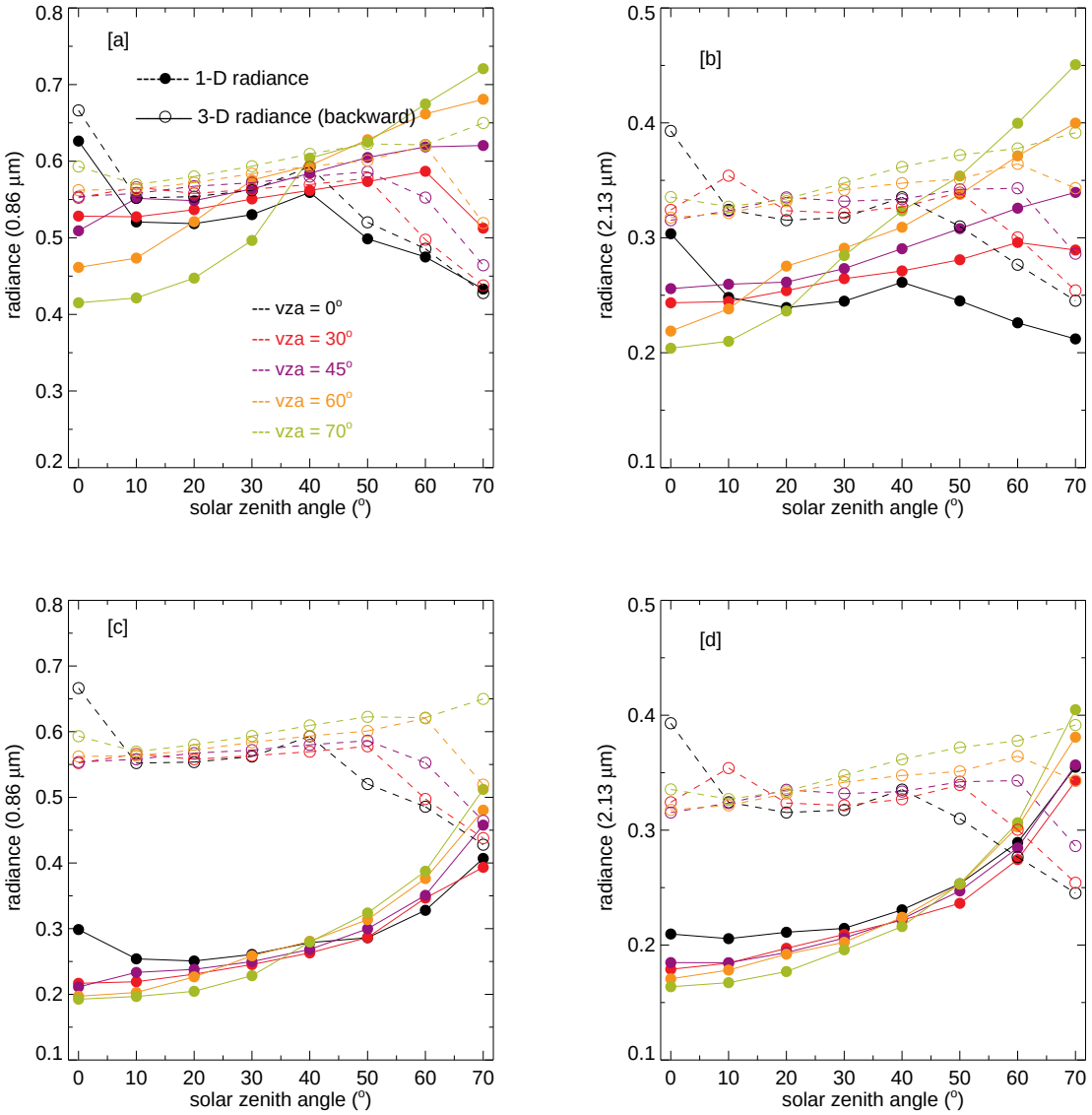

Figure 5.11. The 3D and the 1D radiances as a function of SZA: at (a) VIS and (b) NIR wavelengths for the stratocumulus and at (c) VIS and (d) NIR wavelengths for the scattered cumulus, in the backward scattering direction.

5.3.3. Overview of Heterogeneity Parameters

One can use different measures to study the cloud heterogeneity effects in satellite cloud retrievals. The possible factors that can cause heterogeneity in a cloud field could be horizontal variability of LWP, cloud-top-variability, variability in cloud optical thickness,

droplet effective radius, fractional cloud cover, etc. We evaluate the cloud heterogeneity effects in retrieved cloud properties with three different heterogeneity measures, namely χ to represent within-cloud heterogeneity, σ_{CTOP} to represent the cloud-top-variability, and H_σ to compute the radiative smoothing/roughing factor. A brief discussion of these heterogeneity measures is given below.

(a) Within-Cloud Heterogeneity (χ parameter)

The inhomogeneity parameter χ, first introduced by *Cahalan et al.* [1994], is defined as the ratio of logarithmic and linear average of cloud optical thickness distribution, $\chi = \frac{e^{\overline{\ln\tau}}}{\bar{\tau}}$. This χ parameter can be calculated, in our case, from both LES true and retrieved τ. In general, χ varies from 0 to 1, and the larger the χ values the more homogeneous the scene is. The χ parameter is calculated for individual cloud scenes at their domain size. A comparison of the χ parameter calculated from true *versus* retrieved τ is shown in Figure 5.12. The retrieved χ values are larger than the true χ values at high Sun. However, at low Sun, the retrieved χ values are much smaller than the true χ. When the Sun is above 60^o zenith the retrieved χ values underestimate the true χ due to cloud shadowing and illumination effect. Thus, in the 1D retrievals the clouds appear more homogeneous at high Sun and more heterogeneous at low Sun than the real cloud. However, the use of this parameter brings out the details of horizontal cloud heterogeneity (i.e., how the liquid water path is distributed within a pixel/cloud) of a given cloud field. *Cahalan et al*. [1994] disputes that in-cloud variability leads largest error in calculated albedo, especially when the cloud fraction errors are smaller, and therefore it is important to address the related 3D errors.

Studies such as *Oreopoulos and Cahalan* [2005] and *Seethala and Horvath* [2010] used this χ parameter to study the cloud heterogeneity and reported as a useful parameter to separate the heterogeneity. *Oreopoulos and Cahalan* [2005] found that the cloud heterogeneity is weaker in summer than in winter. *Seethala and Horvath* [2010] also found that the summer hemisphere is more homogeneous than the winter hemisphere. In this study, we have utilized this χ parameter to study the cloud inhomogeneity and found that this parameter effectively separate the cloud heterogeneity. In our data χ varies from 0 – 1 and the first one-third of our total cloud fields show $\chi < 0.85$ and are assumed as more heterogeneous scenes. The last one-third of the data show $\chi > 0.95$ and are considered as more homogeneous scenes.

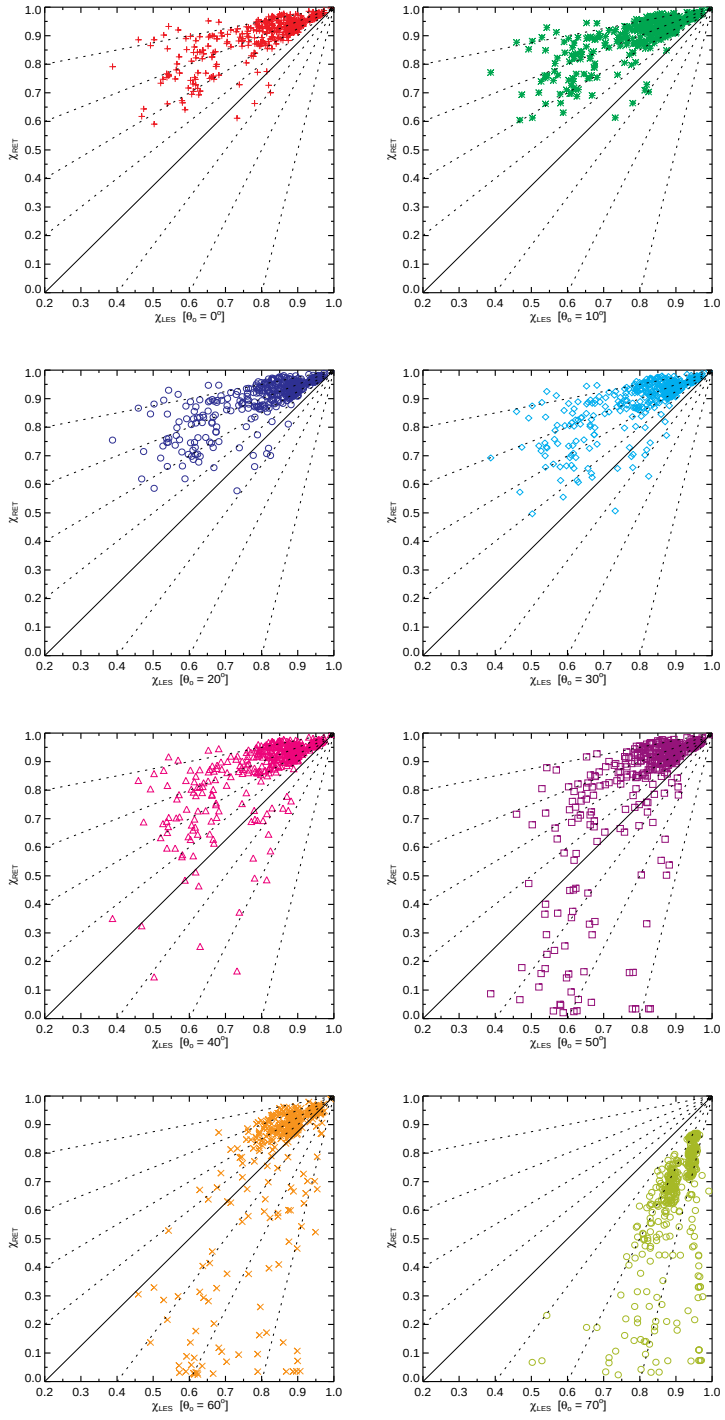

Figure 5.12. scatterplot of χ calculated from true and retrieved τ for different solar zenith angles.

(b) Cloud-top Variability (σ_{CTOP})

Since the original cloud fields are simulated by LES, it is easy for us to calculate the actual cloud top height and its variability within the cloud field. The top most layer of grid cell with LWC above 10 g m^{-3} is assumed as cloud top height. The standard deviation (σ_{CTOP})

is computed for individual scenes from the grid cells. This parameter can separate clouds with flat cloud top from the ones with more cloud top variability. Indeed, σ_{CTOP} provides the information about cloud-top-variability of individual cloud scenes. Our clouds have cloud top variability ranging from a few meters to 1 km. The clouds with $\sigma_{CTOP} < 30$ m (which holds first thrice of our data) are consider as more homogeneous clouds and clouds with $\sigma_{CTOP} >$ 100 m are consider as more heterogeneous clouds. However, *Varnai and Marshak* [2007], asuming a 6 K/km vertical temperature gradient, showed 50–80 m and 180–250 m altitude changes over 1 km horizontal distance for the homogeneous and heterogeneous thresholds, respectively, for the MODIS observations.

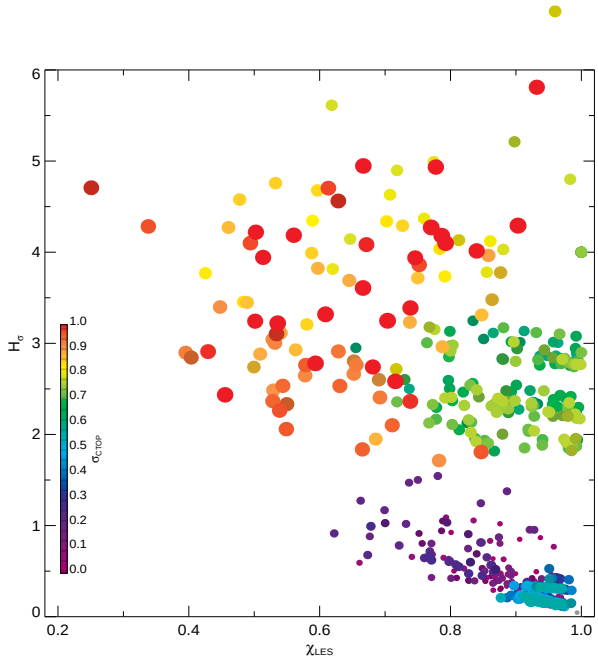

Figure 5.13: The relationship between different inhomogeneity parameter χ, H_σ, σ_{CTOP}

(c) Radiative Smoothing/Roughing (H_σ)

Another important heterogeneity parameter is H_σ proposed by *Liang et al*. [2009], calculated from 0.86 µm radiance measurements. $H_\sigma = \sigma / R$, where R and σ are the mean and standard deviation of 0.86 µm radiance calculated from 1 km pixels for the individual cloud scenes. The assumption is that homogeneous clouds would look radiatively smoother, with smaller values of H_σ, and clouds with larger cloud-top-variability would be rough and indicated by larger H_σ. The values of H_σ can probably have some impact on the solar zenith angle. Clouds can appear smoother under high Sun due to a net horizontal transport of sunlight from thicker to thinner regions [*Zuidema and Evans,* 1998], whereas they can appear

rougher for low Sun due to the cloud illumination and shadowing of cloud sides [*Varnai and Marshak,* 2003]. Regardless of this, when comparing regions under the same solar zenith angles larger values represent more heterogeneous clouds and smaller values represent more homogeneous/smoother clouds. *Girolamo et al*. [2010] evaluated this parameter and quoted this as a most useful parameter to separate the cloud heterogeneity. They also noticed that the summer hemisphere appearing much more locally homogeneous compared to the winter hemisphere, although which could be due to the solar zenith angle effect on H_σ.

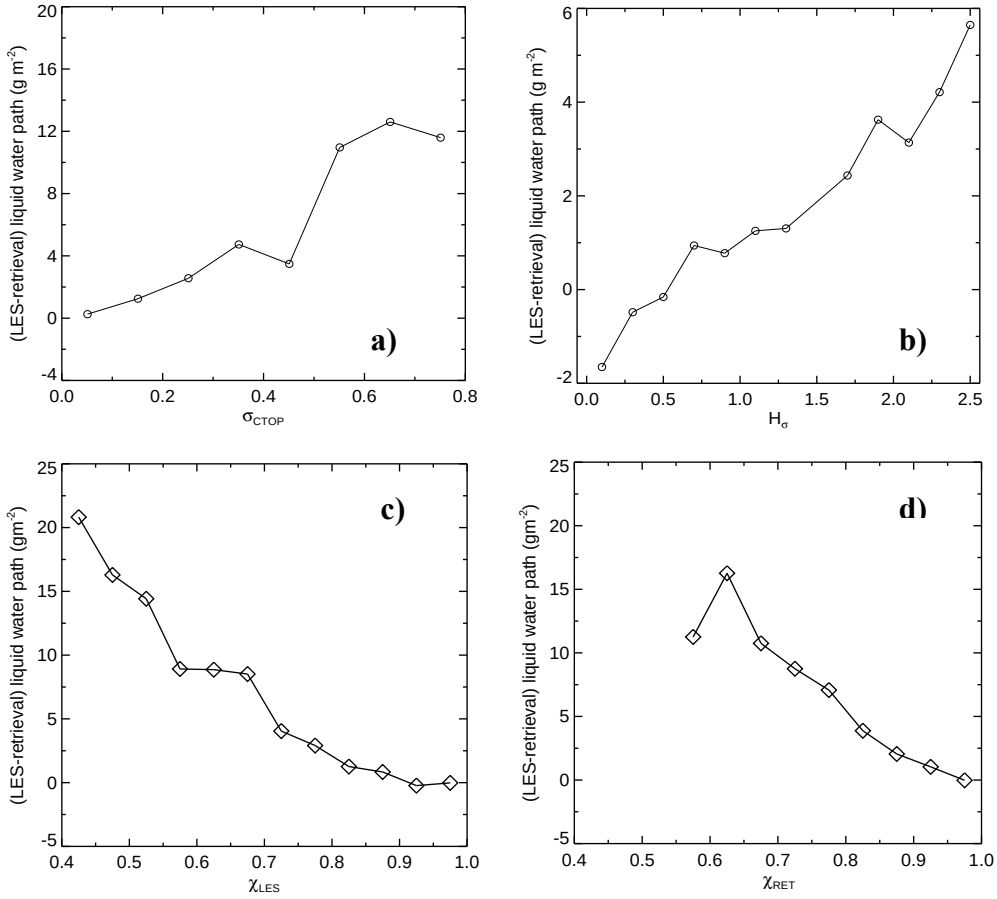

Figure 5.14. The absolute bias in LWP as a function of different heterogeneity parameter (a) H_σ, (b) σ_{CTOP}, (c) χ_{LES}, and (d) χ_{RET}.

(d) Relationship b/w Heterogeneity Parameters

The relationships between all three heterogeneity parameters have been examined. Figure 5.13 shows the scatter-plot of χ (calculated from LES) *versus* H_σ. The color and size of the circles determines σ_{CTOP}. Smaller circles represent clouds with less cloud-top-variability, and bigger circles represent larger cloud-top-variability. Thus χ ranges from 0.2 to

1. H_σ vary from 0 to 6. σ_{CTOP} varies from few meters to 1.2 km. It is evident from the figure, that all three parameters are able to discriminate the homogeneous and the heterogeneous clouds very well. The bias in LWP, τ, and r_e are evaluated independently based on these parameters, and shown in Figure 5.14. The homogeneous cloud scenes show smaller H_σ and σ_{CTOP} and larger χ, and the reverse holds for the heterogeneity.

From Figure 5.14 it is clear that the absolute bias in LWP increase with increasing heterogeneity. All three inhomogeneity parameters σ_{CTOP}, χ_{LES}, and χ_{RET} show a zero LWP bias in the most homogeneous bin except H_σ. The LWP bias is ± 2 g m^{-2} for $H_\sigma < 1.5$. Both LES and retrieved LWP agree very well for $H_\sigma < 1.5$, and above which the retrievals show an underestimation in LWP compared to LES. In fact, the retrieved τ agrees very well with LES τ for $H_\sigma<1.5$, and thereafter a slight underestimation of 0.5 is noticed. The retrieved r_e overestimates the LES truth by ~2 μm for $H_\sigma < 1.5$, thereafter an underestimation of 0.5 μm is noticed. Similar results are observed with all other heterogeneity parameters.

5.3.4. Pixel-Level Analysis

Our primary interest is to evaluate the domain mean retrieval biases which are essential in climate modeling perspective; however, it is also important to study the bias in individual pixels. Thus, in this section, we evaluate how the biases in retrieved cloud properties distribute on a pixel-level basis. The frequency histogram of bias and relative bias in the retrieved liquid water path for both the most homogeneous and the most heterogeneous cloud scenes are shown in Figure 5.15-5.16 for both 100 m and 1 km pixel retrieval. The homogeneity of cloud scene is measured based on H_σ which shows the scene roughness from visible radiance. Clear deviation is seen between most homogeneous (first-tercile) and most heterogeneous (fourth-quarter) bias and relative bias frequency distribution. The first-tercile and fourth-quarter is selected to represent the most homogeneous and most heterogeneous scenes respectively, as our cloud scenes are dominated by homogeneous clouds. The upper limit value of H_σ for the homogeneous case is 0.22 (for 100 m pixels) and 0.26 (for 1 km pixel), and the lower limit value of H_σ used to select heterogeneous scenes is 0.48 (for 100 m pixels) and 0.58 (for 1 km pixel). The homogeneous portion of dataset resembles a narrow gaussian distribution, but negatively skewed, indicating the overestimation in retrieved LWP. The skewness (tail) towards left shows considerable increase with solar zenith angle, indicating the retrieval errors associated with the solar zenith angle. Also, the result is similar for 100 m and 1 km resolution pixels, which indicates that the retrieval resolution is less important if the clouds are homogeneous. Roughly 25% of the data lies in a relative LWP

bias of ±5% and 60% of data in relative bias of ±15%, the amount of data that falls under these bias range decreases to 15% and 40% respectively as the solar zenith angle increases to 70^o. The shape of the frequency distribution of absolute bias in LWP is more symmetric compared to that of relative bias. Around 65-70% of the data showed an absolute bias of ±10 g m^{-2} in LWP regardless of pixel resolution, and the absolute bias is also skewed towards the left admitting the overestimation in retrieved LWP for the homogeneous cloud scenes. Unlike the frequency distribution of homogeneous clouds, the bias and relative bias of heterogeneous clouds distribute differently. It seems the pixel size also plays an important role in this case. As shown in Figure 5.15 100 m pixels shows more like a gaussian distribution, centered at 0 with longer negative tail in the frequency distribution of relative bias, but fewer number of datasets fall with least relative bias compared to homogeneous clouds. In absolute bias, for the solar zenith angle 50^o, 60^o, and 70^o the number of dataset with minimum bias exceeds that in homogeneous cases. Moreover 50% of data shows a bias < ±10 g m^{-2} in 60^o solar zenith angle. This can be due to the cancellation of errors due to the shadowing and the brightening at low Sun or due to 3D cloud radiative effects.

The frequency histogram of relative difference in true and retrieved τ is provided in Figure 5.17, for most homogeneous and most heterogeneous clouds at 100 m and 1 km pixel resolution. In the homogeneous clouds the distribution (peaks) centered at 0 but skew towards larger negative values, indicating an overestimation in retrieved mean τ compared to true LES τ. *Loeb and Davies* [1996] also indicated that, the frequency distributions of cloud optical depth showed a systematic shift towards larger values with increasing solar zenith angle (θ_o), and the increase is much larger for the low Sun. The cause is traced to a fundamental flaw in plane-parallel theory applied to real clouds: the solar zenith angle dependence of model reflectance is opposite to that of the observations. Here, roughly 40–70% of data shows the relative bias within ±15%, the percentage of data with smaller bias decreased with θ_o. The results are similar for both 100 m and 1 km retrievals, indicating that the pixel size is less important if clouds are completely overcast and homogeneous. In contrast to homogeneous clouds, the frequency distribution of heterogeneous clouds is sparse and variable with a fairly large negative tail. The distribution peak shifts to the left (-10%) of 0 relative bias, and also highly depends on θ_o. The distribution peak also shifts with the retrieval resolution, which can be clearly seen in Figure 5.17a-e. Especially 1 km pixels shows different peaks with irregular distributions, however 100 m pixels follows normal distribution with peaks shifted a bit to the left of the distribution centre 0 and negatively skewed. In general, the distribution gets wider with θ_o. There is a small percentage of the data

that in both the most homogeneous and the heterogeneous clouds that show larger than 100% relative bias. The frequency histogram of absolute difference between LES and retrieved τ is shown in Figure 5.18 for different solar zenith angle. In the homogeneous clouds the distribution is symmetric and center at 0 absolute bias in all Sun angles, but with fairly large negative tail. The negative tail decreases with increasing solar zenith angle. It is also clear from the absolute bias histogram of homogeneous cloud scenes that the results are not affected by pixel size, as there is difference in frequency of only 1-2%. Overall, 60 – 80% of the data is within the absolute bias of ±1.5, and the percentage of data that falls in this bias range decrease with increasing solar zenith angle. In this case, the distribution of heterogeneous clouds also peaks at 0 absolute bias except for $\theta=70^o$, however the percentage of data which show no or less τ bias strongly depend on and increased with θ_o. The percentage of data which have nil bias in heterogeneous clouds are less than that in homogeneous clouds for high Sun (0-30^o), stays equal at medium Sun angles (40-50^o), and exceeds thereafter. There is considerable difference in frequency between 100 m and 1 km pixel is observed in certain Sun angles.

Interpreting retrieved r_e with true LES is complex in the sense that satellite retrieval of r_e at NIR is sensitive mostly to the top layer of clouds. To compare the retrieved r_e with the LES true values, we calculated r_e from LES considering only the top layer with optical thickness of 2. The frequency histogram of bias in retrieved r_e relative to LES true is shown in Figure 5.19. In homogeneous clouds, the distribution mostly peaks at relative bias 0 with the exception of 10^o and 70^o Sun angle, and is negatively skewed. Only ~40% of data show smaller relative bias within ±15%. Similar to τ, the resolution effect in r_e is also negligible when the clouds are most homogeneous. The results are further complicated when the clouds are heterogeneous. The frequency histogram of absolute bias in retrieved r_e compared to LES is shown in Figure 5.20. The most homogeneous clouds show a gaussian distribution with a frequency maximum at 0 bias only when the solar zenith angle is 0^o. In all other solar zenith angles the maxima is shifted to -1 μm bias, except 70^o in which the maxima is at +1 μm bias. Like τ, the differences are small between 100 m and 1 km pixel resolution in this case. Unlike the most homogeneous clouds, the distribution of most heterogeneous clouds show multi maxima oriented to both positive and negative side of the 0 bias.

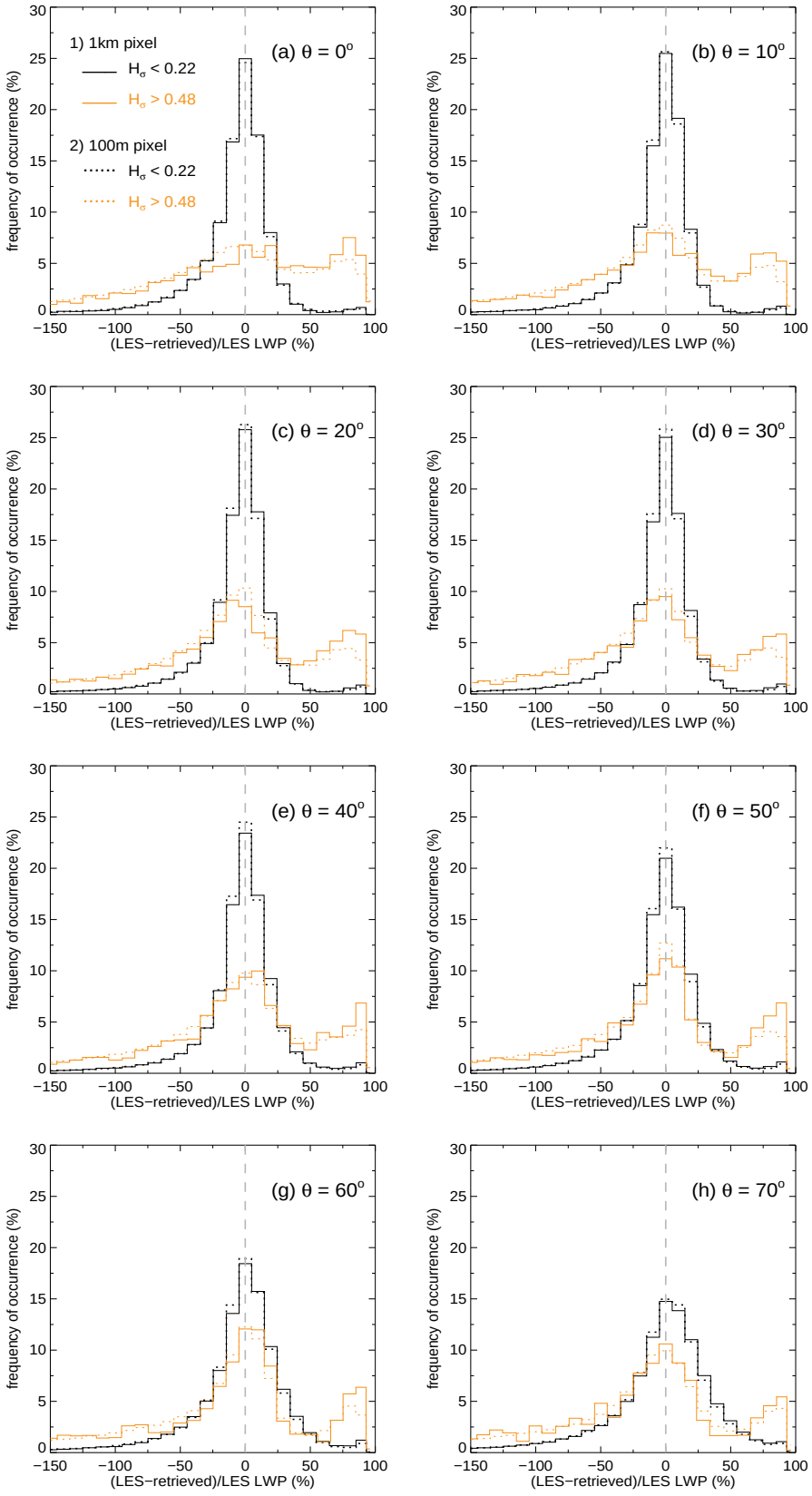

Figure 5.15. The frequency histogram of bias (%) in retrieved liquid water path (LWP) relative to LES values for different solar zenith angle.

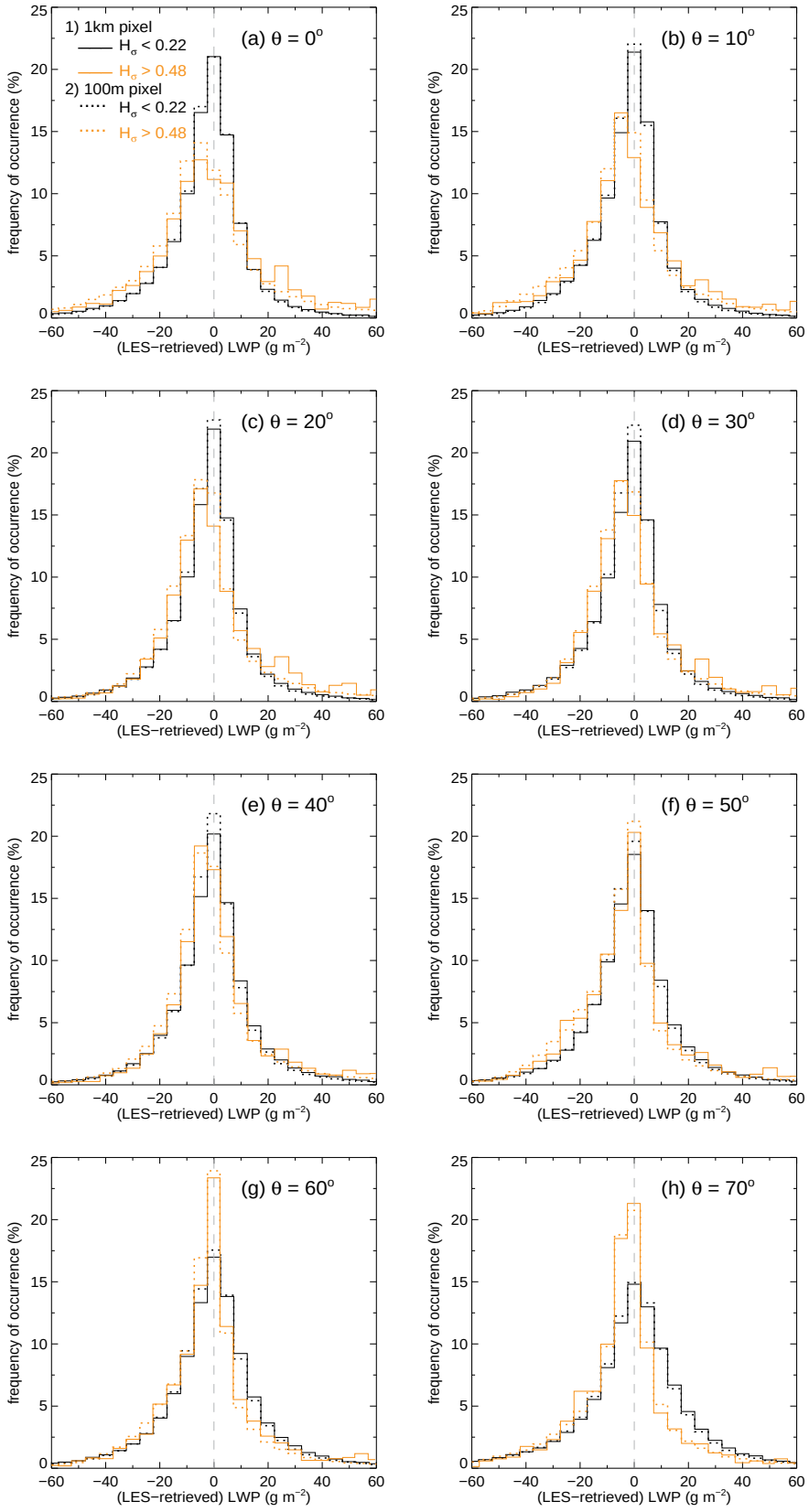

Figure 5.16. The frequency histogram of bias (%) in retrieved liquid water path (LWP) compared to LES values for different solar zenith angle.

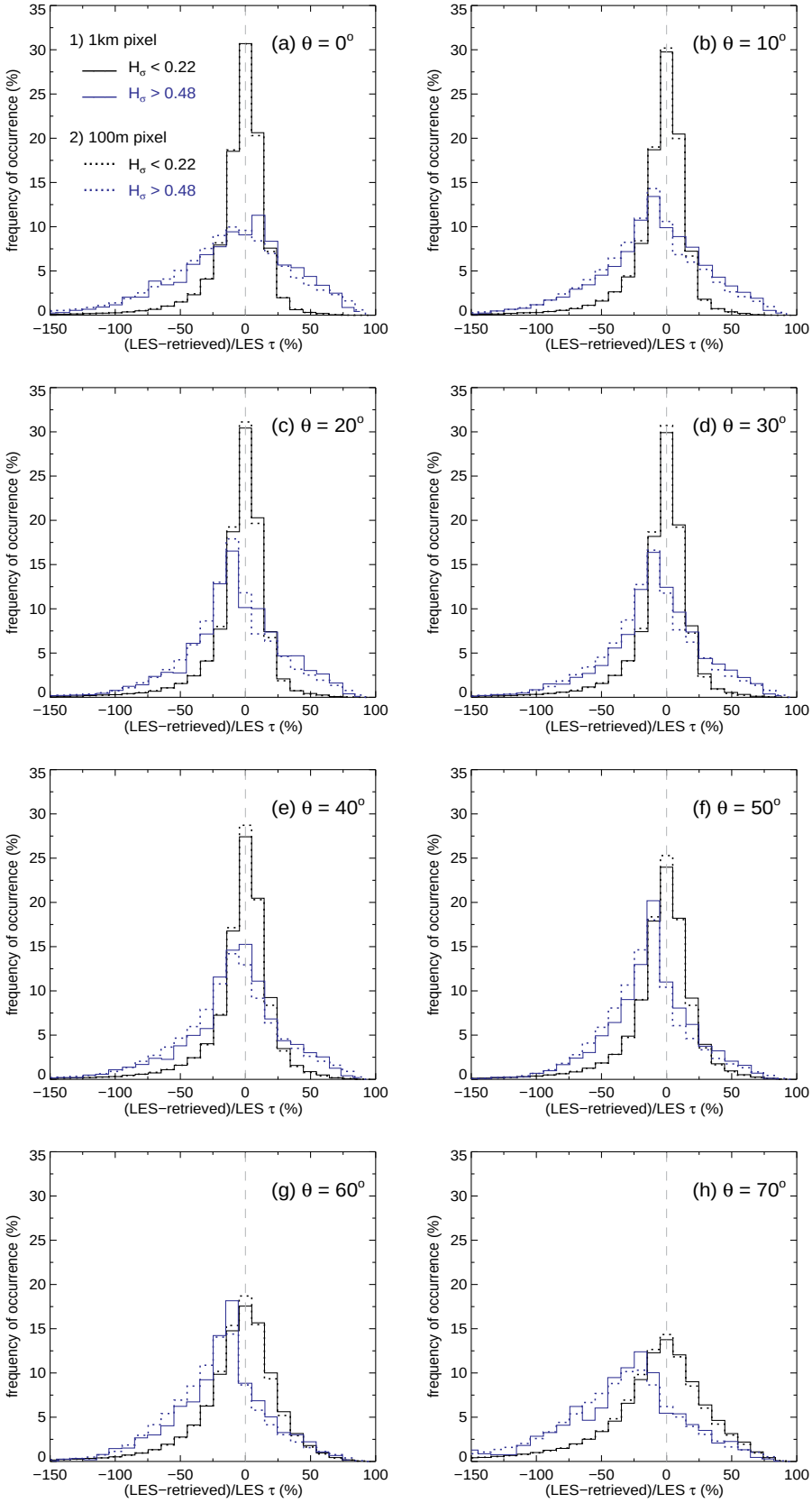

Figure 5.17. The frequency histogram of bias (%) in retrieved optical thickness (τ) relative to LES values for different solar zenith angle.

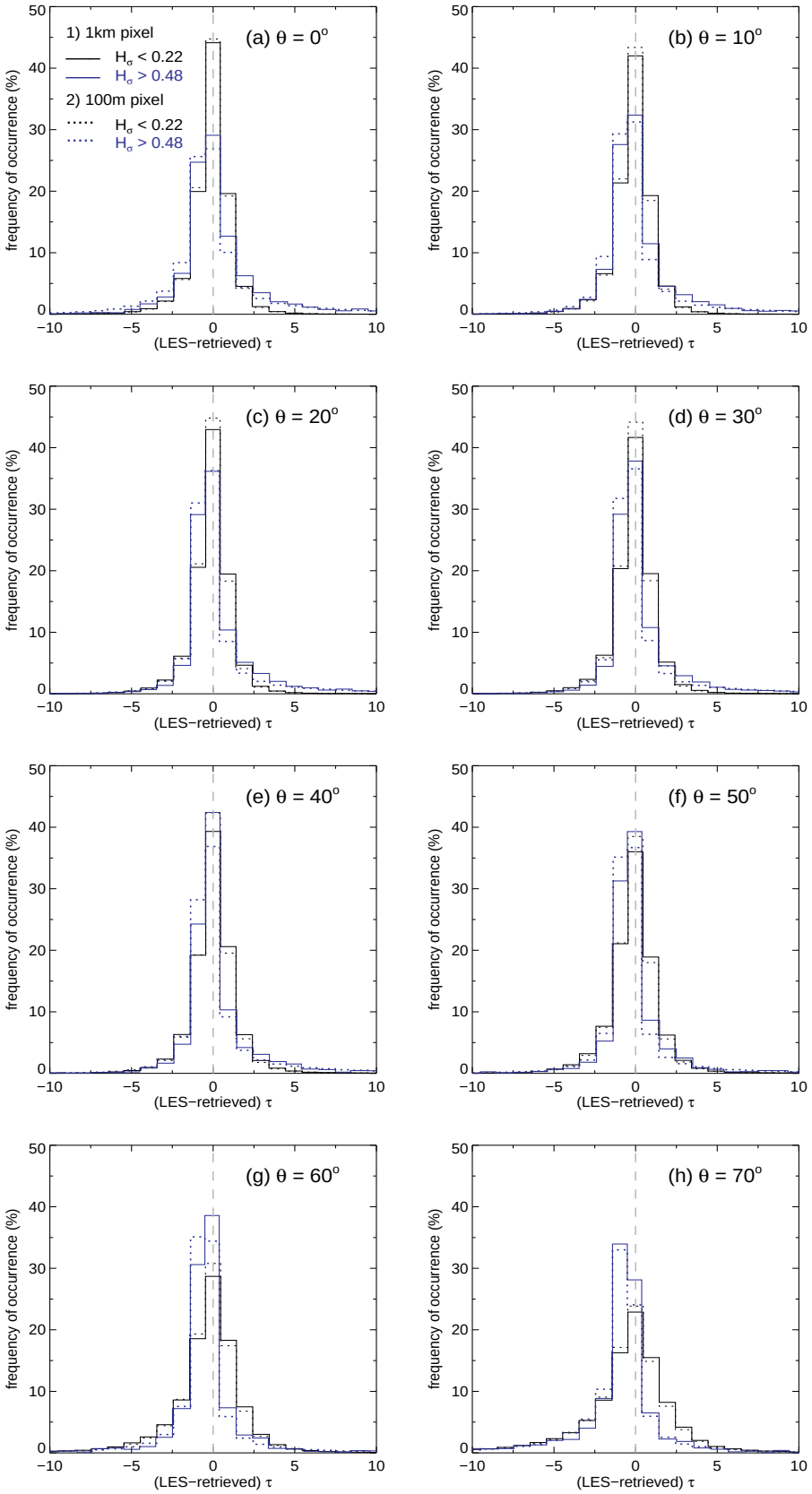

Figure 5.18. The frequency histogram of bias (%) in retrieved optical thickness (τ) compared to LES values for different solar zenith angle.

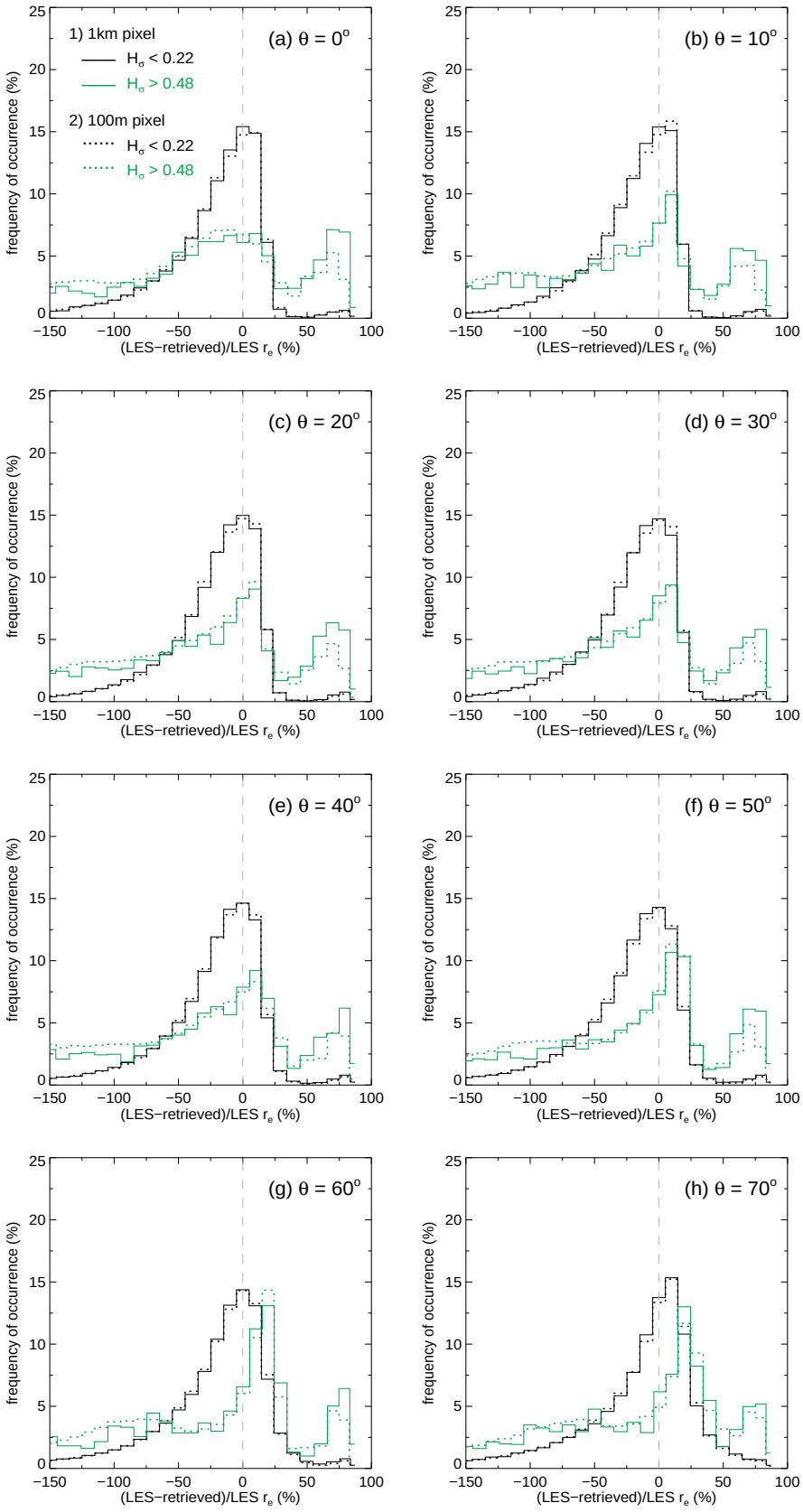

Figure 5.19. The frequency histogram of bias (%) in retrieved droplet effective radius (r_e) relative to representative LES values for different solar zenith angle.

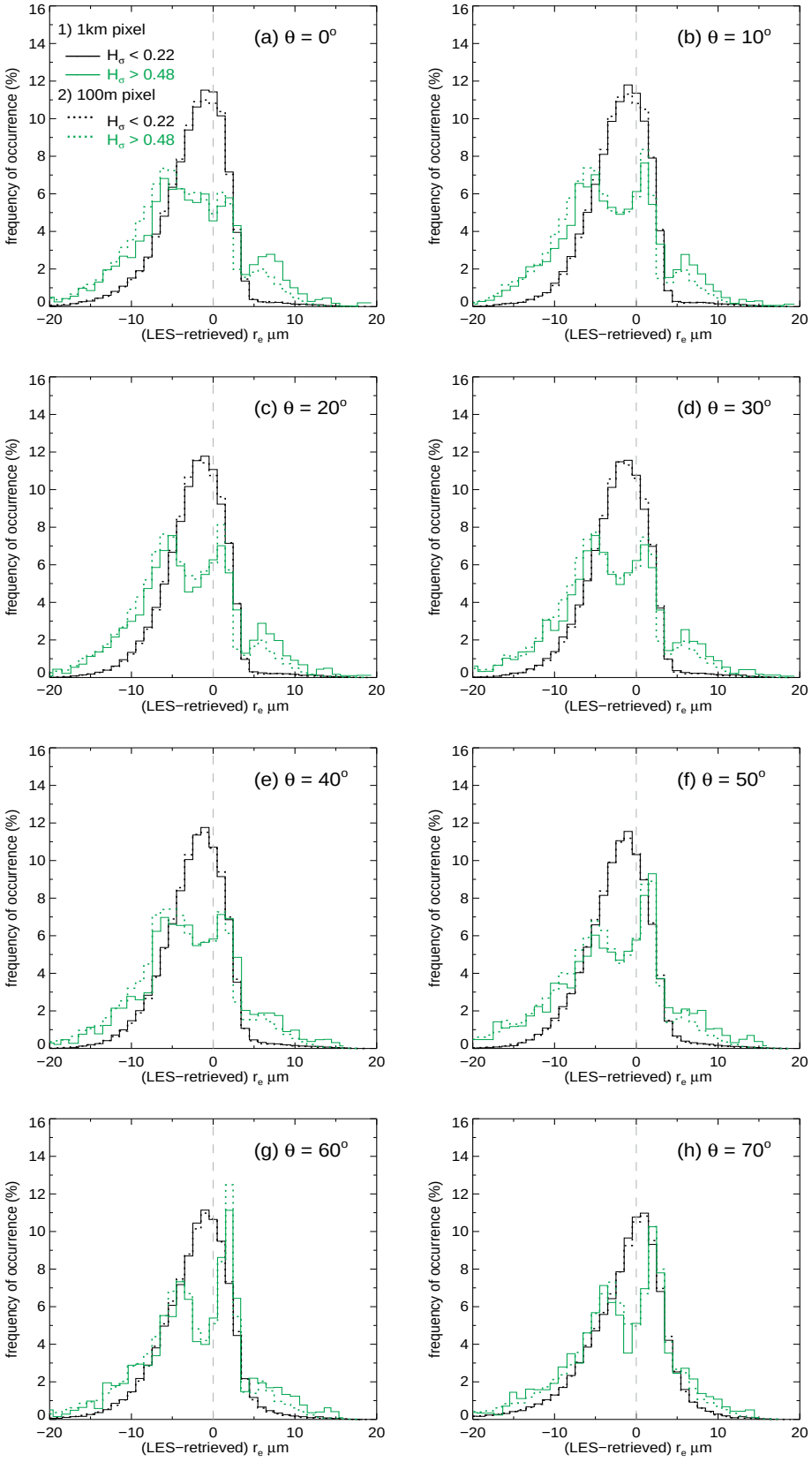

Figure 5.20. The frequency histogram of bias (%) in retrieved droplet effective radius (r_e) compared to representative LES values for different solar zenith angle.

5.3.5. Domain Mean Cloud Properties

Figure 5.21 represents the time series of in-cloud mean LES truth and retrieved cloud water path, τ, r_e of most homogeneous and most heterogeneous clouds for selected Sun-view geometry. We select here and show only very few cases of Sc and scattered Cu to represent the main features of homogeneous and heterogeneous clouds. The retrieved τ for the most-homogeneous clouds agrees very well with the LES τ in all the Sun-view geometry. The results show better agreement in both 100 m and 1 km resolution and also in the in-cloud mean and in the domain mean (figures not shown). The bias between LES truth and retrieved τ varies ~0 – 2. An overestimation in τ of ~2 is noticed at low Sun for nadir view, which follows the hypothesis of *Varnai and Davies* [1999] that the heterogeneities make it more difficult for radiation to leave the clouds in forward directions; the clouds reflect relatively large portion of the incoming solar radiation toward the zenith for oblique than for overhead Sun [*Loeb and Davies*, 1996; *Loeb and Coakley*, 1998; *Varnai and Davies*, 1999]. The difference from the 1D case is shown to be explainable by cloud side illumination as well as by the presence of structured cloud tops. Cloud sides enhance the amount of incident solar radiation intercepted by cloud, allowing more radiation to be scattered upward in the nadir direction. Structured cloud tops change the slope of illuminated cloud top surfaces, such that nadir reflectance at low solar elevations increases with the slope of the illuminated surface. For simple cloud geometries the two effects make equivalent contributions to the increase in nadir reflectance with solar zenith angle. While this increase is most pronounced for vertically extensive broken cloud fields, it also affects reflectance from overcast cloud fields with bumpy cloud tops. Thus the observed solar zenith angle bias in cloud optical depth for the general cloud scene is likely also occurs for extensive overcast cloud fields. However, large discrepancies are observed in the scattered Cu. In most of the cloud fields a strong underestimation (~10-25) in the retrieved τ regardless of viewing and scattering angles is seen. This is possible because, when the clouds are broken, the radiation can escape from the cloudy to clear pixels, or, thicker to thinner pixels, and results less photon available to backscatter. However, at low Sun for nadir view the agreement is somewhat better. The agreement strongly depends on the level of scene heterogeneity. For the homogeneous clouds the retrieved r_e overestimates 2-4 μm compared to the true LES r_e. Similar overestimation is observed in operational MODIS r_e at 2.1 μm retrievals, and probably due to the fact that the 2.1 μm channel samples the top layer of the cloud and results overestimation in clouds (Sc) with adiabatic r_e profile [*Seethala and Horvath*, 2010; *Zhang and Platnick*, 2011]. For the heterogeneous clouds, the retrieved r_e strongly underestimate, except for the nadir view.

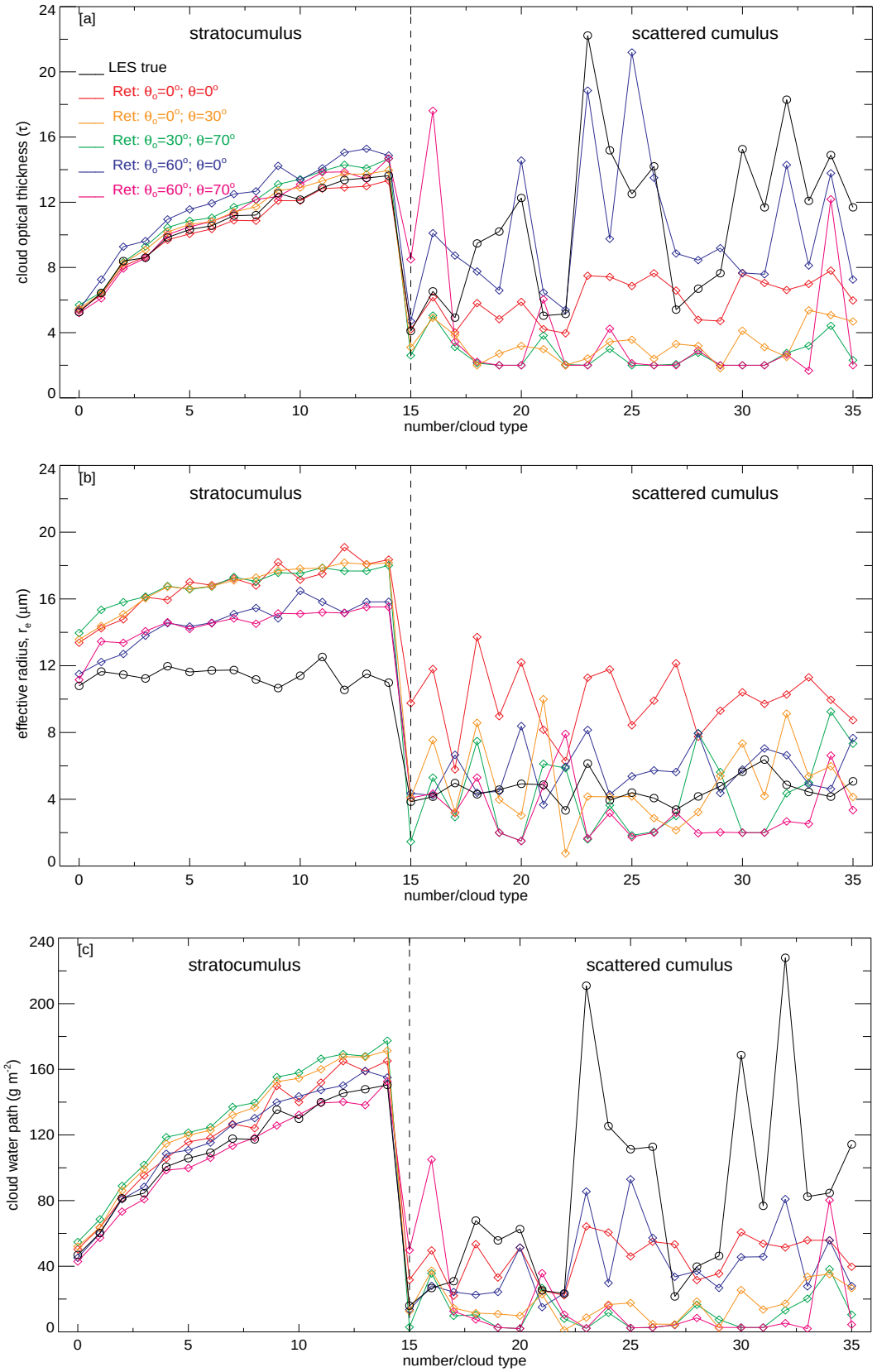

Figure 5.21. Time series of in-cloud mean LES truth and retrieved (a) cloud optical thickness, (b) effective radius, (c) LWP for few cases of Sc (homogeneous) and Cu (heterogeneous) in different Sun-view geometry for backscatter direction (1 km retrievals).

With a similar study as ours, *Kato et al*. [2006] reported that, the retrieved cloud optical thickness averaged over all pixels is high for the overcast cloud, and low for the non-overcast clouds. The magnitude of relative error in the retrieved domain-averaged optical thickness and effective radius increased with heterogeneity. Much of the observed error in the retrieved optical depth and particle size values at the nadir view for Cu can be ascribed to cloud brokenness at scales smaller than the 1 km pixels used in the retrievals. In the extreme case of the Cu scene, for which the retrieval errors are the largest, approximately 90% of the 1 km nadir view pixels are only partially filled by clouds. The underestimation of the optical thickness leads to overestimation of the particle size in the retrieval. Inaccurate treatment of cloud inhomogeneity in the radiative transfer computations contributes to retrieval errors for both partly cloudy and overcast pixels. A wellknown aspect of this mistreatment is the averaging of nonlinear reflectance function values within a pixel, which causes the retrieved optical thickness to be small [*Zuidema and Evans*, 1998; *Oreopoulos and Davies*, 1998]. Error also results because the retrieval algorithm is unable to account for the radiative transport that occurs between neighboring pixels with different scattering coefficients in the true 3D processes.

Finally, the retrieved LWP is in better agreement with the LES true cloud water path, especially for thick homogeneous clouds. The bias is within ±20 g m^{-2} (~15% relative bias). For the heterogeneous clouds, an underestimation in LWP is observed regardless of the Sun-view geometry. The bias is comparably smaller at low Sun and for nadir view, which is due to the good agreement in τ between retrieval and LES at this Sun-view geometry.

5.3.6. Scale Effect on Retrievals

We compare the statistics of domain mean LES true cloud properties with cloud properties retrieved at 100 m and 1 km resolution. While considering all the cloud scenes, the domain mean τ is 3 in both LES and retrieval. The mean r_e is 6 μm in LES and the retrieved r_e overestimate to 7 μm. The domain mean LWP is 31 g m^{-2} in LES, which reduces to 29 g m^{-2} in the retrieval. The retrieved τ bias relative to true τ is 15%, the relative bias in r_e stays within 1%, finally ~25% relative bias is observed in LWP compared to the LES values. The scale effect: The retrievals at high (100 m) and low (1 km) resolution do not show much difference in domain mean cloud properties. A small reduction in relative bias followed by an increase in rms is noticed in 1km retrieval compared to the 100 m retrievals. Consequently, correlation coefficient shows a minor decrease in 1 km than high resolution retrievals. The changes are larger for LWP compared to τ. *Varnai and Marshak* [2003] indicated that the

asymmetries caused by 3D effect can be eliminated from MODIS retrievals with the resolution of ~10 km, but not other consequences of 3D effects. Similarly, *Dagestad* [2005] also noticed a 100% variance in reflectance in a high-resolution run of few meters and no variance at ~4 km resolution for the same scene with different orientation.

Table 2. Domain mean statistics of cloud properties for all scenes.

ALL	100 m retrieval			1 km retrieval		
	τ	r_e (μm)	LWP (g m^{-2})	τ	r_e (μm)	LWP (g m^{-2})
LES	3	6	31	3.5	6	31
Retrieved	3	7	29	3	7	29
Relative Bias	15%	1%	25%	15%	-2%	24%
rms	0.4	1	4	0.5	1.4	6
correlation	0.99	0.98	0.99	0.98	0.97	0.98
No. scenes	622			640		

While considering the fully overcast clouds the domain mean τ increase to 6 in both the LES and in the retrieval. The mean r_e is ~12 μm in LES and 13 μm in retrieval, which results 10% overestimation in retrieved r_e. The mean LWP ranges 56-58 g m^{-2} in LES and 57-60 g m^{-2} in the retrieval. A 5% increase in LWP is observed which is mainly due to the overestimation in r_e. An unbiased τ is retrieved in this case, however 12-15% relative bias is seen in r_e and 1.5-3% in LWP. Very good correlation above 0.99 is observed in τ and LWP, and somehow correlation breaks in r_e. The scale effect is also less important in this case.

Table 3. Domain mean statistics of cloud properties, for overcast scenes only.

CF ≥ 95%	100 m retrieval			1 km retrieval		
	τ	r_e (μm)	LWP (g m^{-2})	τ	r_e (μm)	LWP (g m^{-2})
LES	6	12	56	6	12	58
Retrieved	6	13	57	6	13.5	60
Relative Bias	0.27%	-12%	-1.5%	-1%	-15%	-3%
rms	0.19	1.2	2.2	0.23	1.4	2.7
correlation	0.99	0.13	0.99	0.99	0.31	0.99
No. scenes	239			207		

In broken clouds, the domain mean cloud properties are smaller due to the averaging of clear and cloudy pixels. A 65% underestimation in the retrieved LWP is observed in compared to the LES truth, which is due to the underestimation in the retrieved optical

thickness. A 45% underestimation in domain mean τ and 10% underestimation in r_e are observed.

Table 4. Domain mean statistics of cloud properties for broken scenes.

CF ≤ 50%	100 m retrieval			1 km retrieval		
	τ	r_e (μm)	LWP (g m^{-2})	τ	r_e (μm)	LWP (g m^{-2})
LES	0.9	1.3	7	1	1.3	9
Retrieved	0.5	0.9	3	0.6	1.	3
Relative Bias	35%	26%	59%	34%	20%	56%
rms	0.4	0.5	4	0.6	0.6	7
correlation	0.75	0.77	0.72	0.65	0.74	0.58
No. scenes	277			283		

5.3.7. Cloud Fraction Dependency of Biases

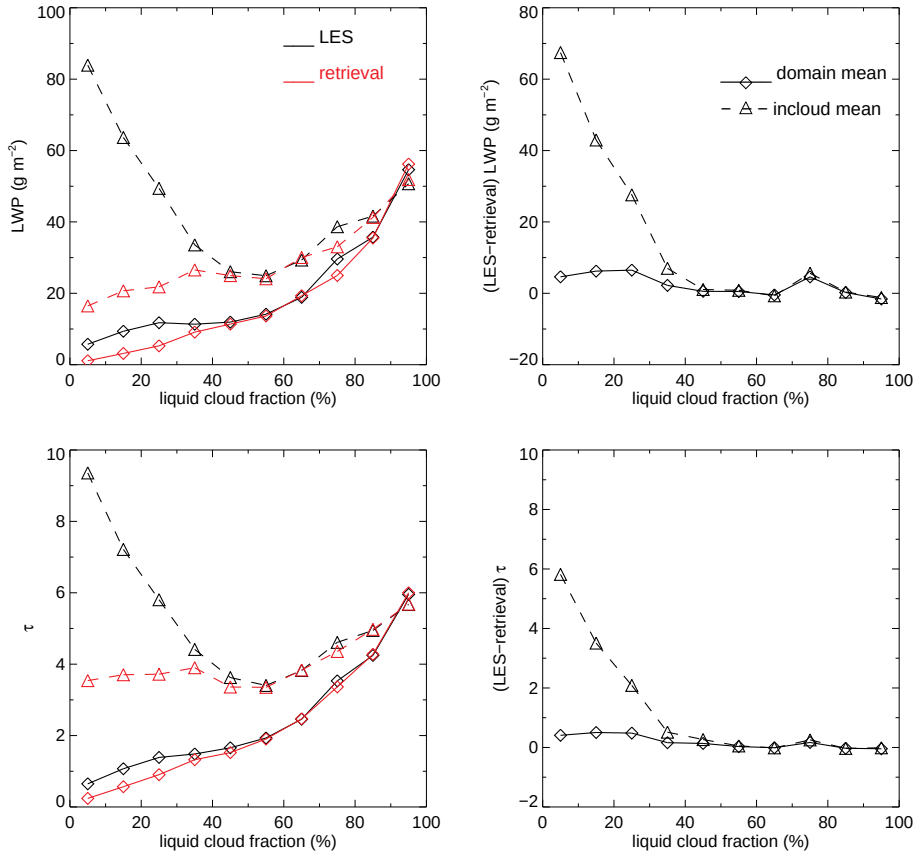

Figure 5.22. Cloud fraction dependency of LES and retrieved within-cloud and domain mean cloud liquid water path, optical thickness, and their biases (1km retrievals).

Due to the non-linear relationship between radiance and optical thickness, the cloud property retrievals are strongly depends on cloud fraction within the pixel. Cloud fraction dependency of τ and LWP retrieved at 1 km resolution are shown in Figure 5.22 for both domain mean and within-cloud mean values. The τ, r_e and LWP increases with increasing cloud fraction in domain mean cases. In general very good agreement is seen between LES and retrieved τ and LWP above 50% cloud fraction. Below 50% cloud fraction slight underestimation in domain mean τ and LWP and a stronger underestimation in within-cloud mean τ and LWP are observed. In contrast, the retrieved effective radius overestimate above 40% cloud fraction and underestimate below which.

5.3.8. Sun-view Geometry Dependence

(a) Solar Zenith Angle Dependence

Indeed, previous studies found systematic SZA-dependent biases in 1D plane-parallel cloud optical thickness retrievals. Based on ERBE observations, *Loeb and Davies* [1996] noted an increasing overestimation in nadir-view cloud optical thickness at higher SZAs, particularly above 60º. *Loeb and Coakley* [1998] obtained similar results in AVHRR measurements even for marine Sc, which is arguably the closest to being plane-parallel. The strong increase in optical thickness was traced back to the fact that the plane-parallel model reflectances, on average, decreased with SZA, while observed reflectances increased. The hypothesis that this discrepancy was due to neglected 3D effects, such as cloud side illumination and bumpy cloud tops were later confirmed through Monte Carlo simulations by *Loeb et al*. [1998] and *Várnai and Marshak* [2001]. The above studies only considered near-nadir views; however, *Várnai and Marshak* [2007] found similarly strong SZA-dependent increases in MODIS cloud optical thickness at all view angles.

The solar zenith angle dependence of retrieved cloud properties in most-homogeneous and heterogeneous clouds is evaluated here aswell. Figure 5.23 shows domain mean (retrieved at 1 km resolution) true and retrieved LWP and optical thickness, and their differences for both homogeneous and heterogeneous cloud scenes. In the homogeneous cloud scenes, the retrieved effective radius agrees well with the true value from LES within 2%, the retrieved optical thickness agrees with 10% underestimation compared to LES values, and finally the retrieved LWP agrees well with LES values within 10% underestimation. Moreover, these homogeneous scenes do not show much variability with solar zenith angles.

In the most heterogeneous cloud scenes, the retrieved domain mean effective radius show good agreement with LES true values in all solar zenith angle. However, the retrieved domain mean optical thickness agrees with LES true value up to the solar zenith angle of 50^o and thereafter an increase towards higher solar zenith angles. At 70^o solar zenith angle the retrieved optical thickness is four times larger than the true LES value. Thus, 20-30% underestimation in retrieved LWP is observed in the solar zenith angles below 50^o, a very good agreement at 60^o solar zenith angle, and the retrieved LWP doubles at 70^o solar zenith angle. Similar results are obtained in comparing MODIS LWP with AMSR-E LWP [*Seethala and Horvath,* 2010]. (The difference seen in true cloud properties with respect to solar zenith angle is due to difference in number of datasets.)

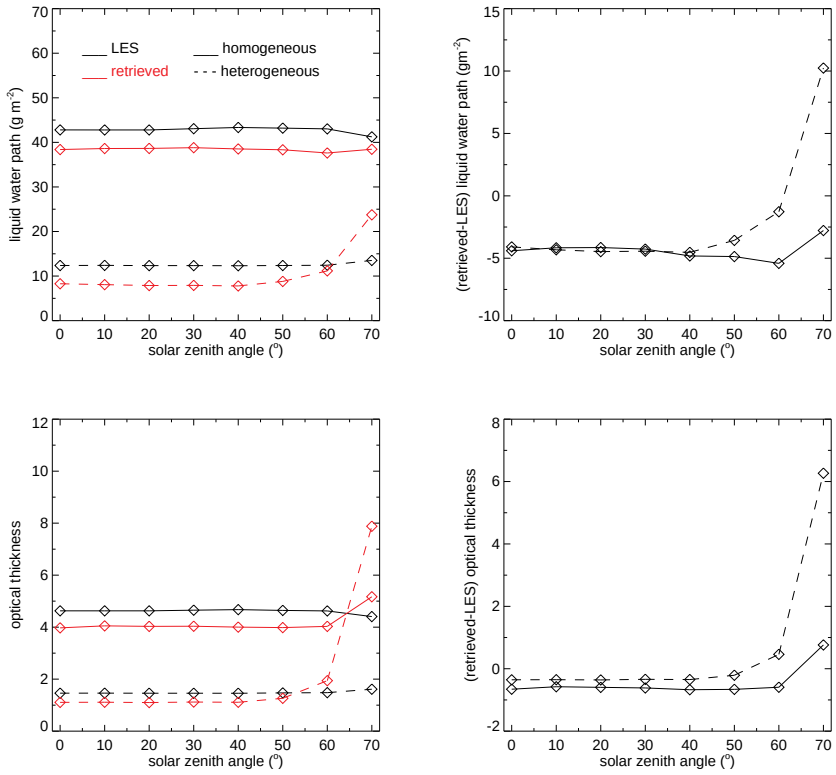

Figure 5.23. Solar zenith angle dependence of domain mean LWP and τ (1 km retrievals).

(b) View Zenith Angle Dependence

This section examines view angle-dependent biases due to cloud inhomogeneity in the 1D cloud property retrievals. *Varnai and Marshak* [2003] noticed an increase in optical thickness with view zenith angle, but larger increase towards oblique view in the backward observing direction, and claimed as, is due to the increase in the ratio of saturated pixels. *Varnai and Marshak* [2007] further examined cloud inhomogeneity influence in VZA-dependence of MODIS τ retrieval. They noticed τ retrievals are remarkably consistent for all

view directions if clouds are homogeneous; they give much higher τ-values for oblique views than for overhead views if clouds are heterogeneous and the Sun is fairly low. The mean optical thickness retrieved for the most heterogeneous third of cloudy pixels is more than 40% higher for oblique views than for overhead views if the solar zenith angle exceeds 60°. They concluded that the most likely reason for the increase lies in three-dimensional radiative interactions that are not considered in current, 1D retrieval algorithms. Namely, the radiative effect of cloud sides viewed at oblique angles seems to contribute most to the enhanced optical thickness values. *Loeb and Coakley* [1998] and *Kato et al.* [2006] showed that 1D retrievals of mean τ decrease by as much as ~40% between nadir and oblique view angles, in the forward scattering direction. *Loeb and Coakley* [1998] indicated τ is fairly insensitive to changes in VZA in the backscattering direction; while *Kato et al.* [2006] shown that the retrieved τ decreases with VZA even in the backscatter direction but that the angular dependence is less pronounced compared to that in the forward direction.

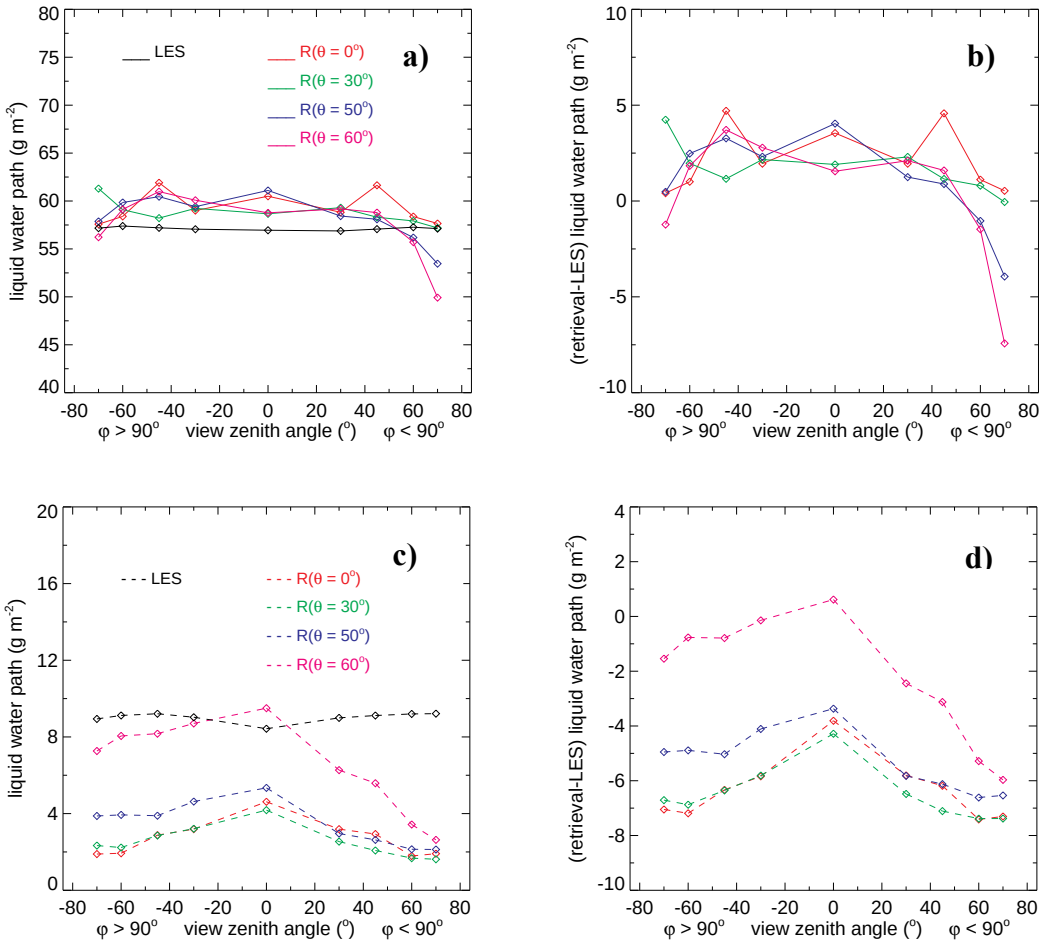

Figure 5.24. View zenith angle dependence of domain mean LWP and LWP bias (a, b) most homogeneous, and (c, d) most heterogeneous (1 km retrievals).

For the forward scattering direction we consider the retrievals with relative azimuth < 90^o (i.e., $\varphi=30^o$ and $\varphi=60^o$), and for the backward scattering direction we consider the retrievals with relative azimuth > 90^o (i.e., $\varphi=120^o$ and $\varphi=150^o$). In homogeneous scenes, the retrieved LWP at different solar zenith angle agrees within 5% with LES LWP, except the underestimation in retrieval in the very oblique view in the forward scattering direction - this underestimation is mainly from the optical thickness underestimation. Otherwise an unbiased optical thickness is retrieved. In agreement with *Kato et al.* [2006], we also found an underestimation in LWP in backscatter direction, which might be due to the domain averaging. The effective radius overestimated the true LES by 1 – 1.5 μm. In the most heterogeneous portion of cloud scenes the retrieved LWP underestimated in all solar zenith angles except at 60^o in the backward scattering direction. This underestimation in LWP is further increased with view zenith angle and the increase is larger in the forward scattering direction than in the backward scattering direction.

In the forward scattering direction, the radiances (in both VIS and NIR) increase with VZA. In the backscatter direction also we noticed an increase in radiance with VZA. However, there is a decrease in retrieved cloud properties with VZA in the forward scattering direction. The reason is according to Mie theory, most part of the reflectance should be in the forward scattering direction for a plane-parallel cloud, and the reflectance should further increase with increasing view zenith angle. This can be clearly seen in the LUT (Figures 5.2-5.3) provided in Section 2.3. At particular view geometry, eventhough visible reflectance increases, we found a decrease in τ (which is clear from Figure 5.3, but for forward scattering LUT). Nevertheless, due to the cloud 3D structure, more reflectance is backscattered in other directions and hence the photons may be reduced which might otherwise travel in the forward scattering direction. Thus, eventhough, the reflectance is larger in the forward scattering direction, according to Mie theory for a plane-parallel cloud it should be even larger than that to get the exact cloud optical thickness and effective radius in the forward direction.

(c) View Azimuth *versus* View Zenith Angle

In this section we evaluate the dependence of retrieval bias as a function of view azimuth angle and view zenith angle. In the most homogeneous portion of clouds the relative bias in LWP is within ±10%. At 60^o SZA, there is a slight overestimation in the backward scattering direction due to the cloud illumination, and an underestimation in the most forward scattering direction at very oblique view of 70^o due to the cloud shadow. Mostly, an unbiased τ is retrieved in the homogeneous clouds and the bias is ±5%, except at SZA 60^o, where a

15% underestimation is observed in the forward scattering direction at very oblique view mainly due to the cloud shadow side viewing. In general, the retrieved r_e overestimated 10-15%, and the overestimation is larger in the forward scattering direction at very oblique view and also in the backward scattering direction in side and fairly oblique views.

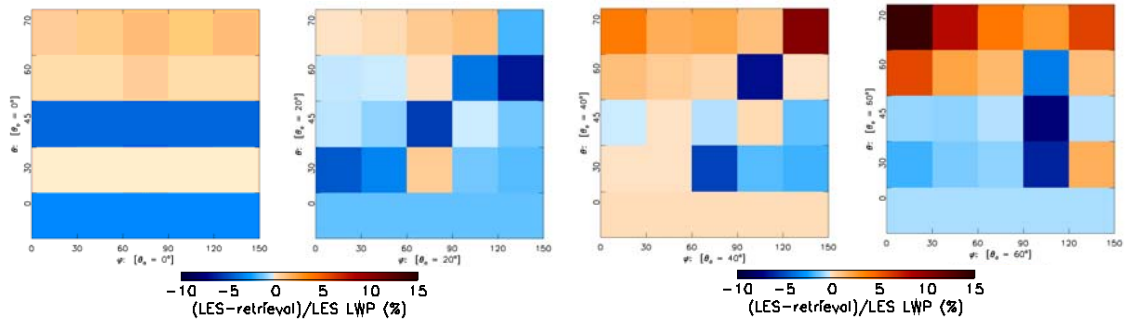

Figure 5.25. The relative bias in domain mean LWP is binned according to view azimuth angle (φ) and view zenith angle (θ) for homogeneous clouds at SZA (0^o, 20^o, 40^o, 60^o).

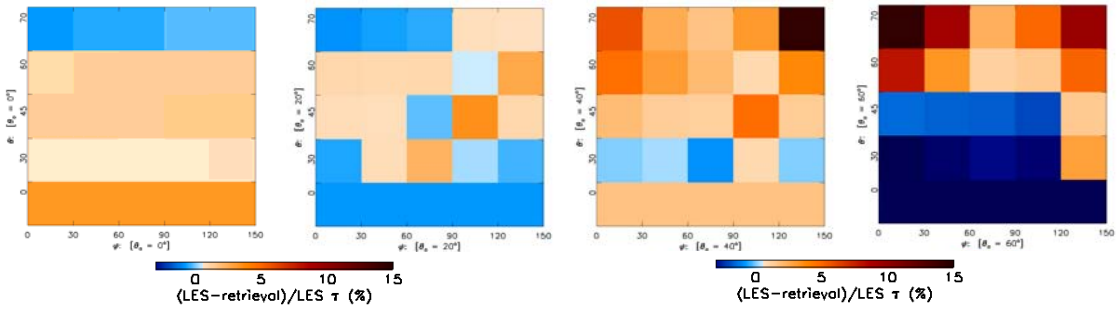

Figure 5.26. The relative bias in domain mean τ is binned according to view azimuth angle (φ) and view zenith angle (θ) for homogeneous clouds at SZA (0^o, 20^o, 40^o, 60^o).

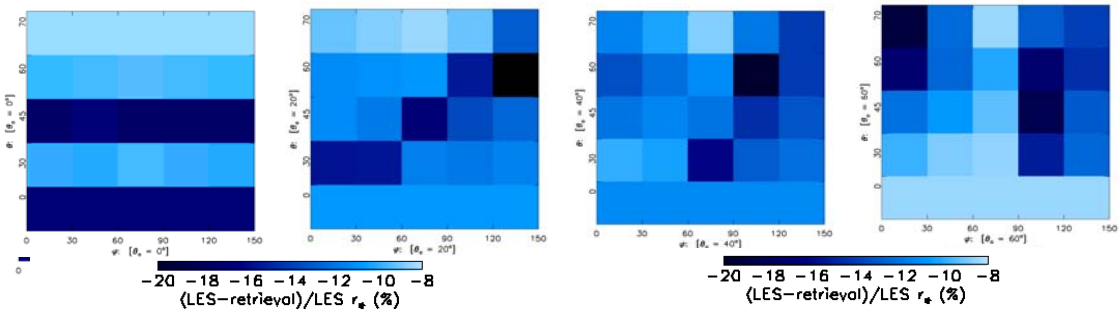

Figure 5.27. The relative bias in domain mean r_e is binned according to view azimuth angle (φ) and view zenith angle (θ) for homogeneous clouds at SZA (0^o, 20^o, 40^o, 60^o).

In the more heterogeneous cloud scenes, the optical thickness errors are smaller and within ±10 % in general, except at the forward scattering direction in the very oblique view. There is large overestimation ~50% in effective radius in the overhead Sun and nadir view. There is 10-20% underestimation in effective radius in the forward scattering direction at oblique views but high Sun. The underestimation increased with solar zenith angle, and at

low Sun, more in the side- and backscattered direction. At high Sun and nadir or side views the bias in retrieved effective radius is negligible.

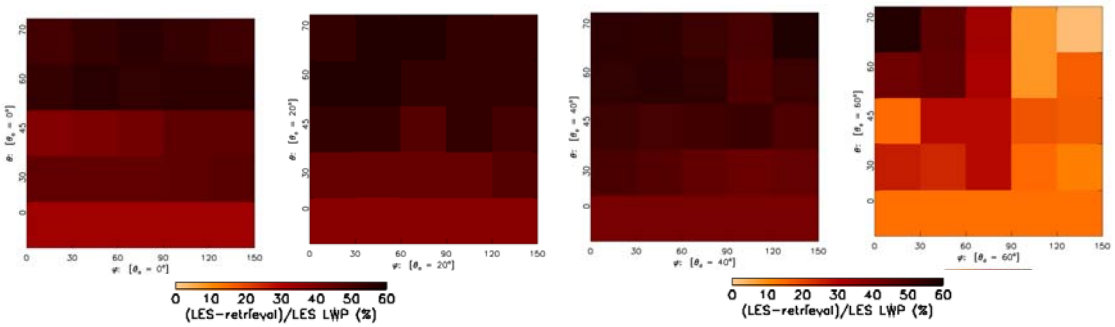

Figure 5.28. The relative bias in domain mean LWP is binned according to view azimuth angle (φ) and view zenith angle (θ) for heterogeneous clouds at SZA (0^o, 20^o, 40^o, 60^o).

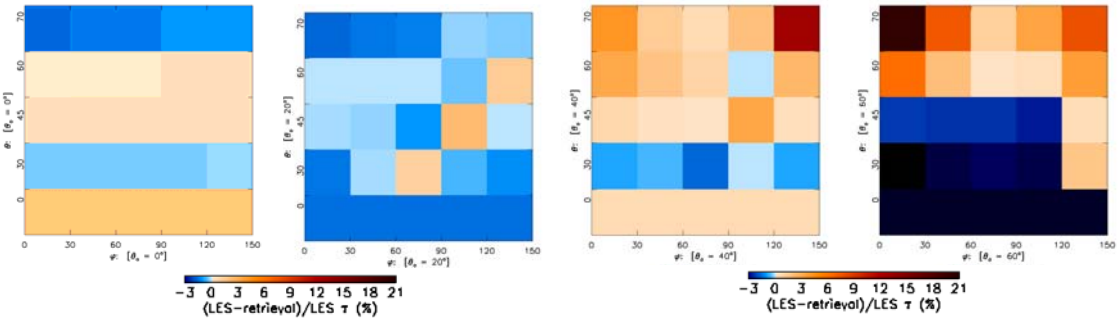

Figure 5.29. The relative bias in domain mean τ is binned according to view azimuth angle (φ) and view zenith angle (θ) for heterogeneous clouds at SZA (0^o, 20^o, 40^o, 60^o).

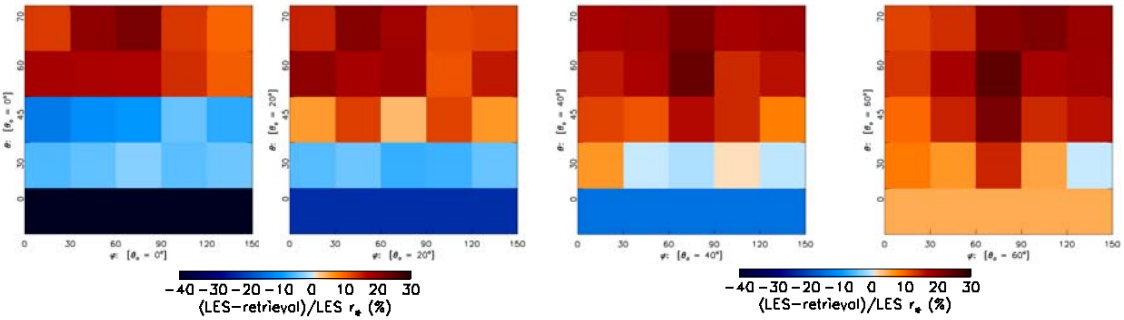

Figure 5.30. The relative bias in domain mean r_e is binned according to view azimuth angle (φ) and view zenith angle (θ) for heterogeneous clouds at SZA (0^o, 20^o, 40^o, 60^o).

5.3.9. Error in Cloud Retrieval and Heterogeneity Measures

In this section the absolute and relative bias in domain mean (based on 1 km pixel retrievals) LWP, optical thickness, and effective radius has been evaluated as a function of different heterogeneity measures. The results were also categorized as a function of solar zenith angle to see the correspondence of solar zenith angle in bias and heterogeneity parameters. The relative bias in LWP and τ is shown in Figure 5.31-5.33 binned with different heterogeneity parameters, but only for θ_o=20^o. The relative bias in LWP shows a

clear dependence of all three heterogeneity parameters. The relative bias in LWP is smaller and within ±10% in the most homogeneous portion and the bias increased with the increasing heterogeneity. In the heterogeneous cases a general underestimation in retrieved LWP is observed and the underestimation goes larger than 80% compared to true LES LWP. When the results are categorized in terms of θ_o it is clear that the overall bias is smaller at θ_o=60^o. When the LWP relative bias is binned with respect to χ (from LES) and H_σ the relative bias showed a clear increase towards H_σ than that in the χ. The relative bias show stronger dependence on H_σ compared to other heterogeneity parameters σ_{CTOP} and χ_{LES} or χ_{RET}. The dependence of χ_{RET} with relative bias is similar to χ_{LES} except the fact that the retrieved χ values moved towards larger values (i.e. more homogeneous) at high Sun and moved towards smaller values (i.e. more heterogeneous) at low Sun.

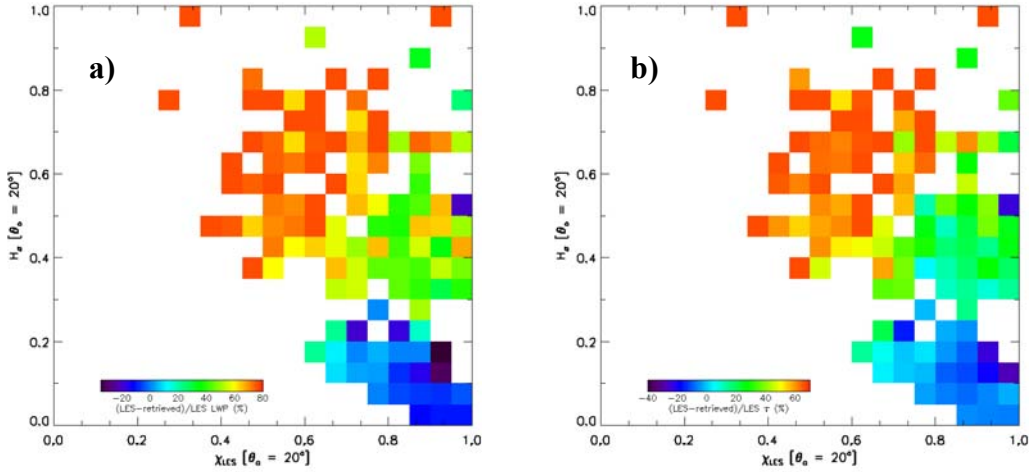

Figure 5.31. The relative bias in domain mean (a) LWP and (b) τ binned according to χ parameter calculated from LES (χ_{LES}) and H_σ for θ_o=20^o.

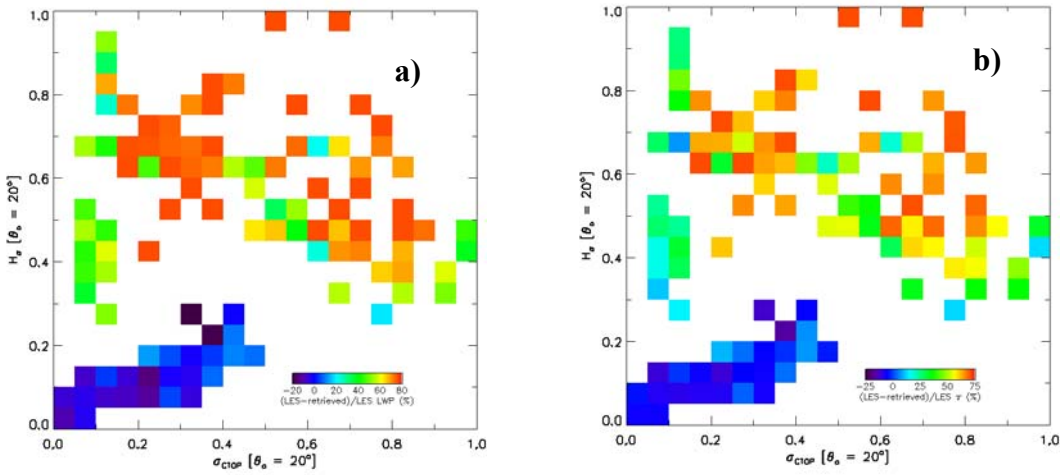

Figure 5.32. The relative bias in domain mean (a) LWP and (b) τ binned according to standard deviation in cloud top height (σ_{CTOP}) and H_σ for θ_o=20^o.

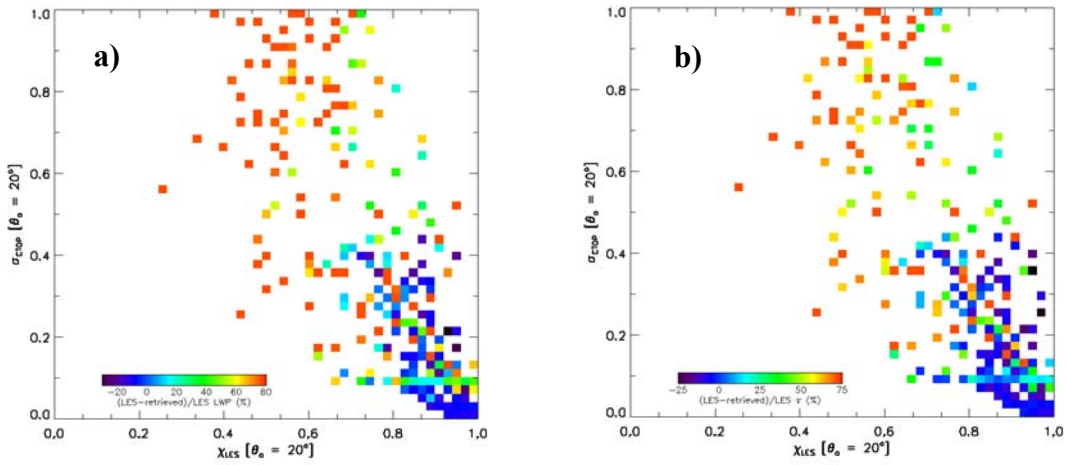

Figure 5.33. The relative bias in domain mean (a) LWP and (b) τ binned according to χ calculated from LES (χ_{LES}) and standard deviation in cloud top height (σ_{CTOP}) for θ_o=20^o.

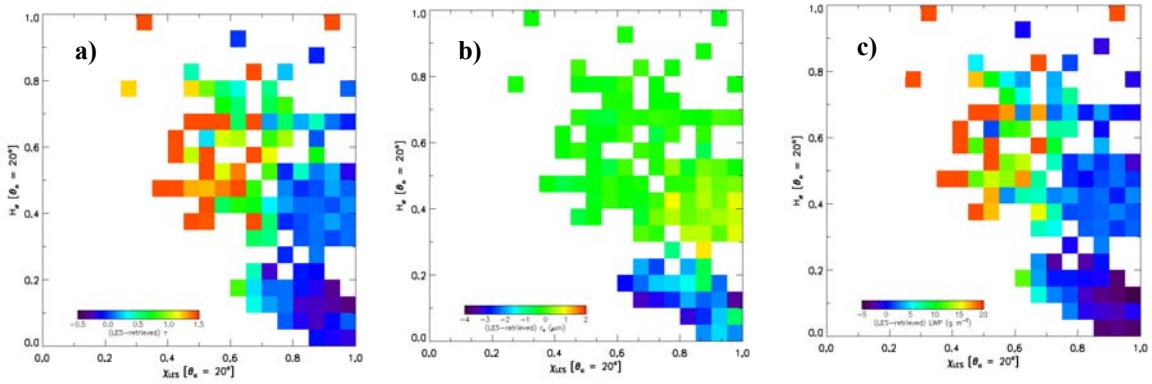

Figure 5.34. The absolute bias in domain mean (a) τ, (b) r_e, and (c) LWP binned according to χ calculated from LES (χ_{LES}) and H_σ for θ_o=20^o.

A clear transition from very small bias to very large positive bias can be observed in τ relative bias plot, in all SZA. The bias is interestingly smaller when the Sun is fairly oblique ~60^o. The bias in r_e also showed a clear dependence on heterogeneity. As *Girolamo* [2010] we have also observed H_σ as the most powerful heterogeneity parameter compared to χ_{RET} and σ_{CTOP}. The absolute bias in LWP, τ and r_e is shown in Figure 5.34. In the most homogeneous portion of data there is almost nil bias or a very small overestimation ~0.5 is observed in retrieved τ. On the otherhand, the retrieved r_e shows an overestimation of 2-3 μm. This leads an overestimation in retrieved LWP upto 5–10 g m^{-2}. However, over the most heterogeneous portion of the data the retrieved r_e seems to be unbiased. Hence the underestimation in retrieved LWP is mainly due to the underestimation in τ. The underestimation in τ is around 1–2, and in LWP is around 20-25 g m^{-2}. Overall, the bias in retrieved cloud properties is smaller for 1 km retrievals and the domain means.

5.3.10. Error Estimation for 1D VNIR Cloud Retrievals

Based on the values of three different heterogeneity parameters H_σ, σ_{CTOP}, and χ_{LES} or χ_{RET} the cloud scenes have been classified into either homogeneous or heterogeneous. The first one-third of the data based on the heterogeneity parameters are assumed as most-homogeneous and the last one-third of the data is assumed as most-heterogeneous. The criteria is as below:

Homogeneity criteria:

$H_\sigma < 0.3$

$\sigma_{CTOP} < 30$ m

χ_{LES} or $\chi_{RET} > 0.95$

Heterogeneous criteria:

$H_\sigma > 1.5$

$\sigma_{CTOP} > 100$ m

χ_{LES} or $\chi_{RET} < 0.85$

We had roughly 310 cloud scenes which satisfy the homogeneity criteria and 230 scenes which satisfy the heterogeneity criteria. Thus from these scenes we calculate the absolute bias and relative bias for τ, r_e, and LWP. The relative bias in all three variables for different Sun-view geometry is provided in Table 5-7. For the homogeneous cloud scenes the relative bias in τ is ± 5% in all the Sun-view geometry except at very low Sun and very oblique view especially in the most forward and most backward direction. Effective radius is mostly overestimated and the relative bias varies from 5 to 25%. The relative bias in LWP is also between ± 10% in most of the Sun-view geometry.

In heterogeneous scenes, the retrieved LWP underestimates at all solar zenith angles except the very low Sun of 60^o and 70^o where they show an overestimation. The relative bias in retrieved LWP is within 40% except 70^o solar zenith angle. The retrieved effective radius show an overestimation compared to LES values in all Sun-view geometry and the relative bias in r_e varies from 5% to 45%. The optical thickness underestimates in general in all solar zenith angles except very low Sun of 60^o and 70^o. The relative bias (underestimation) is roughly 2 to 30%. However, in 60^o solar zenith angle there is a large overestimation in retrieved τ compared to τ from LES, and the relative bias in τ at this solar zenith angle can go even upto 100% especially at nadir view.

Table 5. The relative bias of domain mean (retrieved) τ in most homogeneous clouds. The values in the bracket indicate the relative bias in most heterogeneous clouds.

$(\tau_{LES}-\tau_{RET})/\ \tau_{LES}$ * 100. [homogeneous (heterogeneous)]					
φ→ θ ↓	30 °	60 °	90 °	120 °	150 °
$\theta_o = 0^o$					
0 °	2.2 (20)	2.2(20)	2.2(20)	2.2(20)	2.2(20)
30 °	-0.1(22)	-0.1(23)	-0.2(22)	-0.1(23)	-0.1(23)
45 °	0.6(24)	0.6(24)	0.5(24)	0.6(25)	0.6(24)
60 °	0.5(26)	0.5(26)	0.6(25)	0.7(26)	0.7(26)
70 °	-1.4(22)	-1.2(21)	-1.3(20)	-1.0(21)	-0.9(21)
$\theta_o = 10^o$					
0 °	-2.7(14)	- 2.7(14)	- 2.7(14)	- 2.7(14)	- 2.7(14)
30 °	3.0(26)	2.4(25)	-0.6(22)	-0.3(23)	-0.1(23)
45 °	0.5(26)	0.2(25)	0.3(24)	2.8(28)	3.7(28)
60 °	0.6(26)	0.6(26)	1.0(25)	1.0(26)	0.3(25)
70 °	-1.4(22)	-0.9(22)	-0.9(21)	-0.3(22)	0.4(23)
$\theta_o = 20^o$					
0 °	-0.8(16)	-0.8(16)	-0.8(16)	-0.8(16)	-0.8(16)
30 °	-0.4(23)	0.8(23)	2.0(24)	0.4(23)	-0.2(22)
45 °	1.1(26)	1.0(26)	-0.1(24)	3.6(28)	1.2(25)
60 °	1.2(26)	1.1(26)	1.2(25)	0.8(26)	2.8(27)
70 °	-1.0(22)	-0.6(22)	-0.4(21)	0.9(23)	0.9(23)
$\theta_o = 30^o$					
0 °	-0.7(15)	-0.7(15)	-0.7(15)	-0.7(15)	-0.7(15)
30 °	0.6(17)	-0.1(23)	2.1(24)	0. 5(22)	-0.4(21)
45 °	1.5(26)	1.3(13)	0.7(25)	4.5(28)	1.4(24)
60 °	2.5(28)	1.9(26)	1.5(24)	0.7(25)	6.4(29)
70 °	0.8(23)	0.5(23)	0.4(20)	2.2(23)	0.7(8)
$\theta_o = 40^o$					
0 °	1.7(16)	1.7(16)	1.7(16)	1.7(16)	1.7(16)
30 °	0.3(23)	0.4(23)	-0.8(20)	0.7(19)	0.1(18)
45 °	2.0(26)	1.5(25)	1.4(24)	5.0(26)	1.5(22)
60 °	4.5(28)	3.0(26)	2.0(23)	1.0(22)	3.9(25)
70 °	5.0(26)	2.2(23)	1.4(16)	3.0(20)	15.3(32)
$\theta_o = 50^o$					
0 °	-2.6(-5)	-2.6(-5)	-2.6(-5)	-2.6(-5)	-2.6(-5)
30 °	-0.5(16)	-0.7(16)	-0.4(13)	1.9(8)	0.1(9)
45 °	1.9(18)	1.2(19)	0.9(16)	1.8(17)	1.5(14)
60 °	7.1(25)	4.1(20)	2.6(13)	1.5(14)	4.8(11)
70 °	12.7(26)	5.2(18)	2.4(2)	4.1(7)	4.6(8)
$\theta_o = 60^o$					
0 °	-4.6(-94)	-4.6(-94)	-4.6(-94)	-4.6(-94)	-4.6(-94)
30 °	-4.7(-39)	-4.2(-35)	-3.7(-46)	-4.2(-44)	1.8(-57)
45 °	-2.5(-30)	-2.5(-24)	-2.4(-31)	-2.9(-29)	0.8(-45)
60 °	6.0(-1)	2.0(2)	0.2(-26)	0.5(-34)	4.2(-34)
70 °	21.4(21)	6.9(-3)	0.7(-43)	3.6(-37)	8.4(-59)
$\theta_o = 70^o$					
0 °	-13.4(>100)	-13.4	-13.4	-13.4	-13.4
30 °	-23.0	-17.2	-14.5	-11.3	-11.8
45 °	-65.7	-23.0	-15.8	-9.6	-4.2
60 °	>100	-40.4	-20.0	-8.0	-3.5
70 °	>100	-40.0	-23.2	-6.9	-1.0

Table 6. The relative bias of domain mean (retrieved) r_e in most homogeneous clouds. The values in the bracket indicate the relative bias in most heterogeneous clouds.

$(R_{LES}-R_{RET}) / R_{LES} * 100$. [homogeneous]					
φ→ θ ↓	30 °	60 °	90 °	120 °	150 °
$\theta_o = 0^o$					
0 °	-17 (-45)	-17(-45)	-17(-45)	-17(-45)	-17(-45)
30 °	-9(-27)	-9(-27)	-9(-27)	-9(-28)	-10(-28)
45 °	-16(-43)	-16(-44)	-17(-44)	-16(-44)	-16(-46)
60 °	-10(-18)	-9(-17)	-9(-18)	-9(-19)	-9(-21)
70 °	-7(-14)	-7(-12)	-6(-13)	-7(-15)	-7(-17)
$\theta_o = 10^o$					
0 °	-9(-33)	-9(-33)	-9(-33)	-9(-33)	-9(-33)
30 °	-11(-20)	-10(-35)	-11(-29)	-10(-28)	-10(-28)
45 °	-11(-27)	-13(-30)	-17(-46)	-13(-25)	-11(-28)
60 °	-10(-17)	-9(-17)	-9(-17)	-11(-20)	-13(-27)
70 °	-8(-16)	-7(-13)	-6(-13)	-7(-15)	-7(-15)
$\theta_o = 20^o$					
0 °	-9(-31)	-9(-31)	-9(-31)	-9(-31)	-9(-31)
30 °	-14(-32)	-14(-26)	-10(-31)	-10(-29)	-10(-28)
45 °	-10(-22)	-10(-20)	-15(-29)	-12(-19)	-11(-23)
60 °	-10(-16)	-9(-18)	-9(-16)	-13(-24)	-19(-22)
70 °	-8(-15)	-8(-13)	-7(-13)	-8(-15)	-11(-19)
$\theta_o = 30^o$					
0 °	-9(-32)	-9(-32)	-9(-32)	-9(-32)	-9(-32)
30 °	-10(-25)	-12(-32)	-13(-31)	-10(-27)	-10(-28)
45 °	-10(-20)	-10(-20)	-13(-27)	-12(-20)	-11(-24)
60 °	-11(-18)	-10(-17)	-10(-15)	-16(-26)	-12(-24)
70 °	-9(-15)	-8(-12)	-7(-13)	-8(-13)	-24(-50)
$\theta_o = 40^o$					
0 °	-10(-24)	-10(-24)	-10(-24)	-10(-24)	-10(-24)
30 °	-9(-24)	-9(-26)	-14(-31)	-11(-27)	-10(-25)
45 °	-11(-20)	-10(-20)	-10(-17)	-13(-16)	-11(-22)
60 °	-12(-19)	-11(-16)	-10(-15)	-17(-25)	-12(-19)
70 °	-10(-15)	-9(-14)	-7(-12)	-10(-13)	-12(-11)
$\theta_o = 50^o$					
0 °	-12(-38)	-12(-38)	-12(-38)	-12(-38)	-12(-38)
30 °	-8(-23)	-8(-24)	-9(-21)	-14(-31)	-10(-23)
45 °	-11(-22)	-10(-20)	-9(-16)	-17(-21)	-11(-21)
60 °	-14(-20)	-11(-18)	-9(-15)	-17(-26)	-12(-19)
70 °	-14(-24)	-10(-16)	-7(-13)	-11(-15)	-15(-19)
$\theta_o = 60^o$					
0 °	-6(-22)	-6(-22)	-6(-22)	-6(-22)	-6(-22)
30 °	-9(-22)	-8(-21)	-7(-18)	-13(-29)	-11(-27)
45 °	-11(-22)	-10(-20)	-8(-15)	-16(-24)	-11(-19)
60 °	-16(-25)	-12(-19)	-9(-13)	-15(-21)	-13(-17)
70 °	-19(-25)	-12(-19)	-7(-12)	-11(-13)	-12(-16)
$\theta_o = 70^o$					
0 °	-2(-13)	-2(-13)	-2(-13)	-2(-13)	-2(-13)
30 °	-5(-13)	-4(-16)	-3(-12)	-5(-13)	-23(-43)
45 °	-6(-11)	-6(-12)	-5(-11)	-8(-12)	-12(-17)
60 °	-5(-6)	-8(-13)	-6(-8)	-10(-10)	-11(-12)
70 °	3(-13)	-10(-16)	-4(-6)	-8(-6)	-11(-12)

Table 7. The relative bias of domain mean (retrieved) LWP in most homogeneous clouds. The values in the bracket indicate the relative bias in most heterogeneous clouds.

$(LWP_{LES}-LWP_{RET}) / LWP_{LES} * 100$. [homogeneous]					
φ→ θ ↓	30 °	60 °	90 °	120 °	150 °
$\theta_o = 0^o$					
0 °	-5(20)	-5(20)	-5(20)	-5(20)	-5(20)
30 °	-2(29)	-2(29)	-2(30)	-2(30)	-2(30)
45 °	-6(24)	-6(23)	-7(24)	-6(24)	-6(24)
60 °	-0.5(38)	-0.2(37)	0(36)	-0.2(36)	-0.2(36)
70 °	0.4(36)	1(36)	1(36)	1(35)	1(35)
$\theta_o = 10^o$					
0 °	-4(20)	-4(20)	-4(20)	-4(20)	-4(20)
30 °	-0.2(34)	0.2(29)	-3(28)	-2(30)	-2(30)
45 °	-3(33)	-4(31)	-7(24)	-3(34)	0.5(34)
60 °	-0.5(37)	-0.3(37)	0.3(37)	-1(36)	-4(32)
70 °	0(35)	1(36)	1(36)	1(36)	2(36)
$\theta_o = 20^o$					
0 °	-2(24)	-2(24)	-2(24)	-2(24)	-2(24)
30 °	-6(27)	-5(27)	-1(30)	-2(30)	-2(29)
45 °	-1(36)	-1(36)	-6(30)	-1(37)	-2(32)
60 °	-0.2(38)	0.2(37)	0.2(37)	-4(34)	-7(31)
70 °	0.2(36)	1(36)	2(36)	2(37)	-1(33)
$\theta_o = 30^o$					
0 °	-2(24)	-2(24)	-2(24)	-2(24)	-2(24)
30 °	-1(34)	-4(30)	-3(30)	-2(30)	-2(28)
45 °	-0.3(36)	-1(36)	-3(33)	1(36)	-2(32)
60 °	-0(39)	0(38)	0.3(37)	-6(31)	3(37)
70 °	1(37)	1(38)	2(35)	2(36)	-13(16)
$\theta_o = 40^o$					
0 °	-1(27)	-1(27)	-1(27)	-1(27)	-1(27)
30 °	-0.5(33)	-1(33)	-6(27)	-3(27)	-2(27)
45 °	-0.4(36)	-0.4(36)	-1(36)	0(35)	-2(30)
60 °	1(39)	1(38)	1(36)	-7(28)	0.5(33)
70 °	4(39)	2(37)	3(32)	2(33)	12(43)
$\theta_o = 50^o$					
0 °	-5(12)	-5(12)	-5(12)	-5(12)	-5(12)
30 °	-0.5(29)	-1(29)	-1(28)	-3(20)	-2(21)
45 °	-0(30)	-0(31)	0(30)	-7(23)	-2(24)
60 °	4(36)	2(33)	2(30)	-6(21)	1(19)
70 °	10(36)	5(33)	4(19)	2(21)	0(17)
$\theta_o = 60^o$					
0 °	-1(-9)	-1(-9)	-1(-9)	-1(-9)	-1(-9)
30 °	-3(6)	-2(6)	-1(7)	-7(-2)	0(-9)
45 °	-1(9)	-1(10)	-1(8)	-9(-2)	-1(-7)
60 °	5(22)	2(23)	1(8)	-4(-2)	1(-12)
70 °	20(37)	8(21)	4(-3)	3(0)	6(-23)
$\theta_o = 70^o$					
0 °	-2(-142)	-2(-142)	-2(-142)	-2(-142)	-2(-142)
30 °	-7(-72)	-5(-58)	-3(-87)	-3(-36)	-17(-40)
45 °	-21(-84)	-8(-57)	-4(-82)	-4(-42)	-3(-70)
60 °	-72(-184)	-14(-87)	-6(-66)	-3(-47)	-1(-76)
70 °	-98(-240)	-9(-76)	-6(-88)	0(-65)	3(-162)

5.3.11. Multi-Linear Regression Analysis

A multiple linear regression analysis is carry out to predict the values of relative bias in τ and LWP, from a set of explanatory variables H_σ, σ_{CTOP}, χ_{RET}, χ_{LES}, τ_{LES}. Multiple linear regression attempts to model the relationship between two or more explanatory variables and a response variable by fitting a linear equation to observed data. Every value of the independent variable x is associated with a value of the dependent variable y. The regression line for p explanatory variables $x_1, x_2, \ldots, x_p$ is defined to be $\mu_y = \beta_0 + \beta_1 x_1 + \beta_2 x_2 + \ldots + \beta_p x_p$. The observed values for y vary about their means μ_y and are assumed to have the same standard deviation σ. The fitted values $b_0, b_1, \ldots, b_p$ estimate the parameters $\beta_0, \beta_1, \ldots, \beta_p$ of the population regression line. Formally, the model for multiple linear regression, given n observations, is

$$y_i = \beta_0 + \beta_1 x_{i1} + \beta_2 x_{i2} + \ldots + \beta_p x_{ip} + e_i \quad \text{for } i = 1,2, \ldots n.$$

Where e_i is residual, the difference between observed and predicted relative bias and β_0 is constant.

We predict the bias and relative bias in τ and LWP using true LES τ and different cloud heterogeneity measures calculated from the observed 0.86 μm radiance, cloud top height, retrieved τ, true τ, etc. The observed *versus* predicted relative bias in both τ and LWP is shown in Figure 5.35-5.36. The multi-linear correlation coefficient between the relative bias and the explanatory variables is above 0.9 and the correlation breaks with the solar zenith angle. Good (linear-)relation between true and predicted relative bias is noticed for Sun angles smaller than 60^o and the relation breaks at 60^o solar angle and later. Table 8 summarizes the coefficients of multi-linear regression fit and their root-mean square deviations for specific Sun-view geometry. However, we perform the multi-linear regression simply to demonstrate how these statistical errors derived from LES-SHDOM could be used to statistically correct the VNIR retrievals. In reality, especially for pixel-level retrievals, the errors depend non-linearly on SZA, VZA, heterogeneity, etc., so clearly, a linear regression model is not a good choice. A better model would be a neural network (similar to Cornet et al., [2004, 2005] neural net correction scheme), which can handle the non-linear relationship between retrieval errors and SZA, VZA, heterogeneity, etc.

Table 8. β parameters and their corresponding bias to predict domain mean relative τ bias.

	β_0	β_1 (H_σ)	β_2 (σ_{CTOP})	β_3 (χ_{RET})	β_4 (χ_{LES})	β_5 (τ_{LES})
$\theta_o = 0^o$	$\varphi = 90^o$, $\theta = 0^o$					
coefficients	-5.9	3.5	-16	204	-208	1.3
SD (σ)		0.3	1.8	9.5	5	0.1
	$\varphi = 90^o$, $\theta = 45^o$					
coefficients	10	11.4	10.4	79	-110	1.9
SD (σ)		0.4	3.4	6.7	8.4	0.2
	$\varphi = 90^o$, $\theta = 70^o$					
coefficients	-43	15	28	73	-44	0.9
SD (σ)		0.5	4.2	6.6	9.8	0.2
$\theta_o = 30^o$	$\varphi = 90^o$, $\theta = 0^o$					
coefficients	28	7.5	-6	77	-120	1.2
SD (σ)		0.4	2.4	12.4	7.6	0.1
	$\varphi = 90^o$, $\theta = 45^o$					
coefficients	8	12.8	19.3	30.8	-54	1.3
SD (σ)		0.4	3.4	7.7	9.0	0.2
	$\varphi = 90^o$, $\theta = 70^o$					
coefficients	-42	14	29.5	68	-37	0.6
SD (σ)		0.5	4.3	6.1	10.2	0.2
$\theta_o = 60^o$	$\varphi = 90^o$, $\theta = 0^o$					
coefficients	-58.415	3.109	-50.443	617.560	-558.649	0.149
SD (σ)		3.166	22.951	29.293	74.858	1.270
	$\varphi = 90^o$, $\theta = 45^o$					
coefficients	-72	11	25	284	-225	1.4
SD (σ)		1.4	13.5	12.6	39.8	0.6
	$\varphi = 90^o$, $\theta = 70^o$					
coefficients	-77	7.6	17	296	-219	-0.02
SD (σ)		2.0	20	14	53	0.9

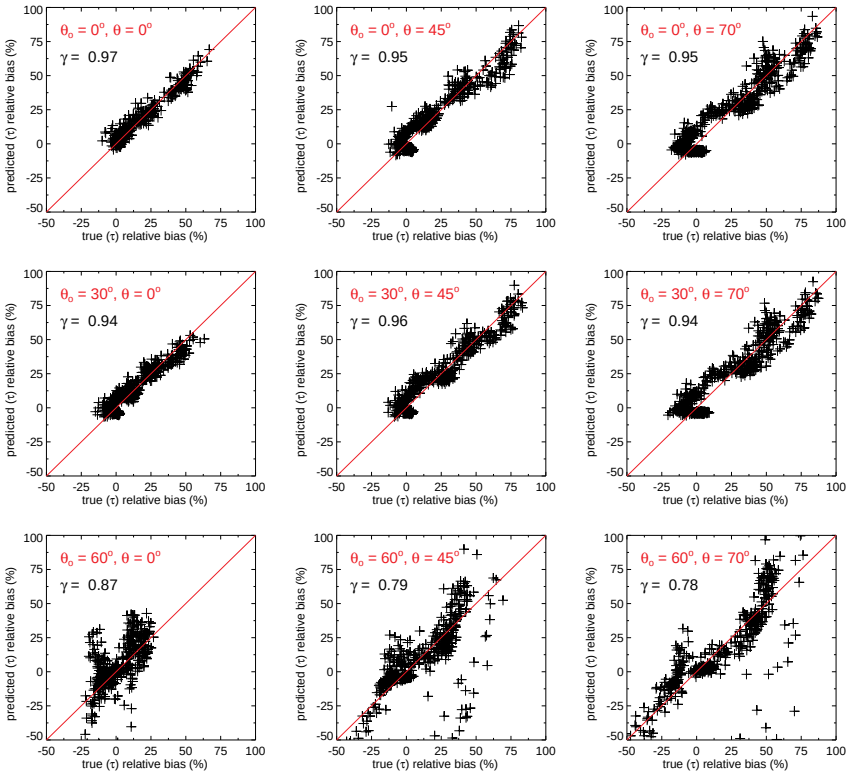

Figure 5.35. Domain mean observed *vs.* modelled relative τ bias for selected Sun-view geometry at relative azimuth φ=90°.

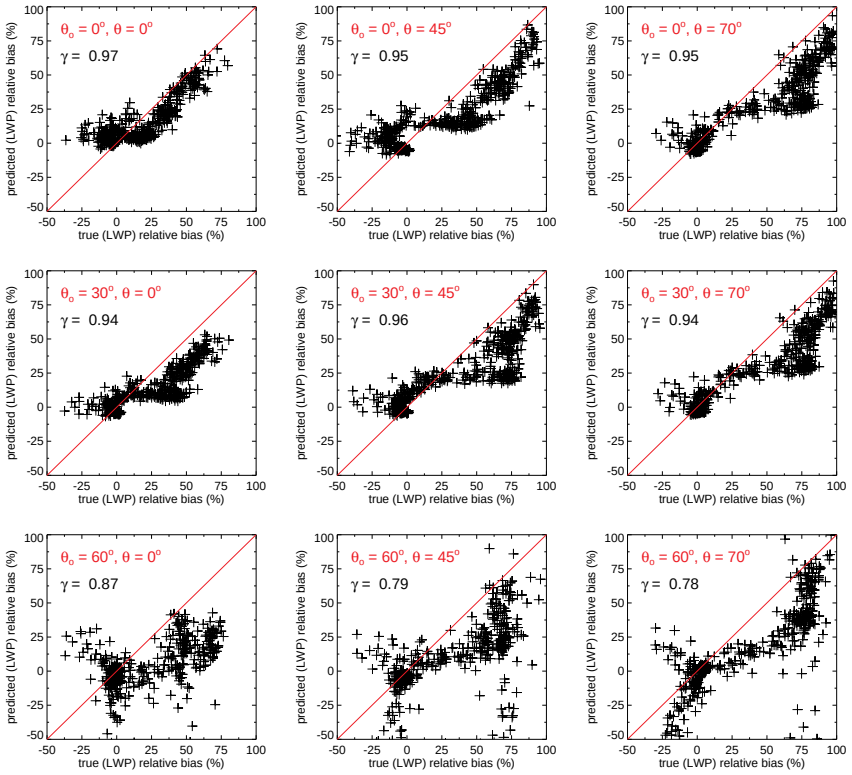

Figure 5.36. Domain mean observed *vs.* modelled relative LWP bias for selected Sun-view geometry at relative azimuth φ=90°.

5.3.12. Optimal Error in Sun-view Geometry

The selection of preferred satellite viewing directions can significantly reduce this error. So, one way of reducing the retrieval error is to find out the view geometries and Sun angles whose retrieval error is minimal and tune the satellite instruments accordingly. Thus, in this section, we seek optimal viewing geometries and solar zenith angles from ~550 cloud scenes that give minimum error in optical thickness.

Davies [1984] reported that the differences are greatest for nadir and limb views, but tend to vanish for radiances with a view zenith angle of 60^o. If a single measurement is to be used to estimate the upwelling irradiance from an arbitrary scene, it therefore appears that both the nadir and limb viewing directions should be avoided, with the best choice being the measurement of radiances with zenith angles close to 60^o. For situations with large potential azimuthal dependence, as for large solar zenith angles, the preferred azimuthal viewing directions appear to be approximately 90^o or 270^o with respect to the solar plane. *Kato et al*. [2009] also attempted to estimate optimal geometry from the stratocumulus cloud fields. They found, when the solar zenith angle is small ($\theta_o = 30^o$), the error is negative but less than 10% (except for $\varphi = 180^o$). However, if the optical thickness is derived from nadir view only for overhead sun, the domain averaged optical thickness is underestimated by more than 10%. The azimuthally averaged τ error is less than 10% in the range of the viewing zenith angle from 0^o to 60^o when the solar zenith angle is around 30^o. When the solar zenith angle increases to 60^o, viewing zenith averaged τ error exceeds 10% especially if viewed from the forward direction while it can be less than 10% in the backward direction. The azimuthally averaged τ error is less than 10% when the viewing zenith angle is less than 30^o and solar zenith angle is 60^o. When the solar zenith angle further increases to 70^o, both internal and external error terms are greater than 10% but with the opposite sign, and hence the retrieved optical thickness error is less than 10%.

We evaluate the bias in retrieved τ at different Sun-view geometry and characterize the frequency of occurrence of minimum (min) and maximum (max) bias as a function of all these different angles, and shown in Figure 5.37-5.38. When the retrieved τ is categorized in terms of viewing zenith angle (θ) the max frequency of min bias is achieved in 30^o view zenith angle. In total of 550 cloud scenes, ~35% of scenes show min bias at $\theta=30^o$, ~25% and ~23% of scenes show min bias at $\theta=45^o$ and 60^o respectively. There are 17% of cloud scenes which show min bias although at very oblique viewing angle ($\theta=70^o$). Nevertheless, there are no clouds which show min bias in the nadir view ($\theta=0^o$), which is somewhat expected because there will be no cancellation of errors due to the cloud brightening and darkening,

which are expected to happen in all other viewing angles. In terms of relative azimuth angle (φ) there is clear difference in frequency of occurrence of minimum (τ) bias between forward and backward scattering direction. ~30% of scenes in the forward scattering direction ($\varphi<90^o$), ~20% of scenes in the side-scattering direction ($\varphi=90^o$), and ~50% of scenes in the backscattered direction ($\varphi>90^o$) show minimum τ bias. This would mean that 70% of total clouds show minimum bias either in side/backscattered radiance. Hence, the retrievals seem less affected if the measuring instruments are tuned to this geometry. Figure 5.37c shows the frequency of minimum τ bias at different solar zenith angles (θ). While considering individual θ_o, the maximum frequency of minimum τ bias is seen at low Sun ($\theta_o=60^o$ and 70^o). At 60^o solar zenith angle there are clouds which show minimum bias regardless of viewing/satellite plane (φ) respect to Sun, probably the errors cancels out as the satellite views cloud shadow side and illuminating side more often. On the other Sun angles there is minimum bias mostly in the side scattering and backscattering direction. At 40^o and 50^o Sun angles the maximum number of minimum bias is observed mostly in the 30^o and 45^o view zenith angles at $\varphi=120^o$. At 20^o and 30^o solar zenith angles the minimum bias is observed mostly in side scattering and backscattering radiance direction especially at 30^o, 45^o, 60^o viewing angles. At 10^o Sun angle there are fewer number of scenes show minimum bias but at all azimuth angles; especially forward scattering and side scattering direction at 30^o view zenith angle and back scattering at 45^o viewing angle. At the overhead Sun, the maximum scenes with minimum τ bias is seen either in $\varphi = 60^o$ or in $\varphi = 120^o$. Overall, 30^o viewing angle in most of the solar zenith angles and additionally 45^o or 60^o viewing angles in few solar zenith angles (especially when the Sun is fairly low) show minimum τ bias. Moreover, 120^o relative azimuth angle seems to be the best in all the Sun- angles, additionally 150^o also show more scenes with less τ bias especially when the Sun is 30^o or 40^o zenith. Interestingly for the 60^o solar zenith angle, 30^o and 150^o relative azimuth angles are the ones giving maximum scenes with minimum bias especially in the viewing angles 30^o and 45^o.

For solar zenith angle below 50^o only very few scenes show max τ bias, which are mostly in the forward scattering direction ($\varphi=30^o$ and 60^o). When the Sun is fairly low (at 60^o and 70^o solar zenith angle) the max scenes with max τ bias is seen in the 30^o relative azimuth angle especially in the very oblique ($\theta=70^o$) view zenith angle.

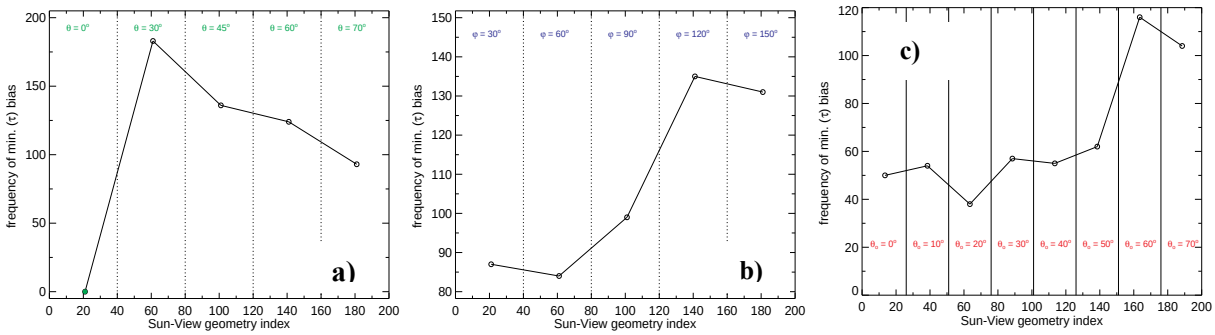

Figure 5.37. The frequency of occurrence of minimum domain mean τ bias in different Sun-view geometry (a) view zenith angle, (b) view azimuth angle, and (c) solar zenith angle.

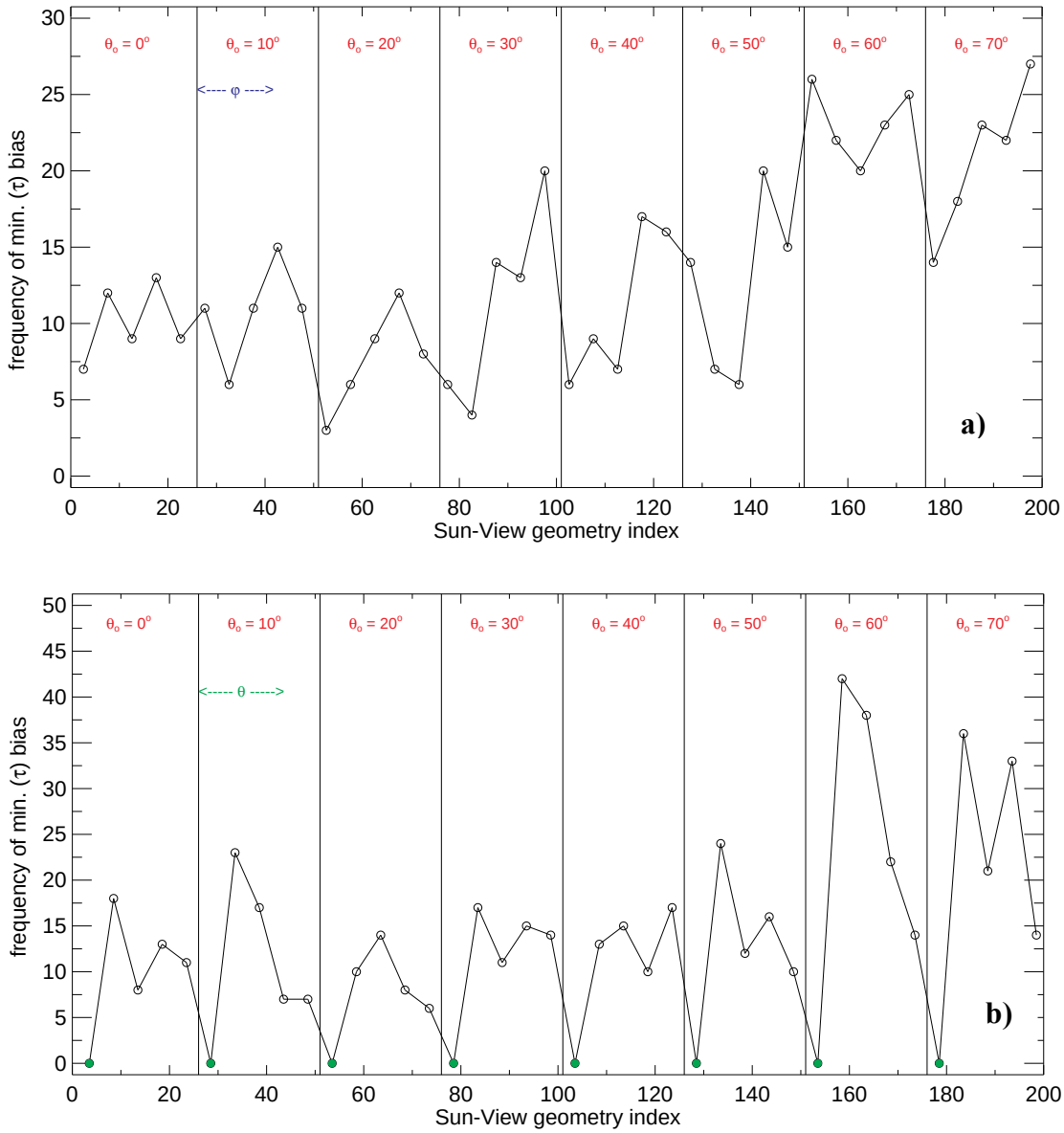

Figure 5.38. The frequency of occurrence of min domain mean τ bias in different Sun-view geometry (a) view azimuth angle and SZA, (b) view zenith angle and SZA.

5.4. Summary

This chapter investigated the three-dimensional radiative effects in 1D VNIR satellite cloud retrievals based on hundreds of large-eddy simulated cloud fields and a 3D radiative transfer model. Satellite cloud retrievals in visible and near-infrared channel is done by assuming clouds as plane-parallel, homogeneous, and independent pixels. However, using MISR data *Girolamo et al.* [2010] showed that the retrieved τ at 1 km resolution are indistinguishable from plane-parallel clouds 79% of the time, for the oceanic stratiform clouds when solar zenith angle < 60^o and for all other cloud types and Sun angles, this frequency drops sharply to as low as a few percent. *Cahalan et al*. [1994] reported an albedo bias of 10% or greater would be introduced into large regions of climate models if clouds were given their observed liquid water amounts, because of the treatment of clouds as plane-parallel. The difficulty in remote sensing of inhomogeneous cloud properties arises from the de-correlation between 3D radiances and cloud properties. An accurate retrieval in satellite based remote sensing of clouds should never be expected. However, it should be possible to estimate error from thousands of cloud fields which meets the conditions of real cloud.

Thus, our goal is to estimate 3D radiative errors in 1D retrievals, based on 650 LES cloud fields ranging from stratocumulus, unbroken stratus, to broken cumulus fields. To calculate the magnitude of cloud retrieval error, we have developed a one-dimensional 2-channel cloud retrieval algorithm based on *Nakajima and King* [1990]. The 1D look-up-table has been prepared based on SHDOMPP, a 1D radiative transfer model. The 3D radiances at two wavelengths (0.86 μm and 2.12 μm in this study) are computed from the 3D LES cloud fields using SHDOM, a 3D radiative transfer model. The retrievals are performed for individual cloud fields at its original higher resolution and also at standard 1 km resolution. The optical thickness and effective radius for each pixel is retrieved simultaneously from the 1D LUT. The resulting retrieved cloud properties are compared to the true LES values at its original resolution and also at 1 km resolution.

The simulated 3D and calculated 1D radiance have been compared. For a plane-parallel cloud, visible and near-infrared radiances increased with view zenith angle in oblique Sun, and the increase is 2 – 3 times larger in the forward scattering direction than the backscatter direction. Nevertheless, for high Sun, the radiances decreased with viewing angle. A case study reveals that the stratocumulus cloud follows this plane-parallel theory very well, however, for a broken shallow cumulus cloud, the increase in radiance with view zenith angle is less pronounced, and a general underestimation in visible radiance is noticed. Besides, the plane-parallel model showed decrease in radiance from medium to larger values of solar

zenith angle, however, 3D radiances increased with solar zenith angle. This increase is larger in both stratocumulus and shallow cumulus field, except a strong underestimation in shallow cumulus radiance for high Sun.

Different heterogeneity measures have been utilized to study the 3D radiative effects of homogeneous and heterogeneous cloud fields. The pixel-level analysis showed that most-homogeneous one-third scenes exhibited narrow Gaussian distribution, but skewed negatively, indicating the overestimation in retrieved LWP. Roughly 40-60% of the data showed the relative LWP bias within ±15% depending on the solar zenith angle, however, one-fourth of most-heterogeneous scenes showed much wider distribution with more than one peak, but skewed negatively, and only 10-25% of datasets are within ±15% relative LWP bias. For most-homogeneous cloud the distribution of relative cloud optical thickness (τ) bias peaks at 0. Roughly 40-70% of the data showed relative bias within ±15%, and the percentage of data that showed minimum bias decreased with increasing solar zenith angle. In contrast to homogeneous clouds, the frequency distribution of heterogeneous clouds is sparse and variable with fairly large negative tail. The distribution peak also shifted to -10% relative bias and also highly depended on solar zenith angle. Interpreting the retrieved droplet effective radius (r_e) with true LES is complex in the sense that satellite retrieval of r_e at near-infrared wavelength is sensitive mostly to the top layer of clouds. To compare retrieved r_e with LES true values, we calculated r_e from LES considering only the top layer with optical thickness of 2, which is a rough estimate of retrieved r_e. In homogeneous clouds, the distribution mostly peaks at relative bias 0 with the exception of 10^o and 70^o Sun angle, and skewed negatively. Only ~40% of data showed small relative bias within ±15%. The results are further complicated when the cloud is inhomogeneous. Also, the results indicated that the pixel size is less important when the cloud is homogeneous.

The domain mean LWP bias is ±10 g m^{-2} for most-homogeneous scenes and a larger underestimation in most heterogeneous scenes is observed. The retrieved τ for the most-homogeneous clouds agreed very well to the LES true τ in all Sun-view geometry. The bias between LES and retrieved τ varies ~0 – 1.5. The minimum bias is seen at the nadir view ($\theta=0^o$) especially in low Sun regardless of scattering direction (φ). The maximum τ bias is seen at low Sun ($\theta_o=60^o$) and oblique view ($\theta=70^o$) especially in the forward scattering ($\varphi=30^o$) direction. However, large discrepancies are observed in the heterogeneous cloud scenes. In most cases, an underestimation in retrieved τ is observed in the overhead Sun ($\theta_o=0^o$) regardless of viewing and scattering angles (θ, φ). This is possible because, when the clouds are broken, the radiation (photon) can escape from the cloudy to clear pixels, or,

thicker to thinner pixels, and results less photon available to backscatter. In the oblique view ($\theta=70^o$) the retrieved τ is underestimated mostly in the forward scattering ($\varphi=30^o$) direction. The bias in domain mean τ is negligible and is <1. The bias is larger for the within-cloud means of 1 km pixels, and maximum bias (overestimation in retrieved τ) is as large as ~25, and is seen in nadir views at oblique Sun, and a small underestimation in overhead Sun and the mean bias is as large as ~5 is seen. For the homogeneous cloud scenes, the retrieved r_e is fairly agreed with the LES r_e. For the domain mean case, mean r_e bias between LES and retrieval is mostly negative indicating an overestimation in retrieved r_e, and the overestimation (bias) is ~0-3 μm. For the heterogeneous cloud scenes, an unbiased mean r_e is observed in the domain mean. However, individually, in the within-cloud means retrieved r_e overestimated especially in nadir view and high Sun, probably compensating for the underestimation of retrieved τ.

In the homogeneous cloud scenes, the retrieved effective radius agreed well with the true value from LES within 2%, the retrieved optical thickness agreed with 10% underestimation compared to LES values, and finally the retrieved LWP agreed well with LES values within 10% underestimation. Moreover, these homogeneous scenes did not show much variability with solar zenith angles. In the most heterogeneous cloud scenes, the retrieved domain mean effective radius show good agreement with LES true values in all solar zenith angle. However, the retrieved domain mean optical thickness agreed with LES true value upto the solar zenith angle of 50^o and thereafter an increase towards higher solar zenith angles. At 70^o solar zenith angle the retrieved optical thickness is four times larger than the true LES value. Thus, 20-30% underestimation is observed in the solar zenith angles below 50^o, a very good agreement at 60^o solar zenith angle, and the retrieved LWP doubles at 70^o solar zenith angle.

Furthermore, the view angle dependency of cloud scenes has been examined. In homogeneous scenes, the retrieved LWP at different solar zenith angles agreed within 5% with LES LWP, except the underestimation in retrieval in the very oblique view in the forward scattering direction - this underestimation is mainly from the optical thickness underestimation. Otherwise an unbiased optical thickness is retrieved. The effective radius overestimated the true LES by 1 – 1.5 μm. In the most heterogeneous portion of cloud scenes the retrieved LWP underestimated in all solar zenith angles except at 60^o solar zenith angle in the backward scattering direction. This underestimation in LWP is further increased with view zenith angle and larger in the forward scattering direction than in the backward scattering direction.

We have prepared an error table to represent the LWP error in most-homogeneous and heterogeneous clouds at different Sun-view geometry. For the homogeneous cloud scenes the relative bias in τ is ± 5% in all the Sun-view geometry except at very low Sun and very oblique view especially in the most forward and most backward direction. Effective radius is mostly overestimated and the relative bias varied from 5 to 25%. The relative bias in LWP is also between ± 10% in most of the Sun-view geometry. In heterogeneous scenes, the retrieved LWP underestimated at all solar zenith angles except at the very low Sun of 60^o and 70^o where they showed an overestimation. The relative bias in retrieved LWP is within 40% except 70^o solar zenith angle. The retrieved effective radius showed an overestimation compared to LES values in all Sun-view geometry and the relative bias in r_e varied from 5% to 45%. The optical thickness underestimated in general in all solar zenith angles except at very low Sun of 60^o and 70^o. The relative bias (underestimation) is roughly 2 to 30%. However, in 60^o solar zenith angle in retrieved τ showed large overestimation compared to true τ from LES, and the relative bias in τ at this solar angle can go even up to 100% especially at nadir view.

Finally, we examined optimal Sun-view geometry for the minimum retrieval bias in τ. When the minimum bias is binned according to viewing angle, maximum (35%) number of minimum bias is seen in 30^o (in total 83% of scenes showed minimum bias in altogether 30^o, 45^o, 60^o view zenith angle). When the bias is binned according to azimuth angle, 70% of clouds showed minimum bias either in side/backscattered direction. Maximum scenes showed minimum bias at 60^o solar zenith angle, mostly due to the cancellation of errors due to cloud side illumination and shadowing.

Chapter 6
Conclusions and Future Scope

The weakest link in climate simulations is the poor representation of clouds, particularly of marine boundary layer clouds, which constitute the main source of uncertainty in modeled cloud feedbacks [*Bony and Dufresne*, 2005]. The dominant part of predicted global cloud forcing change is produced by these ubiquitous warm clouds, the radiative fluxes of which are very sensitive to their vertically integrated liquid water content or liquid water path (LWP) [*Turner et al.*, 2007]. However, both the satellite observations [*Greenwald et al*., 2007; *Horváth and Davies*, 2007] and the climate model simulations [*Cess et al*., 1989; *O'Dell et al.,* 2008; *Roebeling and van Meijgaard,* 2009] show considerable discrepancies in the global distribution and also in the diurnal cycle of this quantity. Therefore, climate-modeling efforts would greatly benefit from accurate cloud LWP measurements with well-established error characteristics. Evaluating two fully independent satellite methods (microwave and vis/near-infrared) against each other using a large set of coincident retrievals could reveal major algorithmic shortcomings. The main source of error is cloud-rain separation in microwave techniques and 3D radiative effects in plane-parallel VNIR retrievals. In addition, both methods suffer from unresolved sub-pixel-scale variability. Our aim is to make a step toward creation of a consensus satellite cloud liquid water climatology that might be more useful in constraining global climate models than existing datasets. More precisely, the research objectives are: i) better constraining cloud liquid water path by systematically investigating inconsistencies between microwave and VNIR cloud liquid water path estimates and ii) better understanding of observed retrieval differences, by combining simulated cloud fields and 3D radiative transfer models. In this dissertation, our objective is addressed in Chapter 3 to 5 and the key results are summarized in this chapter.

6.1. Conclusions

In Chapter 3 we assessed one year of AMSR-E Wentz and MODIS cloud liquid water path estimates, representing the current state-of-the-art in microwave and VNIR retrievals. The comparison was made over the global oceans on a quarter-degree resolution and only included non-raining warm clouds in order to avoid ambiguities due to rain and ice. Our goal was to characterize microwave-VNIR LWP differences in a statistically robust dataset, and identify their potential causes for future studies. Main findings are:

- When all scenes were considered, AMSR-E overestimated MODIS by 45% on average, and retrievals were only moderately correlated with a coefficient of 0.74.
- In broken scenes, AMSR-E increasingly overestimated MODIS and retrievals became gradually uncorrelated as cloud fraction decreased.
- In overcast scenes, estimates were generally better correlated at 0.83, but with significant regional variations and also characterized by a MODIS high bias (Microwave and VNIR retrievals are most consistent in extensive marine Sc clouds with correlations up to 0.95 and typical rms differences of 15 g m^{-2}).
- The overall MODIS high LWP bias in overcast domains could be removed, in a global mean sense, by adiabatic correction; however large regional differences remained.
- MODIS showed strong overestimations at high latitudes, which we traced to 3D effects in plane-parallel VNIR retrievals over heterogeneous clouds at low Sun.
- In the tropics/subtropics, AMSR-E – MODIS LWP differences also depended on cloud type, with MODIS overestimating in stratiform and underestimating in cumuliform clouds, resulting in large-scale coherent bias patterns where marine Sc transitioned into trade wind Cu. We concluded that this bias pattern emerges due to geographic variations in droplet effective radius profile affecting VNIR retrievals, as well as due to uncertainties in cloud temperature parameterization affecting microwave retrievals.
- Cloud-rain partitioning was found to introduce a systematic low bias in Wentz retrievals above 180 g m^{-2} as the microwave algorithm erroneously assigned an increasing portion of the liquid water content of thicker non-precipitating clouds to rain.

In Chapter 4 we evaluated the diurnal cycle of South Atlantic marine boundary layer clouds and its seasonal variability using one year long cloud microphysical and optical properties from SEVIRI VNIR measurements, as well as cloud liquid water path from TMI microwave observations. We further investigated the sub-pixel-scale variability in SEVIRI VNIR cloud retrievals using high resolution MODIS VNIR retrievals. The main findings are:

- Best agreement between SEVIRI VNIR and TMI microwave technique is observed over the marine Sc region, with least bias within ±5 g m^{-2} and high correlation of 0.9.
- The largest disagreement is observed in the trade wind Cu, due to the deficit in both microwave and VNIR measurement technique (addressed in Chapter 3) in the partial cloudy scenes. However, SEVIRI and TMI showed similar variations in diurnal cycle of LWP but with a constant large bias of ~20 g m^{-2} (TMI being larger than SEVIRI).

- The diurnal cycles of TMI and SEVIRI LWP were in good agreement within ±10 g m^{-2} in all seasons (after neglecting aerosol affected pixels). Both TMI and SEVIRI LWP decreased from morning to late afternoon and thereafter a slight increase was observed. The diurnal variation of SEVIRI LWP followed the variation in cloud optical thickness and in fact the cloud fraction and cloud physical thickness; whereas droplet effective radius and droplet number concentration showed negligible variability with time.
- Comparison of SEVIRI and MODIS LWP showed excellent agreement with correlation above 0.9 in the fully overcast cases; however, high MODIS values are observed over broken clouds. We noticed that the use of 1.6 μm channel effective radius applies automatic adiabatic correction to the Sc clouds in SEVIRI LWP retrievals, otherwise a 5/6 correction factor has to be applied for MODIS LWP retrievals (which is based on 2.2 μm channel retrieved effective radius) while comparing them with microwave retrieved LWP.
- We investigated the influence of absorbing aerosols over the Sc domain using aerosol index from OMI. Interestingly, both TMI and SEVIRI LWP increased with aerosol index, but the TMI increase was considerably larger. This was because absorbing aerosols above liquid clouds introduced substantial negative retrieval biases in optical thickness and droplet effective radius and, hence, in the deduced LWP in SEVIRI VNIR retrievals. This SEVIRI LWP bias increased with aerosol index and the mean bias is 27 g m^{-2}.

In Chapter 5 we quantified the uncertainties in (1D) plane-parallel VNIR satellite retrievals from hundreds of LES simulated cloud fields and a 3D radiative transfer model. The 1D retrievals (of 3D radiances) are done for ~650 cloud fields consisting of stratocumulus, unbroken stratus, to broken trade cumulus clouds, at 200 distinct Sun-view geometry. The retrieved cloud properties are compared back to the true LES cloud properties and the retrieval errors has been quantified. The key findings are:

- The 3D radiances of Sc follows plane-parallel theory very well (i.e., at oblique Sun, radiances increased with viewing angle, and the increase is 2–3 times larger in the forward scattering direction than the backscatter direction; at high Sun, radiances decrease with viewing angle). Nevertheless, for a broken shallow Cu, the increase in radiance with view zenith angle is less pronounced, and a general underestimation in visible radiance is noticed. Besides, the plane-parallel model radiance decreased from

medium to larger values of solar zenith angle, however, 3D radiance increased with solar zenith angle. This increase is larger in both Sc and shallow Cu, except a strong underestimation of shallow Cu radiance at high Sun.

- The pixel-level analysis showed that most homogeneous one-third scenes exhibited narrow Gaussian distribution, but skewed negatively, indicating the overestimation in retrieved LWP. Roughly 40-60% of the data showed the relative LWP bias within ±15% depending on SZA, however, most heterogeneous scenes showed much wider distribution with more than one peak, but skewed negatively, and only 10-25% of datasets are within ±15% relative bias.
- The domain mean LWP bias is ±10 g m^{-2} for most homogeneous scenes; however large underestimation is observed for most heterogeneous scenes. Also, the retrieved LWP did not show any variability with SZA for homogeneous scenes, however, for heterogeneous scenes an increase in retrieved LWP with SZA is observed, provided that, 20-30% underestimation in high to medium Sun, agreement at 60^o Sun, and large overestimation (LWP doubles) thereafter.
- For the homogeneous cloud scenes, the retrieved LWP did not show much variability with view zenith angle, and agrees within 5-10% relative error. However, for heterogeneous scenes, LWP decreased with viewing angle, and the decrease is largest in the forward scattering direction, and less pronounced in the backscatter direction.
- We have prepared an error table to represent the LWP error in homogeneous and heterogeneous clouds at different Sun-view geometry. For the homogeneous clouds, the relative LWP bias is within ±10% for most of the Sun-view geometry. Nevertheless for the heterogeneous clouds the relative bias is within 40% when SZA below 60^o and is larger for all other solar angles.
- A multi-linear regression model has been fitted to predict the bias and relative bias in retrieved cloud optical thickness and LWP, using true optical thickness and different heterogeneity measures. The prediction was better for Sun angle below 60^o (with multi-linear correlation coefficient of 0.9), and above which the relationship breaks.
- We examined optimal Sun-view geometry for the minimum (min) retrieval bias in τ. When the min bias is binned according to VZA, maximum no. of min bias is seen in 30^o (in total 83% of scenes showed min bias in altogether 30^o, 45^o, 60^o VZA). When it is binned according to azimuth angle, 70% of clouds shown min bias either in

side/backscatter direction. Maximum scenes showed min bias at 60^o SZA, mostly cancellation of errors due to the cloud side illumination and shadow viewing.

6.2. Future Scope

Our study interpreted many key issues in plane-parallel VNIR and microwave cloud retrievals. Nevertheless, the study is limited in certain aspects and one can elaborate this work by considering the following points.

- The 1D cloud retrievals were done only for few selected Sun-view geometries, as it consumes lot of computation power and time. However, if possible one should repeat the retrievals of all the cloud fields with very fine 1^o resolution of Sun-view geometry. This is essential to sort-out the transition in retrieval bias of cloud properties with respect to different Sun-view geometry.
- We estimated uncertainty in cloud retrievals only in 1D VNIR techniques. As we learnt that similar problem persists in microwave techniques as well, one should apply microwave retrieval algorithm for all these known cloud fields and evaluate microwave retrieved LWP errors. Simultaneous cloud retrievals from both VNIR and microwave techniques could be an additional benefit to estimate the contribution of errors from individual techniques.
- We have estimated the retrieval errors only from few hundred cloud fields. To implement these error estimates in operational cloud retrievals algorithms (e.g., MODIS), one should consider thousands of cloud fields which satisfy different type of existing real clouds.
- We retrieved droplet effective radius only from 2.13 μm channel radiance (because MODIS computes LWP using effective radius retrieved from 2.13 μm channel). However, one can retrieve effective radius at different wavelengths, for e.g., 1.6 μm and 3.17 μm. These wavelengths sample clouds at different levels. Hence one can estimate the r_e profile and compare with the true LES profile, and also can learn the cause for observed differences between retrieved and LES truth.
- We built a multi-linear regression model to predict the error in retrieved cloud optical thickness. A non-linear correction scheme, such as a neuronet, could be developed instead of a multi-linear regression model. The multi-linear regression model was really just a toy model to drive home the point that the errors are dependent on heterogeneity, SZA, VZA, etc. and a simple linear regression can demonstrate it, especially for

domain means. But any practical scheme has to take into account the fact that the errors are NON-LINEARLY depend on parameters such as VZA, SZA, heterogeneity.

- Finally, this study is performed only for the non-raining liquid clouds. The analysis can be repeated for raining or mixed-phase or ice phase clouds.

References

Ackerman, A. S., O.B. Toon, and P.V. Hobbs (1995), Numerical modeling of ship tracks produced by injections of cloud condensation nuclei into marine stratiform clouds. *J. Geophys. Res.*, 100, 7121-7133, doi:10.1029/95JD00026.

Bennartz, R. (2007), Global assessment of marine boundary layer cloud droplet number concentration from satellite, *J. Geophys. Res.*, *112*, D02201, doi:10.1029/2006JD007547.

Bennartz, R. and Harshvardhan (2007), Correction to "Global assessment of marine boundary layer cloud droplet number concentration from satellite", *J. Geophys. Res.*, *112*, D16302, doi:10.1029/2007JD008841.

Blaskovic, M., R. Davies, J.B. Snider (1990), Diurnal variation of marine stratocumulus over San Nicolas island during July, 1987, C2GGR Report No. 90-6

Boers, R., J. R. Acarreta, and J. L. Gras (2006), Satellite monitoring of the first indirect aerosol effect: Retrieval of the droplet concentration of water clouds, *J. Geophys. Res.*, 111, D22208, doi:10.1029/2005JD006838.

Bony, S., and J. L. Dufresne (2005), Marine boundary layer clouds at the heart of tropical cloud feedback uncertainties in climate models, *Geophys. Res. Lett.*, *32*, L20806, doi:10.1029/2005GL023851.

Borg, L. A., and R. Bennartz (2007), Vertical structure of stratiform marine boundary layer clouds and its impact on cloud albedo, *Geophys. Res. Lett*., *34*, L05807, doi:10.1029/2006GL028713.

Brenguier, J. L., H. Pawlowska, L. Schüller, R. Preusker, J. Fischer, Y. Fouquart (2000), Radiative Properties of Boundary Layer Clouds: Droplet Effective Radius versus Number Concentration, *J. Atmos. Sci*. 57, 803-821.

Breon, F. M (1992), Reflectance of broken cloud fields: Simulation and parameterization, *J. Atmos. Sci*., 49, 1221-1232.

Bréon, F. M., and M. Doutriaux-Boucher (2005), A comparison of cloud droplet radii measured from space, *IEEE. Trans. Geosc. Rem. Sens.*, *43*, 1796-1805.

Buriez, J.-C., M. Doutriaux-Boucher, F. Parol, and N. G. Loeb (2001), Angular Variability of the Liquid Water Cloud Optical Thickness Retrieved from ADEOS–POLDER. *J. Atmos. Sci*., 58(20), 3007-3018.

Cahalan, R. F., W. Ridgway, W. J. Wiscombe, T. L. Bell, and J. B. Snider (1994), The albedo of fractal stratocumulus clouds, *J. Atmos. Sci*., *51*, 2434-2455.

Cess et al. (1989), Interpretation of Cloud-Climate Feedback as Produced by 14 Atmospheric General Circulation Models, *Science* 245: 513-16

Chang F.-L., and Z. Li (2003), Retrieving vertical profiles of water-cloud droplet effective radius: Algorithm modification and preliminary application, *J. Geophys. Res.*, *108*(D24), 4763, doi:10.1029/2003JD003906.

Chen, R., F.-L. Chang, Z. Li, R. Ferraro, and F. Weng (2007), Impact of the vertical variation of cloud droplet size on the estimation of cloud liquid water path and rain detection, *J. Atmos. Sci.*, *64*, 3843-3853.

Chen, R., R. Wood, Z. Li, R. Ferraro, and F.-L. Chang (2008), Studying the vertical variation of cloud droplet effective radius using ship and space-borne remote sensing data, *J. Geophys. Res.*, *113*, D00A02, doi:10.1029/2007JD009596.

Chin, M., R. A. Kahn, and S. S.E. (2009), *Atmospheric Aerosol Properties and Climate Impacts*, 139 pp., U.S. Climate Change Science Program Synthesis and Assessment Product 2.3.

Ciesielski, P.E., W. H. Schubert, R. H. Johnson (2001), Diurnal Variability of the Marine Boundary Layer during ASTEX*, J. Atmos. Sci.* 58, 2355-2376.

Coakley, J. A., and R. Davies (1986), The effect of cloud sides on reflected solar radiation as deduced from satellite observations. *J. Atmos. Sci*., 43(10), 1025-1035.

Coddington, O. M., P. Pilewskie, J. Redemann, S. Platnick, P. B. Russell, K. S. Schmidt, W. J. Gore, J. Livingston, G. Wind, and T. Vukicevic (2010), Examining the impact of overlying aerosols on the retrieval of cloud optical properties from passive remote sensing, *J. Geophys. Res.*, *115*, D10211, doi:10.1029/2009JD012829

Cornet, C., H. Isaka, B. Guillemet, and F. Szczap (2004), Neural network retrieval of cloud parameters of inhomogeneous clouds from multispectral and multiscale radiance data: Feasibility study. *J. Geophys. Res*., 109, doi:10.1029/2003JD004186.

Cornet, C., J.-C. Buriez, J. Riédi, H. Isaka, and B. Guillemet (2005), Case study of inhomogeneous cloud parameter retrieval from MODIS data, *Geophys. Res. Lett.*, *32*, L13807, doi:10.1029/2005GL022791.

Dagestad, K. F. (2005), Estimating global radiation at ground level from satellite images. Ph.D. thesis University Bergen, 98pp.

Davies, R. (1984), Reflected solar radiances from broken cloud scenes and the interpretation of scanner measurements. *J. Geophys. Res*., 89, 1259-1266, doi:10.1029/JD089iD01p01259.

Davis, A., A. Marshak, R. F. Cahalan, and W. J. Wiscombe (1997), The Landsat scale break in stratocumulus as a three-dimensional radiative transfer effect, Implications for cloud remote sensing, *J Atmos. Sci*., 54, 241-260.

Duykerke, P.G., S. R. De Roode, M. C. Van Zanthen, J. Calvo, J. Cuxart, S. Cheinet, A. Chlond, H. Grenier, P. J. Jonker, M. Köhler, G. Lenderink, David Lewellen, C. Lappen, A. P. Lock, C. Moeng, F. Müller, D. Olmed, J. Piriou, E. Sanchez, I. Sednev (2004), Observations and numerical simulations of the diurnal cycle of the EUROCS stratocumulus case, *Q. J. R. Meteorol. Soc*. 130, 3269-3296 doi: 10.1256/qj.03.139

Duynkerke, P. G., J. Teixeira (2001), Comparison of the ECMWF reanalysis with FIRE I observations: Diurnal variation of marine stratocumulus. *J. Climate*, 14, 1466-1478.

Evans, K. F (1998), The spherical harmonic discrete ordinate method for three-dimensional atmospheric radiative transfer, *J. Atmos. Sci*., 55, 429-446

Evans, K. F. (2007), SHDOMPPDA: A radiative transfer model for cloudy sky data assimilation. *J. Atmos. Sci*., 64, 3854-3864. doi:10.1175/2006JAS2047.1

Evans, K. F., A. Marshak, and T. Várnai (2008), The potential for improved boundary layer cloud optical depth retrievals from the multiple directions of MISR, *J. Atmos. Sci.*, *65*, 3179-3196. doi:10.1175/2008JAS2627.1.

Fairall, C.W., J.E. Hare, J. B. Snider (1990), An eight-month of marine stratocumulus cloud fraction, albedo, and integrated liquid water*, J. Climate*, 3, 847-864.

Forster, P., et al. (2007), Changes in atmospheric constituents and in radiative forcing, in Climate Change 2007: The Physical Science Basis. Contribution of Working Group I to the Fourth Assessment Report of the *Intergovernmental Panel on Climate Change*, edited by S. Solomon et al., pp. 130–234, Cambridge Univ. Press, New York.

Genkova, I., and R. Davies (2003), Spatial heterogeneity of reflected radiance from globally distributed clouds. *Geophy. Res. Let*., 30, doi:10.1029/2003GL018194.

Girolamo, L., L. Liang, and S. Platnick (2010), A global view of one-dimensional solar radiative transfer through oceanic water clouds. *Geophy. Res. Let*., 37, doi:10.1029/2010GL044094.

Greenwald T.J (2009), A 2 year comparison of AMSR-E and MODIS cloud liquid water path observations, *Geophys Res Lett*, *36*, L20805.

Greenwald, T. J., S. A. Christopher, and J. Chou (1997), Cloud liquid water path comparisons from passive microwave and solar reflectance satellite measurements: Assessment of sub-field-of-view clouds effects in microwave retrievals, *J. Geophys. Res.*, *102*, 19,585-19,596.

Greenwald, T. J., T. S. L'Ecuyer, and S. A. Christopher (2007), Evaluating specific error characteristics of microwave-derived cloud liquid water products, *Geophys. Res. Lett.*, *34*, L22807, doi:10.1029/2007GL031180.

Greuell, W., and R. A. Roebeling (2009), Toward a Standard Procedure for Validation of Satellite-Derived Cloud Liquid Water Path: A Study with SEVIRI Data, *Journal of Applied Meteorology and Climatology*, *48*, 1575-159010.1175/2009jamc2112.1.

Gultepe, I., G. A. Isaac (2004), Aircraft observations of cloud droplet number concentration: Implications for climate studies, *Q. J. R. Meteorol. Soc*. 130, 2377-2390 doi: 10.1256/qj.03.120.

Han Q, W.B. Rossow, A.A. Lasis (1994), Near-Global Survey of Effective Droplet Radii in Liquid Water Clouds Using ISCCP Data, *J. Climate* 7, 465-497

Hansen, J. E. (1969), Exact and approximate solutions for multiple scattering by cloudy and hazy planetary atmospheres. *J. Atmos. Sci*, 26(3), 478-487.

Hartmann, D.L., M.E. Ockert-Bell, and M.L. Michelsen (1992), The effect of cloud type on Earth's energy-balance-global analysis. *J. Climate* 5: 1,281-1,304.

Haywood, J. M., S. R. Osborne, and S. J. Abel (2004), The effect of overlying absorbing aerosol layers on remote sensing retrievals of cloud effective radius and cloud optical depth, *Q. J. R. Meteorol. Soc.*, *130*, 779-800.

Henrich, F., H. Siebert, E. Jäkel, R. A. Shaw, and M. Wendisch (2010), Collocated measurements of boundary layer cloud microphysical and radiative properties: A feasibility study, *J. Geophys. Res*., 115, D24214, doi:10.1029/2010JD013930.

Hilburn, K. A., and F. J. Wentz (2008), Intercalibrated passive microwave rain products from the Unified Microwave Ocean Retrieval Algorithm (UMORA), *J. Appl. Meteor. Climatol*., *47*, 778-794.

Hobbs, P. V (2002), Clean air slots amid atmospheric pollution, *Nature,* 415, 861, 2002.

Horváth, Á., and C. Gentemann (2007), Cloud-fraction-dependent bias in satellite liquid water path retrievals of shallow, non-precipitating marine clouds, *Geophys. Res. Lett*., *34*, L22806, doi:10.1029/2007GL030625.

Horváth, Á., and R. Davies (2004), Anisotropy of water cloud reflectance: A comparison of measurements and 1D theory, *Geophys. Res. Lett.*, *31*, doi:10.1029/2003GL018386.

Horváth, Á., and R. Davies (2007), Comparison of microwave and optical cloud water path estimates from TMI, MODIS, and MISR, *J. Geophys. Res.*, *112*, D01202, doi:10.1029/2006JD007101.

Iwabuchi, H. (2007), Retrieval of cloud optical thickness and effective radius using multispectral remote sensing and accounting for 3D effects. *Light. Scattering. Reviews*., 2, 97-124.

Iwabuchi, H., and T. Hayasaka (2002), Effects of cloud horizontal inhomogeneity on the optical thickness retrieved from moderate-resolution satellite data. *J. Atmos. Sci*., 59, 2227-2242.

Iwabuchi, H., and T. Hayasaka (2003), A multi-spectral non-local method for retrieval of boundary layer cloud properties from optical remote sensing data. *Remote Sens. Environ*., 88, 294-308

Jakob, C. (1999), Clouds in the ECMWF re-analysis. *J. Climate*, 12, 947–959

Johnson, B. T., K.P. Shine, P.M. Forster (2004), The semi-direct aerosol effect: Impact of absorbing aerosols on marine stratocumulus, *Q. J. R. Meteorol. Soc.,* 130, 1407-1422.

Kato, S., and A. Marshak (2009), Solar zenith and viewing geometry-dependent errors in satellite retrieved cloud optical thickness : Marine stratocumulus case. J. *Geophy. Res*., 114, doi:10.1029/2008JD010579.

Kato, S., L. M. Hinkelman, and A. Cheng (2006), Estimate of satellite-derived cloud optical thickness and effective radius errors and their effect on computed domain-averaged irradiances. *J. Geophy. Res*., 111, doi:10.1029/2005JD006668.

Klein S.A., D. L. Hartmann (1993), The seasonal cycle of low stratiform clouds, *J.Climate*, 6, 1587-1606.

Kobayashi, T. (1993), Effects due to cloud geometry on biases in the albedo derived from radiance measurements, *J. Climate*., 6, 120-128.

Lafont, D., and B. Guillemet (2004), Subpixel fractional cloud cover and inhomogeneity effects on microwave beam-filling error, *Atmospheric Research*, *72*, 149-168.

Lebsock, M. D., G. L. Stephens, and C. Kummerow (2008). Multisensor satellite observations of aerosol effects on warm clouds, *J. Geophys. Res.*, *113*, D15205, doi:10.1029/2008JD009876.

Li, J. F., D. Waliser, C. Woods, J. Teixeira, J. Bacmeister, J. Chern, B.W. Shen, A. Tompkins, W.K. Tao, M. Köhler (2008), Comparisons of satellites liquid water estimates to ECMWF and GMAO analyses, 20th century IPCC AR4 climate simulations, and GCM simulations, *Geophy Res. Let*, 35, L19710, doi:10.1029/2008GL035427

Liang, L., L. Di Girolamo, and S. Platnick (2009), View-angle consistency in reflectance, optical thickness and spherical albedo of marine water clouds over the northeastern Pacific through MISR-MODIS fusion, *Geophys. Res. Lett*., 36, L09811, doi:10.1029/2008GL037124.

Liou, K.-N., Q. Fu, and T. Ackerman (1988), A simple formulation of the delta-four-stream approximation for radiative transfer parameterizations. *J. Atmos. Sci*., 45, 1940-1948.

Loeb, N. G., and J. A. Coakley Jr. (1998), Inference of marine stratus cloud optical depths from satellite measurements: Does 1D theory apply?, *J. Clim*., *11*, 215-233.

Loeb, N. G., and R. Davies (1996), Observational evidence of plane parallel model biases: Apparent dependence of cloud optical depth on solar zenith angle, *J. Geophys. Res*., *101*, 1621-1634.

Loeb, N. G., and R. Davies (1997), Angular dependence of observed reflectances: A comparison with plane parallel theory. *J. Geophy. Res*., 102(D6), 6865-6881. doi:10.1029/96JD03586.

Loeb, N. G., T. Várnai, and D. M. Winker (1998), Influence of subpixel-scale cloud-top structure on reflectances from overcast stratiform cloud layers, *J. Atmos. Sci*., *55*, 2960-2973.

Loeb, N. G., T. Várnai, and R. Davies (1997), Effect of cloud inhomogeneities on the solar zenith angle dependence of nadir reflectance. *J. Geophy. Res*., 102, 9387-9395. doi:10.1029/96JD03719.

Ma, C.-C., C.R. Mechoso, A. W.Robertson, A. Arakawa (1996), Peruvian stratus clouds and the tropical Pacific circulation: A coupled ocean-atmosphere GCM study. *J. Climate*, 9, 1635-1645.S

Mace, G. G. (2010), Cloud properties and radiative forcing over the maritime storm tracks of the Southern Ocean and North Atlantic derived from A-Train, *J. Geophys. Res.*, 115, D10201, doi:10.1029/2009JD012517.

Maddux, B. C., S. A. Ackerman, and S. Platnick (2010), Viewing geometry dependencies in MODIS cloud products. *J. Atmos. Oceanic. Tech*, 27(9), 1519-1528.

Malte, R., L. Nuijens, and B. Stevens (2011), Cloud feedbacks in a constant relative humidity atmosphere, *J. Atmos. Sci*. (submitted)

Manabe and Strickler 1964, Thermal Equilibrium of the Atmosphere with a Convective Adjustment, *J. Atmos. Sci*. 21: 361-385

Manabe and Wetherald 1967, Thermal equilibrium of the atmosphere with a given distribution of relative humidity, *J. Atmos. Sci.* 24:241-259

Marchand, R., and T. Ackerman (2004), Evaluation of radiometric measure- ments from the NASA Multiangle Imaging Spectroradiometer (MISR): Two- and three-dimensional radiative transfer modeling of an inhomoge- neous stratocumulus cloud deck, *J. Geophys. Res*., 109, D18208, doi:10.1029/2004JD004710.

Marshak, A., A. Davis, R. F. Cahalan, and W. J. Wiscombe (1998), Nonlocal independent pixel approximation: Direct and inverse problems. *IEEE Trans. Geosci. Remote Sens*., 36, 192-204.

Marshak, A., A. Davis, W. J. Wiscombe, and R.F. Cahalan (1995), Radiative smoothing in fractal clouds, *J. Geophys. Res*., 100, 26,247- 26,261.

Marshak, A., S. Platnick, T. Várnai, G. Wen, and R. F. Cahalan (2006), Impact of three-dimensional radiative effects on satellite retrievals of cloud droplet sizes, *J. Geophys. Res*., *111*, D09207, doi:10.1029/2005JD006686.

McGill, M. J., D.L. Hlavka, W.D. Hart, E.J. Welton, E. J. J.R. Campbell (2003), Airborne lidar measurements of aerosol optical properties during SAFARI-2000, *J. Geophys. Res*., 108, 8493, doi:10.1029/2002JD002370.

Medeiros, B. B. Stevens (2011), Revealing differences in GCM representations of low clouds, *Clim. Dyn*. 36, 385-399, DOI 10.1007/s00382-009-0694-5.

Meirink, J.F., R. Roebeling, E. Wolters and H. Deneke (2010), Cloud Physical Products AVHRR / SEVIRI, Algorithm Theoretical Basis Document, EUMETSAT SAF/CM/KNMI/ATBD/CPP 1.0.

Meirink, J.F., R.A. Roebeling and P. Stammes (2009), Atmospheric correction for the KNMI Cloud Physical Properties retrieval algorithm, KNMI publication: TR-304, 17/2/2009, pp22.

Miller, R. L (1997), Tropical thermostats and low cloud cover. *J. Climate*, 10, 409-440.

Minnis, P. (1989), Viewing zenith angle dependence of cloudiness determined from coincident GOES East and GOES West data, *J. Geophys. Res*., 94, 2303–2320.

Minnis, P., E.F. Harrison (1984), Diurnal variability of regional cloud and clear-sky radiative parameters derived from GOES data. Part I: Analysis method, *J. Climate*, 23, 993-1011.

Minnis. P., and Smith, W. L., Jr. (1998), Cloud and radiative fields derived from GOES-8 during SUCCESS and the ARM-UAV spring 1996 flight series. *Geophys. Res. Lett*., 25, 1113-1116.

Nakajima T. Y., T. Nakajima (1995), Determination of Cloud Microphysical Properties from NOAA-17 Measurements for FIRE and ASTEX regions., *J. Atmos. Sci.,* 52, 4043-4059.

Nakajima, T., and M. D. King (1990), Determination of the optical thickness and effective particle radius of clouds from reflected solar radiation measurements, I, Theory, *J. Atmos. Sci.*, *47*, 1878-1893.

Nigam, S. (1997), The annual warm to cold phase transition in the eastern equatorial pacific: Diagnosis of the role of stratus cloud-top cooling. *J. Climate*, 10, 2447-2467.

O'Dell, C. W., F. J. Wentz, and R. Bennartz (2008), Cloud liquid water path from satellite-based passive microwave observations: A new climatology over the global oceans, *J. Clim.*, *21*, doi:10.1175/2007JCLI1958.1.

Oreopoulos, L., A. Marshak, R. F. Cahalan, and G. Wen (2000), Cloud three-dimensional effects evidenced in Landsat spatial power spectra and autocorrelation functions, *J. Geophys. Res*., 105, 14,777- 14,788.

Oreopoulos, L., and R. Davies (1998), Plane parallel albedo biases from satellite observations. Part I: Dependence on resolution and other factors. *J. Climate*., 11(5), 919-932.

Oreopoulos, L., and R. F. Cahalan (2005), Cloud inhomogeneity from MODIS, *J. Clim.*, *18*, 5110-5124.

Oreopoulos, L., R. F. Cahalan, and S. Platnick (2007), The plane-parallel albedo bias of liquid clouds from MODIS observations. *J. Climate*., 20, 5114-5125. doi:10.1175/JCLI4305.1

Oreopoulos, L., S. Platnick, G. Hong, P. Yang, and R. F. Cahalan (2009): The shortwave radiative forcing bias of liquid and ice clouds from MODIS observations. *Atmos. Chem. Phys*., 9, 5865–5875

Philander, S. G. H., Gu, D., Halpern, D., G. Lambert, N.C. Lau, T. Li, R.C. Pacanowski (1996), Why the ITCZ is mostly north of the equator. *J. Climate*, 9, 2958-2972.

Pincus, R, and K. F., Evans (2009), Computational cost and accuracy in calculating three-dimensional radiative transfer: results for new implementations of Monte Carlo and SHDOM *J. Atmos. Sci.* 66 3131-46

Pincus, R., and B. Stevens (2009), Monte Carlo spectral integration: A consistent approximation for radiative transfer in large eddy simulations. *J. Adv. Model. Earth Syst*., 1 (1), doi:10.3894/ JAMES.2009.1.1.

Platnick, S. (2000), Vertical photon transport in cloud remote sensing problems, *J. Geophys. Res*., 105, 22,919-22,935.

Platnick, S., M. D. King, S. A. Ackerman, W. P. Menzel, B. A. Baum, J. C. Riedi, and R. A. Frey (2003), The MODIS cloud products: algorithms and examples from Terra, *IEEE Trans. Geosci. Remote Sens.*, 41, 459-473.

Randall, D.A., J. A. Coakley Jr., C. W. Fairall, R. A. and D. H. Lenschow (1984): Outlook for research on subtropical marine stratiform clouds. *Bull. Am. Met. Soc*., 65, 1290 – 1301.

Randles, C.A., V. Ramaswamy (2010), Impacts of absorbing biomass burning aerosol on the climate of southern Africa: a Geophysical Fluid Dynamics Laboratory GCM sensitivity study, *Atmos. Chem. Phys. Discuss*. 10, 9731-9752.

Rauber, R. M., et al. (2007), Rain in shallow cumulus over the ocean - The RICO campaign. *Bull. American Meteorol. Soc*., 88 (12), 1912.

Roebeling, R. A., A. J. Feijt, and P. Stammes (2006), Cloud property retrievals for climate monitoring: Implications of differences between Spinning Enhanced Visible and Infrared Imager (SEVIRI) on METEOSAT-8 and Advanced Very High Resolution Radiometer (AVHRR) on NOAA-17, *J. Geophys. Res.*,,*111*D20210 10.1029/2005jd006990.

Roebeling, R. A., and E. van Meijgaard (2009), Evaluation of the Daylight Cycle of Model-Predicted Cloud Amount and Condensed Water Path over Europe with Observations from MSG SEVIRI, *J. Climate*, *22*, 1749-176610.1175/2008jcli2391.1.

Roebeling, R. A., H. M. Deneke, and A. J. Feijt (2008a), Validation of cloud liquid water path retrievals from SEVIRI using one year of CloudNET observations, *Journal of Applied Meteorology and Climatology*, *47*, 206-22210.1175/2007jamc1661.1.

Roebeling, R. A., S. Placidi, D. P. Donovan, H. W. J. Russchenberg, and A. J. Feijt (2008b), Validation of liquid cloud property retrievals from SEVIRI using ground-based observations, *Geophys. Res. Lett.*, *35*L05814, doi:10.1029/2007gl032115.

Rossow, W.B., C. Delo, and B. Cairns (2002), Implications of the observed mesoscale variations of clouds for the Earth's radiation budget. *J. Climate*, 15, 557-585, doi:10.1175/1520-0442

Rozendaal M.A., C.B. Leovy and S.A. Klein (1995), An observational study of diurnal variations of marine stratiform cloud, *J. Climate*, 8, 1795-1809.

Sandu, I. and B. Stevens (2011), On the factors modulating the stratocumulus to cumulus transitions. *J. Atmos. Sci*., 68, 1865-1881.

Sandu, I., B. Stevens, and R. Pincus (2009), On the transitions in marine boundary layer cloudiness. *Atmos. Chem. Phy. Discussions*, 9, 23589-23622. doi:10.5194/acpd-9-23589-2009

Savic-Jovcic, V. and B. Stevens (2008), The Structure and Mesoscale Organization of Precipitating Stratocumulus. *J. Atmos. Sci*., 65 (5), 1587-1605.

Schulz, J., and Co-authors (2009), Operational climate monitoring from space: the EUMETSAT Satellite Application Facility on Climate Monitoring (CM-SAF), *Atmospheric Chemistry and Physics*, *9*, 1687-1709

Seethala, C., and Á. Horváth (2010), Global assessment of AMSR-E and MODIS cloud liquid water path retrievals in warm oceanic clouds, *J. Geophys. Res*., 115, D13202, doi:10.1029/2009JD012662.

Slingo, A. (1990), Sensitivity of the Earth's radiation budget to changes in low clouds. *Nature*, 343, 49-51.

Stephens G. L., G. W. Paltridge and C. M. R. Platt, (1978): Radiation profiles in extended water clouds. III. Observations. *J. Atmos. Sci*, 35, 2133-2141

Stevens, B, and Coauthors (2005), Evaluation of large-eddy simulations via observations of nocturnal marine stratocumulus. *Mon. Wea. Rev*., 133, 1443-1462.

Stevens, B. (2005), Atmospheric moist convection, *Annu. Rev. Earth Planet. Sci.*, *33*, doi:10.1146/annurev.earth.33.092203.122658.

Stevens, B., and A. Seifert (2008), Understanding macrophysical outcomes of microphysical choices in simulations of shallow cumulus convection. *J. Meteor. Soc. Japan*, 86, 143-162.

Stevens, B., G. Feingold, W. C. Cotton, and R. L. Walko (1996), Elements of the microphysical structure of numerically simulated non-precipitating stratocumulus. *J. Atmos. Sci*., 53, 980-1006.

Stevens, B., W. C. Cotton, G. Feingold, and C.-H. Moeng (1998), Large eddy simulations of strongly precipitating, shallow, stratocumulus- topped boundary layers. *J. Atmos. Sci*., 55, 3616-3638.

Stevens, D. E., S. A. Ackerman, and C. S. Bretherton (2002), Effect of domain size and numerical resolution on the simulation of shallow cumulus convection. *J. Atmos. Sci*., 59, 3285- 3301.

Szczodrak, M., P. H. Austin, and P. B. Krummel (2001), Variability of optical depth and effective radius in marine stratocumulus clouds. *J. Atmos. Sci*., 58, 2912-2926.

Torres, O., A. Tanskanen, B. Veihelmann, C. Ahn, R. Braak, P. K. Bhartia, P. Veefkind, and P. Levelt (2007), Aerosols and surface UV products from Ozone Monitoring Instrument observations: An overview, *J. Geophys. Res*., *112*, D24S47, doi:10.1029/2007JD008809.

Turner, D. D., et al. (2007), Thin liquid water clouds: their importance and our challenge, *Bull. Am. Meteorol. Soc.*, *88(2)*, 177–190.

VanZanten, M. C., B. Stevens, L. Nuijens, and Co-authors (2011), Controls on precipitation and cloudiness in simulations of trade-wind cumulus as observed during RICO. *J. Adv. Model. Earth. Syst*., 3, M06001, 13 pp., doi:10.1029/2011MS000056.

Várnai, T., and A. Marshak (2001), Statistical analysis of the uncertainties in cloud optical depth retrievals caused by three-dimensional radiative effects, *J. Atmos. Sci.*, *58*, 1540-1548.

Várnai, T., and A. Marshak (2002a), Observations of three-dimensional radiative effects that influence MODIS cloud optical thickness retrievals, *J. Atmos. Sci*., 59, 1607–1618.

Várnai, T., and A. Marshak (2002b), Observations of three-dimensional radiative effects that influence satellite retrievals of cloud properties, *Q. J. Hung. Meteorol. Serv*., 106, 265-278.

Várnai, T., and A. Marshak (2003), A method for analyzing how various parts of clouds influence each other's brightness, *J. Geophys. Res*., 108(D22), 4706, doi:10.1029/2003JD003561.

Várnai, T., and A. Marshak (2007), View angle dependence of cloud optical thicknesses retrieved by Moderate Resolution Imaging Spectroradiometer (MODIS), *J. Geophys. Res.*, *112*, D06203, doi:10.1029/2005JD006912.

Várnai, T., and R. Davies (1999), Effects of cloud heterogeneities on shortwave radiation: Comparison of cloud-top variability and internal heterogeneity. *J. Atmos. Sci*., 56(24), 4206-4224.

Watts P.D., Mutlow C.T., Baran A.J., and Zavody A.M., (1998), "Study on Cloud Properties derived from Meteosat Second Generation Observations," Final Report, EUMETSAT ITT no. 97/181

Wentz, F. J, and R. Spencer (1998), SSM/I rain retrievals within a unified all-weather ocean algorithm, *J. Atmos. Sci.*, *55*, 1613-1627.

Wentz, F. J. (1997), A well-calibrated ocean algorithm for special sensor microwave/imager, *J. Geophys. Res.*, *102*, 8703-8718.

Wentz, F. J., and T. Meissner (2000), AMSR ocean algorithm, version 2, *RSS Tech. Rep. 121599A-1*, Remote Sensing Systems, 66 pp.

Whiteman, D. N., and S. H. Melfi (1999), Cloud liquid water, mean droplet radius, and number density measurements using a Raman lidar. *J. Geophy. Res*., 104(D24), 31411-31419. doi:10.1029/1999JD901004

Wilcox, E. M., Harshvardhan, and S. Platnick (2009), Estimate of the impact of absorbing aerosol over cloud on the MODIS retrievals of cloud optical thickness and effective radius using two independent retrievals of liquid water path, *J. Geophys. Res*., *114*, D05210, doi:10.1029/2008JD010589.

Wilcox, E.M. (2010), Stratocumulus cloud thickening beneath layers of absorbing smoke Aerosol, *Atmos. Chem. Phys.,* 10, 11769-11777.

Wilson, C.A., J.F.B. Mitchell (1986), Diurnal variation and cloud in a general circulation model, *Quart. J. R. Met. Soc.* 112, 347-369.

Wood, R., C. S. Bretherton, and D. L. Hartmann (2002), Diurnal cycle of liquid water path over the subtropical and tropical oceans, *Geophys. Res. Lett.*, 29 (23), 2092, doi:10.1029/2002GL015371.

Wood, R.and D. L. Hartmann (2006), Spatial Variability of Liquid Water Path in Marine Low Cloud: The Importance of Mesoscale Cellular Convection, *J. Climate, 19*, 1748-1764

Wyser, K.,W. O'Hirok, C. Gautier, and C. Jones (2002), Remote sensing of surface solar irradiance with corrections for 3-D cloud effects, *Remote Sens. Environ*., 80, 272-284.

Yu, J.-Y., C. R. Mechoso (1999), Links between annual variations of Peruvian stratocumulus clouds and of SST in the eastern equatorial Pacific. *J. Climate*, 12, 3305-3318.

Zhang, M., and C. Bretherton (2008), Mechanisms of low cloud-climate feedback in idealized single-column simulations with the Community Atmospheric Model, Version 3 (CAM3), *J. Climate*., 21(18), 4859-4878.

Zhang, Z., and S. Platnick (2011), An assessment of differences between cloud effective particle radius retrievals for marine water clouds from three MODIS spectral bands, *J. Geophys. Res.*, 116, D20215, doi:10.1029/2011JD016216.

Zhao, G., and L. Di Girolamo (2006), Cloud fraction errors for trade wind cumuli from EOS Terra instruments, *Geophys. Res. Lett.*, *33*, L20802, doi:10.1029/2006GL027088.

Zinner, T., and B. Mayer (2006), Remote sensing of stratocumulus clouds: Uncertainties and biases due to inhomogeneity. *J. Geophys*. Res., 111, D14209, doi:10.1029/2005JD006955.

Zinner, T., and B. Mayer and M. Schröder (2006), Determination of three-dimensional cloud structures from high-resolution radiance data. *J. Geophys. Res*., 111, D08204, doi:10.1029/2005JD006062.

Zuidema P., D. L. Hartmann (1995), Satellite determination of stratus cloud microphysical properties, *J. Climate*, 8, 1638-1657.

Zuidema, P., and K. F. Evans (1998), On the validity of the independent pixel approximation for boundary layer clouds observed during ASTEX, *J. Geophys. Res*., 103, 6059–6074, doi:10.1029/98JD00080.

Zuidema, P., E. Westwater, C. Fairall, and D. Hazen (2005), Ship-based liquid water path estimates in marine stratocumulus, *J. Geophys. Res*., *110*, doi:10.1029/2005JD005833.

Zuidema, P., R. Davies, and C. Moroney (2003), On the angular radiance closure of tropical cumulus congestus clouds observed by MISR, *J. Geophys. Res*., 108(D20), 4626, doi:10.1029/2003JD003401.

ISSN 1614-1199